Tidal inlet systems: bottom pattern formation and outer delta development

Getijbekkens: vorming van bodempatronen en ontwikkeling van de buitendelta

(met een samenvatting in het Nederlands)

PROEFSCHRIFT

ter verkrijging van de graad van doctor aan de Universiteit Utrecht
op gezag van de Rector Magnificus, Prof. dr. W.H. Gispen,
ingevolge het besluit van het College voor Promoties
in het openbaar te verdedigen op

woensdag 11 september 2002 des ochtends om 10.30 uur

door

Sonja Maria van Leeuwen

geboren op 18 augustus 1972 te Schiedam

Promotor:	**Prof. dr. W.P.M. de Ruijter**
Co-promotor:	**Dr. H.E. de Swart**
	Instituut voor Marien en Atmosferisch onderzoek Utrecht (IMAU),
	Faculteit Natuur- en Sterrenkunde, Universiteit Utrecht
Samenstelling van	
de leescommissie:	Prof. dr. ir. M.J.F. Stive, Technische Universiteit Delft
	Prof. dr. ir. H.A. Dijkstra, IMAU/Universiteit Utrecht
	Prof. dr. J. Dronkers, IMAU/Universiteit Utrecht, Rijkswaterstaat
	Dr. H. Ridderinkhof, Nederlands Instituut voor Onderzoek der Zee

Dit proefschrift werd mogelijk gemaakt door financiële steun van de Nederlandse organisatie voor Wetenschappelijk Onderzoek (NWO), onder contract nr. 750-19-707.

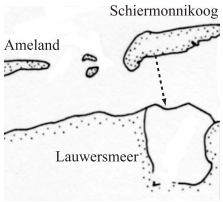

Cover: photo of a part of the Zoutkamperlaag, the eastern inlet system of the Frisian Inlet. The photo is taken from the harbour of the barrier island Schiermonnikoog towards the mainland: in the distance the sluices of the Lauwersmeer are visible. The orientation of the photograph is indicated in the graph above by the dashed line. Front cover: low water situation. Back cover: approximately 1.5 hours before high water. The poles are used to indicate the channels during high water.

ISBN 90-393-3126-X

Contents

Chapter 1

Introduction

This thesis focuses on tidal inlet systems and their morphodynamic behaviour and characteristics. In this introductory chapter an overview is given of the locations where tidal inlet systems are found, how they are characterised and how they originate. This is followed by a more detailed description of two specific inlet systems and a short introduction to morphodynamic research. Next, different morphodynamic models are briefly discussed, followed by a review of previous research results. Finally the research questions that will be addressed in this thesis are formulated, followed by a short description of the contents of the subsequent chapters.

1.1 Tidal inlet systems

Inlet systems are common features all around the world, accounting for some 12 % of the worlds coastline (Glaeser, 1978). The global occurrence of barrier island systems and inlets is depicted in figure 1.1, together with the local tidal regime. The latter is defined as either microtidal (spring tidal range $<$ 2 m), mesotidal (2 m $<$ spring tidal range $<$ 4 m) or macrotidal (spring tidal range $>$ 4 m) (Pugh, 1987).

An inlet system consists of a backbarrier lagoon or basin which is connected to the adjacent sea by means of a narrow strait. The basin is bounded by land and/or tidal watersheds. The latter form wet boundaries between adjacent basins at which the normal water velocity component is zero, thus minimising exchange between the basins. Inlet systems are called tidal inlet systems when the main channel through the strait is maintained by the tides (Escoffier, 1940). Thus they are different from open bays or rock-sided passageways. Figure 1.2 shows the general geometry of an inlet system. Tidal inlets can occur as single features (e.g. Arcachon Basin in France, Michel and Howa (1997)) or as a part of a string of barrier islands with inlets in between, e.g. the Wadden Sea in northern Europe (Ehlers, 1988), the east coast of the USA (Hayes, 1980; Stauble, 1993; Davis, 1998) or the coast of New Zealand (Hicks et al., 1999). Estuaries with small river discharge and strong tides, such that the water column is vertically well-mixed and no stratification occurs, can also be described as such (e.g the Western Scheldt in the Netherlands, see Van den Berg et al. (1990); Jeuken (2000)).

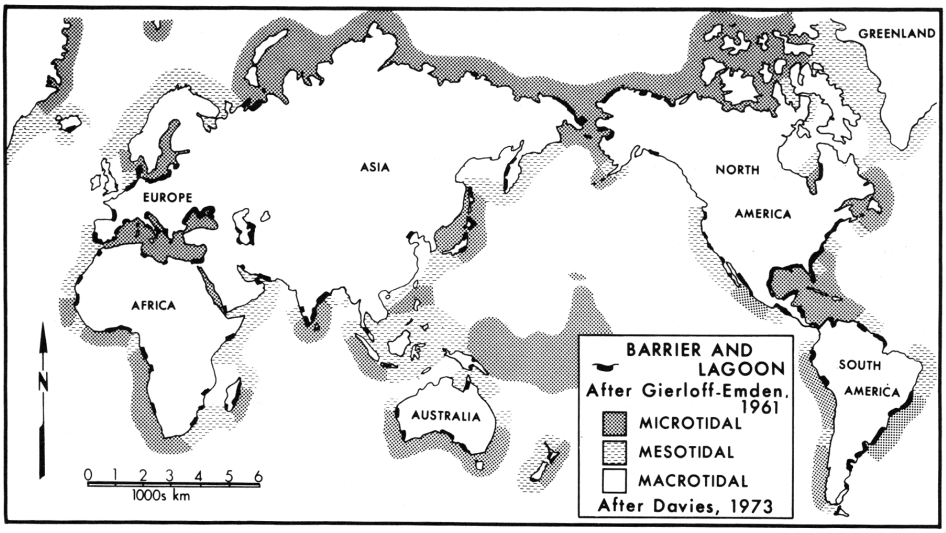

Figure 1.1: The global occurrence of barrier island and lagoon systems, from Hayes (1979).

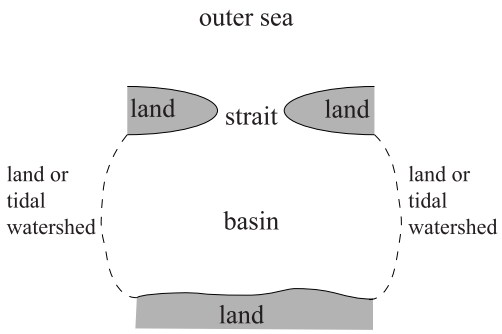

Figure 1.2: The general geometry of an inlet system, consisting of a basin which is connected to the adjacent sea by a strait. Grey areas are land. The sides of the basin represent the edges of the area which drains through the inlet. They are formed by either land or a tidal watershed.

Tidal inlet systems are mostly observed along continental margins which are tectonically passive in areas backed predominantly by coastal plains (Inman and Nordstrom, 1971; Glaeser, 1978). They form when dune ridges are breeched or become submerged, or when spits grow from a headland. Barrier island systems can also develop from emerging shoals (which can grow due to aeolian processes) or spit growth followed by spit breeching (Leatherman, 1988). Many tidal inlets are found in old river valleys, which were drowned when the global sea level rose and submerged the dune ridges (Ehlers, 1988; Oost, 1995).

Most tidal inlet systems have a bottom consisting of sediment which can be eroded, transported and redeposited by the prevailing currents.

Various areas can be identified within tidal inlet systems which are characterised by different physical forcing conditions and different morphological features. On the seaward side of the strait an outer delta (or ebb-tidal delta) occurs in mesotidal regimes. These shallow areas owe their existence to the transport of sediment by ebb-tidal currents from the basin to the sea. Their large-scale spatial pattern (on the scale of the basin length) consists of a deep, ebb-dominated channel (in which peak ebb currents are larger than peak flood currents) in the centre, flanked by two smaller-size flood channels on the sides. Superimposed on that pattern smaller-scale bars and channels are observed which have a strong variability, both in space and time (cf. FitzGerald (1996); Israel and Dunsbergen (2000) and references herein). Both tides and incoming waves are important for the hydro- and morphodynamics of outer deltas (Oertel, 1975; FitzGerald, 1996; Sha, 1989a). In microtidal regimes outer deltas are usually not observed.

The strait and basin are more sheltered against the waves, here the tide usually is the dominant hydrodynamic agency. On the basin side of the strait flood deltas are observed in inlet systems with microtidal conditions. Apart from the flood delta few morphological features are found inside the basin (Hayes, 1979). In inlet systems experiencing mesotidal conditions the entire embayment is often characterised by a fractal pattern of channels, separated by shoals, with depths generally decreasing from the sea towards the land (Hayes, 1979; Cleveringa and Oost, 2000). In macrotidal conditions inlet systems are usually not observed: the strong hydrodynamic conditions there prevent the settling of sediment. However, figure 1.1 shows that a small number of inlet systems are found in macrotidal regimes. The reason for this is not yet understood.

The description given above indicates that the hydro- and morphodynamics of tidal inlet systems will strongly depend on the local wave field and tidal range. Figure 1.3 shows some different types of inlet systems from around the world which experience different wave and tidal conditions. The hydro- and morphodynamics of inlet systems are also determined by sediment availability, geological setting and the storm climate.

A classification of inlet systems based on the relative importance of the different forcings was made by Hayes (1979). As it is impossible to include all different forcings this classification is based upon the ratio of tidal range and wave energy effects. In this thesis the focus will be on those inlet systems which Hayes classifies as mixed energy, tidally dominated inlet systems. They are characterised by large outer deltas and drumstick barrier islands. The tidal inlets located in the Dutch Wadden Sea are of this type. The motivation for this choice is explained in the next sections.

1.2 The relevance of tidal inlet systems

Tidal inlet systems are important because they strongly influence the sediment budget of the coast. As such they can affect the stability of neighbouring beaches or barrier island shorelines (FitzGerald, 1988; Fenster and Dolan, 1996). They also have a strong ecological significance because they serve as nurseries for fish larvae and as feeding

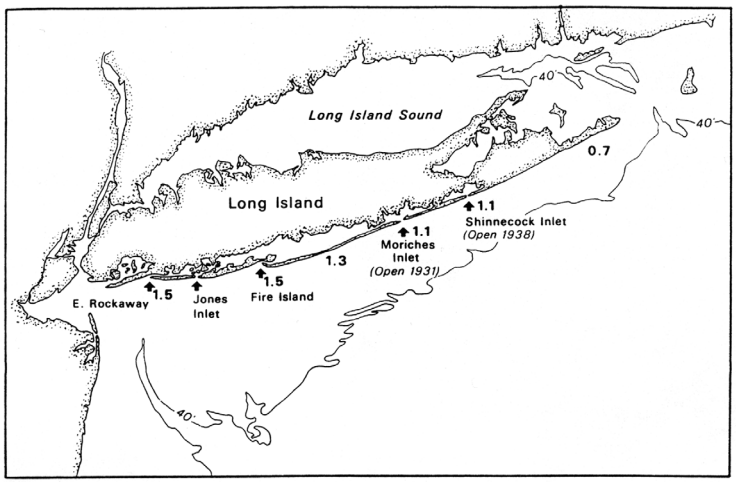

(a)

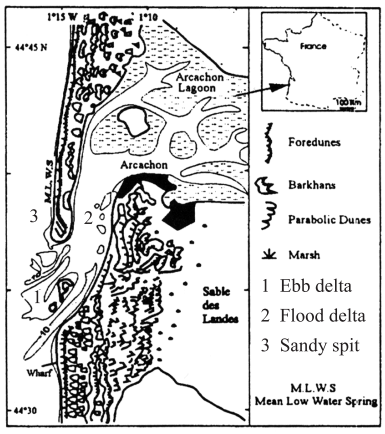

(b)

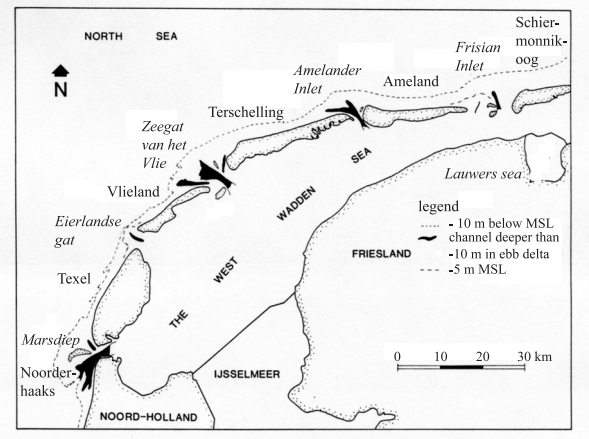

(c)

Figure 1.3: Different inlet systems, (a) barrier island system in a microtidal regime: Long Island shoreline on the east coast of the United States, from Fitzgerald (1996). The numbers indicate the local tidal range (m). Note the decrease of barrier island length with increasing tidal range, (b) wave dominated single inlet: Arcachon inlet in France, from Michel and Howa (1997), (c) barrier islands system in a mesotidal regime: the western Dutch Wadden Sea, located in the north of Europe, from Ehlers (1988). The black areas indicate channel depth of 10 m or more located in the outer delta.

grounds for many different species, including migrating birds. Moreover, the sheltered nature of the embayments gives them a strong economical and recreational importance, and many inlet channels are important navigation channels for harbours located within the basins.

Below two inlets in which significant human interference has taken place are discussed to demonstrate the complexity of tidal inlet dynamics and to illustrate some important differences between tidal inlets: the Marsdiep Inlet (or Texel Inlet) and the Frisian Inlet. Both are located in the Dutch Wadden Sea (see figure 1.3(c)) and serve as prototype tidal inlet systems in subsequent chapters of this thesis. A noticeable characteristic of the Wadden Sea is the presence of a semi-diurnal tidal wave following the coast from the southwest to the northeast. The mean tidal range varies from ~ 1.4 m near Marsdiep inlet to about ~ 2.3 m near the Frisian Inlet system, so that both inlets experience mesotidal conditions. The tidal wave following the coast ensures the dominance of tidal forcing over wave forcing in these inlets.

1.2.1 The Marsdiep Inlet system

The Marsdiep Inlet is the most westerly tidal inlet of the Wadden Sea and is located between the mainland of the Netherlands and the island of Texel. Figure 1.4 shows the present-day geometry and bathymetry of the western part of the Wadden Sea, with the Marsdiep Inlet as the first inlet from the left. The well-developed outer delta extends about 10 km to the west and 20 km from north to south and contains a supra-tidal (i.e. not submerged during high water) shoal (Noorderhaaks), a main ebb-channel (Schulpengat) and a flood channel (Molengat). The strait is relatively deep and narrow, with a maximum depth of 53 m and with a width of about 2.5 km. The backbarrier basin has a length of ~ 60 km and shows a complex pattern of channels and shoals. About 17 % of the basin area consists of tidal flats. Most of the bottom consists of fine sand with a grain size of 200 μm, but closer to the landward boundaries significant mud fractions are found. The tidal prism (the volume of water transported through the strait during one tidal cycle) is $\sim 10^9$ m^3 and the mean tidal range is 1.38 m near the inlet (Postma, 1982). Tidal currents reach values of more than 1.5 ms^{-1} during spring tide. Averaged wave heights on the outer delta are approximately 2 m and waves come predominantly from the southwest. However, during storms wave heights can be up to 4 m. Cyclic behaviour of bars and channels has been observed on the outer delta on the timescale of $\sim$ 70 years Sha (1989a). This involves the generation of shoals at the end of the ebb channel, which subsequently migrate in a clockwise direction over the outer delta. Each cycle ends with the attachment of the shoal to the island of Texel. Because the inlet is situated between two Pleistocene outcrops (consolidated material) the main inlet channel itself does not show migrating behaviour (Oost, 1995).

In 1927-1932 the Afsluitdijk was built, closing off the Zuiderzee (now called IJsselmeer, see figure 1.3(c)). The length of the main drainage channel (then through the Zeegat van het Vlie, the third inlet from the west in figure 1.4, see also figure 1.3(c)) was reduced by about 66 %. This changed the nature of the tidal wave entering the western Wadden Sea from a dominant travelling wave character to a more standing wave character. Also, the Marsdiep inlet system expanded by capturing parts of the truncated Zeegat van het Vlie system. The

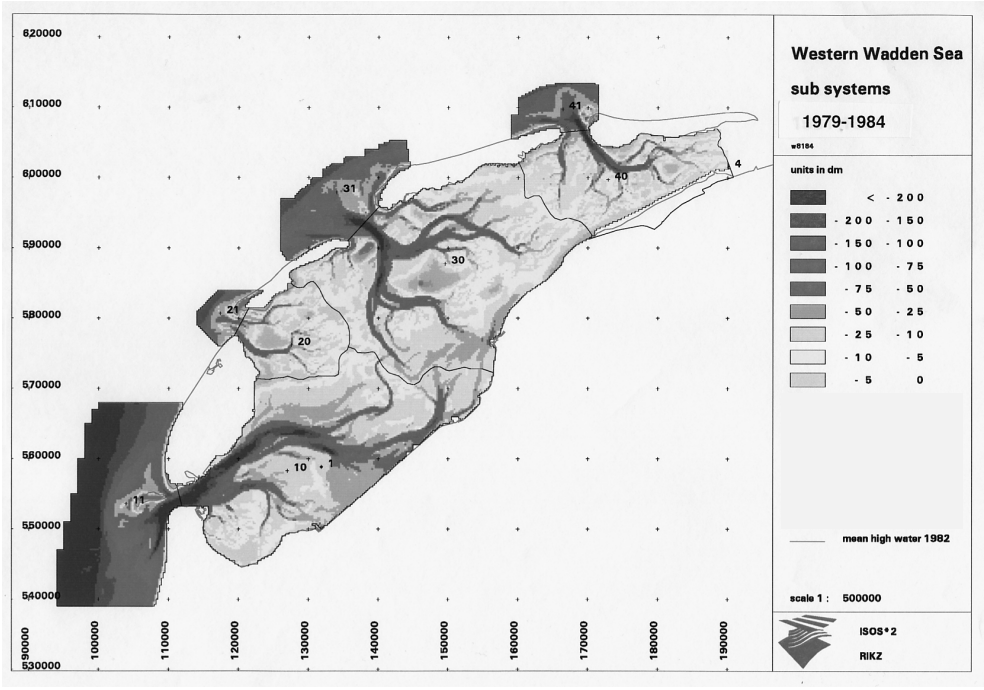

Figure 1.4: The bathymetry of the western part of the Dutch Wadden Sea, including the Marsdiep or Texel Inlet system (southern most inlet system). From RIKZ, Min. of Public Works, The Hague.

tidal amplitude near Marsdiep Inlet increased some 20 %. As a result of the increased tidal amplitude and the larger backbarrier area the tidal prism increased and the main channel became deeper (Oost and De Boer, 1994; Oost, 1995). These authors also expect a total net sedimentation in the backbarrier area of Marsdiep Inlet of about $200 \cdot 10^6$ m^3 over a period of 60 years due to the construction of the Afsluitdijk. Also, sea-level rise causes a continuous import of sediment into the backbarrier area.

Since 1993 data of currents and suspended matter concentrations are collected in the Marsdiep as part of the so-called TESO project, see Ridderinkhof et al. (accepted,a). It involves both regular collections of water samples, water depth and 13 h current+CTD (Current, Temperature, Density) measurements as well as the collection of data with an ADCP (Acoustic Doppler Current Profiler) mounted on the ferry which crosses the strait each 30 minutes between 6 a.m. and 9 p.m.. So far results indicate a mean export of water from the basin to the sea and a mean import of both suspended matter and sand into the backbarrier area (Ridderinkhof, pers. comm.). The latter seems consistent with bathymetric data.

1.2.2 The Frisian Inlet system

The Frisian Inlet system is located between the barrier islands of Ameland and Schiermonnikoog. Figure 1.5 shows its present-day morphology. The Frisian Inlet is a double inlet

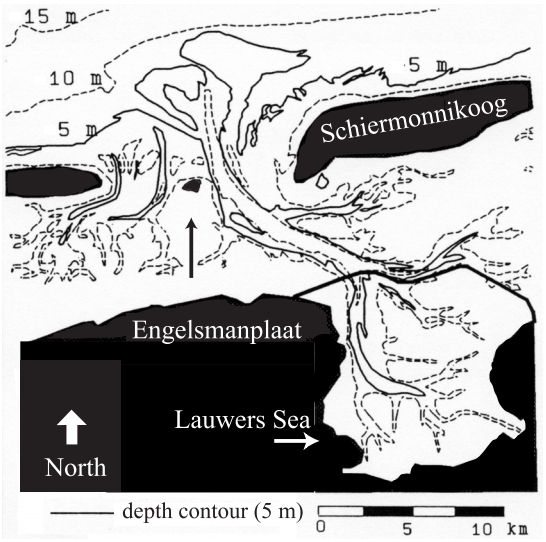

Figure 1.5: The bathymetry of the Frisian Inlet system before the closure of the Lauwers Sea. The dyke built in 1969 is indicated by a black line. From Wang et al. (1991).

system, consisting of the Pinkegat Inlet system on the west and the Zoutkamperlaag Inlet system on the east. A supra-tidal shoal, the Engelsmanplaat, is located in between. This shoal is a geological relict with a core of compact Holocene clay. Two distinct outer deltas have formed on the seaward side. The extent of the outer delta of the Zoutkamperlaag ($\sim$ 5 km) is considerably larger than that of the Pinkegat ($\sim$ 3 km). The basin area of the Zoutkamperlaag is also much larger than that of the Pinkegat. Nowadays, the tidal prisms for the Pinkegat and the Zoutkamperlaag are $160 \cdot 10^6$ m^3 and $200 \cdot 10^6$ m^3, respectively. The average grain size of the sediment is $\sim$ 200 μm (fine sand), but the mud content increases significantly towards the land. Figure 1.5 shows that the main channels on the outer delta of the Pinkegat and Zoutkamperlaag have an upstream orientation with respect to both the direction of the mean alongshore current and the direction of the tidal wave. In the Pinkegat, cyclic behaviour is observed, with channels forming at the western boundary of the inlet which subsequently migrate towards the Engelsmanplaat and ultimately disappear. Within this cycle, which has a timescale of $\sim$ 20 to 40 years, the Pinkegat system contains alternatively one or two ebb-channels on the outer delta, with both upstream and downstream orientations (Oost, 1995).

In 1969 the artificial closure of the Lauwers Sea (now called Lauwersmeer, see figure 1.5) led to a one third reduction in the tidal prism of the Zoutkamperlaag. As the basin area

was reduced by 30 % the morphology was no longer in equilibrium with the hydrodynamic conditions. An extensive monitoring of the system showed that between 1969 and 1987 sediment was imported into the basin and deposited there. The main channel rapidly decreased in depth and the watershed south of the barrier island Schiermonnikoog shifted eastward in this period. As a result of the sediment import the outer delta of the Zoutkamperlaag eroded. The net sedimentation in the Zoutkamperlaag backbarrier area is estimated at $70{\cdot}10^{6}$ m^3 over a period of 60 years (Oost and De Boer, 1994). Before 1969 cyclic behaviour of channels and shoals was observed in both inlets, in a similar fashion as that described for the Pinkegat Inlet. After 1969 cyclic behaviour has not been observed anymore in the Zoutkamperlaag (Oost and De Boer, 1994).

Information about the hydrodynamics, suspended sediment concentrations and sedimentological characteristics of the Frisian Inlet was discussed by Mulder (1993), see also Van de Kreeke and Dunsbergen (2000). They showed that in this area significant residual currents and higher harmonics of the principle M_2 tide occur and that these characteristics show strong spatial variability. They also found strong variations in the composition of the bottom.

1.3 Morphodynamic modelling

The strong morphodynamic response of the bottom that occurred in the Marsdiep and Frisian Inlet systems demonstrates the strong need for research on tidal inlet systems in order to understand, model and predict their highly complex dynamics. The processes that occur in tidal inlets and basins are very sensitive to changes in the exogenous conditions. Thus sea-level rise and human activities such as harbour construction, sand mining, extensive fishing or shipping channel maintenance can have a considerable impact on the system, and cause unforeseen problems. In order to predict and/or understand the response of a coastal system to such impacts morphodynamic models have been developed. Below some different types of morphodynamic models are briefly discussed and the physical concepts of sediment transport are explained.

1.3.1 Different morphodynamic models

Morphodynamic models can be divided in different categories, each with their own advantages and disadvantages. For an overview see De Vriend and Ribberink (1996). Here the basic differences between the various model approaches are summarised. The first category comprises data-based models, which only use observations and statistical techniques for prediction purposes. Empirical models are based on relationships which relate two or more variables characterising tidal inlet systems. The coefficients used in the powerlaws are estimated from observations. Empirical models are strongly linked to field data, but provide little insight into the physical mechanisms. Secondly, there are conceptual models which aim at describing a certain mechanism without using (or testing them with) equations of motion based on fundamental physical laws (like mass and momentum balances). A review of conceptual models with regard to processes on the outer delta was given by FitzGerald (1996).

The last category to be discussed is process-based models, which are based on first physical principles (e.g. mass conservation) and use mathematical equations to describe water motion, sediment transport and bottom change. There is a large variety of process-based models, but roughly they can be divided in two categories: 1. quasi-realistic models and 2. idealised models. The first of these include as many processes as is possible in order to give an accurate description of the physical world. As a result the models have a (limited) realistic prediction capability. However, their structure is too complex to yield insight into the dominant physical mechanisms. As an alternative, idealised models have been used over the past decade to gain fundamental knowledge about physical processes. Based on the governing laws of physics simplified equations of motion and sediment transport are used to construct the models and facilitate interpretation of the results. In this way, basic mechanisms can be identified but the models cannot be used to describe realistic physical settings. However, single mechanisms can sometimes be observed in the field and the knowledge gained from idealised models can be used to interpret the results obtained with quasi-realistic models.

1.3.2 Problems in morphodynamic modelling

One of the major problems in modelling is the wide range of different length and time scales involved. For instance, turbulence occurs on the timescale of seconds but tidal motion occurs on a timescale of hours. Bed ripples are formed and washed away within the time of one tidal cycle, whilst local channel and shoal formation occurs on the time scale of months to many years. The spectrum of the different time and length scales is illustrated in figure 1.6. The stochastic nature of the forcing is another problem, as well as the parameterisation of sediment transport. This latter aspect is addressed in more detail below.

1.3.3 Principles of sediment transport and morphological change

Sediment transport

Sediment particles resting on the bed only start to move when the shear stress (τ) acting on them exceeds a certain threshold value (τ_c). As the shear stress can be related to the flow velocity above the bed this means that the flow velocity must exceed a critical value before particles start to move. At critical conditions the lift force exerted on the particle together with the drag force vectorially equals the gravitational force acting on the particle. When the flow velocity exceeds the critical velocity the lift and drag force are able to release the particle from the bed. The transport of sediments is often divided in two different types. This requires the introduction of two quantities, the friction velocity u_* and the settling velocity w_s. The first is defined by $\tau = \rho u_*^2$, where τ is the bottom shear stress and ρ the water density. The settling velocity is the velocity by which a sediment particle sinks to the bottom in stagnant water. When the local friction velocity is larger than the critical friction velocity u_{*c}, but smaller than the settling velocity ($u_{*c} < u_* < w_s$) the particles will remain in contact with the bed. This is called bedload transport and involves the rolling, gliding and jumping of sediment particles in a thin layer (thickness of order 1 cm) close to the bed. When the local flow velocity exceeds both the critical friction velocity and the settling velocity ($u_{*c} < w_s < u_*$) the particles become suspended in the water column and lose

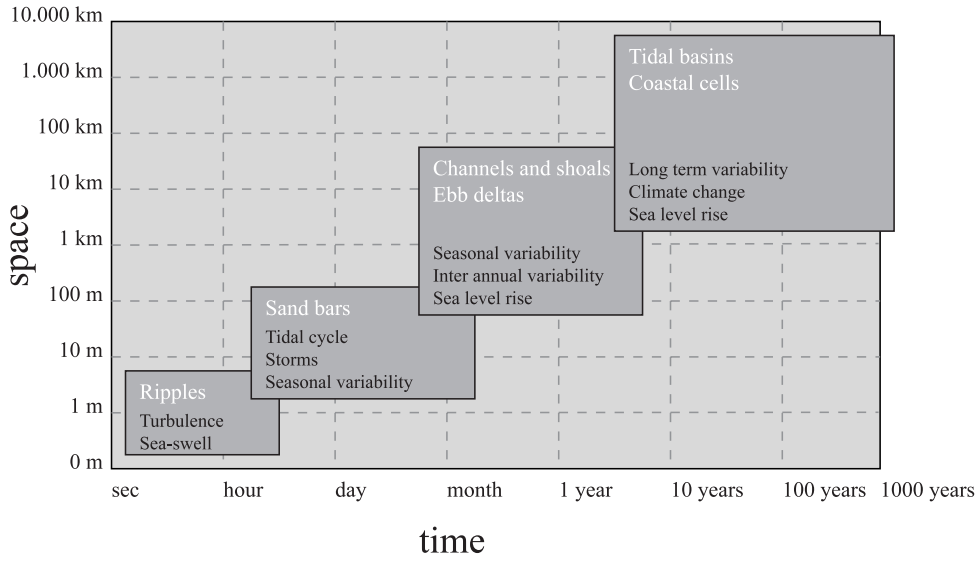

Figure 1.6: Tidal inlet system features (white) and their main forcings (black) as a function of time and space, based on the concept of De Vriend (1991).

contact with the bed. This is called suspended load transport: the movement of particles is supported by fluid motion. The combined bedload and suspended load transport is referred to as total load transport. An important property of particles suspended in the water column is that they need a certain time to reach the bed. This time span is referred to as the settling lag and implies a significant difference between bedload and suspended load transport of sediment. Effectively it means that there is a time lag between the maximum velocity and the maximum concentration of sediment in the water column. This is particularly relevant for oscillating, hydrodynamical conditions. Further details can be found in Dyer (1986); Fredsoe and Deigaard (1992); Van Rijn (1993) and Soulsby (1997).

A difficult point in any process-based model is the parameterisation of sediment transport. It is generally not possible to derive a formulation from the movement of many individual particles because the underlying dynamics are very complex: they involve turbulent processes and intergranular collisions. In most models so-called bulk formulations are used. They describe the average flux due to the movement of many particles. Bedload transport is often parameterised as an algebraic and monotonically increasing function of the instantaneous velocity (see for example the references given above). This can also be done for suspended load and total load sediment transport in case that the settling period of particles is small compared with the hydrodynamic timescale. For fine sand (diameter $\leq$ 250 μm) settling lag effects are important and the computation of suspended load transport then involves the solution of a concentration equation with parameterisations for the erosion and deposition fluxes near the bed (in fact at the top of the bedload layer). These parameterisations are subject to many uncertainties, as they depend on specific hydro-

and morphodynamic conditions. Effects of local bottom slopes are often incorporated into the bedload formulation to model the preferred downhill transport of sediment.

Mechanisms for net sediment transport due to tides

In tidally dominated areas there are 4 principal mechanisms to induce sediment transport. The first is stirring of sediment by the leading tidal constituent, for the Dutch Wadden Sea this is the M_2 tidal component (semi-diurnal lunar tide). The sediment is subsequently transported by the residual current M_0, which is defined as the time-independent flow and is generated by tide-topography interactions (Van de Kreeke and Robaczewska, 1993). The second mechanism is tidal asymmetry. Here the generation of oscillating overtides (e.g. M_4, M_6) by tide-topography or tide-geometry interactions causes a deformation of the tidal curve, resulting in a longer duration of the flood or ebb period. Peak velocities change as the time over which the water is transported in- or outwards changes, leading to erosion and deposition patterns. Thirdly, there is the settling lag effect of fine sediments, causing landward particle transport in tidal embayments as sketched in figure 1.7. A particle

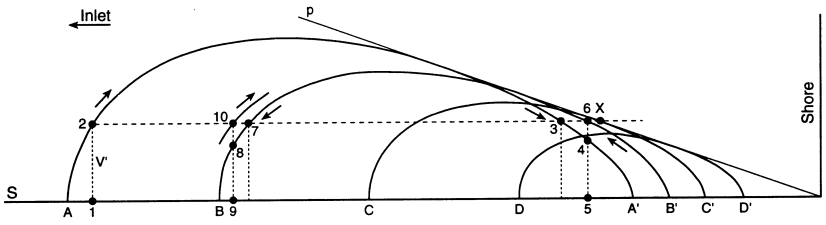

Figure 1.7: The settling lag effect of fine sediments, causing a landward sediment transport. Numbers indicate the successive pathways of suspended particles during a number of successive tidal cycles. Letters indicate the pathway of the successive water masses capable of (eroding and) transporting the particle. From Van Straaten and Kuenen (1958).

transported landwards by the flood current will settle at a point closer to the coast (position 4) than the point where the velocity becomes to weak to transport the particle (position 3). The reason is that it takes time for the particle to reach the bottom. At this point the tidal current amplitude is weaker than at points located further seaward. Therefore, it can only be eroded by a water mass which is closer to the shore (water mass B, reaches B') than the water mass which originally transported the particle (water mass A, reaches A'). Because of this the particle will be deposited landwards of its original position (9) by the ebb current. Repetition of this movement brings the particle closer to shore.

Morphodynamic feedback and equilibrium

Once the sediment transport is determined, the bed level change can be calculated. But the changing bed level will affect the hydrodynamics, and thus the sediment transport. Morphodynamic models must incorporate the feedback mechanism between water motion, sediment transport and bottom change in order to yield realistic results. This is done in what is called a morphodynamic loop (see figure 1.8): first the water motion and sediment concentration are calculated for an initial, given bathymetry. Then the erosion and deposition pattern is determined by calculating the spatial convergence and divergence of the net sediment flux. For example, in the case of tide-dominated water motion (as is considered in this thesis) this is the flux averaged over a tidal cycle. Next the bottom is adjusted according to the erosion and deposition pattern. The loop is completed by again calculating the water motion and sediment transport using the updated bathymetry. Note that it is assumed that

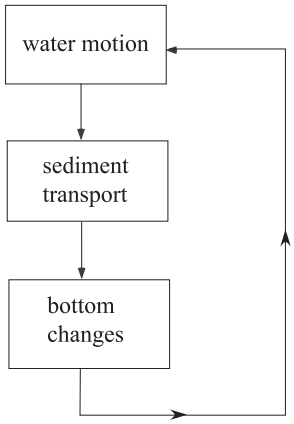

Figure 1.8: The loop used in morphodynamic models

the bathymetry does not change during the calculation of the hydro- and sediment dynamics. This because the timescale of bottom change (months or longer) is much larger than the timescale for water motion (hours).

The morphodynamic loop can be applied for a specific timespan or until a situation with very small sediment transport is found. In the latter case the bathymetry will hardly change in time and the system is said to be in morphodynamic equilibrium. This refers to a situation in which the hydrodynamics are in equilibrium with the morphology, resulting in negligible net sediment transport throughout the domain with no changes in the bottom topography. This does not imply that currents are also steady in morphodynamic equilibrium. For example, in the case of tide-dominated motion the currents will be oscillatory. Morphodynamic equilibrium means that the amplitude and the phase of the current will be time-independent.

1.4 Results from previous studies

In the following, recent results from studies with different models which are relevant for the context of this thesis are briefly discussed.

A conceptual model for cyclic bar behaviour and outer delta characteristics of the Marsdiep Inlet was formulated by Sha (1989b,c). Its main statement is that the interaction between shore-parallel tidal currents and tidal currents in the strait is important to understand the formation of shoals in this area and the characteristics of the outer delta. The phase difference of these currents causes tidal currents to be strong and bidirectional on the southern (updrift) side of the seaward part in front of the inlet entrance and more circular and weaker on the northern (downdrift) side. These differences would result in preferred deposition of sediment on the downdrift side of the outer delta which would explain the observed updrift orientation of the main ebb channel. Besides, bars could easily form at the end of the ebb channel (deposition of sediments transported by the ebb current) which would subsequently migrate due to aeolian processes and wave effects. A similar conceptual model for cyclic bar behaviour in the Frisian Inlet was discussed by Oost (1995).

As examples of recent quasi-realistic morphodynamic model results the work of Wang et al. (1991), Ranasinghe et al. (1999); Ranasinghe and Pattiaratchi (1999) and Cayocca (2001) are worth mentioning. Wang et al. (1991) used the model DELFT3D (developed by WL/Delft Hydraulics) to simulate the long-term evolution of the Frisian Inlet system in depth-averaged terms. Wave effects were neglected. They suggested the importance of the Engelsmanplaat for the stability of the Frisian Inlet system as a double inlet system. Long-term morphological simulation reproduced some gross features observed in the Frisian Inlet system since the closure of the Lauwers Sea. However, detailed morphological changes could not be reproduced by the model and the gross comparison of observed and modelled changes in the outer delta was not entirely satisfactory. Observed sediment loss on the outer delta due to sediment demand in the basin was found in the model results but the observed morphological development of the outer delta since the closure could not be reproduced.

Ranasinghe et al. (1999) studied the seasonal closure and opening of a small inlet on the Australian coast. They showed that the joint effect of (seasonally varying) wave and tide conditions are important to simulate such behaviour.

Cayocca (2001) applied a two-dimensional horizontal (2DH) model with realistic geometry to Arcachon Inlet in France. The results show that starting from a flat bed, sediment is deposited in the outer delta region under wave and tidal forcing. Experiments were performed with semi-diurnal tidal forcing only and with combined wave and tidal forcing while using a realistic bathymetry, but no migration of channels was found. The model did produce several observed features like the opening of a new channel. Mechanisms for outer delta development could not be identified since the original bathymetry was only flattened in the strait and basin area, thus including the already existing outer delta shape.

In the last decade, idealised models have been developed to facilitate interpretation of both field data and quasi-realistic model results. Motivated by the work of Krol (1991) and Van Dongeren and De Vriend (1994) , which was largely numerical, a semi-analytical

1D morphodynamic model for a sheltered semi-enclosed tidal embayment was developed by Schuttelaars and De Swart (1996). In this model the embayment has a constant width and its length is small with respect to the tidal wave-length (i.e., it is short). Forcing of the water motion is due to prescribed sea level elevations at the seaward boundary which have an M_2 and M_4 component. Suspended load transport of fine sand with a uniform grain size is considered, which involves both advective and diffusive transport components. Furthermore simple formulations for the sediment pick-up function and deposition flux near the bed are used; in particular the deposition flux depends on the depth-integrated sediment concentration. They showed that, for all combinations of the parameters, the system has a unique morphodynamic equilibrium, i.e. a state for which the bottom is steady. It was also demonstrated that this equilibrium is stable in the context of their model, i.e. if it is perturbed the system which return to this state. Moreover, time integrations indicated that this morphodynamic equilibrium is globally stable, i.e. solutions starting from arbitrary initial bottom profiles tend to this state. In case of only M_2 forcing this equilibrium is characterised by a linearly sloping bottom with decreasing depth towards the land and the amplitudes of both the free surface elevations and of the tidal currents are spatially uniform. These results are in agreement with the field data discussed by Friedrichs (1995) which indicate that a tidal channel in morphodynamic equilibrium is characterised by a spatially uniform bottom shear stress (as is also found in the model). Computed bottom profiles also turned out to be consistent with observed bottom profiles in various embayments of the Dutch Wadden Sea (De Swart and Blaas, 1998). Later on it was demonstrated by Schuttelaars and De Swart (2000) that morphodynamic equilibria also occur in longer embayments and that the corresponding bottom profiles compare favourably well with field observations. If the external M_4 forcing at the seaward entrance is sufficiently strong their model even allows for multiple morphodynamic equilibria for the same set of parameters. However such conditions seem not to be met in the field.

A different approach was followed by De Jong and Heemink (1995, 1996) and De Jong (1998). They considered a one-dimensional tidally averaged model of an estuary or a medium to short tidal basin. River inflow is accounted for in the case of an estuary. Hypsometric effects due to tidal flats are not included and both a straight and a converging geometry are used. The applied forcing consists of the leading tidal constituent (M_2, the main semi-diurnal tide) and its first overtide (M_4). Internal generation of overtides by non-linear terms in the equations of motion is neglected. They also consider suspended load transport of fine sediment but their formulation of the deposition flux near the bed differs from that used by Schuttelaars and De Swart (1996), since it is proportional to the depth-averaged, rather than the depth-integrated concentration. The results showed that length and shape of the geometry have a strong influence on the resulting equilibrium bed profile. Furthermore, there is a significant difference between modelling short, medium and long estuaries: results obtained with a model for short embayments cannot be extrapolated to long embayments. The results are sensitive to the boundary condition imposed at the seaward side, the ratio of diffusive and advective transport of sediment and the strength of bottom friction. Interestingly, the medium size basin shortens itself to the size of a short basin for some parameter choices.

Although morphodynamic equilibria are always stable within a 1D context, they can

be unstable with respect to perturbations with a two-dimensional structure. The study of Seminara and Tubino (1998) showed that bars can develop in an open, narrow and strongly dissipative tidal channel as free morphodynamic instabilities of the coupled water-bottom system. Sediment in this model is transported as suspended load by advective processes (no diffusion). The perturbations with the largest growth rates (which become dominant after some time) have lengths which scale with the channel width. Migration of the bars was not found in this study.

Schuttelaars and De Swart (1999) studied the initial formation of a different class of bottom patterns which arise as free instabilities of a morphodynamic equilibrium in a weakly dissipative, semi-enclosed short tidal embayment. Their model accounts for suspended load transport which only has a diffusive component. This is the dominant transport mode in short embayments which are only forced by M_2 tides. The results show that if bottom friction is sufficiently strong the 1D morphodynamic equilibrium becomes unstable: 2D perturbations grow and form a channel/shoal like structure. The most preferred perturbations turn out to have an along-channel spatial scale which is of the order of the embayment length. The physical mechanism is described as a competition between the stabilising effect of continuity and the destabilising effect of bottom frictional torques on the bed perturbations. Applying non-linear stability analysis migration of features was found (Schuttelaars and De Swart, 1999).

1.5 Open problems in tidal inlet systems research

From the description of the research given in the previous section a number of open problems emerge which require further investigation. With regard to the modelling of morphodynamic equilibria and the adjustment towards such equilibria, different models have been used (viz. Schuttelaars and De Swart (1996); De Jong (1998)) which focus on different physical aspects. No attempts have yet been made to link them. In particular the sensitivity of the model results to the sediment transport formulation, the degree of channel convergence and the presence of tidal flats along the boundaries of the channel is not clear. Another relevant issue is to investigate the effect of human interferences (e.g. dike constructions) and sea-level rise on the characteristics of morphodynamic equilibria and related sediment import or export. A final aspect that deserves attention is the robustness of results obtained from 1D models with respect to the model formulation. In other words, are morphodynamic equilibria also captured by more complex models?

With regard to channel-shoal formation due to tide-topography interaction two classes of bed forms have been detected so far: the tidal bars of Seminara and Tubino (1998) and the tidal shoals of Schuttelaars and De Swart (1999). However, both classes apply to rather different geometrical and physical settings. It is therefore interesting to investigate the link between these two types of bed forms: can they be studied within the context of one overall model? Another important point is the potentially large influence of exchange processes between the tidal basin and the adjacent sea. In the idealised morphodynamic embayment models studied so far simple boundary conditions at the seaward entrance have been imposed,

but it is important to study the influence of processes which occur in the outer sea on the hydro- and morphodynamics of the embayment.

The fact that exchange processes are indeed important can be seen from the presence of outer deltas on the seaward side of embayments. The main ebb channel of outer deltas of mixed energy, tide-dominated inlet systems has an updrift orientation and repetitive formation, migration and attachment of shoals on barrier islands is observed on outer deltas. Conceptual ideas about the underlying physical processes have been presented by Sha (1989b,c), but these concepts have never been tested with process-based morphodynamic models.

These considerations lead to the research questions that will be addressed in this thesis. They are:

Q_1 : What are the effects of changes in sediment transport formulation, channel width convergence and the presence of tidal flats on the adjustment towards and the properties of morphodynamic equilibria?

Q_2 : Which type of 2D bottom patterns develop as free instabilities on a 1D morphodynamic equilibrium in a model of a short, semi-enclosed tidal embayment if suspended load transport related to both advective and diffusive processes is taken into account and are such bed forms also found if more complex models are used?

Q_3 : How do exchange processes between the outer sea and inner basin influence the hydro- and morphodynamics inside the embayment?

Q_4 : What physical mechanism causes the initial formation of outer deltas and what mechanism is responsible for the observed asymmetry in the orientation of the main ebb channel on the outer delta?

Q_5 : Which physical mechanisms determine cyclic bar behaviour on outer deltas?

The research questions are listed with reference numbers that will recur throughout the thesis.

1.6 Research approach of the thesis

To address the research questions listed above different approaches are used in this thesis. In Chapter 2, research question Q_1 will be addressed. Schuttelaars and De Swart (1996) have shown the existence of a unique morphodynamic equilibrium for a one-dimensional, idealised model. The same type of model is used here to investigate the influence of different sediment transport formulations on the morphodynamic equilibrium. The model is derived for a funnel-shaped basin consisting of a channel bordered with tidal flats. The one-dimensional model solutions can be extended in the cross-channel direction, and as such are solutions of the two-dimensional (horizontal) problem without Coriolis effects. This way, they form the basis of the two-dimensional perturbation model used in Chapter 3.

Research question Q_2 is addressed in Chapter 3. For this purpose the two-dimensional model of Schuttelaars and De Swart (1999) is extended to account for advective processes in

the water motion and in the sediment transport module. As a basis a one-dimensional solution of Chapter 2 is used. The effect of the joint action of diffusive and advective transport on the initial formation of bed forms can thus be investigated. The results will be compared to those of the quasi-realistic model DELFT3D. This numerical model will be referred to in this thesis as DELFT2D-MOR, because only the depth-averaged version is used here to calculate morphological changes.

As the simplified geometry of an idealised model prevents the inclusion of an outer delta, a model of intermediate complexity is constructed in Chapter 4 to address research questions Q_3, Q_4 and Q_5. This model is named an intermediate model as the hydrodynamics are calculated with a numerical model that solves the full 2D shallow water equations, whilst the sediment transport is represented by an idealised formulation, and in addition simplified geometries are used. Thus, this model serves as a link between quasi-realistic models and idealised models. In Chapter 4 the model is used to assess the influence of the hydrodynamic conditions in the outer area of the system on the hydrodynamics and sediment-transport patterns within the basin (research question Q_3). Experiments are performed to investigate the effect of the Coriolis force and a longshore travelling tidal wave on the basin hydrodynamics. These forcings are not applied in idealised model studies of basin hydrodynamics. Therefore, a rectangular basin geometry without a narrow strait or outer delta (as used in the idealised model of Schuttelaars and De Swart (1996, 1999)) is also considered, with the same forcings applied at the open boundary. This allows for a comparison of the idealised model with the more complex intermediate model. In addition to these experiments, the hydrodynamic part of the existing conceptual model of Sha (1989b) explaining the preferred direction of the main ebb channel on the outer delta is tested (part of research questions Q_4 and Q_5).

In Chapter 5 both the intermediate model and the quasi-realistic model DELFT2D-MOR are used to investigate research question Q_4 and Q_5. The use of the intermediate model allows for a detailed physical interpretation of the results on initial sediment erosion and deposition patterns, whilst the quasi-realistic model is able to simulate long-term morphodynamic evolution of the inlet system. The geometry used here consists of an outer delta, a strait and an embayment resembling the Frisian Inlet system. Starting from a flat bathymetry with an off-shore slope initial erosion and deposition patterns are investigated with the intermediate model in order to determine mechanisms for initial outer delta formation. Here the existing theory mentioned above, explaining the orientation of the main ebb channel on the outer delta, is tested with respect to sediment deposition patterns. The research in this chapter will also show the capability of the intermediate model (i.e. the simplified sediment routine) for calculating initial sediment transport patterns compared to the quasi-realistic model.

Finally, the results of the previous chapters are summarised in chapter 6. The research questions will again be addressed in order to see to what respect they have been answered and what remaining and new research questions are.

Chapter 2

Effect of geometry and sediment flux formulation on equilibrium bottom profiles

Abstract

The characteristics of morphodynamic equilibria, as well as the adjustment towards a morphodynamic equilibrium in short tidal embayments are investigated by using a one-dimensional idealised model. The embayment is schematised as a semi-enclosed domain with an open boundary at the seaward side and an exponentially decreasing width towards the landward side. Furthermore, it has a rectangular cross section below the low water level and sloping side-walls above it. Only the bottom in the area below low water level is erodible. The model is driven by prescribed sea level variations at the entrance which consist of a leading tidal constituent (M_2 tide) and its first overtide (M_4 tide). It describes the dynamics of the cross-sectionally averaged shallow water equations for a homogeneous fluid, supplemented with a depth-integrated and width-averaged concentration equation and a bottom evolution equation. The influence of combined diffusive and advective transport of sediment, as well as the separate effects of these sediment fluxes, on morphodynamic pattern formation are examined for different cases. The new elements in that respect are the consideration of a funnel-shape of the embayment, hypsometric effects due to the presence of tidal flats and explicit depth-dependent erosion and deposition of sediment.

The results show that the system allows for a stable morphodynamic equilibrium, of which the properties hardly depend on the geometrical parameters, and weakly depend on the sediment flux parameterisation. The tidal forcing characteristics have a strong influence on the equilibrium properties. In case of external forcing by only an M_2 tide both an increasing channel width convergence and stronger hypsometric effects tend to favour concave bottom profiles if advective sediment fluxes dominate. With increasing influence of diffusive sediment fluxes more convex bottom profiles are found. Adding a first overtide to the external forcing generates additional advective sediment transport and can cause a partial fill-up of the basin. Similar results are found in case that explicit depth-dependent formulations for erosion and deposition fluxes near the bed are used. Both a partial closure and a sea-level rise cause a net sediment flux into the embayment. These results seem consistent with both field data and results obtained with a complex morphodynamic model.

2.1 Introduction

Semi-enclosed tidal embayments are common features along the world's coastlines. Examples can be found along the UK coast (Uncles and Stephens, 1989), in the German and Dutch Wadden Sea (Ehlers, 1988), in the delta area in the southwest of the Netherlands (Van den Berg et al., 1990; Jeuken, 2000) and along the east coast of the United States (FitzGerald, 1996). Many of them have a sandy and/or muddy bottom and are characterised by strong tidal currents of the order of 1 ms^{-1}. Waves, wind-driven flows and density-driven currents (caused by river discharge) also play a role. Due to their mutual feedbacks the water motion and the morphology are highly complex both in space and time. For example, embayments often have a large-scale fractal pattern of channels (Cleveringa and Oost, 2000) with decreasing depth towards the landside. On a smaller scale bars are observed which often show cyclic behaviour of generation, migration and disappearance on timescales of $\sim 7-100$ years, see Robinson (1975); FitzGerald (1996); Israel and Dunsbergen (2000).

Many numerical models have been developed to yield an accurate simulation of the hydrodynamics of realistic tidal embayments, see for instance Ridderinkhof (1988a); Ridderinkhof and Zimmerman (1992). In these studies it is shown that tide-topography interaction results in residual circulation cells which cause efficient mixing of dissolved matter. Nowadays, also models are available which are able to successfully simulate the interaction between water motion, erosion and deposition of sediment and the evolving morphology, see Wang et al. (1991, 1995); Ranasinghe et al. (1999) and Cayocca (2001). However, due to their complexity such models are not well suited for gaining fundamental knowledge about the basic mechanisms generating the observed patterns. Alternatively, more simple models, designed to gain understanding about basic physical mechanisms, have been investigated. Speer and Aubrey (1985) studied tidal propagation in a well-mixed estuary with a fixed width and depth, using a one-dimensional (cross-sectionally averaged) model, and demonstrated the importance of non-linear terms and the presence of tidal flats in generating flood- or ebb-dominated water motion. This work was generalised to channels with exponentially decreasing widths by Friedrichs and Aubrey (1994). They showed that the spatial distribution of tidal amplitude and phase is largely determined by the competing effects of width convergence and bottom friction. Later on Lanzoni and Seminara (1998) showed that tidal propagation in strongly dissipative estuaries is sensitive to the precise formulation for the bottom shear stress: a non-linear formulation results in the formation of bores.

An idealised one-dimensional morphodynamical model of a sheltered tidal embayment was studied by Schuttelaars and De Swart (1996). They considered a rectangular and short embayment (its length being small compared to the tidal wave-length) with fixed coast-lines and an erodible bottom. The water motion is driven by tides and no waves or density currents are included in this model. Using simple formulations for sediment erosion and deposition they showed the existence of a unique morphodynamic equilibrium which consists of a constantly sloping bottom in the landward direction and which has spatially uniform sea surface elevations and spatially uniform tidal currents. Later on this work was extended to longer basins (De Jong, 1998; Schuttelaars and De Swart, 2000). The results obtained with such idealised models are consistent with field data. In De Swart and Blaas (1998) along-channel bottom profiles are shown which have been reconstructed from bathymetric data of seven tidal channels in the Dutch Wadden Sea, see figure 2.1. As can be seen the depths of all channels

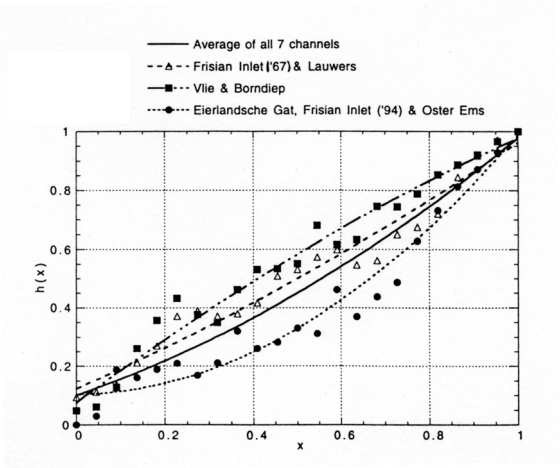

Figure 2.1: Scaled along-channel bottom profiles of several tidal channels in the Dutch Wadden Sea. Markers indicate actual data, curves are the best fits with quadratic polynomials. From De Swart and Blaas (1998).

decrease in the landward direction. Some channels are characterised by convex bottom profiles, whilst those of other channels have more concave profiles. What causes a bottom profile to becomes convex or concave is not yet understood. Schuttelaars and De Swart (1996) found both convex and concave bottom profiles, depending on the phase difference between the M_2 and M_4 tidal components in the forcing. Without the first overtide only the linearly sloping bottom was found. De Jong (1998) (also published in De Jong and Heemink (1995, 1996)) found similar results.

Both studies mentioned above use different formulations for sediment deposition, but the influence of these different formulations on the results was not investigated. Furthermore, they both considered erosion of sediment which did not depend explicitly on the depth. However, erosion is determined by the bed shear stress, which involves a drag coefficient and the latter is often formulated as an explicit function of the local depth, see Soulsby (1997). Also, the effects of a funnel-shaped estuary with tidal flats were not studied in a morphodynamic model.

The aim of the present work is therefore to extend the one-dimensional morphodynamic model of Schuttelaars and De Swart (1996) mentioned above in two ways. The first is to study the sensitivity of the model results to different formulations for sediment erosion and deposition. The second extension is to consider funnel-shaped embayments which have a deep channel and lateral shoals which fall dry during low tide. These generalisations can have profound implications for the shape and the stability properties of morphodynamic equilibria. The extensions create a link between the model used by Schuttelaars and De Swart (1996) and that used by De Jong (1998).

In section 2.2 the model is derived, including the scaling and the boundary conditions. Section 2.3 contains the results and this is followed by a discussion and conclusions.

2.2 The model

2.2.1 Geometry

The embayment is schematised as a rectangular basin below low water level and sloping sides above the low water level (LWL), representing tidal flats (see fig. 2.2). Similar geometries were also considered in Friedrichs and Aubrey (1994) and Lanzoni and Seminara (1998), but their analysis was limited to the tidal hydrodynamics. De Jong (1998) considered funnel-shaped estuaries but ignored the hypsometric effects caused by drying and flooding of the tidal flats. Here it is assumed that the bottom below LWL is erodible and flow velocities are assumed to vanish in the tidal flat area. The embayment has an open connection to the adjacent sea and is bounded on the landward side. A Cartesian coordinate system is chosen, with the x, y, z axis denoting the along-channel, cross-channel and vertical direction respectively. The actual width $\tilde{b}$ of the embayment can be expressed in the width at mean slack level (MSL)

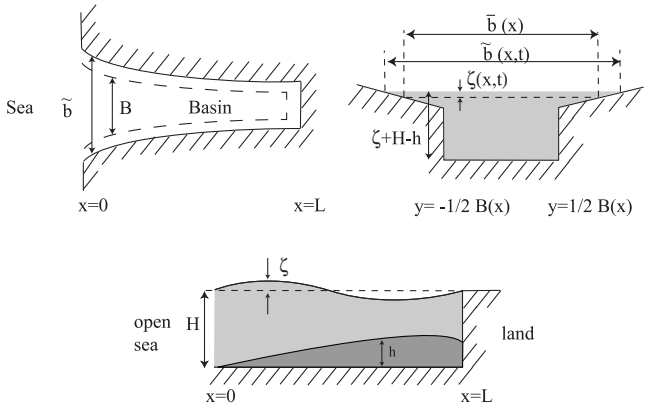

Figure 2.2: Embayment geometry with tidal flats, topview (left), cross-section (right) and sideview (below). Here $B(x)$, and $\overline{b}(x)$ are the channel width during low water and mean slack level, respectively. The actual width of the channel is denoted by $\tilde{b}(x,t)$. Furthermore, ζ is the sea surface elevation with respect to MSL, H is the undisturbed water depth at $x = 0$ and h is the bottom elevation with respect to $z = -H$.

$\overline{b}(x)$ and the width at low water $B(x)$ by

$$\tilde{b}(x,t) = B(x) + \left(\overline{b}(x) - B(x)\right)\left(1 + \frac{\zeta}{A}\right),$$

with ζ the elevation of the free surface with respect to MSL and A the local amplitude of the vertical tide. These variables are both assumed to decrease exponentially in the landward direction, thus

$$\overline{b}(x) = \overline{b}_0 e^{-s_* x}, \qquad B(x) = B_0 e^{-s_* x}.$$

Here $\overline{b}_0$ and B_0 are the width at MSL and LWL at the entrance of the embayment. The parameter s_* is the reciprocal of the e-folding length scale of the width of the embayment. It has been shown by Friedrichs and Aubrey (1994) that many estuaries have such a shape. If s_* equals zero a rectangular basin remains. The basin contains fine sediment ($d \sim 2 \cdot 10^{-4}$ m) and bottom shear-stresses induced by tidal currents are so large that bed load transport of sediment can be neglected and only suspended load transport is taken into account. The geometry represents a tidal embayment or an estuary with negligible river discharge.

2.2.2 Hydrodynamics

The model is based upon the depth- and width-averaged shallow water equations without wind stress. Density differences are neglected. For an embayment as shown in fig. 2.2 these equations read (Speer and Aubrey, 1985)

$$\tilde{b}\frac{\partial \zeta}{\partial t} - B\frac{\partial h}{\partial t} + \frac{\partial}{\partial x}\left[B(\zeta + H - h)u\right] = 0, \tag{2.1}$$

$$\frac{\partial u}{\partial t} + u\frac{\partial u}{\partial x} + \frac{\tau_b}{\rho(\zeta + H - h)} = -g\frac{\partial \zeta}{\partial x}. \tag{2.2}$$

Here $\tilde{b}, B$ and ζ are defined above, h is the bed level with respect to the undisturbed water depth H at the entrance of the embayment and u the velocity in the landward (x) direction. Furthermore, τ_b is the bed shear stress and ρ is the density of water. The hydrodynamic boundary conditions are

$$\zeta = \zeta_{tide} \qquad \text{at } x = 0, \qquad\qquad \tilde{b}(\zeta + H - h)u = 0 \qquad \text{at } x = L,$$

which state that the vertical tide should match the forcing at the open boundary and no net water flux through the solid boundary at the landward side should occur. The function ζ_{tide} will be specified in section 2.2.5.

2.2.3 Suspended load sediment transport and bottom evolution

The concentration equation used here is derived in appendix 2.A and reads

$$\frac{1}{B}\frac{\partial}{\partial t}(\tilde{b}C) + \frac{1}{B}\frac{\partial}{\partial x}(BuC) - \frac{1}{B}\frac{\partial}{\partial x}\left(\mu_* \frac{\partial}{\partial x}(BC)\right) = \alpha u^2 - \gamma\beta C. \tag{2.3}$$

Here C is the depth-integrated and width-averaged sediment concentration. Furthermore, μ_* is a horizontal turbulent diffusion coefficient (containing fluctuations caused by turbulence in the vertical and cross-channel direction, see appendix 2.A), α a sediment erosion parameter and β and γ are deposition parameters. Typical orders of magnitude are $\mu_* \sim 100$ m^{2}s^{-1} (Ridderinkhof and Zimmerman, 1992), $\alpha \sim 10^{-2}$ kgsm^{-4}, $\beta \sim 1$ and $\gamma \sim 10^{-3}$ s^{-1} (Van Rijn, 1993). The terms on the left-hand side of equation (2.3) are related to local inertia and divergence of the advective and diffusive sediment fluxes, respectively. The contributions on the right-hand side represent the erosion and deposition of sediment at the bed.

In earlier work by Schuttelaars and De Swart (1996)) the coefficients α, β and γ were considered to be constant. However, the erosion coefficient α is linearly related to the drag

coefficient c_d because the erosion of sediment is proportional to the local bed shear stress $\tau_b = \rho c_d |u| u$. In this paper two formulations will be considered: a constant c_d and one according to the Manning formulation, see Soulsby (1997) in which c_d (and hence α) is proportional to $(\zeta + H - h)^{-1/3}$. This formulation is often used in quasi-realistic models for Wadden Sea embayments, cf. Ridderinkhof (1988a) and Van de Kreeke and Robaczewska (1993). With regard to the deposition flux it is shown in appendix 2.A.3 that the parameters β and γ depend on the vertical eddy diffusion coefficient of sediment, μ_v, see equation (2.17). Two cases are distinguished, the first being that γ is inversely proportional to the water depth and β is a constant. This is obtained when the vertical eddy diffusion coefficient is assumed to be proportional to the local water depth. The latter follows from a simple mixing length argument and is supported by field data (Friedrichs and Hammick, 1996). The second case is that $\mu_v = \hat{\mu}_v$ is a constant such that γ is a constant and β depends exponentially on depth. This formulation generalises the one used by Schuttelaars and De Swart (1996) to water depths which are not necessarily large with respect to the thickness of the suspended load layer. The assumption of zero velocity on the flats implies that no erosion occurs here. Hence, it is assumed that deposition can only occur in the channel area. Equation (2.3) differs from the models presented by Prandle (1991); Van Rijn (1993); De Jong (1998) in that it does not assume the actual concentration profile to be uniform over the vertical. Field data of the concentration distribution over the vertical support this different model approach (Mulder, 1993; Williams and Rose, 2001). It differs from the work of Friedrichs et al. (1998) in assuming the concentration at the transition between channel and tidal flat to be zero, whereas they assume well-mixed conditions in the cross-channel direction. The use of depth-integrated concentration implies that the concentration will be zero as the water depth approaches zero on the tidal flats. More details on the model differences can be found in appendix 2.A.

The bed evolution is described by the net effect of erosion and deposition averaged over a tidal cycle:

$$\rho_s (1-p) \frac{\partial h}{\partial t} = -(\alpha u^2 - \gamma \beta C).$$

The bed porosity p is 0.4 (Dyer, 1986) and the density of the sand ρ_s is 2650 kgm^{-3}. The accompanying boundary conditions apply to the quantities $< C >$ and $\tilde{C} = C - < C >$, which are the time-mean and fluctuating part of the concentration. They read

$$\begin{aligned} \tilde{C}(x,t,\mu_*) = \tilde{C}(x,t,\mu_* = 0) \qquad & \text{at} \quad x = 0, x = L, \\ < \alpha u^2 - \beta\gamma C >= 0 \qquad & \text{at} \quad x = 0, \\ < BuC - \mu_* \frac{\partial}{\partial x}(BC) >= 0 \qquad & \text{at} \quad x = L, \end{aligned}$$

with $< \cdot >$ denoting an average over the principal tidal period. The formulation of these conditions is based on the fact that diffusive terms in the concentration equation are generally small with respect to other terms (in particular those related to local inertia, erosion and deposition). However, they can become very large near the boundaries due to the imposed conditions at such locations. The first condition states that, consistent with observations, there are no diffusive boundary layers in the fluctuating part of the concentration near the entrance and the land. The second condition states that the tidally-averaged bed level is kept fixed at

the entrance. In fact this condition defines the seaward boundary of the embayment under consideration. Finally there can be no net sediment flux through the landward boundary.

2.2.4 Scaling and derivation of the short embayment model

The governing equations are now made dimensionless in order to derive a reduced system which can be analysed by mathematical-physical methods. A scaling is performed by introducing a characteristic velocity scale U, free surface amplitude A and frequency σ of the tidal forcing, the embayment length L and its depth H and width B_0 at the entrance. For the scaling of the concentration characteristic values $\hat{\alpha}$ and $\hat{\gamma}$ for the erosion and deposition parameters are introduced. With the dimensional variables denoted with *, the non-dimensional variables are defined as

$$x^* = Lx, \qquad t^* = \frac{t}{\sigma}, \qquad \zeta^* = A\zeta = \frac{HU}{\sigma L}\zeta, \qquad s^* = \frac{s}{L},$$
$$u^* = Uu, \qquad C^* = \frac{\hat{\alpha}U^2}{\hat{\gamma}}C, \qquad h^* = Hh, \qquad B^* = B_0 b.$$

The scaling of the surface elevation follows from the continuity equation by demanding that the two terms are of comparable order ($A/H = U/(\sigma L)$). The velocity scale U is therefore related to the tidal forcing at the entrance of the embayment. The scaling of the concentration is based on an approximate balance between erosion and deposition, which turn out to be the most dominant terms in equation (2.3). In this scaling $\beta \sim 1$ is used.

Applying this scaling to the momentum equation (2.2) yields

$$\zeta_x + \lambda^2 \left\{ \frac{\partial u}{\partial t} + \epsilon u \frac{\partial u}{\partial x} + \frac{ru}{\epsilon\zeta + 1 - h} \right\} = 0,$$

where λ is the ratio of the embayment length over the tidal wave length. In this paper short embayments are considered of which the lengths are small compared with the tidal wavelength. A prototype example of such an embayment is the Frisian Inlet, located in the Dutch Wadden Sea between the barrier islands Ameland and Schiermonnikoog. Typical values of the model parameters for this inlet are given in table 2.1; they are extracted from the data presented by Oost (1995). As can be seen the non-dimensional parameter $\lambda \ll 1$ for the

Table 2.1: Characteristic values of the model parameters for the Frisian Inlet

$H \sim 10$ m	$\hat{\zeta} = \frac{HU}{\sigma L} \sim 1.2$ m	$\rho_s \sim 2650$ kg m^{-3}
$L \sim 2 \cdot 10^4$ m	$p \sim 0.4$	$\mu_* \sim 10^2$ m^2 s^{-1}
$\sigma \sim 1.4 \cdot 10^{-4}$ s^{-1}	$w_s \sim 2 \cdot 10^{-2}$m s^{-1}	$\mu_v \sim 0.1$ m^2 s^{-1}
$s_* \sim 5 \cdot 10^{-4}$ m^{-1}	$A_4 \sim 0.3$ m	$\phi \sim 7^\circ$
$B_0 = 2 \cdot 10^3$ m	$\hat{\alpha} \sim 10^{-2}$ kg s m^{-4}	$\hat{\gamma} \sim 4.0 \cdot 10^{-3}$ s^{-1}

Frisian Inlet. For such short embayments the momentum equation is reduced by neglecting the terms with λ^2 with the result that the free surface elevations must be spatially uniform (pumping mode).

From here on, derivatives are denoted by subscripts, e.g. $\frac{\partial u}{\partial x} = u_x$. The final non-dimensional model equations become

$$\hat{b}\zeta_t - \frac{b}{\epsilon}h_t + \left[b(\epsilon\zeta + 1 - h)u\right]_x = 0, \tag{2.4}$$

$$\zeta_x = 0, \tag{2.5}$$

$$a\left\{(\hat{b}C)_t + \left[\epsilon buC - \mu(bC)_x\right]_x\right\} = \frac{bu^2}{(\epsilon\zeta + 1 - h)^{\xi_e}} - \frac{b\beta C}{(\epsilon\zeta + 1 - h)^{\xi_d}}, \tag{2.6}$$

$$h_t = -\delta\left\{\frac{u^2}{(\epsilon\zeta + 1 - h)^{\xi_e}} - \frac{\beta C}{(\epsilon\zeta + 1 - h)^{\xi_d}}\right\}. \tag{2.7}$$

Here

$$b = \tfrac{B}{B_0} = e^{-sx}, \qquad \hat{b} = 1 + \epsilon_b(1 + \zeta),$$
$$\epsilon_b = \tfrac{\overline{b}-B}{B_0} = \hat{\epsilon}_b e^{-sx}, \quad \beta^{-1} = 1 - e^{-G(\epsilon\zeta+1-h)^{\xi_\mu}},$$

and all dimensionless parameters are defined in table 2.2, together with their characteristic values for the Frisian inlet. The contributions on the right-hand side of equation (2.6) show

Table 2.2: Nondimensional model parameters for the Frisian Inlet

$a = \frac{\sigma}{\tilde{\gamma}} \sim 0.04$	$\frac{\text{deposition timescale}}{\text{tidal time scale}}$
$\mu = \frac{\mu^*}{\sigma L^2} \sim 1.8 \cdot 10^{-3}$	$\frac{\text{tidal period}}{\text{diffusive timescale}}$
$\delta = \frac{\hat{\alpha}U^2}{\rho_s(1-p)\sigma H} \sim 8 \cdot 10^{-4}$	$\frac{\text{tidal period}}{\text{morphodynamic timescale}}$
$\epsilon_4 = \frac{A_4}{A_2} \sim 0.25$	$\frac{\text{M4 amplitude}}{\text{M2 amplitude}}$
$\hat{\epsilon}_b = \frac{\overline{b}-B}{B_0} \sim 0.15$	hypsometry parameter
$\epsilon = \frac{U}{\sigma L} \sim 0.15$	$\frac{\text{tidal excursion length}}{\text{embayment length}}$
$\lambda^2 = \frac{\sigma^2 L^2}{gH} \sim 0.07$	$\left(\frac{\text{embayment length}}{\text{tidal wave}-\text{length}}\right)^2$
$G = \frac{w_s H}{\hat{\mu}_v} \sim 2.0$	$\frac{\text{vertical diffusion timescale}}{\text{deposition timescale}}$
$s = s_* L \sim 1.0$	$\frac{\text{embayment length}}{\text{length scale width convergence}}$
$\beta \sim 1$	deposition parameter

that the explicit depth dependence of the erosion and deposition flux at the bed is given by the coefficients ξ_e, ξ_d and ξ_μ. As explained in the previous subsection the physical choices

for the first coefficient are $\xi_e = 0$ (constant drag coefficient) or $\xi_e = 1/3$ (Manning formulation). With regard to the modelling of the deposition flux the three physical choices are $\xi_d = 0/\xi_\mu = 0$ (depth-independent deposition), $\xi_d = 0/\xi_\mu = 1$ (constant vertical eddy diffusion coefficient) and $\xi_d = 1/\xi_\mu = 0$ (vertical eddy diffusion coefficient proportional to the local water depth).

From equation (2.7) it can be seen that the bottom evolves on a timescale which is a factor $\delta^{-1} \sim 10^3$ larger than the tidal period. This implies that the bottom can considered to be steady on the fast hydrodynamic timescale. Moreover, only the tidally averaged difference between sediment erosion and deposition at the bed determines the bottom evolution. Then, with the use of the concentration equation (2.6) the final bottom evolution equation reads

$$h_\tau = -\frac{1}{b} F_x,$$

where $\tau = \delta t$ is a slow time coordinate and

$$F = F_{diff} + F_{adv}, \qquad F_{diff} = -a\mu < bC >_x, \qquad F_{adv} = a\epsilon b < uC >,$$

and the brackets $< \cdot >$ denote an average over a tidal period. So the bed evolution is determined by the convergence and divergence of the net sediment flux, which consists of a diffusive component F_{diff} and an advective component F_{adv}. The scaled boundary conditions read

$$\begin{aligned} &\zeta = \zeta_{tide}, && h = 0, \quad \tilde{C}(x,t,\mu) = \tilde{C}(x,t,\mu=0) \quad \text{at } x = 0, \\ &b(\epsilon\zeta + 1 - h)u = 0, && F = 0, \quad \tilde{C}(x,t,\mu) = \tilde{C}(x,t,\mu=0), \quad \text{at } x = 1. \end{aligned}$$

2.2.5 Analysis

Equation (2.5) states that the free surface is spatially uniform. Therefore it is determined by the tidal elevation at the open boundary, which is prescribed as

$$\zeta(t) = \zeta_{tide}(t) = \cos(t) + \epsilon_4 \cos(2t + \phi),$$

consisting of the M_2 and M_4 tidal constituents (ϵ_4 is the scaled amplitude of the first overtide and ϕ its phase difference with M_2). With the surface elevation given the velocity can be solved explicitly from eq. (2.4). The result is

$$u(x,t) = \frac{(1 + \hat{\epsilon}_b(1 + \zeta_{tide}))\zeta_{tide,t}}{\epsilon\zeta_{tide} + 1 - h} \left(\frac{1 - e^{-s(1-x)}}{s} \right).$$

Assuming that $\hat{\epsilon}_b, \epsilon_4 = \mathcal{O}(\epsilon)$ and with $\epsilon \ll 1$, an approximate solution of the velocity field can be obtained as a perturbation series in ϵ. This yields

$$\begin{aligned} u(x,t) &= u_0 + \epsilon u_1 + \mathcal{O}(\epsilon^2), \\ u_0 &= \hat{u}_0^s \sin(t), \\ u_1 &= \hat{u}_1^s \sin(t) + \hat{u}_1^{2c} \cos(2t) + \hat{u}_1^{2s} \sin(2t), \end{aligned}$$

where the superscripts of the amplitudes refer to its time dependence and the subscripts indicate the order contribution in ϵ. The amplitudes are given by

$$\hat{u}_0^s = -\left(\tfrac{1-e^{-s(1-x)}}{s(1-h)}\right), \quad \hat{u}_1^s = \hat{u}_0^s \tfrac{\hat{\epsilon}_b}{\epsilon},$$
$$\hat{u}_1^{2c} = 2\hat{u}_0^s \tfrac{\epsilon_4}{\epsilon}\sin(\phi), \qquad \hat{u}_1^{2s} = \hat{u}_0^s\left(2\tfrac{\epsilon_4}{\epsilon}\cos(\phi) + \tfrac{1}{2}\tfrac{\hat{\epsilon}_b}{\epsilon} - \tfrac{1}{2(1-h)}\right),$$

and show the influence of different mechanisms on the velocity profile. The zeroth order velocity is determined by the external M_2 forcing, but the first order solution contains contributions from hypsometric effects on M_2 ($\hat{u}_1^s$), external forcing by M_4 ($\hat{u}_1^{2c}$ and first term in $\hat{u}_1^{2s}$), hypsometric effects on M_4 (second term in $\hat{u}_1^{2s}$) and internal shallow water generation of M_4 (third term in $\hat{u}_1^{2s}$). Thus, with only the leading order tidal constituent represented in the forcing ($\epsilon_4 = 0$), overtides are still generated internally. Note that $\hat{u}_0^s$ is always negative as long as the bottom does not exceed the mean water level. The expression for the velocity leads to a concentration profile of the form

$$\begin{aligned} C &= C_0 + \epsilon C_1 + \mathcal{O}(\epsilon^2), \\ C_0 &= < C_0 > + \hat{C}_0^{2c}\cos(2t) + \hat{C}_0^{2s}\sin(2t), \\ C_1 &= < C_1 > + \hat{C}_1^{s}\sin(t) + \hat{C}_1^{c}\cos(t) \\ &\quad + \hat{C}_1^{2c}\cos(2t) + \hat{C}_1^{2s}\sin(2t) + \hat{C}_1^{3s}\sin(3t) + \hat{C}_1^{3c}\cos(3t). \end{aligned}$$

The amplitudes of the different components of the concentration depend on the parameterisation of the deposition term. For both parameterisations the expressions for the zeroth order amplitudes are given in appendix B. When an embayment without tidal flats is considered ($\hat{\epsilon}_b = 0$), the order ϵ concentration only consists of contributions which oscillate with the frequency of the M_2 tide and the M_6 tide. With the concentration profile the net diffusive and advective sediment fluxes can be constructed:

$$F_{adv} = a\epsilon b < u_0 C_0 > + a\epsilon^2 b < u_0 C_1 + u_1 C_0 > \tag{2.8}$$
$$= \frac{1}{2} a\epsilon^2 b(\hat{u}_0^s \hat{C}_1^s + \hat{u}_1^{2c}\hat{C}_0^{2c} + \hat{u}_1^{2s}\hat{C}_0^{2s}), \tag{2.9}$$
$$F_{diff} = -a\mu < bC_0 >_x . \tag{2.10}$$

These fluxes are calculated from the complete model equations, i.e. eq. (2.4) -(2.7). This leads to two different expressions for the fluxes, one representing the exponential dependence of deposition on local depth (vertical eddy viscosity coefficient μ_v depth-independent) and one representing the linear dependence of deposition on depth (μ_v depth-dependent). They are specified in appendix B.

When forcing with the leading tidal constituent and its first overtide is applied the advective flux contribution is larger ($\mathcal{O}(a\epsilon\epsilon_4)$) than with only M_2 ($\mathcal{O}(a^2\epsilon^2)$) forcing. However, the largest contribution to the diffusive flux is not affected by the first overtide. The advective sediment flux is determined by the phase difference between the M_2 and M_4 tidal components. For values of $\phi \in [0, 180°]$ sand is imported into the basin because the ebb period of the tidal current has a longer duration than the flood period. This causes higher velocities during flood (flood-dominance) due to mass conservation, resulting in sediment import. For $\phi \in [-180°, 0]$ sediment is exported because the system experiences a longer flood period and a shorter ebb period of the tidal current, resulting in higher ebb velocities (ebb-dominance) and sediment export. As the sediment flux is always non-zero no equilibrium exists in the case of dominant advective transport with M_2+M_4 forcing.

Solutions of this system were examined for combined transport and for dominant diffusive transport and dominant advective transport. This was done in order to concentrate on the influence of diffusive and advective mechanisms on the bed evolution and equilibrium properties. The morphological timescale can be either the diffusive timescale or the advective one. When M_2 forcing is applied the ratio of diffusive transport over advective transport in the bottom evolution equation becomes $\mu/(a\epsilon^2) \approx 2$. Thus the combined sediment flux should be considered. Adding the first overtide to the forcing leads to a ratio of $\mu/(\epsilon\epsilon_4)$ which is ≈ 0.05. In this case the advectively dominated case is more representative for the Frisian Inlet system.

2.2.6 Morphodynamic equilibria and time evolution

A morphodynamic equilibrium is defined as a situation with a steady bottom, i.e. $h_\tau = 0$. The net sediment flux therefore has to be constant ($F_x = 0$), and the boundary condition of no net sediment flux at the landward side states that in equilibrium the sediment flux is zero throughout the basin. Note that only the total transport must vanish, the advective and diffusive flux contributions can still vary in equilibrium conditions. As will be shown in the next section, for certain combinations of the model parameters morphodynamic equilibria can be obtained analytically. For other cases time integration is performed, which also yield insight in the evolution of bottom patterns. In order to calculate the time evolution of the bed a numerical programme has been constructed. Because of the different timescales for water motion and bed development these two processes are separated. First, the water motion and concentration profile are determined for a given bottom topography (i.e. the Fourier amplitudes of u and C as discussed in the previous subsection). These are then inserted in the bottom evolution equation and integrated one step in time (long or morphological timescale). The new velocity and concentration profiles are then calculated and the bed profile is integrated again. This continues until there is no more change in the bed profile and an equilibrium is reached.

The programme uses finite differences for spatial derivatives and the Runga Kutta fourth order scheme for time integration. A total number of 100 grid points was used and the morphodynamic timestep was chosen such that it yields numerically stable and accurate solutions.

2.3 Results

2.3.1 No explicit depth-dependent sediment deposition

First, the model without explicit depth dependence is considered, i.e. $\beta = 1$ and $\xi_e = \xi_d = \xi_\mu = 0$ in equations (2.6). Hence the focus is here on the sensitivity of one-dimensional (1D) morphodynamic pattern formation on the funnel shape of the embayment (measured by the parameter s) and hypsometric effects (measured by the parameter $\hat{\epsilon}_b$).

M_2 forcing

Schuttelaars and De Swart (1996) showed that for rectangular embayments without tidal flats ($s = 0, \hat{\epsilon}_b = 0$) a unique, stable morphodynamic equilibrium exists which involves the lin-

early sloping bottom $h_{eq} = x$. This solution is characterised by both zero advective and diffusive sediment fluxes, thus it is also a solution of the separate advectively and diffusively dominated cases. Now the effects of width convergence and the presence of tidal flats are considered. Figure 2.3(a) shows the equilibrium profiles for the separate geometries. Three additional situations are considered: a rectangular basin with tidal flats (model rt), a funnel-shaped basin without tidal flats (model c) and a funnel-shaped basin with tidal flats (model ct). Figure 2.3(b) shows the bottom evolution starting from a flat bed for the geometry including width convergence and tidal flats ($s = 1, \hat{\epsilon}_b = 0.15$). Note that the equilibrium is reached at $\tilde{\tau} \sim 1$ (where $\tilde{\tau} = a^2\epsilon^2\tau$), such that $\tilde{\tau} = 1$ corresponds to about 7,800 years. A discussion on the large timescale found here is presented in section 2.4. Apparently, the width convergence

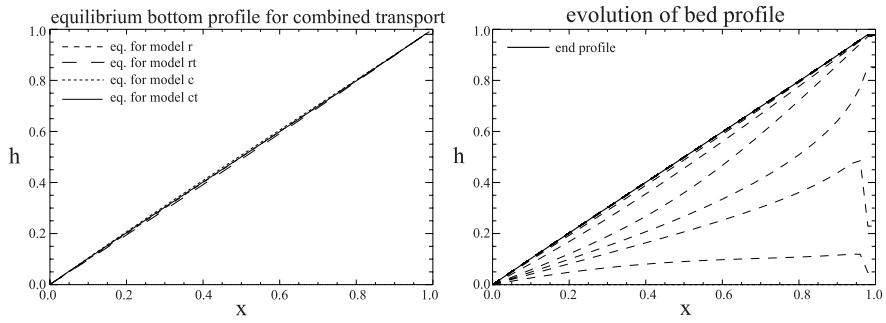

(a) (b)

Figure 2.3: Equilibrium bottom profiles for models with different geometries: r = rectangular basin without tidal flats ($s = 0, \hat{\epsilon}_b = 0$), rt = rectangular basin with tidal flats ($s = 0, \hat{\epsilon}_b = 0.15$), c = funnel-shaped basin without tidal flats ($s = 1, \hat{\epsilon}_b = 0$) and ct = funnel-shaped basin with tidal flats ($s = 1, \hat{\epsilon}_b = 0.15$), (a) equilibrium bottom profiles for the combined sediment flux and (b) time evolution of the bed starting from a flat bed for the geometry with decreasing width and tidal flats (model ct). Dashed lines indicate subsequent bottom profiles: time intervals are $\Delta\tilde{\tau} = 0.2$. The drawn thick line represents the final equilibrium profile.

and the presence of tidal flats hardly affect the final equilibrium profile. This means that for depth-independent erosion and deposition the consideration of a rectangular basin without tidal flats suffices. However, the evolution of the bed depicted in figure 2.3(b) is different from that of a rectangular embayment without tidal flats. In the latter case (see Schuttelaars and De Swart (1996)) the initial behaviour consists of the advective propagation of a sediment wave entering the embayment which is subsequently modified by diffusion processes. The manifestation of such a wave is due to the fact that the bed evolution related to advective sediment fluxes is of a hyperbolic nature. In the funnel shaped geometry with tidal flats (ct model) diffusive processes are much stronger than advective processes as is apparent from the fact that no clear sediment wave front is observed. Figure 2.4 shows the velocity, concentration and the separate sediment fluxes amplitudes for the case of a funnel-shaped basin with tidal flats. The velocity amplitude shows an almost linear profile with values increas-

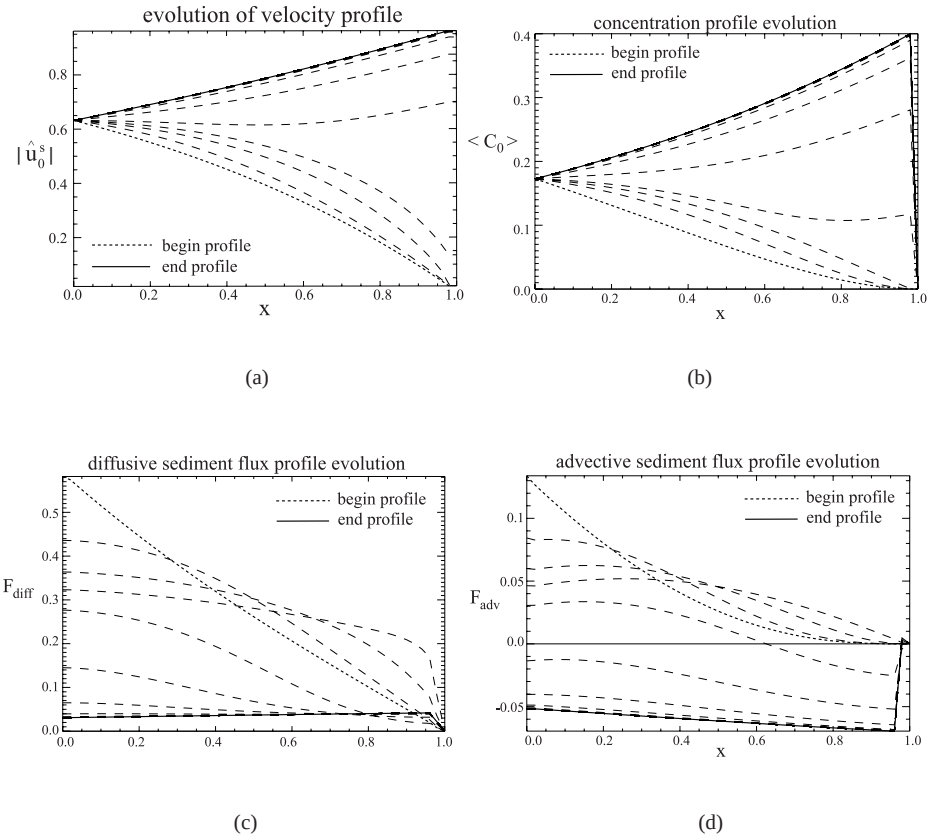

Figure 2.4: Amplitude evolution for a converging basin with tidal flats, (a) velocity component $\hat{u}_0^s$, (b) concentration component $< C_0 >$, (c) diffusive sediment flux and (d) advective sediment flux. Long dashed lines represent subsequent evolution profiles with time intervals $\Delta\tilde{\tau} = 0.1$.

ing towards the land, while the negative values of $\hat{u}_0^s$ indicate that the free surface elevation lags the tidal currents by $90°$. The depth-integrated concentration also weakly increases in the landward direction. The behaviour shown in figures 2.3(a) and 2.3(b) is caused by additional sediment fluxes and the velocity gradient along the basin. When tidal flats are included in a rectangular geometry an additional advective sediment flux is induced in the seaward direction. This implies that the net advective sediment flux will have a weaker landward component or can even change its direction. Indeed, a net seaward advective flux is found in equilibrium when only tidal flats are included (results not shown). The velocity profile for this case shows slightly decreasing values towards the end of the basin, which induces a small landward directed advective sediment flux in equilibrium conditions. The additional seaward transport of sediment leads to a slightly lower bottom profile (case rt, see figure 2.3(a)). This effect is counteracted when width convergence is applied, which induces both advective and

diffusive fluxes in the landward direction. The velocity at the entrance of the basin is reduced with respect to the case of a rectangular basin because of the reduced volume of the embayment. However, the velocity amplitude increases along the basin with decreasing width in the final equilibrium state due to mass conservation. This causes a change in velocity gradient (see figure 2.4(a)) during the evolution of the bottom profile, which means that the advective transport of sediment due to the velocity gradient changes from a landward directed flux to a seaward directed flux near equilibrium conditions. The net effect of the fluxes in different directions on the equilibrium bottom profile is negligible. In all the new cases examined here the morphodynamic equilibrium is characterised by a balance between a seaward-directed advective flux and a landward-directed diffusive flux, as shown in figures 2.4(c) and 2.4(d) for a funnel-shaped basin with tidal flats.

Net advective sediment fluxes are much weaker in the case of a converging basin (both in an absolute sense and in a relative sense when compared with diffusive fluxes) than in the case of a rectangular embayment. This is mainly due to a decrease of the tidal current amplitude. The results presented here are in agreement with those of Friedrichs and Aubrey (1994). They found that tidal flats and width convergence in weakly dissipative embayments tend to change the asymmetry of tidal currents from flood-dominance (as found for straight channels without tidal flats) to ebb-dominance, indicating a change from landward directed to seaward directed advective sediment transport. Here, the absence of bottom friction prevents the tidal current from becoming asymmetrical, but the system shows a net seaward advective transport of sediment near and in equilibrium conditions when tidal flats and width convergence are taken into account. For a rectangular basin without tidal flats only landward directed advective transport is found.

In order to further assess the effects of tidal flat presence and converging width on the separate fluxes, the morphodynamic equilibrium profiles for either purely advective or purely diffusive transport of sediment are considered. The case of dominant advective transport is discussed first and its results are shown in figure 2.5(a). Here the advectively generated equilibrium bottom profile does show a small sensitivity to both the presence of tidal flats and width convergence. The decrease in sedimentation is due to the reduced import of sediment by the advective flux in each case as explained in the last paragraph. Without a compensation from the diffusive flux both effects now lead to a slightly concave equilibrium bottom profile. The separate effects are added when both tidal flats and width convergence are accounted for and the profile becomes more strongly concave.

The diffusive sediment flux is not influenced by the presence of tidal flats, but only by the width convergence parameter s. In figure 2.5(b) the diffusive equilibrium bottom profile is shown for different values of s. When $s \to 0$ the profile reduces to $h_{eq} = x$, the diffusive equilibrium bottom profile for the rectangular basin found by Schuttelaars and De Swart (1996). The equilibrium bottom profile can be calculated analytically for dominant diffusive transport of sediment:

$$\text{model c or ct} \; : \; h_{eq} = 1 - e^{-\frac{1}{2}sx} \left(\frac{1 - e^{-s(1-x)}}{1 - e^{-s}} \right).$$

A convex profile is always found in this case. This can be understood from the morphodyna-

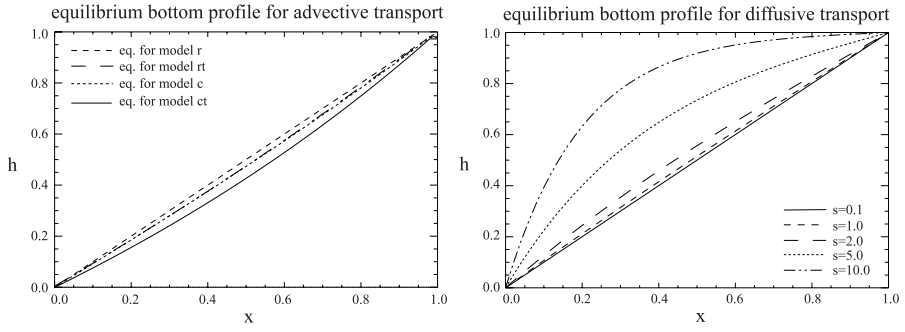

(a) (b)

Figure 2.5: Equilibrium bottom profiles for different limiting cases: (a) dominant advective fluxes, (b) dominant diffusive fluxes for different values of s.

mic equilibrium condition which reads $F_{diff} = 0$, hence $< bC >=$ constant (see eq. (2.10)). The analysis discussed in section 2.2.5 shows that the erosion and deposition fluxes are by far the largest terms in the concentration equation. Thus the concentration can be approximated by the squared tidal current amplitude $(\hat{u}_0^s)^2$ and the condition becomes $b(\hat{u}_0^s)^2 =$ constant. As the channel width b decreases exponentially the velocity will increase in an exponential way to satisfy this condition. The tidal current amplitude is determined by the continuity equation and its expression is given in section 2.2.5. The bottom profile becomes convex due to continuity effects. These results indicate that for strongly converging channels the diffusive sediment flux will lead to convex bottom profiles when combined sediment transport is considered.

M_2 and M_4 forcing

With the M_4 tidal component included in the forcing at the entrance M_4 tides in the model are now caused by external forcing, besides that they are internally generated by self-interaction of the M_2 tide. Thus the magnitude and direction of the advective flux is also affected by the sign of the relative phase difference ϕ between M_2 and M_4. It is important to remark that external forcing with an additional M_4 component does not affect the diffusive flux. For a rectangular basin without tidal flats the equilibrium bottom profile for combined advective and diffusive transport can be calculated analytically and is given by (Schuttelaars and De Swart, 1996)

$$h_{eq} = x + \tilde{D}x - \tilde{D}x^2 \quad \text{with} \quad \tilde{D} = \frac{3\epsilon\epsilon_4 \sin(\phi)}{2\mu}. \tag{2.11}$$

Thus a convex profile is obtained if $\phi > 0$ and a concave one whenever $\phi < 0$. Since a positive phase difference is related to a flood-dominance of the tidal current, the net advective import of sediment causes the profile to become convex. For a negative phase difference the

export of sediment by advective processes creates a concave profile. The same conclusion with respect to the effect of the M_4 phase was reached by De Jong and Heemink (1996). For the positive phase difference found outside the Frisian Inlet system ($\phi = 7\,^\circ$) the equilibrium profile already exceeds the water level before the landward boundary. Physically this means that the embayment partly fills up and reduces its effective length. Note that for the Frisian Inlet system $\tilde{D} \sim 3.8$, which results in a length reduction of the basin of about 75 %. However, the use of a combined sediment flux implies $D \sim 1$, since $\tilde{D}$ is the ratio of advective processes over diffusive processes. For forcing with the M_2 and M_4 tidal components the advectively dominanted case is more representative for the Frisian Inlet system.

Within the model context the process of length reduction is difficult to model. Hence, in order to demonstrate the influence of external M_4 forcing and width convergence on the morphodynamics of the system a much smaller phase difference ($\phi = 1\,^\circ$) was chosen. Figure 2.6(a) shows the equilibrium bottom profiles for $\phi = 1\,^\circ$ for the different geometries. Figure 2.6(b) shows the evolution of the bed profile for the geometry with converging width. The results show a decrease in the degree of convexity of the bottom profile when width con-

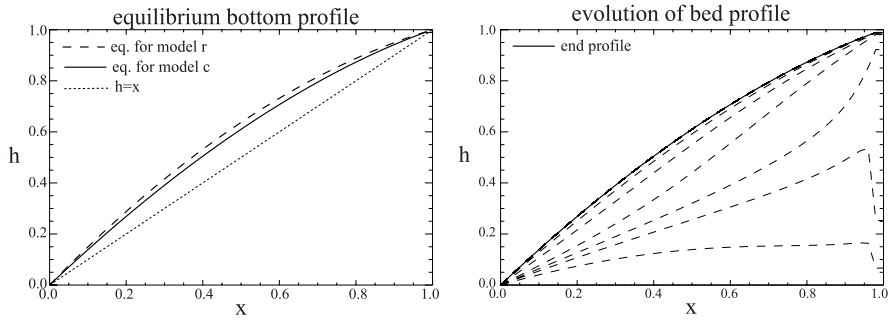

Figure 2.6: Results for combined sediment flux and M_2+M_4 forcing and $\phi = 1^\circ$, (a) equilibrium bottom profile for model r (rectangular basin) and model c (exponentially converging basin), (b) time evolution of the bed for model c, dashed lines represent subsequent bottom profiles with time intervals $\Delta\tilde{\tau} = 0.1$. The thick drawn line is the final equilibrium profile.

vergence is taken into account. This is again a result of seaward directed advective sediment fluxes caused by width convergence. Less sediment is thus imported and the equilibrium bottom profile is less convex than in the case of a rectangular basin.

2.3.2 Depth-dependent erosion and deposition

Here the results for depth-dependent erosion and deposition are presented, i.e. the Manning formulation of the drag coefficient is used and the vertical diffusion coefficient depends on local depth. This means that in equation (2.6) $\xi_e = \frac{1}{3}, \xi_d = 1$ and $\beta = 1$ are taken. Experiments showed that when only the vertical eddy viscosity coefficient is taken depth-dependent

the water flux can become unbounded near the landward side, which is physically unrealistic. Therefore, it is important to include depth-dependent erosion as well, in order to compensate for the increased deposition. Only forcing with the leading tidal constituent M_2 is considered here. Applying the combined forcing of M_2+M_4 leads to numerical problems with the bottom profile exceeding the water level. The convex profile found in section 2.3.1 will be even more convex as depth-dependent erosion and deposition causes more sedimentation to occur, in particular on the landward side.

The results are shown in figure 2.7(a) for the different geometries: a straight channel without tidal flats (model r), a straigth channel with tidal flats (model rt) and a converging channel without and with tidal flats (models c and ct, respectively). Figure 2.7(b) shows the bottom evolution in time towards the equilibrium profile for the converging basin with tidal flats. Again, the presence of the tidal flats and width convergence seem to have only a

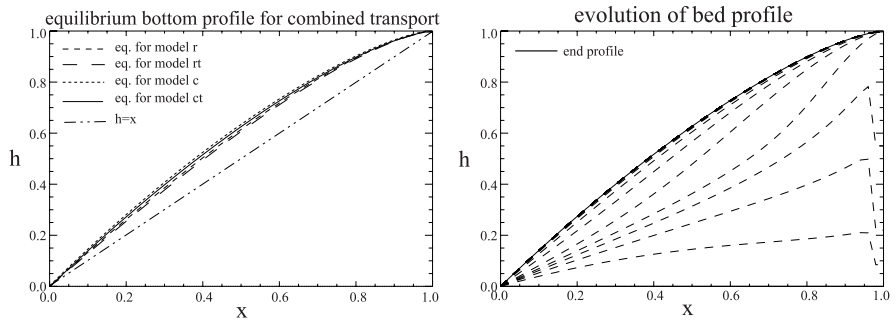

(a) (b)

Figure 2.7: Equilibrium bottom profile for the combined flux with M_2 forcing (a) for models with different geometries: r = rectangular basin without tidal flats ($s = 0, \hat{\epsilon}_b = 0$), rt = rectangular basin with tidal flats ($s = 0, \hat{\epsilon}_b \neq 0$), c = converging estuary without tidal flats ($s \neq 0, \hat{\epsilon}_b = 0$) and ct = converging estuary with tidal flats ($s \neq 0, \hat{\epsilon}_b \neq 0$), the line $h = x$ is shown for reference, (b) time evolution of the bed for the geometry including width convergence and tidal flats. Dashed lines represent subsequent bottom profiles with time intervals of $\Delta\tilde{\tau} = 0.2$.

marginal effect on the shape of the equilibrium bottom profile. An increase in sedimentation is observed compared to the cases discussed in section 2.3.1 (no explicit depth dependence in the erosion and deposition fluxes). This results in more convex bottom profiles. The evolution of the bed shows that the equilibrium is first reached at the landward border.

The different fluxes are studied separately to gain more insight into the influence of advective and diffusive processes. Figure 2.8(a) shows the equilibrium bottom profiles for the different geometries which are due to net advective sediment fluxes only. Figure 2.8(b) shows the influence of converging width on the equilibrium bottom profile generated by diffusive sediment fluxes. For dominant advective transport the equilibrium bed profile can be calculated analytically for a rectangular basin without tidal flats, resulting in $h_{eq} = 1-(1-x)^{23/21}$

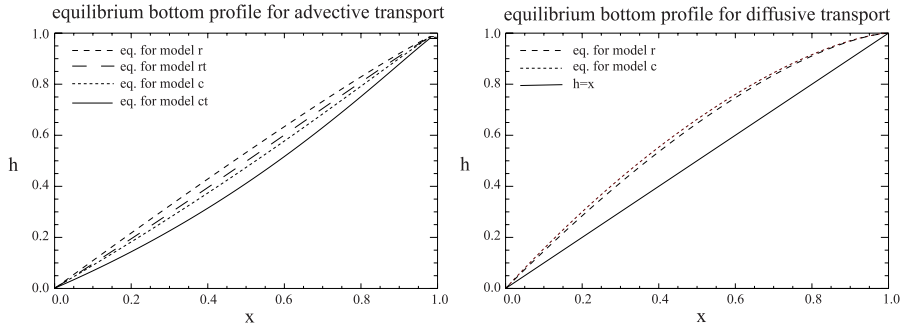

(a) (b)

Figure 2.8: Equilibrium bottom profiles for models with different geometries: (a) dominant advective case, (b) dominant diffusive case. For the model descriptions see text.

which is an almost linearly sloping bottom. For a converging geometry the morphodynamic equilibrium has to be calculated numerically. Again, a concave bottom profile is found in this case, although here the separate effects of tidal flat presence and width convergence leads to slightly different bed profiles. However, the results are very similar to those obtained for the depth-independent case, so that advective processes cannot explain the increased sedimentation found with the combined sediment flux.

In the case of dominant diffusive transport of sediment the equilibrium bed profile can be calculated analytically. For the different geometries they are

$$\begin{aligned} \text{model r, rt} \; : \; h_{eq} &= 1-(1-x)^{\frac{3}{2}}, \\ \text{model c, ct} \; : \; h_{eq} &= 1-e^{-\frac{3}{4}sx}\left(\frac{1-e^{-s(1-x)}}{1-e^{-s}}\right)^{\frac{3}{2}}, \end{aligned}$$

which represent convex profiles as can be seen in figure 2.8(b). Here also a small difference is found between the two profiles, as in the case of depth-independent erosion and deposition. More sediment is being deposited than in the depth-independent case studied in the previous section. Thus diffusive processes are responsible for the increased deposition found in figure 2.7(a) with respect to the case of depth-independent erosion and deposition.

2.3.3 Exponential dependence of sediment deposition on local depth

Finally, the drag coefficient is assumed to be depth-independent while the deposition term depends exponentially on the local depth (vertical eddy viscosity coefficient μ_v depth-independent, i.e. $\xi_e = \xi_d = 0$ and $\xi_\mu = 1$ in eq. (2.6)). The results are calculated for rectangular embayments without tidal flats. The motivation for these experiments is that $\xi_\mu = 1$ allows for arbitrary ratios between the thickness of the suspended load sediment layer and the water depth. In Schuttelaars and De Swart (1996) this ratio was assumed to

be small (with $\xi_\mu = 0$) but clearly this assumption is violated near the landward boundary because depths become small in that region. Again, only forcing with the leading tidal constituent is considered, for the same reason as stated before. The results are shown in figure 2.9(a) for the combined sediment flux together with the equilibrium profile obtained by Schuttelaars and De Swart (1996). The evolution of the bed starting from a flat bottom is shown in figure 2.9(b). With the depth-dependent sediment deposition incorporated, the

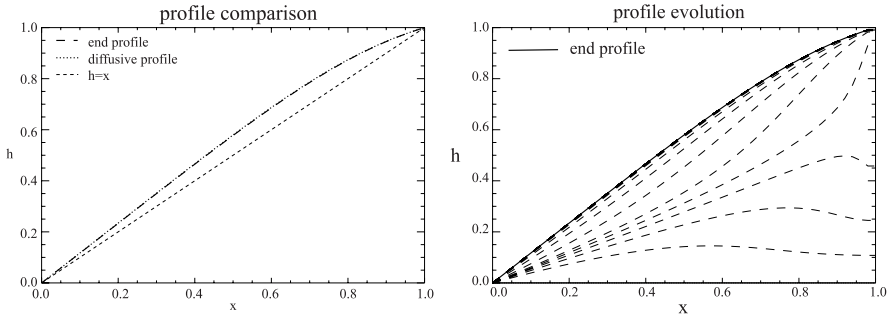

(a) (b)

Figure 2.9: Results for exponential dependence of deposition on local depth in a rectangular channel without tidal flats, (a) equilibrium profile together with the equilibrium profile for the diffusive dominated case and the profile obtained by Schuttelaars and De Swart (1996) for depth-independent deposition and (b) evolution of equilibrium bottom profile. Dashed lines represent subsequent bottom profiles with time intervals of $\Delta\tilde{\tau} = 0.05$.

amount of deposition is larger and the equilibrium bottom profile becomes convex. The amount of additional sediment deposited at the landward side with respect to that at the entrance is larger because the deposition parameter β favours sedimentation in shallow areas. The evolution of the bed shows initially a sediment wave entering the embayment with sediment finally accumulating at the landward border. The equilibrium state is reached first in the shallow part of the embayment. Figure 2.10 shows the time evolution of the scaled tidal velocity amplitude ($|\hat{u}_0^s|$) and of the deposition parameter β_0. The increased deposition in the shallower part of the embayment can be seen in figure 2.10(b): the deposition parameter is 5 times more effective at the landward side than near the entrance. The increase of the tidal current amplitude towards the land is due to the convex shape of the bottom profile.

In order to understand more of the evolution process shown in figure 2.9(b) the sediment fluxes are considered separately. Considering only the diffusive sediment flux in equation (2.7) yields the bottom profile shown in figure 2.11(a), with the time evolution starting from a flat bed. Remarkably, diffusive transport of sediment results in the same equilibrium bottom profile as combined transport of sediment (see figure 2.9(a)). Figure 2.11(a) shows that the bed evolves initially quite uniformly, with sediment accumulating at the landward side. So the deposition at the landward side of the embayment in figure 2.9(b) is due to

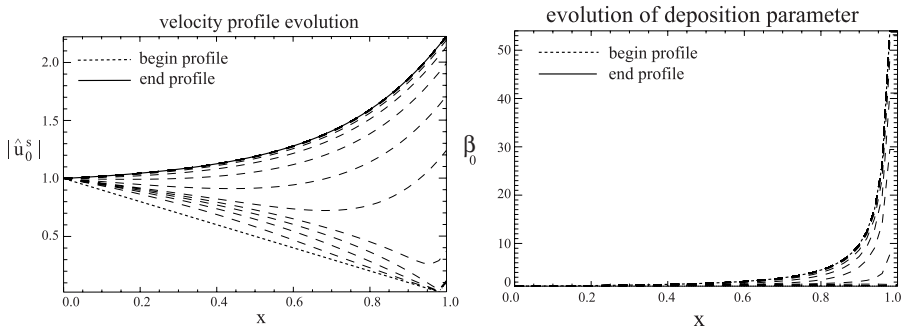

(a) (b)

Figure 2.10: Time evolution plots for combined transport of sediment (a) tidal velocity amplitude and (b) deposition parameter. Dashed lines represent subsequent profiles with time intervals of $\Delta\tilde{\tau} = 0.05$.

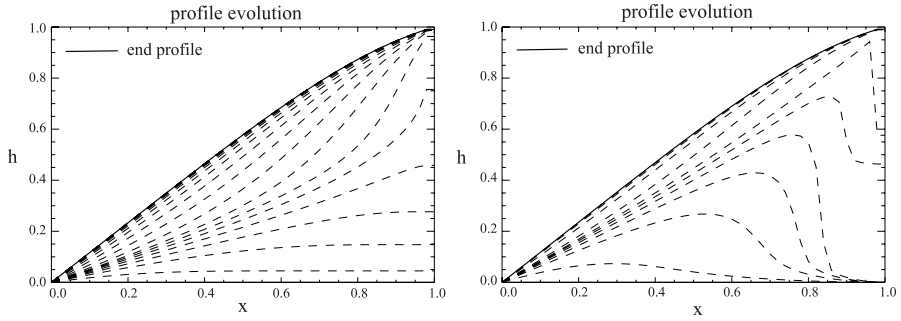

(a) (b)

Figure 2.11: The equilibrium bottom profile evolution starting from a flat bed and using exponentially depth-dependent deposition for (a) diffusively dominated transport and (b) advectively dominated transport. Dashed lines represent subsequent bottom profiles with time intervals of (a) $\Delta\tilde{\tau} = 0.1$ and (b) $\Delta\tilde{\tau} = 0.2$.

diffusive processes.

Next, only advective transport of sediment is considered. As the equilibrium profile for diffusive transport equals the equilibrium profile for combined transport, the contribution of F_{diff} to the combined flux is zero and hence F_{adv} has to be zero as well. Thus the same equilibrium profile should be found in the advective dominated case. The time evolution of the advective generated bottom profile is shown in figure 2.11(b). The equilibrium bottom

profile is indeed the same as in the previous two cases. Note that the bed evolution related to advective sediment fluxes appears as a sediment wave entering the basin. This is not surprising because the bottom evolution equation in this case has a hyperbolic nature. Thus the equilibrium profile found in figure 2.9(a) is characterised by zero net advective and diffusive sediment fluxes.

2.4 Discussion

The interesting overall result of the present study is that the 1D morphodynamic model for short tidal embayments has solutions which tend to a stable morphodynamic equilibrium. Different formulations for the erosion and deposition fluxes, different channel geometries and the presence of tidal flats only affect the detailed characteristics of the equilibrium and the adjustment process. Thus, the linearly sloping bottom is a good approximation of the equilibrium bottom profile in a short tidal embayment. Additional experiments, starting from arbitrary initial conditions, also suggest that this equilibrium is unique and globally stable.

It is of course important to investigate to what extent these results, obtained with an idealised model, are consistent with field data and whether these results are also reproduced by more complex morphodynamic models. The field data shown in figure 2.1 indicates that the bottom profiles can be convex or concave, but that generally the along-channel bottom profiles found in the Dutch Wadden Sea are close to the linearly sloping bottom with zero depth at the landward side. This is also found in the model results presented in this chapter, which suggest that convex or concave profiles are related to the relative importance of advective and diffusive sediment fluxes: smaller diffusive (with respect to advective) fluxes results in more concave profiles. This flux ratio is determined by the diffusion coefficient, channel width convergence and the amount of tidal flats. Clearly, the present model cannot give a full explanation of why certain channels are convex and others are concave. Rather, it indicates which physical mechanisms are relevant factors which determine the final bottom profile. Many embayments in the Wadden Sea may not be in equilibrium because they are subject to human interferences such as dredging and land reclamation.

It is also possible to compare model results with field data for the case of a tidal embayment responding to a reduction of its length. This occurred to the Frisian Inlet in 1969, when the closure of the Lauwers Sea reduced the effective length from approximately 40 km to its present value of 20 km. According to field observations described by Oost and De Boer (1994) this will cause a net sediment import of approximately $70 \cdot 10^6$ m^3 over a period of 60 years following the closure. The model response to a partial closure was tested for a rectangular embayment with exponential depth-dependent deposition. For other parameterisations the adjustment process slightly differs. The embayment length was reduced to half its original value. The results, presented in figure 2.12 for both dominant diffusive and advective sediment fluxes show net sediment import and adjustment towards a new equilibrium. This behaviour can be understood from the fact that the equilibrium bottom profile of the originally longer embayment is not an equilibrium profile of the shorter embayment. In particular there is lack of sediment at the landward boundary, thus sediment is imported and the bed adjusts to a new equilibrium. The estimated amount of sediment imported is, according to the model, approximately $80 \cdot 10^6$ m^3. This is in agreement with the total volume reconstructed from

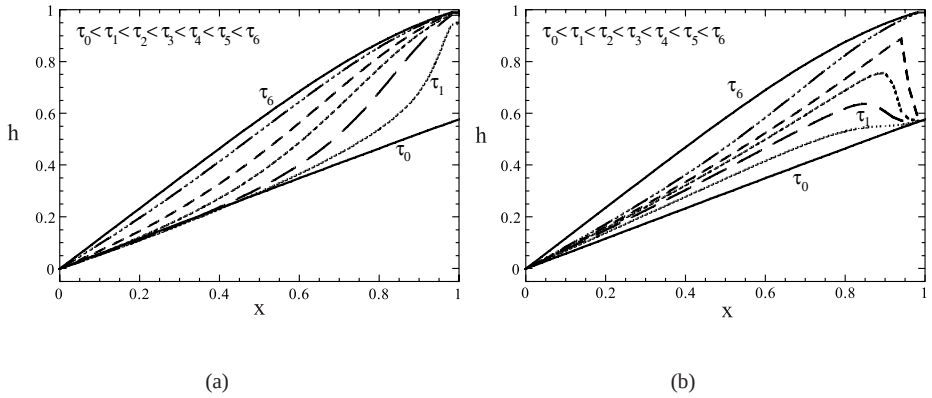

Figure 2.12: The bed adjustment to partial closure for diffusive (a) and advective (b) dominated transport. Time to reach new equilibrium is approximately (a) 3500 years and (b) 8000 years.

bathymetric data by Oost and De Boer (1994).

A drawback of the model is that the timescales needed to reach morphodynamic equilibrium are rather long compared to observations. According to Oost (1995) realistic adjustment timescales are of the order of decades. It should be noted that this discrepancy is also found in quasi-realistic models, see e.g. Wang et al. (1991). A possible explanation may be that in most of these models the effect of waves on the erosion and transport of sediment is underestimated. As discussed by Van Rijn (1993), see also references therein, waves are very effective in resuspension of sediment which is then available for transport by current. Effectively this would mean that the erosion coefficient $\hat{\alpha}$ considered in the model used here should be increased. This would have no effects on the results shown, besides the fact that the morphological timescale would become much shorter.

Another point of discussion is whether results of the present idealised model are also sensitive to the addition of physical processes which have been neglected. An important assumption underlying the present model is that of a short embayment, which effectively means that the tidal motion is a pumping mode, without any spatial variation in the water level elevations. Moreover, bottom friction does not play a role in these models. This aspect was investigated by Van Leeuwen et al. (2000) and Schuttelaars and De Swart (2000) who showed that for basins with properties comparable to the Frisian Inlet the limit of a short embayment can be safely made. An increasing embayment length (with respect to the tidal wave-length) tends to favour more concave bottom profiles. A different test was made by performing experiments with a complex process-based morphodynamic model, i.e. the DELFT2D-MOR model developed by WL|Delft Hydraulics. The latter, which was already used by Wang et al. (1991, 1995) in a different context, solves the equations of motion for water motion, sediment transport and bottom evolution by direct numerical methods without making a priori assumptions on the relative strength of the different terms. Moreover, DELFT2D-MOR accounts for partial drying and flooding in case water depths are smaller than the local tidal amplitude and it uses a different boundary condition at the open boundary. An embayment with a

fixed width was considered and parameters were taken such that they were representative for the Frisian Inlet, see table 2.1. Differences were that the water depth and length were taken smaller (5 m and 10 km, respectively) in order to decrease the morphodynamic timescale. A suspended load sediment transport formulation was selected. Figure 2.13 shows the bed profiles at different time steps as calculated with this model, starting from an initially horizontal bottom. Clearly these results resemble those shown in figure 2.9b which were obtained with

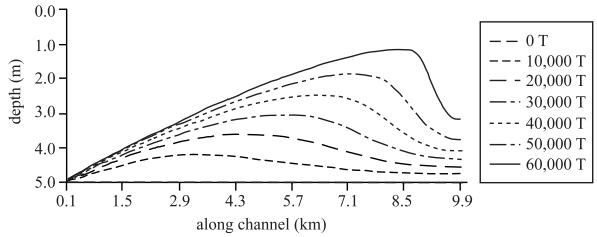

Figure 2.13: Bed evolution plot from the complex numerical model DELFT2D-MOR. Here T is the tidal period. The initial state is a flat bed with a depth of 5 m. The vertical axis shows depth (m), the horizontal axis shows the distance from the entrance of the embayment (m).

the 1D idealised model. So the results of the 1D model are robust in the sense that they are also found by using complex models. Similar conclusions were reached in a recent complex model study by Hibma (personal communications) in which also longer embayments were considered. Here it is demonstrated that the model results are merely sensitive to the conditions at the seaward entrance, whereas the formulations for partial drying and flooding and bottom friction are of minor importance.

A final point of discussion is that the present idealised model allows for a morphodynamic equilibrium in the absence of any sea level changes. This differs from the view, expressed by e.g. Oost (1995), that net sediment import continues to exist in the absence of sea level changes. Hence Wadden Sea embayments owe their existence to relative sea level rise because otherwise they would fill up. The idealised model results on the other hand suggest that the morphology will indeed respond to sea level changes but not tend to fill up. This was investigated for the case of a rectangular embayment with exponential depth-dependent deposition. In the northern part of the Netherlands, where the Frisian Inlet is situated, the land level is subsiding due to both natural and human causes. This is expected to be the dominant factor for relative sea level rise in this area. The model results shown here concern two metres of land level subsidence. This large value was only chosen to get a clear picture of the bed adjustment, for more realistic values the development towards a new equilibrium is essentially the same. Here it was assumed that the timescale of land subsidence is short compared to the morphodynamic adjustment timescale. This is not realistic, but it is not expected to change the final equilibrium response. Figure 2.14 shows that in both cases the bed level near the entrance initially drops. This is due to the large demand for sediment at the landward side of the basin, which initially cannot be supplied by the sediment imported from outside the basin. When the depth at the landward side has become sufficiently small the need for sediment becomes less extreme and the eroded parts in the basin are filled with sand imported

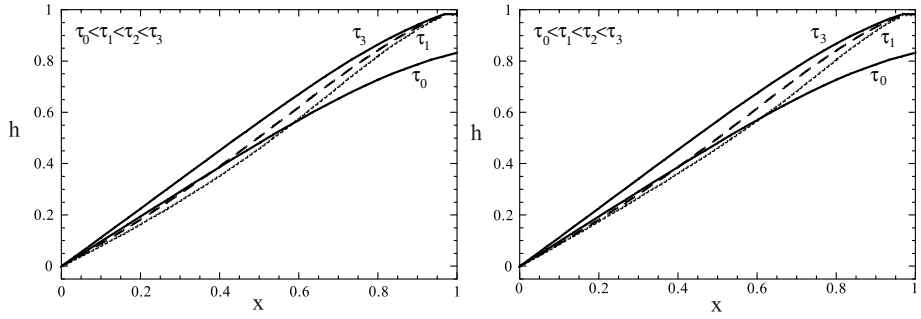

Figure 2.14: The bed adjustment to a sea level rise for diffusive (a) and advective (b) dominated transport, τ_0 represents the old situation before the sea level rise. Timescales: (a) $\tilde{\tau}_3 = 0.3 \sim 1350$ years, (b) $\tilde{\tau}_2 = 0.3 \sim 3080$ years.

from outside the embayment. Thus, the results for the case of a sea level rise show an import of sediment. The amount of sediment imported is estimated at $40{\cdot}10^6$ m^3 for a sea level rise of 2 m.

2.5 Conclusions

In this paper an idealised one-dimensional (1D) morphodynamic model of a tidal embayment has been derived and analysed. The tidal motion, suspended load transport of noncohesive sediment and bottom evolution are governed by the cross-sectionally averaged shallow water equations and the mass conservation equations for the sediment in the water column and in the bottom, respectively. Forcing of the water motion is due to prescribed free surface elevations at the seaward boundary which consist of an M_2 and M_4 tidal constituent. The embayment has a funnel shape with sloping tidal flats along its side-boundaries and its length is considered to be short compared to the tidal wave-length. Field observations indicate that many embayments obey this latter condition. The advantage is that the model in the short embayment limit allows for semi-analytical solutions which facilitate physical interpretation. The main objectives of this study were to link and extend earlier models analysed by De Jong and Heemink (1996); De Jong (1998) and Schuttelaars and De Swart (1996). In particular the sensitivity of 1D morphodynamic pattern formation to channel width convergence, hypsometric effects and formulations for erosion and deposition fluxes near the bed has been investigated. The default parameter values were taken such that they are representative for the Frisian Inlet, a tidal embayment located in the Dutch Wadden Sea.

The main overall result of the model is that, for all combinations of the model parameter values studied, solutions tend to a morphodynamic equilibrium which is characterised by a steady bottom profile and a zero net sediment flux in the entire embayment. Numerical expe-

riments indicate that for short embayments this equilibrium is unique and globally stable. The properties of this morphodynamic equilibrium, as well as the adjustment towards this equilibrium depend on the model formulation. The effects of width convergence and the presence of tidal flats seems to be minor. Also, the precise formulation of the erosion and deposition fluxes seems to have only a small influence on the resulting equilibrium profile. Here the use of a sediment deposition formulation related to the depth-averaged concentration leads to increased sedimentation and a convex equilibrium bottom profile compared to the case of sediment deposition related to the depth-integrated concentration. As long as the width convergence parameter s is of $\mathcal{O}(1)$ all equilibrium profiles are close the linearly sloping bottom. The summary below is based on a default model which considers a straight channel, no tidal flats, a depth-independent erosion coefficient and a deposition flux which is proportional to the depth-integrated concentration. As the latter is a state variable in the present model this case is referred to as no explicit depth-dependent deposition flux.

It turns out that the relatively small effect of increasing channel width convergence and presence of tidal flats on the morphodynamics depends on the ratio between the magnitudes of advective and diffusive sediment fluxes. In the case of dominant advective processes the equilibrium bottom profile tends to become more concave with respect to the profiles obtained in the absence of width convergence and tidal flats. This is explained by the fact that seaward directed sediment fluxes are induced by tidal flat presence and width convergence (through the velocity gradient), which decreases the advective sediment import. However, with increasing effect of diffusive sediment fluxes bottom profiles become more convex. This tendency was explained by analysing the corresponding morphodynamic equilibrium condition which shows that sediment erosion (and thereby the bottom shear stress) should increase towards the land. Mass continuity of water then imposes a convex bottom profile. In case of forcing with both an M_2 and M_4 tidal constituent an additional advective sediment flux is generated of which the direction depends on the phase difference between the M_2 and M_4 tide at the open boundary. In case of the Frisian Inlet this results in more sediment import, with the consequence that equilibrium profiles become more convex (with respect to those obtained without M_4 external forcing with the same parameter values). The effect of using formulations for explicit depth-dependent deposition fluxes results in more convex equilibrium bottom profiles. The reason for this behaviour is that deposition is more enhanced in shallower water. The results of the present study have been qualitatively compared with both field data and with the results of a complex morphodynamic model. The overall agreement is satisfactory: bottom profiles reconstructed from bathymetric data show similar characteristics as the profiles obtained with the 1D model. Also the morphologic evolution calculated with a process-based numerical model (DELFT2D-MOR) shows the same features as those obtained with the 1D model.

A limitation of the present model is that it is one-dimensional and tidal flats along the side-walls have been a priori prescribed. In nature channels and flats are expected to form by tide-topography interactions. To study their formation a two-dimensional model with a constant width is necessary. This will be the topic of the next chapter. Another aspect that deserves specific attention is the formulation of the boundary condition at the seaward entrance of the embayment. In the present study a fixed bed level has been taken and its choice seems to yield reliable results. Instead of considering other conditions, which are difficult to motivate by physical arguments, a useful approach would be to study explicitly

the interaction between embayment and outer sea. This will be the subject of Chapters 4 and 5 of this thesis.

Acknowledgement

The authors thank WL|Delft Hydraulics for providing the DELFT2D-MOR (Delft3D) code.

2.A Derivation of the one-dimensional concentration equation

2.A.1 Reduction from 3D to depth-integrated 2DH version

The equation describing the time evolution of the sediment concentration in the water in three dimensions reads

$$\begin{aligned}\frac{\partial C_3}{\partial t}+\frac{\partial}{\partial x}\left[u_3C_3-\mu_h\frac{\partial C_3}{\partial x}\right]+\frac{\partial}{\partial y}\left[v_3C_3-\mu_h\frac{\partial C_3}{\partial y}\right]&\\ +\frac{\partial}{\partial z}\left[(w_3-w_s)C_3-\mu_v\frac{\partial C_3}{\partial z}\right] &= 0, \qquad (2.12)\end{aligned}$$

with (u_3, v_3, w_3) the components of the three-dimensional velocity vector, C_3 the three-dimensional concentration and w_s the settling velocity. Furthermore, μ_h and μ_v are turbulent horizontal and vertical viscosity coefficients. The corresponding boundary conditions are the kinematic boundary condition for the flow at the surface and no vertical sediment flux at the surface. At the bottom the vertical sediment flux must equal the local sum of erosion and deposition, and there is no sediment flux across solid boundaries.

Integrating equation (2.12) over depth and using the boundary conditions and the Leibniz' rule results in

$$\begin{aligned}\frac{\partial C_2}{\partial t}+\frac{\partial}{\partial x}\int_{-H+h}^{\zeta}\left[u_3C_3-\mu_h\frac{\partial C_3}{\partial x}\right]dz&\\ +\frac{\partial}{\partial y}\int_{-H+h}^{\zeta}\left[v_3C_3-\mu_h\frac{\partial C_3}{\partial y}\right]dz &= E_2-D_2, \qquad (2.13)\end{aligned}$$

with $C_2 = \int_{-H+h}^{\zeta} C_3 dz$ the depth-integrated concentration. The term E_2 and D_2 on the right-hand side of eq. (2.13) represent the erosion and deposition flux at the bed, respectively.

Now the variables are split in a depth-independent part and a depth-dependent part:

$$\begin{aligned}u_3(x,y,z,t) &= u_2(x,y,t)+u''(x,y,z,t),\\ v_3(x,y,z,t) &= v_2(x,y,t)+v''(x,y,z,t),\\ C_3(x,y,z,t) &= \frac{C_2(x,y,t)}{\zeta+H-h}+C''(x,y,z,t).\end{aligned}$$

The depth-dependent part of each variable is assumed to have a zero depth-averaged value. Substituting this in the along-channel advective part of equation (2.13) gives

$$\int_{-H+h}^{\zeta} u_3 C_3 dz = u_2 C_2 + \int_{-H+h}^{\zeta} u^{''} C^{''} dz,$$

and the same applies to the cross-channel advective term. In the right-hand side of this equation the assumption is made that $u_3^{''} C_3^{''} = -\mu_d \frac{\partial C_3}{\partial x}$, i.e. the sediment fluxes due to turbulent fluctuations are incorporated as extra dispersion in the horizontal. This leads to the equation

$$\begin{aligned} \frac{\partial C_2}{\partial t} + \frac{\partial}{\partial x}\left[u_2 C_2 - \int_{-H+h}^{\zeta} \tilde{\mu} \frac{\partial C_3}{\partial x} dz\right] \\ + \frac{\partial}{\partial y}\left[v_2 C_2 - \int_{-H+h}^{\zeta} \tilde{\mu} \frac{\partial C_3}{\partial y} dz\right] \quad = \quad E_2 - D_2. \end{aligned} \tag{2.14}$$

The horizontal diffusion coefficient is now given by $\tilde{\mu} = \mu_h + \mu_d$ and is assumed to be depth-independent.

The treatment of the left-over integral term in equation (2.14) leads to a difference in models used. With the use of Leibniz' rule the term can be rewritten as

$$-\int_{-H+h}^{\zeta} \tilde{\mu} \frac{\partial C_3}{\partial x} dz = -\tilde{\mu} \frac{\partial C_2}{\partial x} + \tilde{\mu} \left\{ C_3|_{\zeta} \frac{\partial \zeta}{\partial x} - C_3|_{-H+h} \frac{\partial(-H+h)}{\partial x} \right\}. \tag{2.15}$$

The first model approach is adopted by Van Rijn (1993); De Jong (1998) and many others and assumes that the concentration has a uniform distribution over the vertical (well-mixed vertical conditions). This means that the right-hand side of eq. (2.15) reduces to $\frac{\tilde{\mu}}{(\zeta+H-h)} \frac{\partial}{\partial x}(\frac{C_2}{\zeta+H-h})$. The same applies for the turbulent diffusion term in the cross-channel direction.

The second model approach assumes that $C_3|_{\zeta} \ll C_3|_{-H+h}$ and thus the stock term including the concentration at the surface is negligible. The other stock term is assumed to be compensated by a wave-induced flux. This assumption reduces the right-hand side of eq. (2.15) to $-\mu \frac{\partial C_2}{\partial x}$. Using this approach, it has been shown by Schuttelaars and De Swart (1996) that this parameterisation is necessary in order to obtain realistic morphodynamic equilibria. Ridderinkhof (1998) also showed that wave effects cannot be neglected. Therefore the second model approach is adopted here. These assumptions form one of the main differences between the model used in this chapter and the model of De Jong (1998).

2.A.2 Reduction from 2DH to 1D version

Next equation (2.14) is integrated over the actual width $\tilde{b}$ of the embayment. Application Leibniz' rule and the no-flux conditions for water and sediment through solid boundaries

results in

$$\frac{\partial}{\partial t}\int_{-\frac{1}{2}\tilde{b}}^{\frac{1}{2}\tilde{b}} C_2 dy + \frac{\partial}{\partial x}\int_{-\frac{1}{2}\tilde{b}}^{\frac{1}{2}\tilde{b}} \left[u_2 C_2 - \tilde{\mu}\frac{\partial C_2}{\partial x}\right] dy = \int_{-\frac{1}{2}\tilde{b}}^{\frac{1}{2}\tilde{b}} (E_2 - D_2) dy.$$

Now define $C = \frac{1}{\tilde{b}}\int_{-\frac{1}{2}\tilde{b}}^{\frac{1}{2}\tilde{b}} C_2 dy$ and $u = \frac{1}{B}\int_{-\frac{1}{2}B}^{\frac{1}{2}B} u_2 dy$. Note that it is assumed that $u_2 = 0$ above the tidal flats; furthermore there is neither erosion nor deposition above the flats. Finally the bottom in the deep channel has no transverse structure. Again the velocity and the concentration are split in a width-averaged part and a width-fluctuating part with the fluctuating part not contributing to the width-averaged value: $u_2(x,y,t) = u(x,t) + u'(x,y,t), C_2(x,y,t) = C(x,t) + C'(x,y,t)$. Substituting these expressions in the advective term yields

$$\int_{-\frac{1}{2}\tilde{b}}^{\frac{1}{2}\tilde{b}} u_2 C_2 dy = BuC + \int_{-\frac{1}{2}\tilde{b}}^{\frac{1}{2}\tilde{b}} u' C' dy.$$

Again, the fluctuating contribution is modelled as extra dispersion in the along-channel direction: $\int_{-\frac{1}{2}\tilde{b}}^{\frac{1}{2}\tilde{b}} u' C' dy = -\mu_w \frac{\partial C}{\partial x}$. Then the one-dimensional concentration equation becomes

$$\frac{\partial}{\partial t}(\tilde{b}C) + \frac{\partial}{\partial x}(\tilde{b}uC) - \frac{\partial}{\partial x}\int_{-\frac{1}{2}\tilde{b}}^{\frac{1}{2}\tilde{b}} \mu_* \frac{\partial C_2}{\partial x} dy = B\left[E - D\right], \tag{2.16}$$

with $\mu_* = \tilde{\mu} + \mu_w$ and E, D the width-averaged erosion and deposition fluxes. As before, different model approaches can be used here to determine the diffusive flux term. This term can be rewritten as

$$-\int_{-\frac{1}{2}\tilde{b}}^{\frac{1}{2}\tilde{b}} \mu_* \frac{\partial C_2}{\partial x} dy = -\frac{\partial}{\partial x}\int_{-\frac{1}{2}\tilde{b}}^{\frac{1}{2}\tilde{b}} \mu_* C_2 dy + \frac{1}{2}\mu_* \left(C_2|_{\frac{1}{2}\tilde{b}} + C_2|_{-\frac{1}{2}\tilde{b}}\right)\frac{\partial \tilde{b}}{\partial x}.$$

The first approach is to assume that the sediment in the channel is well mixed in the cross-channel direction so that C_2 is independent of y and $\int_{-\frac{1}{2}\tilde{b}}^{\frac{1}{2}\tilde{b}} \mu_* \frac{\partial C_2}{\partial x} dy = \mu_* \tilde{b}\frac{\partial C}{\partial x}$. This has been applied by Friedrichs et al. (1998). The second approach is to assume $C_2|_{\frac{1}{2}\tilde{b}} = C_2|_{-\frac{1}{2}\tilde{b}} = 0$. The motivation for this assumption is that the depth-integrated concentration has to be zero when the depth is zero (at $y = \pm\frac{1}{2}\tilde{b}$). Note that the depth-averaged concentration is still finite there. This approach yields for the integrated diffusive flux $-\int_{-\frac{1}{2}\tilde{b}}^{\frac{1}{2}\tilde{b}} \mu_* \frac{\partial C_2}{\partial x} dy = -\mu_* \frac{\partial(\tilde{b}C)}{\partial x}$. The model used in this paper follows the second approach.

2.A.3 Sediment erosion and deposition

Here the formulation for the erosive flux E, as given in equation (2.16) is discussed. This flux is defined as $E = w_s c_a$, with w_s being the settling velocity and c_a the reference concentration. On the condition that the bottom shear stress is much larger than the critical bottom

shear stress for erosion, it appears that the erosion term can be parameterised as (Smith and McLean, 1977; Dyer, 1986)

$$E = w_s \rho_s (1-p) \Gamma \frac{|\tau_b|}{\tau_c}.$$

Here ρ_s is the sediment density, p the bed porosity, τ_b the bed shear stress, Γ an empirical constant and τ_c the critical shear stress for erosion. With $\tau_b = \rho c_d |u| u$ and $\tau_c = \rho u_*^2$ (u_{*c} is the critical friction velocity) the erosion term becomes

$$E = \rho_s (1-p) \frac{\Gamma w_s}{u_*^2} c_d u^2 = \alpha u^2.$$

The deposition flux D in eq. (2.16) is defined as $D = w_s c_b$, with c_b the sediment concentration at the bed. In order to express c_b in the concentration C an approximate balance is assumed between the dominant terms in the 3D concentration equation are considered. The latter are the settling and vertical turbulent flux, such that this balance reads

$$w_s C_3 + \mu_v \frac{\partial C_3}{\partial z} = 0.$$

The vertical dispersion coefficient is assumed to be independent of z. Then the solution of this equation is $C_3 = c_b e^{-\frac{w_s}{\mu_v}(z+H-h)}$. Integration over depth gives the concentration near the bottom expressed in the depth-integrated concentration. This results in

$$D = \gamma \beta C, \quad \gamma = \frac{w_s^2}{\mu_v}, \qquad\qquad \beta = \frac{1}{\left(1 - e^{-\frac{w_s}{\mu_v}(\zeta+H-h)}\right)}. \tag{2.17}$$

Combination of equations (2.16)-(2.17) yields the concentration equation (2.3) used in this paper.

2.B Concentration amplitudes and net fluxes

Here the amplitudes of the $\mathcal{O}(1)$ concentration are given, together with the net advective and diffusive sediment fluxes. The amplitudes of C_1 are not presented because of their complexity. For the case that $\xi_d = 0, \xi_\mu = 1$ (exponential dependence of deposition flux on depth) the $\mathcal{O}(1)$ coefficients read

$$\begin{aligned} < C_0 > &= \frac{1}{2} \frac{1}{\beta_0 (1-h)^{\xi_e}} (\hat{u}_0^s)^2, \\ C_0^{2c} &= -\frac{1}{2} \frac{1}{\beta_0 (1-h)^{\xi_e}} (\hat{u}_0^s)^2, \\ C_0^{2s} &= -a \frac{1}{\beta_0^2 (1-h)^{\xi_e}} (\hat{u}_0^s)^2, \end{aligned}$$

with the assumption $a \ll \beta_0$ and $\beta_0 = (1 - e^{-G(1-h)})^{-1}$. The net fluxes for this case read

$$\begin{aligned} F_{adv} &= a\epsilon\epsilon_4\delta\frac{3}{2}\sin(\phi)\frac{e^{-sx}}{\beta_0(1-h)^{\xi_e}}|\hat{u}_0^s|^3 \\ &\quad +a^2\epsilon^2\delta e^{-sx}\left\{\frac{(\hat{u}_0^s)^3}{2\beta_0^2(1-h)^{\xi_e}}\left(\frac{\xi_e}{4(1-h)}+\frac{1}{4}(1-\beta_0)G+\frac{\hat{\epsilon}_b}{4\epsilon}+\frac{3}{4}s\hat{u}_0^s\right)\right. \\ &\quad \left. -\frac{3\hat{u}_0^s}{4\beta_0}\left[(\hat{u}_0^s)^3\frac{1}{\beta_0(1-h)^{\xi_e}}\right]_x\right\}, \\ F_{diff} &= -a\mu\delta\frac{1}{2}\left[\frac{(\hat{u}_0^s)^2e^{-sx}}{\beta_0(1-h)^{\xi_e}}\right]_x. \end{aligned}$$

For the case that $\xi_d = 1$ and $\xi_\mu = 0$ (linear dependence of deposition flux on depth) the concentration amplitudes are

$$\begin{aligned} < C_0 > &= \frac{1}{2}\frac{(1-h)^{\xi_d-\xi_e}}{\tilde{\beta}}(\hat{u}_0^s)^2, \\ C_0^{2c} &= -\frac{1}{2}\frac{(1-h)^{\xi_d-\xi_e}}{\tilde{\beta}}(\hat{u}_0^s)^2, \\ C_0^{2s} &= -a\frac{(1-h)^{2\xi_d-\xi_e}}{\tilde{\beta}^2}(\hat{u}_0^s)^2, \end{aligned}$$

where the assumption $a \ll \frac{\tilde{\beta}}{(1-h)^{\xi_d}}$ is used and with $\tilde{\beta} = (1 - e^{-G})^{-1}$. The corresponding net advective and diffusive flux are

$$\begin{aligned} F_{adv} &= a\epsilon\epsilon_4\delta\frac{3}{2}\sin(\phi)e^{-sx}\frac{(1-h)^{\xi_d-\xi_e}}{\tilde{\beta}}|\hat{u}_0^s|^3 \\ &\quad +a^2\epsilon^2\frac{1}{2}e^{-sx}\left\{\frac{(\hat{u}_0^s)^3(1-h)^{2\xi_d-\xi_e}}{\tilde{\beta}^2}\left(\frac{\hat{\epsilon}_b}{4\epsilon}+\frac{\xi_d+\xi_e}{4(1-h)}+\frac{3}{4}s\hat{u}_0^s\right)\right. \\ &\quad \left. -\frac{3}{4}\hat{u}_0^s\frac{(1-h)^{\xi_d}}{\tilde{\beta}}\left[(\hat{u}_0^s)^3\frac{(1-h)^{\xi_d-\xi_e}}{\tilde{\beta}}\right]_x\right\}, \\ F_{diff} &= -a\mu\delta\frac{1}{2}\left[\frac{(1-h)^{\xi_d-\xi_e}}{\tilde{\beta}}(\hat{u}_0^s)^2e^{-sx}\right]_x. \end{aligned}$$

Chapter 3

Tide-bottom interaction in an embayment model

Abstract

An idealised model of a rectangular tidal embayment, with fixed side-walls and an erodible bed, is studied to gain further knowledge about the dynamics of bottom patterns. The water motion is described by the depth-averaged shallow water equations and is forced by a prescribed vertical tide at the seaward entrance. Sediment is transported as suspended load and standard formulations for the erosion and deposition fluxes near the bottom are adopted. By assuming the embayment length to be short with respect to the tidal wave-length, the model allows for a one-dimensional morphodynamic equilibrium, characterised by a spatially uniform tide moving over a bottom which slopes upward towards the landward boundary. It is shown that, for a range of values of the model parameters, this equilibrium is unstable with respect to bottom perturbations such that the growth of bed forms will occur.

One new aspect of this study is that the competition between diffusive sediment fluxes and fluxes induced by non-linearly generated overtides and residual circulations in the formation and characteristics of bottom patterns is analysed. It appears that advective processes generate a completely different sediment transport pattern than purely diffusive processes. For strong advection this pattern coincides with the residual flow pattern, which forms circulation cells located in between the bars and the troughs. Increasing the bottom friction coefficient or reducing the diffusion coefficient can result in a major change of the bed forms. Small bars and troughs then form near the entrance of the embayment, resembling tidal sand bars. These features have a length scale which is proportional to the width of the embayment, while the earlier found bed forms are proportional to the basin length scale. The second new aspect is that the generic value of the idealised model is investigated by comparing its results with those of a complex numerical model. It turns out that the physical mechanism which occurs in the idealised model is also detected in the complex model. Quantitative differences between the two models are discussed and are attributed to the different formulations of bottom shear stress and the boundary conditions at the seaward and landward side.

3.1 Introduction

Many coastal areas around the world are characterised by the presence of embayments and estuaries in which the water is predominantly driven by tides. Perillo (1995) gives an overview of different kinds of estuaries and embayments and how they were formed. Estuaries differ from tidal embayments in the sense that river discharge affects the water motion. In particular gravitational circulation induced by density differences is important. The emphasis of the present paper will be merely on embayments or estuaries with small river discharge in which density differences are negligible. Examples of such systems are those located in the Wadden Sea (Ehlers (1988), Oost (1995)), along the east coast of the United States (Davis (1996)) and New Zealand (Hicks et al. (1999)).

The morphology of a tidal embayment is often quite complex. Embayments in the Wadden Sea, which all have lengths that are small compared to the tidal wave-length, are characterised by decreasing water depths when moving from the seaward entrance towards the landward boundary. Besides, a complex pattern of deep tidal channels, separated by sandy shoals, is observed. Analysis of field data in other embayments (cf. Perillo (1995), Rinaldo et al. (1999)) has revealed that often two different classes of bed forms can be distinguished. First, there is the fractal-like pattern of channels and shoals throughout the basin, and secondly there are the tidal sand bars that are found near the entrance of the embayment.

Modelling and understanding the morphodynamics of tidal embayments is scientifically of great interest, whilst the results are also worth while for management purposes. Since external and internal (human induced) changes can cause significant changes in the embayment, it is important to understand more about the physical mechanisms which determine these bottom profiles. Changes may include sea level rise, partial closure, dredging activities or harbour construction.

Many different ways of studying this problem have been applied. Speer and Aubrey (1985), Friedrichs and Madsen (1992), Friedrichs and Aubrey (1994); Lanzoni and Seminara (1998) have studied the water motion in a tidal embayment, using cross-sectionally averaged idealised models and have demonstrated the importance of overtides, channel convergence and bottom friction formulation for tidal dynamics. Ridderinkhof (1988a,b) used a depth-averaged hydrodynamic model to study the water motion in the Dutch Wadden Sea, which has a very irregular bathymetry. He demonstrated that tide-topography interaction is very effective in generating overtides and residual circulations. In particular his results show that net circulations occur which are shifted with respect to the centre of the shoals, in the landward direction.

Recently, Wang et al. (1995) and Cayocca (2001) demonstrated that the formation of channels and shoals in tidal embayments can be successfully simulated with state-of-the-art complex numerical morphodynamic models. These results motivated further studies on analysing the underlying mechanisms responsible for the occurrence of these features. For this purpose idealised models were designed and analysed, which attempt to include only the dominant physical processes. In such a study, carried out by Seminara and Tubino (1998), it was shown that tidal bars may form as an inherent instability of a tidal wave propagating over an erodible bottom of a straight open channel. They used a local 3D shallow water model in which sediment was transported as suspended load and well-established formulations for erosion and deposition fluxes near the bed were used. The channel was considered to be

narrow (its width being much smaller than the tidal excursion length: the maximum distance travelled by a fluid particle in one tidal period). The dynamics were assumed to be frictionally dominated, i.e., the frictional timescales are much smaller than the tidal period. In that case it turns out that the preferred wave-length of the bars scales with the channel width. Schuttelaars and De Swart (1999) modelled the feedback between tidal currents and the erodible bottom in a semi-enclosed tidal embayment, rather than an open channel. Their model is therefore a global model and they considered moderately frictional embayments. They showed that in such domains channels and shoals can form which scale with the embayment length. These growing bed forms extract their energy from an underlying morphodynamic equilibrium. The latter represents a spatially uniform vertical and horizontal tide moving over a bottom with a constant slope. Their model is depth-averaged and only diffusive sediment fluxes are considered. They could justify these assumptions for embayment lengths which are small compared to the tidal wave-length.

However, in many embayments sediment fluxes due to non-linear, advective fluxes are of the same magnitude as diffusive contributions. The advective fluxes include the transport of sediment by overtides and residual circulations, the latter being generated by tide-topography interactions (Zimmerman, 1981). Moreover, numerical values for horizontal dispersion coefficients are subject to large uncertainties. These considerations motivated the objectives of the present paper, which are twofold. The first is to investigate the effect of advective processes on the dynamics of channels and shoals in a tidal embayment. Based on the work of Seminara and Tubino (1998) it is expected that advective processes will favour the formation of a different type of bottom mode, viz. tidal bars (with wave-lengths of the order of the channel width). It is important to quantify the conditions under which the different types of bottom modes (of diffusive and advective nature) form. The second objective is to test the generic value of the idealised model by comparing its results with those of a more complex, numerical morphodynamic model which includes much more physics.

The procedure followed in this paper is that the model of Schuttelaars and De Swart (1999) is extended with non-linear terms in the equations of motion for both the water motion and the sediment transport and subsequently its solutions are analysed. In section 3.2 the geometry and full equations of motion of the idealised model are discussed. Next, by applying a systematic scaling of the equations of motion, a reduced model is derived for a short embayment (i.e. its length is small compared to the tidal wave-length). Approximate solutions of this system are constructed in section 3.3 by expanding the physical variables in perturbation series in the small Strouhal number. The latter is the ratio between tidal excursion length and embayment length and measures the strength of non-linear terms in the equations of motion. Results are discussed in section 3.4 for a diffusive / advective embayment. In section 3.5 it is investigated to what extent the results of the idealised model are reproduced by a complex numerical model DELFT2D-MOR (the same model as used by Wang et al. (1995)) . Finally a discussion and the conclusions are presented.

3.2 Model description

First the model set-up is discussed. In order to focus on the basic physical mechanisms a simplified geometry is used. The equations of motion are kept as transparent as possible in

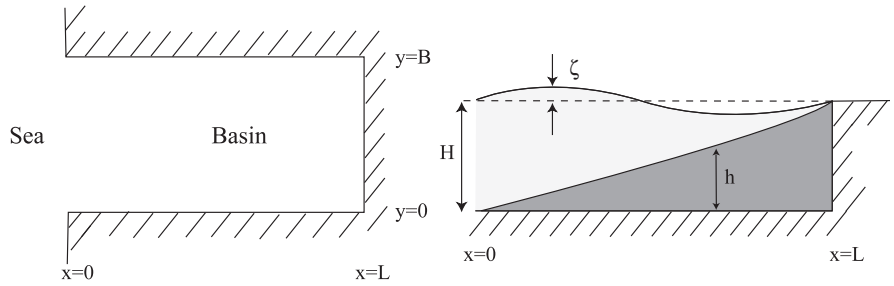

Figure 3.1: Model geometry; left: top view, right: cross-sectional view.

order to allow for a mathematical-physical analysis.

3.2.1 Geometry

The embayment is represented as a rectangular basin (width B, average length L) with non-erodible walls and an erodible bottom, see figure 3.1. One side is connected to the adjacent sea. The origin is taken at the lower-left corner and the x-axis and y-axis point in the longitudinal and lateral direction, respectively. The corresponding velocity components are u and v. The free surface elevation ζ is defined as the difference between the free surface and the tidally averaged surface level $\zeta = 0$. The height of the bed profile h is defined as the distance between the bed and a reference depth H, the depth at the entrance of the embayment which is considered to be constant. The actual depths at the side-walls $y = 0$ and $y = B$ are assumed to be always finite, but at the landward side of the embayment the depth $\zeta + H - h$ vanishes. This choice is motivated by both field data and the results of simple analytical models, see e.g. Schuttelaars and De Swart (1996). Thus $x = L$ is just the average position of the landward boundary. For typical Wadden Sea embayments $B \sim 2$ km, $L \sim 20$ km and $H \sim 10$ m, see e.g. Ehlers (1988).

3.2.2 Water motion

The hydrodynamic part of the model is based on the two-dimensional depth-averaged shallow water equations:

$$\begin{aligned}
\frac{\partial}{\partial t}(\zeta - h) + \frac{\partial}{\partial x}\left[(\zeta + H - h)u\right] + \frac{\partial}{\partial y}\left[(\zeta + H - h)v\right] &= 0, \\
\frac{\partial u}{\partial t} + u\frac{\partial u}{\partial x} + v\frac{\partial u}{\partial y} &= -g\frac{\partial \zeta}{\partial x} - \frac{\tau_{b1}}{\rho(\zeta + H - h)}, \\
\frac{\partial v}{\partial t} + u\frac{\partial v}{\partial x} + v\frac{\partial v}{\partial y} &= -g\frac{\partial \zeta}{\partial y} - \frac{\tau_{b2}}{\rho(\zeta + H - h)}.
\end{aligned}$$

The variables u and v therefore represent *depth-averaged* velocities. Furthermore, t is time, g the acceleration due to gravity, ρ the water density and τ_{b1} and τ_{b2} are the components of

the bed shear stress in the x- and y-direction, respectively. In the present model a linearised formulation of the bed shear stress is used:

$$\tau_{b1} = \rho r_* \, u, \qquad\qquad \tau_{b2} = \rho r_* \, v.$$

Here $r_* = (8/(3\pi))c_d U$ is a friction coefficient, with $c_d \sim 0.0025$ a drag coefficient and U (~ 1 ms^{-1}) the tidal velocity amplitude at the entrance of the embayment. This formulation follows from application of the Lorentz linearisation concept to the original quadratic bottom stress, as discussed in Zimmerman (1992) and references therein. The parameter r_* is chosen such that the linear bottom stress provides for the same tidally-averaged energy dissipation in the embayment as the non-linear stress. The success of this linearisation concept is well-known in tidal hydrodynamics (Li and O'Donnell, 1997). A recent study by Schramkowski et al. (2002) shows that using the linear bottom stress concept instead of the quadratic formulation has only marginal effects on the morphodynamics of tidal embayments.

Finally note that Coriolis terms and Reynolds stresses related to turbulent mixing of momentum in the horizontal direction are neglected in the model. Furthermore, no wind forcing is used. Boundary conditions include a prescribed M_2 tide at the entrance, no water flux through solid boundaries $y = 0$ and $y = B$ and a kinematic condition at the landward boundary. More specifically, they read

$$\begin{aligned} v &= 0 && \text{at} && y = 0,\ y = B, \\ \zeta &= A\,\cos(\sigma t) && \text{at} && x = 0, \\ u &= \frac{d\hat{x}}{dt} && \text{at} && x = \hat{x}. \end{aligned}$$

Here $\sigma \sim 1.4 \cdot 10^{-4}$ s^{-1} is the radian frequency of the M_2 tide and A is the free surface amplitude at the seaward boundary. Furthermore, $\hat{x}$ is the position of the moving water front, i.e., the intersection line of the free surface $z = \zeta$ and the bottom $z = -H + h$. It obeys $< \hat{x} >= L$, where $< \cdot >$ denotes an average over the tidal period. Thus it is assumed that the water depth vanishes at this location. Subsequent analysis of the equations of motion will show that this is a necessary condition for obtaining solutions.

3.2.3 Suspended sediment concentration

In the model it is assumed that the bottom of the embayment consists of fine sand (typical grain size $d \sim 2 \cdot 10^{-4}$ m). This sediment can be eroded by shear stresses acting at the bed and is subsequently transported as suspended load. The concentration of suspended sediment in the water is described by

$$\frac{\partial C}{\partial t} + \frac{\partial}{\partial x}\left[uC - \mu_* \frac{\partial C}{\partial x}\right] + \frac{\partial}{\partial y}\left[vC - \mu_* \frac{\partial C}{\partial y}\right] = \alpha(u^2 + v^2) - \gamma C. \tag{3.1}$$

Here C represents the *depth-integrated* sediment concentration, μ_* (~ 50 m^{2}s^{-1}) is a horizontal diffusion coefficient and α and γ are constants which depend on the sediment properties. The last two terms on the left-hand side of this equation describe the divergence of the suspended load sediment flux due to advective and diffusive processes. The contributions on

the right-hand side are the sediment pick-up function at the bottom, induced by the bed shear stress, and the deposition flux due to settling effects. A derivation of this equation can be found in Van Rijn (1993).

The erosion term is modelled as being proportional to the squared magnitude of the velocity field, in accordance with the suggested parametrisation (based on the analysis of field data) by Dyer (1986). It is further assumed that the actual depth-averaged velocities are well above the critical depth-averaged velocity for erosion (approximately 0.25 ms $^{-1}$ for fine sand) during the major part of the tidal cycle. Then the erosion coefficient is $\alpha \sim 10^{-2}$ kg s m^{-4}. The deposition flux near the bed is proportional to the depth-integrated concentration and for fine sand the deposition coefficient $\gamma \sim 10^{-3}$ s^{-1} (for a discussion see Schuttelaars and De Swart (1996) and appendix 2.A.3 in Chapter 2).

The boundary conditions for the concentration at the side-walls read

$$vC - \mu_* \frac{\partial C}{\partial y} = 0 \qquad \text{at} \qquad y = 0,\ y = B,$$

in other words, the normal component of the suspended load flux vanishes at these locations. Those at the open boundary $x = 0$ and landward boundary $x = L$ require some more discussion. First, note that, when considered on a global scale, diffusive sediment fluxes are small compared with advective fluxes. Their ratio is measured by the parameter $P = \mu_*/(U\,B)$, which turns out to be much smaller than 1. However, diffusive fluxes can be locally large, in particular near boundaries where specific conditions must be fulfilled. In this model there are two of such conditions. One specifies the normal component of the tidally averaged suspended load flux at the landward boundary which will be discussed later on. The other reads

$$< \alpha u^2 - \gamma C >= 0 \qquad \text{at} \qquad x = 0,$$

which states that at the seaward boundary there is an average balance between erosion and deposition of sediment. In fact the latter *defines* the location $x = 0$ of the boundary between embayment and outer sea in this model. Note that it is equivalent to stating that the divergence of the tidally averaged suspended load sediment flux vanishes at this location.

The condition given above only determines the time-mean part of the concentration, denoted as $< C >$. Thus locally large gradients in this quantity may occur. Field data indicate that no boundary layer behaviour in the fluctuating part of the concentration, denoted as $\tilde{C} = C - < C >$, is to be expected. In order to avoid the latter it is therefore required that

$$\tilde{C}(x, y, t; \mu_*) = \tilde{C}(x, y, t; \mu_* = 0) \qquad \text{at} \qquad x = 0,\ x = L.$$

This implies that diffusive sediment fluxes related to the fluctuating part of the concentration are always small compared to advective sediment fluxes.

3.2.4 Bottom evolution

The bottom evolution equation follows from conservation of sediment mass and reads

$$\rho_s(1-p)\left\{\frac{\partial h}{\partial t} + \vec{\nabla}\cdot\vec{F}_b\right\} = -\left(\alpha(u^2+v^2) - \gamma C\right). \tag{3.2}$$

Here $\rho_s (\sim 2650$ kgm$^{-3})$ is the grain density, $p \sim 0.4$ the bed porosity, $\vec{F_b}$ the volumetric bed load sediment flux per width unit and $\vec{\nabla}$ is the nabla vector with components $\partial/\partial x$ and $\partial/\partial y$ in the x- and y-direction. On the right-hand side of equation (3.2) the difference between erosion and deposition fluxes at top of the bed load layer appear. In this study the formulation of Bailard (1981) for the bed load flux is adopted, because it is based on physical arguments (compared to empirical formulations) and it explicitly accounts for bed slope effects (preferred downhill transport of sediment). Schuttelaars and De Swart (1999) showed that slope effects in the bed load flux have to be included to prevent unlimited growth of the perturbations. This way, a preferred length scale of the perturbations can be found and fast oscillating modes are damped. In the present depth-averaged model context it reads

$$\vec{F_b} = \frac{\hat{\kappa} c_d}{g'} |\vec{u}|^3 \left\{ \frac{\vec{u}}{|\vec{u}|} - \frac{1}{\tan\phi} \vec{\nabla} h \right\},$$

where $\hat{\kappa} \sim 6$ is a dimensionless constant, $g' = (\rho_s - \rho)\, g/\rho$, $\phi \sim 30^o$ the angle of repose and $\vec{u}$ the depth-averaged velocity vector.

The corresponding boundary conditions are

$$\begin{aligned} \vec{F_b} &= 0 \qquad \text{at} \qquad y = 0,\ y = B, \\ < \vec{F_b} \cdot \vec{n} + \vec{u} C - \mu_* \vec{\nabla} C > \cdot \vec{n} &= 0 \qquad \text{at} \qquad x = L, \\ \frac{\partial h}{\partial t} &= 0 \qquad \text{at} \qquad x = 0, \end{aligned}$$

with $\vec{n}$ the normal vector at each boundary. The condition at $x = L$ states that the time-mean of the normal component of the *total* sediment flux vanishes at the landward boundary. The model is now fully determined.

3.2.5 Scaling and derivation of the short embayment model

Scaling

The equations of motion, as specified in the previous section, are now made non-dimensional by using characteristic scales of motion for the phenonema under investigation. This is done in order to be able to derive a reduced model which describes the dynamics in a short tidal embayment. The scaling is performed by using the velocity scale U, free surface amplitude A and frequency σ of the tidal forcing, the length L of the basin and the reference depth H at the entrance of the embayment. The dimensional parameters are denoted with * and are shown below:

$$\begin{aligned} &x^* = Lx, \quad y^* = Ly, \quad t^* = \sigma^{-1} t, \quad u^* = Uu, \quad v^* = Uv, \\ &h^* = Hh, \quad \zeta^* = A\zeta = \tfrac{HU}{\sigma L}\zeta, \quad C^* = \tfrac{\alpha U^2}{\gamma} C, \quad r_* = \sigma H r \quad \mu_* = \sigma L^2 \mu. \end{aligned}$$

Note that the width B is not used as a separate length scale. In fact in the subsequent analysis the ratio L/B will be considered as a model parameter. The motivation for the scale of the free surface elevation ζ is that in the continuity equation the divergence of the mass transport should be of the same order of magnitude as the local changes of the sea surface.

The non-dimensional flow equations

In non-dimensional form the governing equations for water motion and free surface become

$$(\zeta - \frac{1}{\epsilon}h)_t + [(\epsilon\zeta + 1 - h)u]_x + [(\epsilon\zeta + 1 - h)v]_y = 0, \tag{3.3}$$

$$\lambda^2 \left[u_t + \epsilon(uu_x + vu_y) + \frac{r}{(\epsilon\zeta + 1 - h)}\, u \right] = -\zeta_x, \tag{3.4a}$$

$$\lambda^2 \left[v_t + \epsilon(uv_x + vv_y) + \frac{r}{(\epsilon\zeta + 1 - h)}\, v \right] = -\zeta_y. \tag{3.4b}$$

Here the subscripts denote differentation with respect to that (dimensionless) variable. The non-dimensional parameters include λ^2, the ratio of embayment length over the tidal wave length, r the non-dimensional friction parameter and the Strouhal number ϵ, being the ratio of the tidal excursion length U/σ and the embayment length L. This last parameter will be a key parameter in this work, as the influence of advection on the sediment transport processes is investigated. For details and values of the non-dimensional parameters see table 3.1. The value of r is set at 0.45 in table 3.1 because the calculated value for the Frisian Inlet system ($r = 0.64$) gives numerical problems in the chosen solution method.

Reduced equations for short embayments

In this study the specific class of short tidal embayments will be considered, i.e., their lengths are small with respect to the tidal wave-length. This means that parameter λ^2 is small and the friction parameter is of order 1. Many embayments are of this type: e.g. those in the Wadden Sea have $\lambda^2 \sim 0.1$ and $r \sim 1$, as can be seen from table 3.1. Therefore the velocity components and the free surface elevation are expanded in the parameter λ^2. The zeroth order momentum equations become

$$\zeta_x = 0, \qquad \zeta_y = 0. \tag{3.5}$$

These two equations state that the free surface is spatially constant and thus $\zeta = \cos(t)$. However, these equations are degenerated from the original momentum equations and are not sufficient to close the system. Additional information follows from the first-order (λ^2) momentum equations. Elimination of the first-order free surface elevations, by taking cross derivatives of the momentum equations and subtracting the results, yields the vorticity equation

$$\Omega_t + \epsilon\left[(u\Omega)_x + (v\Omega)_y\right] = \left[\frac{r\,u}{\epsilon\zeta + 1 - h}\right]_y - \left[\frac{r\,v}{\epsilon\zeta + 1 - h}\right]_x, \tag{3.6}$$

in which $\Omega = v_x - u_y$ is the relative vorticity. The terms on the left-hand side are the local change of relative vorticity and the divergence of the vorticity flux, respectively. The terms on the right-hand side describe the dissipation of vorticity by bottom friction, as well as vorticity production by bottom frictional torques. The latter are due to the fact that the direction of the bottom frictional force opposes that of the velocity, whilst the strength of the

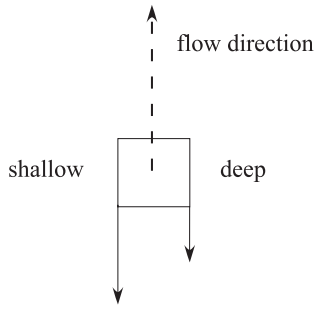

Figure 3.2: Top view sketch of a fluid column moving over an irregular bottom topography; flow direction is indicated by the dashed arrow. Since the bottom frictional force (denoted by the solid arrow) is larger in shallow water than in deeper water the column experiences a torque. In this example positive vorticity is generated.

force increases with decreasing water depths. Hence a fluid parcel moving over an uneven bottom will experience a torque, as sketched in figure 3.2, see also Zimmerman (1981).

To summarize: for short, moderate-frictional embayments the hydrodynamics are to first order governed by the continuity equation (3.3), by equations (3.5), which state that the free surface is spatially constant, and by the vorticity equation (3.6). The boundary conditions read

$$v = 0 \qquad \text{at} \qquad y = 0,\ y = \frac{B}{L}, \tag{3.7a}$$

$$v_t + \epsilon u v_x + \epsilon v v_y = -\frac{rv}{\epsilon\zeta + 1} \qquad \text{at} \qquad x = 0, \tag{3.7b}$$

$$\epsilon u = \frac{d\hat{x}}{dt} \qquad \text{at} \qquad x = \hat{x}. \tag{3.7c}$$

The condition for the cross-channel velocity component at the seaward boundary has been derived from the $\mathcal{O}(\lambda^2)$-momentum balance and follows from the condition that there is no cross-channel sea surface gradient at that location.

In non-dimensional form the concentration equation (3.1) becomes

$$a\left\{C_t + \left[\epsilon u C - \mu C_x\right]_x + \left[\epsilon v C - \mu C_y\right]_y\right\} = (u^2 + v^2) - C. \tag{3.8}$$

Here a is the ratio of the deposition timescale over the tidal period and μ the non-dimensional horizontal diffusion parameter. The corresponding non-dimensional boundary conditions can be straightforwardly derived from the original conditions.

The non-dimensional bottom evolution equation and tidal averaging

Finally the scaled bottom evolution equation becomes

$$h_t + \hat{\delta}\vec{\nabla} \cdot \left[|\vec{u}|^3 \left\{\frac{\vec{u}}{|\vec{u}|} - \frac{H}{L\tan\phi}\vec{\nabla}h\right\}\right] = -\delta\left(u^2 + v^2 - C\right).$$

Table 3.1: Non-dimensional model parameters

$\lambda^2 = \frac{\sigma^2 L^2}{gH} \sim 0.078$	$\left(\frac{\text{embayment length}}{\text{tidal wave length}}\right)^2$
$\epsilon = \frac{U}{\sigma L} \sim 0.15$	$\frac{\text{tidal excursion length}}{\text{length of embayment}}$
$r = \frac{r_*}{\sigma H} \sim 0.45$	$\frac{\text{tidal period}}{\text{dissipation timescale}}$
$a = \frac{\sigma}{\gamma} \sim 0.04$	$\frac{\text{deposition timescale}}{\text{tidal period}}$
$\delta = \frac{\alpha U^2}{\rho_s(1-p)\sigma H} \sim 8 \cdot 10^{-4}$	$\frac{\text{tidal period}}{\text{susp. load timescale}}$
$\mu = \frac{\mu^*}{\gamma L^2} \sim 1.8 \cdot 10^{-3}$	$\frac{\text{tidal period}}{\text{diffusive time scale}}$
$\hat{\delta} = \frac{\hat{\kappa} c_d}{\sigma g' H L} U^3 \sim 5.4 \cdot 10^{-7}$	$\frac{\text{tidal period}}{\text{bedload timescale}}$
$\kappa = \frac{\hat{\delta}}{\delta} \frac{H}{L \tan\phi} \sim 3.4 \cdot 10^{-7}$	bed slope coefficient

Here $\delta \sim \mathcal{O}(10^{-4}), \hat{\delta} \sim \mathcal{O}(10^{-7})$ are the ratios of the tidal period and the suspended load timescale and bed load timescale, respectively. Based on these values it can be concluded that bedload transport of sediment is negligible. However, the contribution related to bed slope effects will be retained, for the reasons stated before. The second conclusion is that, since $\delta \ll 1$, the bed evolves on a much longer time scale than the tidal period. Thus the bottom profile is only a function of the slow morphodynamic time coordinate $\tau = \delta t$. It is well known, cf. Sanders and Verhulst (1985), that accurate solutions of such a system can be obtained by replacing the instantaneous fluxes by tidally averaged fluxes and by considering the bed level to be fixed in the hydrodynamic and concentration equations. After substitution of the non-dimensional concentration equation (3.8) the final bottom evolution equation reads

$$h_\tau = -\left\langle a\left[\epsilon u C - \mu C_x\right]_x + a\left[\epsilon v C - \mu C_y\right]_y \right\rangle + \kappa \nabla^2 h, \tag{3.9}$$

where the bed slope coefficient κ is given in table 3.1.

The non-dimensional model equations for the short embayment are given by the equations (3.3) with $h_t = 0$, (3.5), (3.6), (3.8) and (3.9), with corresponding boundary conditions.

3.3 Basic state and linear stability analysis for short embayments

3.3.1 Basic state

The system of equations, as specified in section 3.2.5, describe the feedback between tidal motion and the sandy bottom in short embayments. In Schuttelaars and De Swart (1999) this system was analysed in the limit $\epsilon \to 0$ (no advective processes). They demonstrated for

that case that channels and shoals can form due to an inherent morphodynamic instability mechanism. This was done by first constructing a simple morphodynamic equilibrium which is characterised by a steady bed level and which is uniform in the cross-channel direction. Next it was demonstrated that, for realistic values of the model parameters, this basic state is unstable with respect to small bottom perturbations having a cross-channel structure.

The new aspect of the present study is that small, but finite values of the Strouhal number ϵ are considered. Following the approach as described above the first concern is to find a simple morphodynamic equilibrium. Such solutions, having no cross-channel structure, have been found by Schuttelaars and De Swart (1996), although the boundary conditions differ slightly from what is used here. Their results indicate that morphodynamic equilibria in short embayments are characterised by a spatially uniform tidal flow over a bottom which slopes in the landward direction. These solutions are consistent with field data (Friedrichs, 1995) which show that in morphodynamic equilibrium the bed shear stress is spatially uniform.

These considerations motivate the investigation of the existence of a simple basic state for which

$$\zeta = \zeta_{\rm eq}(t), \quad u = u_{\rm eq}(t), \quad v = v_{\rm eq} = 0, \quad C = C_{\rm eq}(t), \quad h = h_{\rm eq}(x). \tag{3.10}$$

In this case the solutions turn out to be

$$\zeta_{\rm eq} = \hat{\zeta}^c \cos(t) \equiv \cos(t), \quad u_{\rm eq}(t) = \hat{u}^s \sin(t) \equiv -\sin t, \quad h_{\rm eq}(x) = x, \tag{3.11a}$$

and

$$C_{\rm eq}(t) = < \hat{C}_{\rm eq} > + \hat{C}^{c2} \cos(2t) + \hat{C}^{s2} \sin(2t), \tag{3.11b}$$

see appendix 3.A, where $< \hat{C}_{\rm eq} >$ and the coefficients $\hat{C}^{c2}$ and $\hat{C}^{s2}$ are given. Note that this basic state is equivalent to that used by Schuttelaars and De Swart (1999), hence advective processes do not modify the characteristics of the 1D morphodynamic equilibrium. However, they strongly affect the stability properties of this equilibrium, as will be shown.

3.3.2 Linear stability analysis

The stability properties of the basic state are investigated by analysing the dynamics of perturbations, which are x, y dependent, evolving on this basic state. The free surface remains unperturbed, since the elevation is spatially uniform. Thus solutions are considered of the form

$$\begin{aligned} &\zeta = \zeta_{\rm eq}, \quad u = u_{\rm eq} + u', \quad v = v', \\ &\Omega = \Omega', \quad C = C_{\rm eq} + C', \quad h = h_{\rm eq} + h', \end{aligned} \tag{3.12}$$

with the equilibrium solution as stated in eq. (3.11). The perturbations (represented with $'$) are supposed to be small compared to the basic variables.

Substitution of (3.12) in (3.3), (3.6), (3.8) and (3.9) yields, after linearising,

$$[-h'u_{\rm eq} + (\epsilon\zeta_{\rm eq} + 1 - h_{\rm eq})u']_x + [(\epsilon\zeta_{\rm eq} + 1 - h_{\rm eq})v']_y = 0, \tag{3.13a}$$

$$\Omega'_t + \epsilon(u_{\rm eq}\Omega')_x = [ru_{\rm eq}h' + ru'(1 + h_{\rm eq} - \epsilon\zeta_{\rm eq})]_y - [rv'(1 + h_{\rm eq} - \epsilon\zeta_{\rm eq})]_x\,, \tag{3.13b}$$

$$\Omega' = v'_x - u'_y, \tag{3.13c}$$

$$aC'_t + a\epsilon\left[(u_{\rm eq}C' + u'C_{\rm eq})_x + (v'C_{eq})_y\right] - \mu(C'_{xx} + C'_{yy}) = 2u_{eq}u' - C', \tag{3.13d}$$

$$h'_\tau = -a\epsilon\left[< u'C_{eq} + u_{eq}C' >_x + < v'C_{eq} >_y\right] + a\mu < C'_{xx} + C'_{yy} > +\kappa\nabla^2 h'. \tag{3.13e}$$

It should be remarked that the terms on the right-hand side of the vorticity equations follow from replacing in eq. (3.6) the term

$$\frac{r\vec{u}}{\epsilon\zeta + 1 - h} \;\rightarrow\; r\vec{u}(1 + h - \epsilon\zeta),$$

which means that the bottom frictional force is expanded in a Taylor series around the reference depth, such that only the first-order effect of depth variations is taken into account. This is done in order to prevent the frictional terms to become singular near the landward boundary, where the water depth vanishes. In fact it is a crude way of accounting for drying and flooding of shoals in this area. An alternative method to include such effects has been suggested and investigated by Delfina (2000), but this also comes down to regularisation of the bottom frictional force in areas where partial drying and flooding occurs.

The equations given above have a number of new effects which were not considered by Schuttelaars and De Swart (1999). The continuity equation includes mass transport related to free surface variations. The vorticity equation includes the advection of perturbed vorticity by the basic tidal current. Moreover, dissipation of vorticity and bottom frictional torques are affected by the free surface elevations. As discussed by Zimmerman (1981) and Li and O'Donnell (1997) these terms have important consequences for the dynamics, such as generation of tidal residual circulations and topographically trapped overtides.

The accompanying boundary conditions are

$$\begin{array}{lllll} \text{at } x = 0: & v' = 0, & < C' > = < 2u_{\rm eq}u' >, & h' = 0, \\ \text{at } y = 0, y = B/L: & v' = 0, & \mu C'_y = 0, & \kappa h'_y = 0, \end{array}$$

and at the landward boundary they read

$$\begin{aligned} -h_{\rm eq,x}u' - u_{\rm eq}h'_x + \epsilon\zeta_{\rm eq}u'_x + \epsilon\zeta_{\rm eq}v'_y = 0 \quad &\text{at} \quad x = 1, \\ a\epsilon < u_{\rm eq}C' + u'C_{\rm eq} > -a\mu < C' >_x - \kappa h'_x = 0 \quad &\text{at} \quad x = 1, \\ h' = 0 \quad &\text{at} \quad x = 1. \end{aligned}$$

The latter conditions are obtained by using the fact that the intersection point $\hat{x}$ of bottom and water level obeys the relation $\epsilon\zeta = -1 + h(x, y)$. If this expression is expanded around the

average position of the landward boundary, i.e. $x = 1$, it follows immediately that $h(1, y) = 1$. Since the bed level $h_{\mathrm{eq}}(x = 1) = 1$ it is clear that $h' = 0$ at this location. Substituting these two expressions in the continuity equation yields the given condition for the along-channel velocity component u' at this location. Thus the last condition is an alternative formulation for the kinematic boundary condition used previously.

3.3.3 Derivation and analysis of the eigenvalue problem

The equations and boundary conditions presented in the previous subsection allow for solutions of the type

$$\begin{array}{llll} u' = \mathrm{Re}\left\{\tilde{u}(x,t)\cos(ly)\,\mathrm{e}^{\omega\tau}\right\}, & v' = & \mathrm{Re}\left\{\tilde{v}(x,t)\sin(ly)\,\mathrm{e}^{\omega\tau}\right\}, \\ C' = \mathrm{Re}\left\{\tilde{C}(x,t)\cos(ly)\,\mathrm{e}^{\omega\tau}\right\}, & h' = & \mathrm{Re}\left\{\tilde{h}(x)\cos(ly)\,\mathrm{e}^{\omega\tau}\right\}, \end{array} \tag{3.14}$$

with

$$l = \frac{n\pi L}{B}, \qquad n = 0, 1, 2, \ldots . \tag{3.15}$$

Here ω is an eigenvalue, its real part being the growth rate on the slow (i.e., morphological) timescale and its imaginary part representing the frequency of the perturbations. The quantity l is the dimensionless cross-channel wavenumber of the perturbations. Note that the velocity components and suspended sediment concentration vary on the slow morphological timescale, but also vary harmonically on the fast, tidal timescale.

Approximate solutions for the 'fast' variables u, v and C can be found as perturbation series in the small Strouhal number, thus

$$\tilde{u} = u_0 + \epsilon u_1 + \epsilon^2 u_2 + \ldots , \tag{3.16}$$

and similar expressions for v and C. Substitution in continuity equation (3.3), vorticity equation (3.6) and concentration equation (3.8) and collection of terms with equal powers in ϵ yields in lowest order a system of equations that describes the generation of perturbed velocity components u_0, v_0 which vary harmonically with the basic frequency of the tide. They are generated by interaction of the basic tidal current with the perturbed bottom topography, which causes both a perturbed mass flux and a frictional torque. This results in a perturbed sediment pick-up function which in turn generates a concentration C_0 consisting of a time-independent, residual part and an M_4-part which varies harmonically with twice the basic frequency. Hence solutions of the $\mathcal{O}(1)$-system are of the form

$$\begin{aligned} u_0 &= u_0^c \cos(t) + u_0^s \sin(t), \\ v_0 &= v_0^c \cos(t) + v_0^s \sin(t), \\ C_0 &= < C_0 > + C_0^{c2} \cos(2t) + C_0^{s2} \sin(2t). \end{aligned}$$

Substituting these results in the $\mathcal{O}(1)$-equations yields the first 6 differential equations for the $x-$ dependent Fourier coefficients, as presented in appendix 3.B. The equation for the steady part of the concentration will be discussed later on.

In this study also the effects of advective processes on the dynamics of the perturbations is investigated. They are described by the $\mathcal{O}(\epsilon)$-equations of motion. Taking into account the known structure of the $\mathcal{O}(1)$-solutions, it can be seen that the non-linear advection and bottom friction terms cause the generation of perturbed velocity components u_1, v_1 which have residual parts and harmonic parts varying with twice the basic tidal frequency. Then the concentration C_1 has an M_2-part and an M_6-part, thus

$$\begin{aligned} u_1 &= < u_1 > + u_1^{c2}\cos(2t) + u_1^{s2}\sin(2t), \\ v_1 &= < v_1 > + v_1^{c2}\cos(2t) + v_1^{s2}\sin(2t), \\ C_1 &= C_1^c\cos(t) + C_1^s\sin(t) + C_1^{c3}\cos(3t) + C_1^{s3}\sin(3t). \end{aligned}$$

The equations for these 10 Fourier coefficients are also given in appendix 3.B. The corresponding boundary conditions can be derived in a straightforward manner.

If now the solutions for the velocity and sediment concentration are substituted in bottom equation (3.13e) it follows that the net advective sediment fluxes are of order ϵ^2. Thus, also the net diffusive fluxes must be known up to this order which requires the calculation of the $\mathcal{O}(\epsilon^2)$ steady concentration $< C_2 >$. Instead of separately considering the contributions $< C_0 >$ and $< C_2 >$ it is more convenient to solve the equation for $< C >=< C_0 > + \epsilon^2 < C_2 >$. This variable describes the along-channel structure of the steady concentration up to $\mathcal{O}(\epsilon^2)$. This result is also given in appendix 3.B and it shows that the steady concentration is determined both by diffusive and advective processes. The diffusive sediment flux will therefore include an implicit advective part.

Finally the bottom evolution equation is considered. After substitution of (3.14) and (3.16) in eq. (3.13e) it follows

$$\omega\tilde{h} = -(F_x^x + lF^y).$$

Expressions for F^x, F^y are given in appendix 3.B; these variables denote the along-channel structure of the x-component and y-component of the perturbed net total-load sediment flux vector $\vec{F}$. As can be traced back from eq. (3.13e) and (3.14) it follows that this flux vector reads

$$\vec{F} = (\mathrm{Re}\left\{F^x\cos(ly)e^{\omega\tau}\right\}, \mathrm{Re}\left\{F^y\sin(ly)e^{\omega\tau}\right\}). \tag{3.17}$$

Now the equations and corresponding boundary conditions in appendix 3.B define an eigenvalue problem for the 18 variables u_0^c, u_0^s, v_0^c, v_0^s, $< u_1 >$, u_1^{c2}, u_1^{s2}, $< v_1 >$, v_1^{c2}, v_1^{s2}, C_0^{c2}, C_0^{s2}, C_1^c, C_1^s, C_1^{c3}, C_1^{s3}, $< C >$ and $\tilde{h}$. The ordinary differential equations and boundary conditions for these variables are given in appendix 3.B. They are solved numerically on an equidistant grid (N grid points $x_1, x_2, \ldots, x_N$) using central finite difference schemes. Then the eigenvalue problem is of the type

$$\omega \mathrm{B}\Psi = \mathrm{A}\Psi,$$

where Ψ is a vector with $18N$ components specifying the values of the 18 state variables mentioned above at the N grid points. Furthermore, A and B are $18N \times 18N$ matrices, with all components of B being zero except the diagonal elements which act on the $\tilde{h}(x_n)$ variable. Solving the eigenvalue problem given above yields a set of eigenvalues and eigenfunctions.

For each cross-channel wavenumber l, given in eq. (3.15), different along-channel modes are obtained. The main interest is in the eigenvalue with the largest real part, since the perturbation with the fastest growth rate will be dominant over the other solutions. Amplitudes are not known, since the solution is determined up to an arbitrary constant. However, relative differences are correct.

The numerical computations were carried out for $N = 101$ gridpoints in the longitudinal direction. It was checked that results remained unchanged if a larger number of gridpoints was taken. Experiments focused on the sensitivity of results for different values of the lateral wavenumber l, the friction parameter r, the non-linear (advection) parameter ϵ and the diffusion coefficient μ.

3.4 Results

3.4.1 Default case and weak bottom friction case

First, results are presented for two cases. One is the default case, representative for the Frisian Inlet (see Chapter 1), in which parameters have values as given in table 3.1. The second case concerns the situation in which the bottom friction coefficient is much weaker: $r = 0.15$. The motivation for studying the latter case is that it allows for a comparison with results discussed by Schuttelaars and De Swart (1999). They demonstrated that in their model, which accounts only for diffusive sediment transport, this value of r is close to the critical friction value r_c for which the 1D morphodynamic equilibrium becomes unstable. Moreover, the weak bottom friction case is more easy to analyse and yields insight in the behaviour of the system for larger bottom friction.

Figure 3.3 shows the scaled growth rates of the perturbations for the two cases as a function of the lateral modenumber n. The different curves represent different longitudinal modenumbers m. Note that $l = l(n) = n\pi L/B$, so for an embayment with a fixed length and width the cross-channel wavenumber l can only attain discrete values. The latter are indicated by the dashed vertical lines in the plot. It turns out that the imaginary part of most eigenvalues is zero, hence their perturbations show only exponential growth or decay in time, without any oscillatory and migration behaviour. The presence of a longitudinal slope in the 1D bottom structure imposes an asymmetry in the system which may cause eigenvalues to be complex. This occurs only for the $m = 2$ mode found for $\epsilon = 0.2$ in the case of strong bottom friction. Its imaginary part is shown in figure 3.3(d) and decreases with increasing lateral wavenumbers. The absence, presence or behaviour of imaginary parts is not yet fully understood. Clearly the plots show that growth rates are positive for a range of l-values and longitudinal modenumbers m. Note that perturbations with $l = 0$ (i.e. 1D perturbations) always have negative growth rates. Hence the 1D morphodynamic equilibrium is always stable with respect to 1D perturbations, but often unstable with respect to 2D perturbations. The latter grow exponentially due to a positive feedback between tidal currents and the erodible bottom. The plots also show that the first longitudinal mode ($m = 1$) always has the largest growth rate and that growth rates increase with increasing values of the bottom friction parameter r. These results are consistent with earlier findings by Seminara and Tubino (1998) and Schuttelaars and De Swart (1999). The important extension is that in the present model

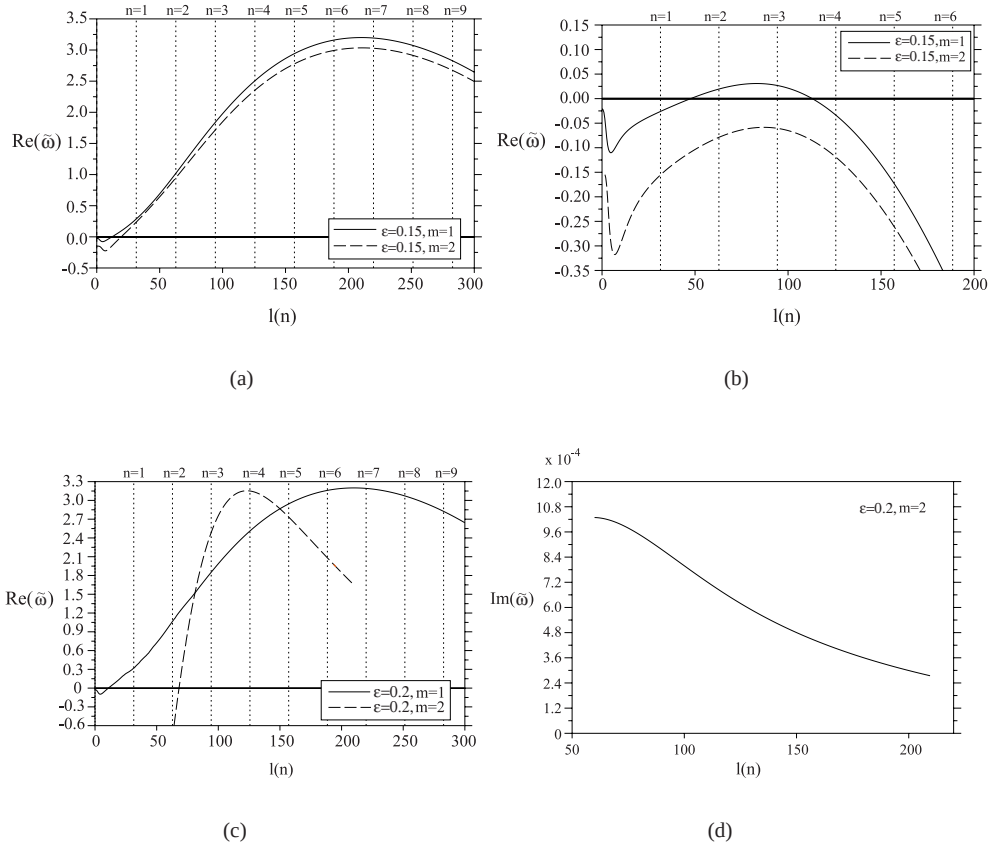

Figure 3.3: Scaled growth rate $\tilde{\omega} = \omega/a$ of the bottom perturbations versus the lateral modenumber $l(n)$ for (a) the default case ($r = 0.45$), (b) weak bottom friction ($r = 0.15$) and (c) default case with $\epsilon = 0.2$, real part and (d) imaginary part. All other parameters have default values as given in table 3.1.

both diffusive and advective sediment transport in a semi-enclosed embayment is taken into account.

Note that all growth rate curves attend a maximum for a specific value of $l = l_p$. The mode with a possible $l(n)$ value (indicated by the dashed vertical lines) closest to l_p is called the preferred mode: within the context of linear stability theory this is the mode that will be dominant after a certain time. The dimensional e-folding timescale of the preferred mode is given by

$$T^* = \frac{1}{a^2 \mu \delta \sigma \mathrm{Re}\left\{\tilde{\omega}\right\}}.$$

Hence a dimensionless growth rate $\tilde{\omega} = 1$ corresponds to an e-folding timescale of the order of decades. For the default case T^* turns out to be approximately 30 years ($n = 4$), whereas for the weak bottom friction case $T^* \sim 3500$ years ($n = 3$). In the latter case the timescale

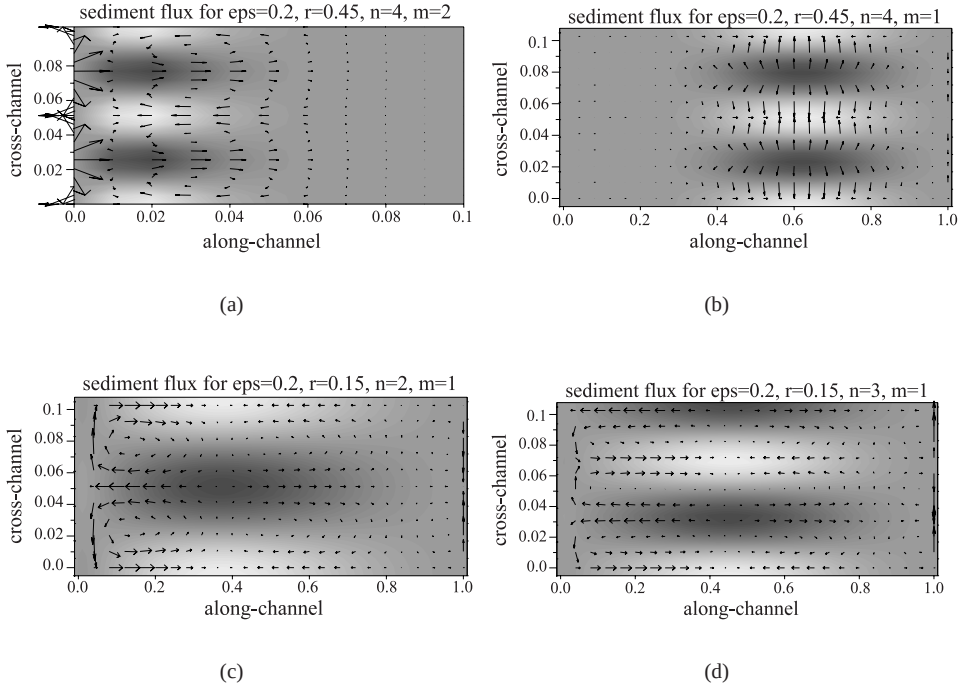

Figure 3.4: The most preferred bottom modes. Colours indicates the bottom profile, with white areas represent bars and dark areas representing troughs. The arrows represent the net sediment fluxes corresponding to these modes. Default case (a) $n = 4, m = 1$, (b) $n = 4, m = 2$ and weak bottom friction case (c) $n = 2, m = 1$, (d) $n = 3, m = 1$. Note the different along-channel length scale for figure (a).

is much longer than decades because of the small value of Re $\{\tilde{\omega}\}$. The spatial patterns of the most preferred bottom modes are shown in figure 3.4. The arrows in the plots indicate the direction of mean total sediment fluxes. The fluxes are directed from troughs to crests, thereby indicating the exponential growth of these modes.

Notice that two types of bottom modes are obtained. The first are local modes (figure 3.4(a)), in which the bed forms scale with the width of the embayment. The patterns shown in figure 3.4(b),(c),(d) on the other hand scale with the embayment length: they are referred to as global modes. In the following subsections both the weak and realistic bottom friction case will be discussed separately in order to unravel the physical mechanism causing the formation of the two different types of bottom patterns.

3.4.2 Analysis of global bottom patterns

In this subsection the weak bottom friction case ($r = 0.15$) is analysed; all other parameters have their default values as given in table 3.1. This value is close to critical conditions were bars start to form, as can be seen in figure 3.5. The value of the non-linear parameter ϵ is var-

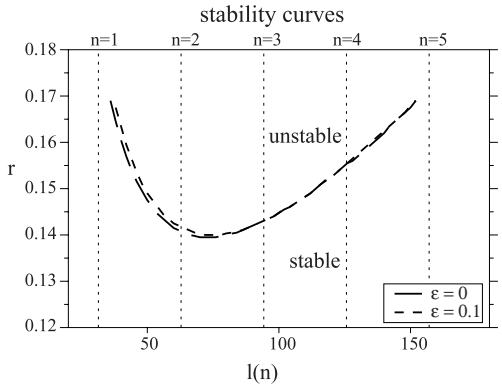

Figure 3.5: The non-dimensional friction parameter at the stability boundary as a function of the lateral wavenumber. Indicated are the stable and unstable areas, where perturbations will decay and grow, respectively.

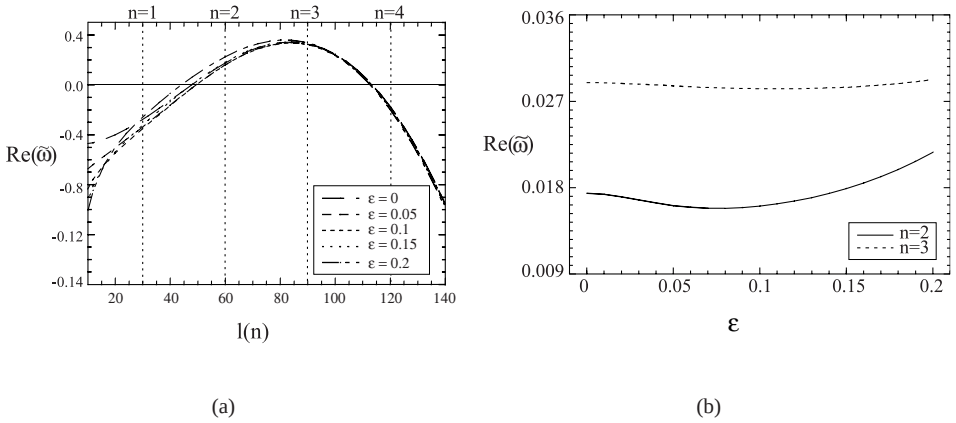

(a) (b)

Figure 3.6: (a) growth rate of the $m = 1$ longitudinal modes versus lateral wavenumber for different values of the non-linear parameter ϵ, (b) growth rate of the $m = 1$-mode versus the non-linear parameter ϵ, for $l = 60$ and $l = 90$. Parameter values are specified in table 3.1, except that $r = 0.15$.

ied in order to analyse the competition between diffusive and advective sediment fluxes which control the morphodynamic instability mechanism. From figure 3.5 it can be seen that advective processes only have a weak influence on the stability of the system. Figure 3.6(a) shows the growth rate of the first longitudinal mode ($m = 1$) as a function of the lateral wavenumber, for different values of ϵ. It appears that for every value of ϵ between 0 and 0.2 there is a regime of lateral wavenumbers, approximately between $l = 40$ and $l = 120$, for which

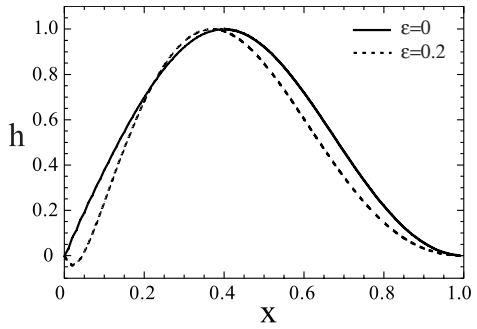

Figure 3.7: Bottom profiles for $\epsilon = 0$ and $\epsilon = 0.2$; modenumbers are $m = 1$ and $n = 2$ (i.e. lateral wavenumber $l = 60$),

perturbations have positive growth rates. We focus therefore on this region. Figure 3.6(b) shows the growth rate of the $m = 1$ mode as a function of the non-linear parameter ϵ for the two natural lateral wavenumbers which have positive growth rates, i.e. $l = 60$ and $l = 90$. For small numbers of ϵ the growth rates decrease, but for larger values they increase again. Apparently the influence of advection is at first stabilising (the instabilities grow less fast), but for stronger advection destabilising. Eventually, the growth rate becomes larger than for the purely diffusive case ($\epsilon = 0$).

This behaviour can be most clearly analysed for the mode with $l = 60$, i.e. natural mode $n = 2$, because its growth rate shows the largest variations with ϵ. However, it should be realised that the mode with $l = 90$ (natural mode number $n = 3$) is more dominant for these parameter values since it has slightly larger growth rate. The spatial patterns of the $n = 2$ and $n = 3$ mode were already shown in figure 3.4(c),(d). Remember that the total bottom pattern consists of the perturbed modes superimposed on the equilibrium profile $h_{\,\mathrm{eq}}(x) = x$. The effect of stronger advection (increasing ϵ) on the longitudinal structure of the bottom profile is shown in figure 3.7. The main difference between the results for $\epsilon = 0$ and $\epsilon = 0.2$ is that with increasing degree of non-linearity the crest slightly shifts towards the entrance and near the entrance a small trough appears.

As shown in figure 3.4 the most preferred bottom mode in the weak friction case has a global structure. In order to understand the physical mechanism causing its formation, knowledge is required about the divergence of the net sediment fluxes which in turn are determined by the flow and concentration fields. Here a systematic analysis is done for a fixed cross-channel wavenumber $l = 60$ and a Strouhal number $\epsilon = 0.2$. Figure 3.8 shows the along-channel spatial distribution of the most dominant components of the perturbed velocity, vorticity and concentration field. Because only a linear stability analysis is performed, the amplitudes are not known. All variables are scaled with the maximum bed height of the perturbation. Relative differences between variables are therefore correct. Each subplot contains variables as a function of the along-channel coordinate (x); the corresponding bed profile is indicated by a thick line. The amplitude of this bed profile has been adapted for each subplot such that the relevant variables are shown in the most optimal manner. For reasons of

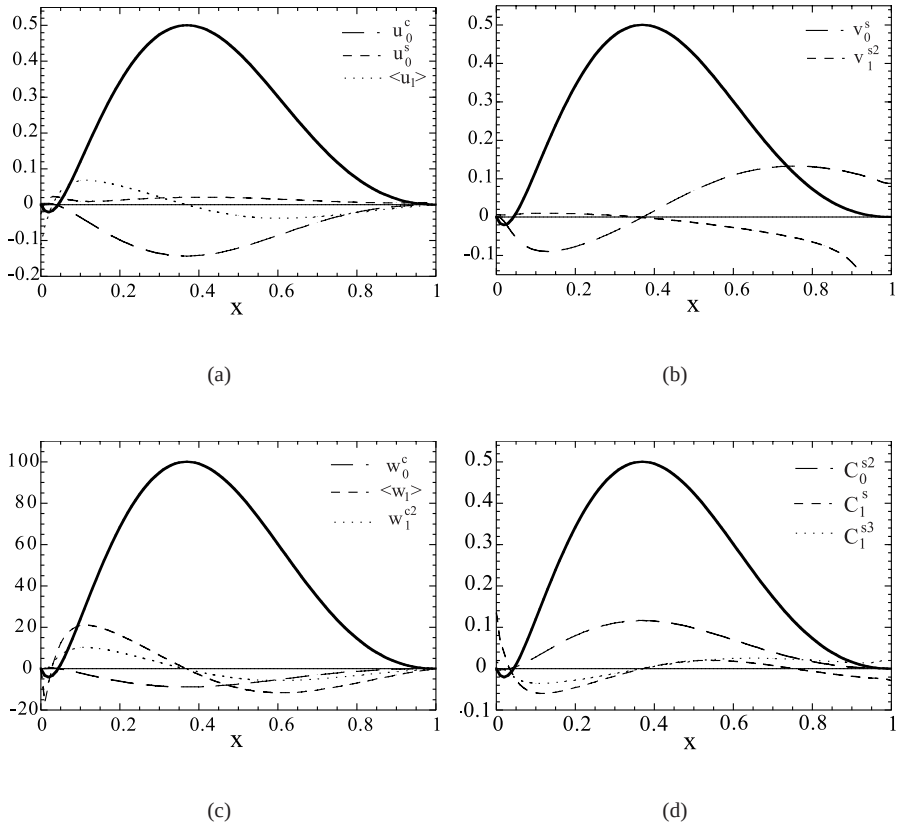

Figure 3.8: Along-channel structure of tidal flow and concentration components for $l = 60$ and $\epsilon = 0.2$, (a) largest along-channel tidal velocity components, (b) largest cross-channel velocity components, (c) largest tidal vorticity components and (d) largest tidal concentration components. The thick line is the bed perturbation profile.

clarity not all components were plotted; those not shown are at least a factor 10 smaller. This however does not imply that they are not important for the instability mechanism, since the advective sediment fluxes include interactions between the velocity field and the concentration field. Small variables can therefore have a significant influence on the total net sediment flux, both in value and direction. Clearly, the perturbed flow field is dominated by the u_0^c and v_0^s, i.e., the cosine-component of the lowest-order along-channel velocity field and the sine-component of the lowest-order cross-channel velocity field. In the along-channel direction the maximum velocity is reached above the bar, while in the cross-channel direction the maximum velocities are found on the sides of the bar. The highest concentration forms above the crest.

The spatial patterns of the residual flow and of the mean concentration are shown in fi-

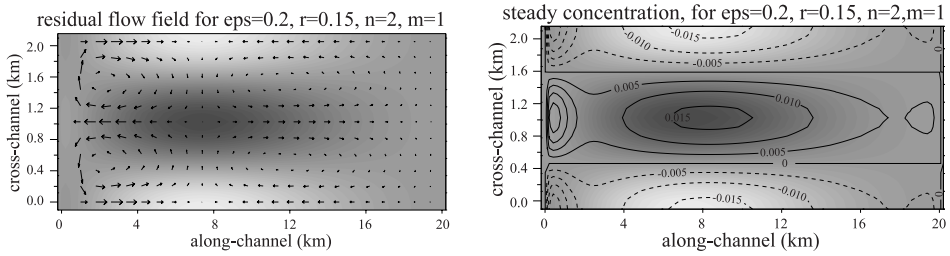

(a) (b)

Figure 3.9: For the $n = 2$ mode, $l = 60$ (a) perturbed residual circulation and (b) steady part of the perturbed concentration. The solid lines are positive contour lines, the dashed lines denote negative contour lines with intervals of 0.05, $\epsilon = 0.2$. White represents a bar, black a trough.

gure 3.9. The tidal rectification mechanism (see Zimmerman (1981)) explains, to a large extent, the presence of these residual eddies. Since bottom friction is felt stronger in shallower regions, frictional torques will be created at locations where the flow moves over a bottom with a non-zero slope in the cross-flow direction. This means that positive (negative) vorticity is generated in the upper half of the basin (in the positive y-direction), whilst negative (positive) vorticity is generated in the lower half during flood (ebb). Advection then causes a divergence in the vorticity flux near the entrance and a convergence in the vorticity flux on the landward side (note that both the velocity and the vorticity change sign, when flood becomes ebb). The residual vorticity field will, therefore, consist of negative vorticity near the entrance and positive vorticity near the landward side in the upper half of the basin. The reverse holds for the lower half.

Figure 3.9(b) shows that the spatial distribution of the steady part of the perturbed concentration is such that diffusive transport of suspended sediment occurs from the trough (high concentration) to the bar (low concentration). This is due to the depth dependency of the bottom friction term in the momentum equation: since friction is felt more strongly in shallower parts, the flow will decelerate over the bars. This causes less stirring and, therefore, less suspended material over the bars.

Next the sediment fluxes are analysed, as defined in eq. (3.17). To identify the role of the different contributing processes the amplitudes F^x and F^y of the along-channel and cross-channel component of the sediment flux are split as follows:

$$\begin{aligned} F^x &= F^x_{adv1} + F^x_{adv2} + F^x_{adv3} + F^x_{adv4} + F^x_{diff} + F^x_{bl}, \\ F^y &= F^y_{adv5} + F^y_{adv6} + F^y_{adv7} + F^y_{diff} + F^y_{bl}. \end{aligned} \tag{3.18}$$

The full expressions for F^x and F^y are given in appendix 3.B. In the result above F_{diff} represents sediment fluxes due to diffusion, whilst F_{adv} denotes the sediment fluxes due to advection. The sediment flux has a bed load component F_{bl}, which represents the downslope transport. The advective terms in equation (3.18) are related to different physical processes,

as indicated below:

F^x_{adv1}	$\sim$ settling lag effects,		
F^x_{adv2}	$\sim$ residual current,	F^y_{adv5}	$\sim$ residual current,
F^x_{adv3}	$\sim$ overtide,	F^y_{adv6}	$\sim$ overtide,
F^x_{adv4}	$\sim$ overtide,	F^y_{adv7}	$\sim$ overtide.

The terms denoted by "overtide" are all related to the first overtide. Now the role of the separate contributions to the total sediment flux is quantified. First, the divergence of the perturbed sediment flux is analysed for two different values of the Strouhal number: $\epsilon = 0.05$ and $\epsilon = 0.2$. This is done because the lower value corresponds to the case where advection has a stabilising effect, whilst the larger value corresponds to the destabilising effect (see figure 3.6(b)). Results are shown in figure 3.10 and 3.11, where in each subplot the along-channel structures of the different terms contributing to the total flux divergence are plotted. The plots in 3.10 correspond to $\epsilon = 0.05$ and the plots in 3.11 are for the case $\epsilon = 0.2$. The corresponding bed profiles are added as thick lines. This bed profile has been rescaled in each subplot to clarify the along-channel structure of the variables shown. The spatial patterns of the total sediment flux are shown in figure 3.12 for a slightly larger bottom friction value ($r = 0.18$) and for different values of the Strouhal number ϵ. From the different subplots in figures 3.11 and 3.11 it can be seen that for weak advection ($\epsilon = 0.05$, fig. 3.10), the advective flux is two orders of magnitude smaller than the diffusive flux. For $\epsilon = 0.2$, fig. 3.11, these fluxes are of the same order of magnitude. It also turns out that for $\epsilon = 0.05$ the cross-channel flux divergence acts destabilising (negative divergence on top of the bar, sediment transport from trough to bar, the perturbation grows) whilst for $\epsilon = 0.2$ it acts stabilising (transport from bar to trough, the perturbation is decaying). This can be understood from the behaviour of the different flux components shown in the subplots. The terms contributing most to the cross-channel sediment flux are the advective term F^y_{adv5} (related to the residual current) and the diffusive flux. In the along-channel direction the dominant sediment flux contribution is F^y_{adv2}. Clearly the fluxes related to settling lag effects and overtides do not contribute significantly to the divergence of the sediment flux.

In the cross-channel direction the diffusive flux always acts destabilising (convergence on top of the bar, see fig. 3.10(b), 3.11(b)), whilst the advective flux related to the residual current (F^y_{adv5}) has a stabilising effect (fig. 3.10(d), 3.11(d)). In the along-channel direction the largest advective flux terms both have a destabilising effect (fig. 3.10(c),3.11(c)). This explains why the growth rate for increasing ϵ (fig. 3.6(b)) first decreases and then increases again. For small values of the advective parameter ϵ, the dominant cross-channel diffusive flux is internally reduced due to advective processes affecting the mean concentration. This has a stabilising effect. The weak along-channel advective flux (which acts destabilising) has no significant influence yet. For stronger advection, the advective sediment fluxes become of the same order of magnitude as the diffusive sediment flux. In the cross-channel direction, this causes further reduction of the trough to bar transport, finally resulting ($\epsilon = 0.2$) in a weak transport from bar to trough. The now strong along-channel advective sediment flux causes the destabilising effect found in figure 3.6(b).

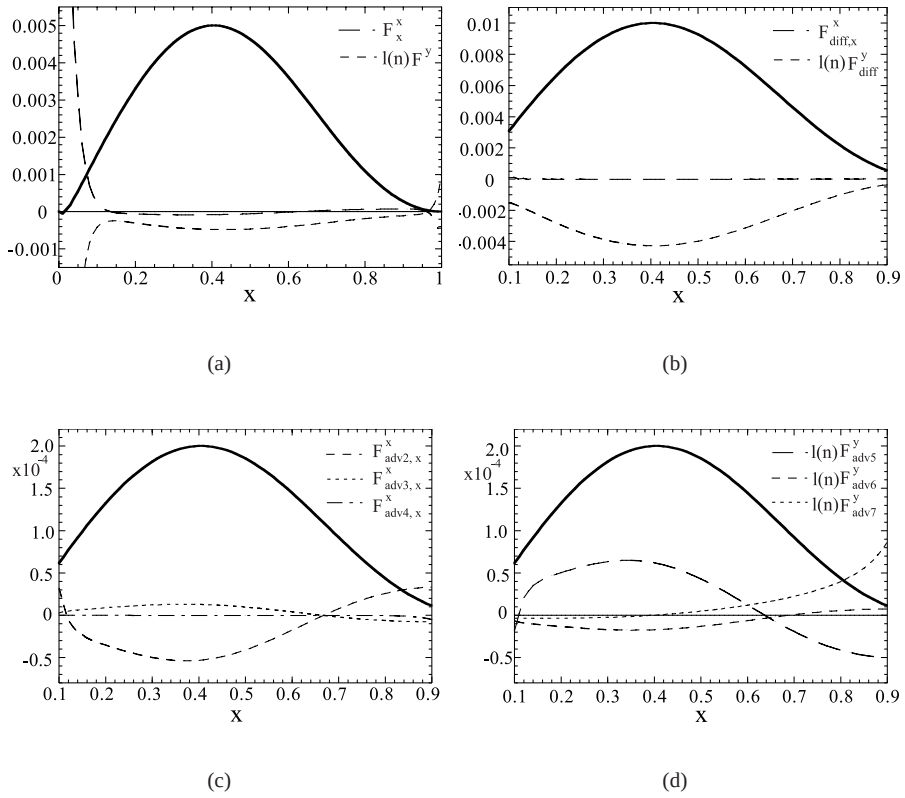

Figure 3.10: Along-channel structure of divergence of sediment fluxes; results for $l = 60$ and $\epsilon = 0.05$. (a) divergence of sediment flux, (b) divergence of diffusive sediment flux, (c) divergence of advective sediment flux terms in the x-direction, (d) divergence of advective sediment flux terms in the y-direction. See the text for further explanation. The thick line denotes the bed perturbation profile.

It is also evident from figures 3.11(c) and 3.11(d) that the components $(F^{\,x}_{adv2}, F^{y}_{adv5})$ describe a flux of sediment of which the direction coincides with that of the residual current. Using the definitions given in appendix 3.B the divergence of this flux can be estimated as

$$\begin{aligned} F^{x}_{adv2,x} + l\,F^{y}_{adv5} &= a\epsilon^2 < \hat{C} > [< u_1 >_x + l < v_1 >] \\ &\sim a\epsilon^2 < \hat{C} > \frac{< u_1 >}{1-x}. \end{aligned} \tag{3.19}$$

In the last step the $\mathcal{O}(\epsilon)$ continuity equation given in appendix 3.B is used with its right-hand side put equal to zero (these terms turn out to be very small with respect to the terms on the left-hand side). Thus the formation of the bottom pattern for $\epsilon = 0.2$ is controlled by the along-channel component of the residual current. This change in net sediment fluxes with increasing values of the Strouhal number ϵ can also be observed in figure 3.12. For small ϵ the

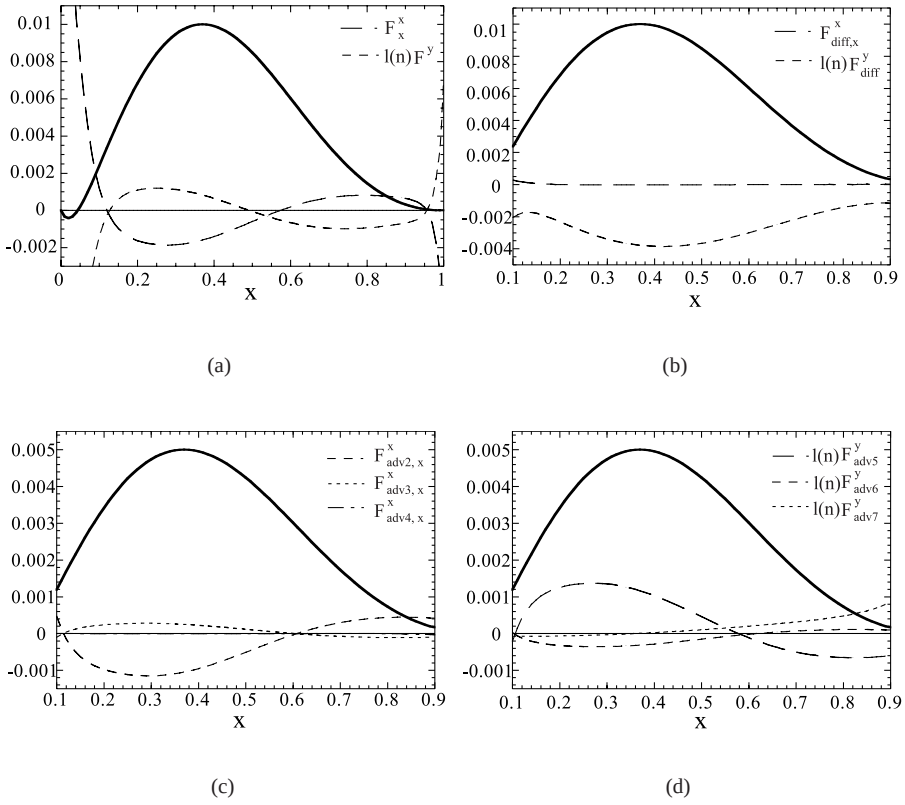

Figure 3.11: Along-channel structure of divergence of sediment fluxes; results for $l = 60$ and $\epsilon = 0.2$. (a): divergence of sediment flux, (b): divergence of diffusive sediment flux, (c): divergence of advective sediment flux terms in the x-direction, (d): divergence of advective sediment flux terms in the y-direction. See the text for further explanation. The thick line denotes the bed perturbation profile.

fluxes are mainly of diffusive origin and point in the cross-channel direction. However with increasing ϵ the advective fluxes become more important and the formation of the bottom pattern is then determined by the divergence of the flux of mean concentration by the tidal residual current.

3.4.3 Analysis of local bottom patterns

As already shown in figure 3.4 for large values of the bottom friction parameter local bed forms can be found which scale with the embayment width. In fact it is found from model experiments that such patterns always emerge if advective fluxes are much larger than diffusive fluxes. To illustrate this, results are shown for the case that the diffusion parameter μ is a factor of 4 smaller than in the default case. Figure 3.13 shows the growth rate as a function

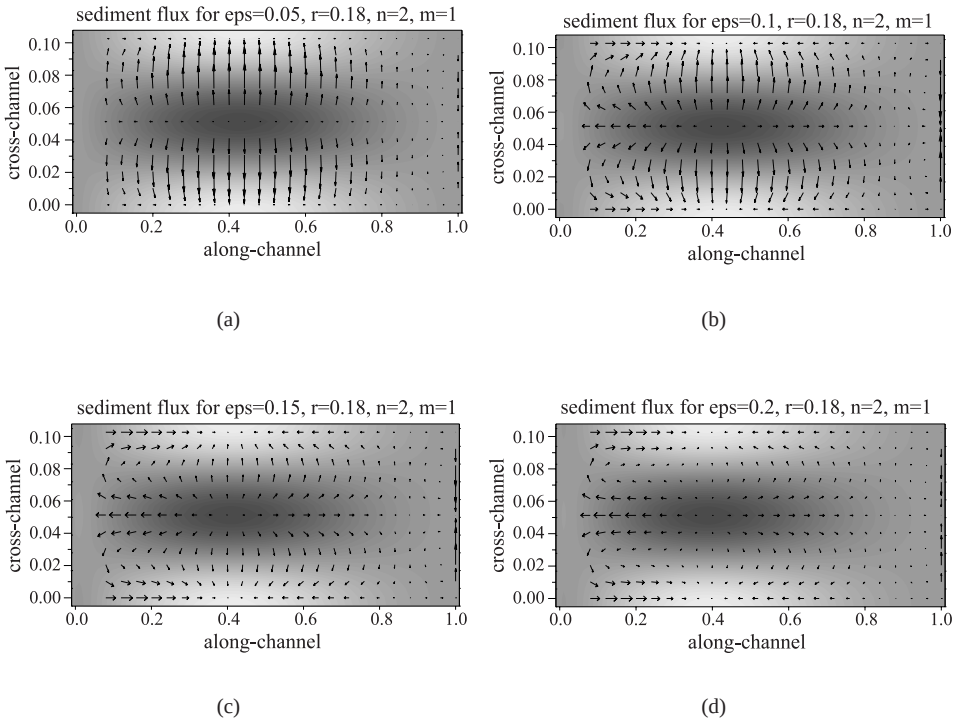

Figure 3.12: Bottom patterns and sediment fluxes for $l = 60$ and $r = 0.18$; (a) $\epsilon = 0.05$, (b) $\epsilon = 0.1$, (c) $\epsilon = 0.15$ and (d) $\epsilon = 0.2$. Troughs are dark, bars are light. The vectors denote the direction and relative strength of the sediment flux.

of the Strouhal number, whilst figure 3.14 shows bottom patterns for different values of the Strouhal number. The situations in figure 3.14(a),(b),(c) are stable while figure 3.14(d) shows an unstable situation. Clearly it can be seen that up to $\epsilon = 0.14$ a global bottom mode is the most preferred mode. However, for larger values of the non-linear parameter a local pattern prevails which manifests itself near the seaward entrance. Such patterns are referred to as tidal bars, in accordance with Seminara and Tubino (1998). Note that the only difference between figure 3.14(d) representing a local mode and figure 3.4(c) representing a global mode is the value of the diffusion parameter μ. The eigenvalues all have zero imaginary parts, so that no migration is found here.

A detailed analysis of the flow, concentration and sediment flux fields for tidal bars revealed that the flux components F^x_{adv2} and F^y_{adv5} are always dominant for these bars. This means that, to a good approximation, the direction of the net sediment flux coincides with that of the residual current. The divergence of this flux is therefore described by equation (3.19) and thus controlled by the along-channel component of the residual current.

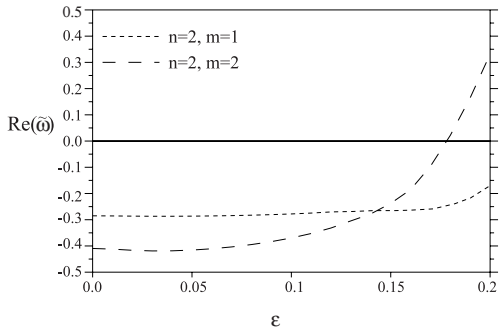

Figure 3.13: The growth rate for the case of small diffusion as a function of the Strouhal number for n=2. Shown are the first two longitudinal modes, m=1 and m=2.

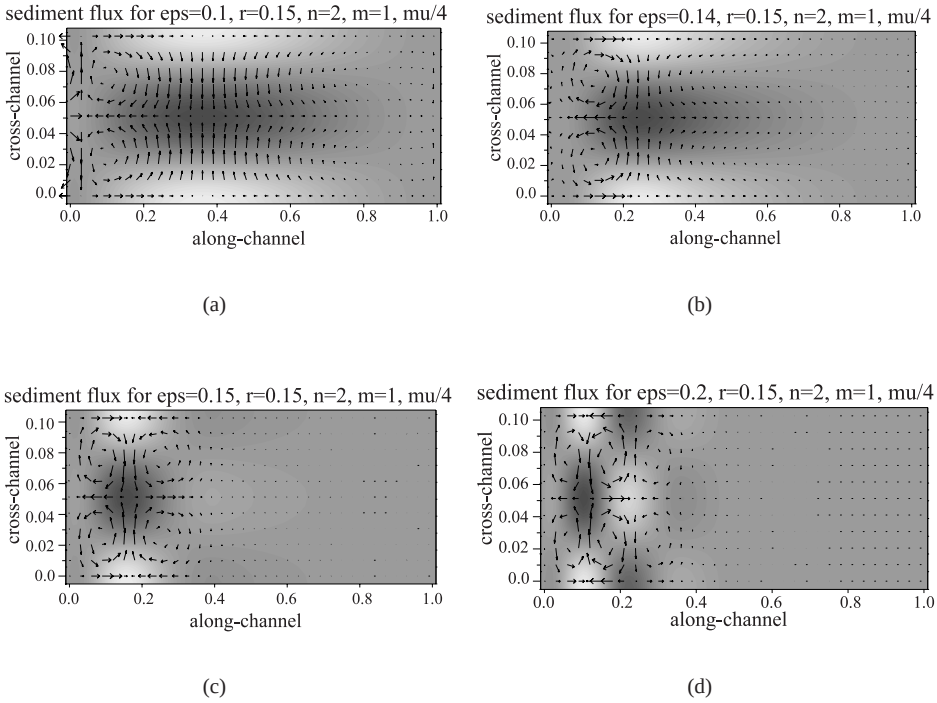

Figure 3.14: Bottom patterns and corresponding sediment fluxes for cross-channel wavenumber $l = 60$ and $\epsilon = 0.1, 0.14, 0.15$ and 0.2. The diffusion parameter μ is a factor 4 smaller than its default value and $r = 0.15$; other parameters have their default values.

3.5 Robustness of the results: runs with a complex model

It is important to check whether the results of the present idealised model can also be identified in a more complex model. Therefore runs were carried out with Delft2D-MOR (hereafter abbreviated as DMOR), a numerical morphodynamical model developed by WL|Delft Hydraulics. This model, of which only the executable version is available, solves the depth-averaged shallow water equations, supplemented with a user-specified formulation for the sediment transport and a bottom evolution equation. A staggered grid is used and the Alternating Direction Implicit (ADI) technique is applied in the numerical scheme (for details see Stelling and Leendertse (1992)). The model uses a drying- and flooding procedure that keeps at least 30 cm of water in every gridpoint. The sediment transport is computed during a tidal cycle, using a fixed bed. A new bottom is then computed from the divergence of the net sediment flux using a morphodynamic timestep of 3 months. The main difference with the idealised model is that DMOR solves the full equations of motion, rather than solving asymptotic expansions of these equations. Another difference with the idealised model is that DMOR does not allow for a bottom shear stress which is linear in the depth-averaged velocity; instead it uses the standard quadratic friction law. Also boundary conditions at the seaward entrance and landward side were slightly different.

The experiments with DMOR were designed as follows. The model domain was chosen identical to that of the idealised model, i.e. a rectangular embayment with physical dimensions which are representative for the main channel of Frisian Inlet, see table 3.1. Also the options in the numerical model and parameter values were chosen such that they are as close as possible to those used in the idealised model. Here the weak bottom friction case was considered, i.e., friction parameter $r = 0.15$. The equivalence between this linear friction coefficient and the drag coefficient which appears in the quadratic friction law was discussed in section 3.2.2. Then, for fixed parameter values different initial bathymetries were introduced, which consisted of a superposition of an equilibrium bottom profile and a natural bottom eigenmode, as computed from the idealised model. Next the DMOR was integrated in time and it was tested whether the bottom evolution could be fitted with an exponential function, as is to be expected for eigenmodes of the system. In case of success the growth rates could be computed from this fitting procedure.

In practise this approach met difficulties. The first problem was that the equilibrium profile of the idealised model ($h = x$) turned out not to be an equilibrium bottom profile of the complex model. Instead, steady sedimentation (2 mm with peaks up to 1 cm for each morphological time step of about 1 year) occurred in the basin with large deposits at the landward side. This could be understood from the fact that DMOR forces the normal velocity at the landward side to vanish; run-up of the tidal wave is not allowed for. The corresponding gradients in the velocity, in combination with the drying-flooding routine of DMOR, cause large sediment deposition in this area. Fortunately, this problem was not crucial, because the corresponding evolution timescale (order of centuries) turned out to be much longer than the e-folding time of the most preferred bottom modes (order of decades). Furthermore, the problems with the drying-flooding routine could be avoided by choosing a slightly different equilibrium profile. In order to discriminate between these slow profile changes and the growth of two-dimensional bottom modes the bottom evolution was split in two parts, a trend function (depending on along-channel coordinate x and time t) representing the bottom

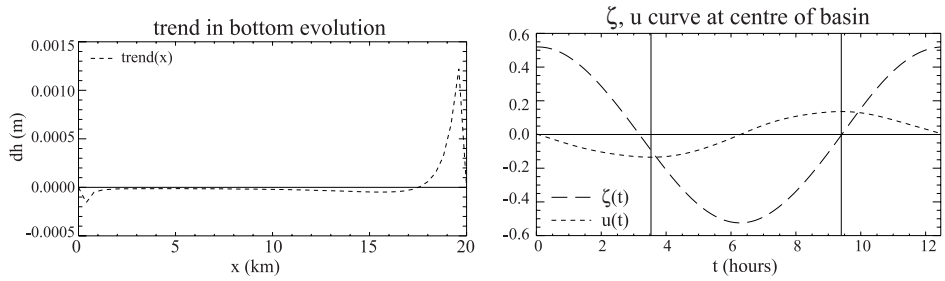

(a) (b)

Figure 3.15: Numerical model results; (a) trend (m) found in bottom evolution for $h_{\rm eq} = 0.9x$, (b) longitudinal velocity (m/s) and surface elevation (m) for one tidal period at the center of the basin ($x = 10$ km,$y = 1$ km), the vertical lines denote time of maximum velocity.

change due to the non-equilibrium state and a mode function (depending on x, y and t) representing the perturbation evolution. The mode evolution was extracted from the full evolution by application of the condition that trough and bar evolution should have equal magnitudes and opposite signs. The remaining evolution is then part of the trend. In order to minimize the trend the equilibrium profile was chosen as $h_{\rm eq} = 0.9x$; this avoids drying and flooding at the landward side, which greatly reduces the trend. Figure 3.15(a) shows the new trend, which indicates sedimentation at the end of the basin and smaller erosion near the entrance. For this reason the analysis of bottom evolution is limited to the middle part of the embayment, ranging from $x = 2$ km to $x = 18$ km. Figure 3.15(b) shows the longitudinal velocity u and the surface elevation ζ in the middle of the basin ($x = 10$ km, $y = 1$ km) for one tidal period. The idealised model results indicate that along-channel velocity and free surface have a phase shift of a quarter tidal period, which is consistent with these complex model results. However, the vertical lines in figure 3.15(b), which denote the time of maximum tidal velocity, indicate that the velocity and free surface are not completely out of phase. Thus the tidal wave is subject to some dissipation due to bottom friction, which causes a net water flux into the embayment. In order to satisfy mass conservation a small seaward-directed flow is generated within the complex model. As will be shown this has consequences for the further interpretation of the results.

As with the idealised model, runs were made for different lateral wavenumbers. The evolution of the bottom modes could be fitted well with exponential functions. This is a strong indication that the bottom eigenmodes obtained with the idealised model are also good approximations of the eigenmodes of the complex model. In figure 3.16 the growth rates of the bottom perturbations, as reconstructed from the complex model, are shown as a function of the cross-channel wavenumber l. The corresponding results obtained with the idealised model are shown in figure 3.3(b). Because of the different friction laws used the complex model produces a maximum at $l = 150$ instead of $l = 90$ (idealised result for weak bottom

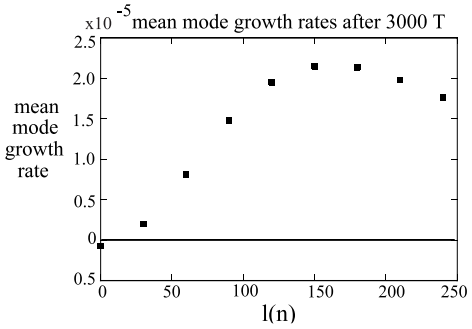

Figure 3.16: Numerical model results: growth rate versus lateral wave number for the default situation, see table 3.1, weak bottom friction: $r = 0.15$. A growth rate of $1.0 \cdot 10^{-5}$ corresponds to an e-folding timescale of $\sim$ 200 years.

friction). For larger lateral wavenumbers the maximum of the perturbation shifts towards the end of the embayment. This is also found in the idealised model for the default case ($r = 0.45$). Figure 3.16 resembles much more the results obtained with the idealised model for the default case than for the case of weak friction. This can be attributed to the differences in bottom friction formulation: the quadratic friction law used by Delft2D-MOR is more effective than the linear friction used in the idealised model. The complex model includes a stability term of diffusive origin which is similar to the slope term used in the idealised model.

Comparing the perturbation bottom evolution of the complex model with the idealised model results yields good agreement. Figure 3.17(a) shows the erosion-deposition pattern for lateral wave number $l = 60$ and advective parameter $\epsilon = 0.05$. Equal growth is demanded for the lower bar and trough but is also found for the opposite bar. The spatial pattern is similar to the idealised pattern shown in figure 3.4(c). Figure 3.17(b) shows the mean transport velocity field for the same case of $l_n = 60, \epsilon = 0.05$. Because in the idealised model the tidal wave does not induce net transport of water, the velocity pattern is compared to the mean transport velocity of the complex model, defined as

$$< u_T >= \frac{< u(t)(H + \zeta(t)) >}{< (H + \zeta(t)) >},$$

with brackets denoting tidal averaging. This eliminates the Stokes drift from the mean velocity field. The pattern (figure 3.17(b)) corresponds well to the idealised result shown in fig. 3.9. The same mechanism of positive feedback is found, with large transports in the x-direction and lesser transport in the y-direction. The mean transport velocity pattern shows the same characteristics as the idealised sediment transport pattern, that is transport of sediment from trough to bar at the end of the basin and near the entrance, with virtually no return transport in the middle of the embayment.

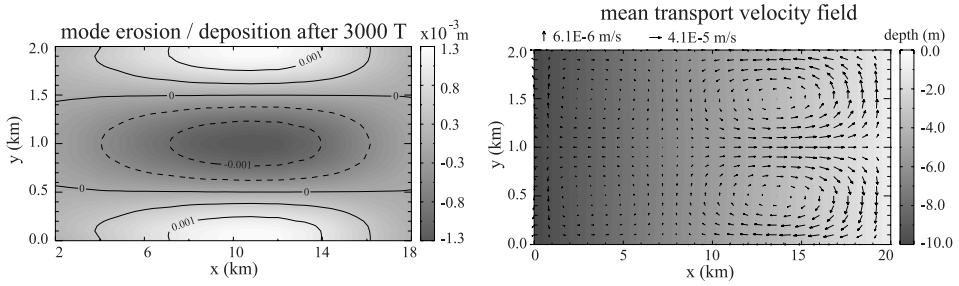

(a) (b)

Figure 3.17: Numerical model results: (a) erosion / deposition pattern (m). Dashed lines represent negative contour lines (b) mean transport velocity field, the arrows in the top right corner indicate the maximum velocity values.

3.6 Discussion

The previous section demonstrates that the main results of the idealised model are not critically dependent on the precise formulations for bottom friction and boundary conditions. Also the limitation to short embayments is not crucial: Schuttelaars et al. (2001) computed the formation of bottom patterns in longer embayments and also found both global and local modes. However, in the latter case the complicated dynamics obstructs a detailed physical analysis, as was carried out in the present study.

It is also interesting to compare the results presented in section 3.4 with those obtained by Seminara and Tubino (1998). As stated before, in the latter study it was demonstrated that in an open channel tidal bars form which scale with the channel width. Both their characteristics and underlying physical mechanism are similar to that of the local bottom modes found with the idealised model investigated in this paper. This is not surprising as it has been shown here that local modes are induced by advective sediment fluxes and these are also the fluxes considered by Seminara and Tubino (1998). A full merging of the two models is however not possible, because there are fundamental differences in their designs. The present model yields a global description of tide-topography interactions in semi-enclosed embayments. It thus explicitly deals with four different horizontal length scales: the frictional length scale r_*/σ, embayment width B, length L and the tidal excursion length U/σ. The model of Seminara and Tubino (1998) on the other hand yields a local description in a short stretch of a long tidal channel; in other words they consider the limit $(B/L) \rightarrow 0$. Besides also the narrow channel limit $B\sigma/U \ll 1$ is considered in their study. Thereby the channel length and tidal excursion length are not explicitly dealt with. Another difference is that they use 3D shallow water equations for the tidal motion and sediment transport, instead of the depth-averaged equations used in the present study. However, this is not crucial for the final results because the horizontal extent of the bars is much larger than the local water depth and the

suspended load sediment transport takes place in a layer with appreciable thickness. Indeed Schramkowski et al. (2002) demonstrated that a local depth-averaged model yields similar features as those obtained by Seminara and Tubino (1998).

Finally a few other aspects are addressed. The models discussed in this paper do not account for waves and density gradients. Hence they are designed for sheltered and well-mixed tidal embayments such as those in the Dutch Wadden Sea. Furthermore, no external forcing by the M_4 tide is taken into account: overtides are only generated within the model by internal non-linear interactions related to advection and friction terms in the equations of motion. As Wadden Sea embayments are characterised by quite a strong amplitude of M_4 tidal motion at the seaward entrance (Oost, 1995) it is interesting to consider their effect on the formation of bottom patterns. Also the model assumes simple formulations for sediment erosion and deposition. As shown in the previous chapter their parameterisations change the properties of morphodynamic equilibria of tidal embayments. Thus they will affect the formation of bottom patterns which emerge as free instabilities from these equilibria. The coupling between processes within the embayment and processes in the adjacent sea is also neglected, by stating that the bed level is fixed at the seaward entrance. This is quite a strong assumption as field data indicate that on the seaward side of most tidal embayments shallow outer deltas (also known as ebb-tidal deltas) exist, cf. Ehlers (1988); FitzGerald (1996). Both field measurements and conceptual models (Sha and Van den Berg, 1993; Kana et al., 1999) indicate that there are strong exchanges between outer sea and embayment. This will be investigated in more detail in the forthcoming chapters.

3.7 Conclusions

In this paper an idealised morphodynamic model was investigated to gain further knowledge about the initial formation of bottom patterns in a tidal embayment. The model consists of equations for depth-averaged tidal motion and depth-integrated sediment transport, as well as for the bottom evolution. Idealisations concern the geometry of the embayment (rectangular, with a length which is short compared to the tidal wave-length) and the formulations for bottom frictional forces and sediment fluxes (of suspended load nature). Furthermore, the tidal excursion length is considered to be small with respect to the embayment length. These assumptions allow for a gross analytical treatment of the model and facilitate the physical analysis of the results. One aim of the present study was to quantify and understand the role of diffusive and advective sediment fluxes in the generation of bottom patterns in semi-enclosed embayments. The second aim was to verify whether the results, found with the idealised model, would also be recovered with a more complex morphodynamic model.

The present model shows that bottom patterns with a cross-channel structure can form as free morphodynamic instabilities evolving on a basic state having only an along-channel structure. This basic state is a morphodynamic equilibrium and represents spatially uniform tidal motion over a bottom with a constant slope in the landward direction. Experiments revealed that both diffusive and advective fluxes contribute to the formation of bottom structures. Two different types of bottom modes are found. The first are global modes which have length-scales of the order of the embayment length and which occur if the magnitude of the diffusive flux is larger (or of the same order) than that of the advective flux. The spatial

bottom patterns of these global modes resemble the patterns already found by Schuttelaars and De Swart (1999) for a purely diffusive model. However, the mechanism causing the formation of these modes depends largely on the relative strength of diffusive and advective fluxes. If non-linear advective terms are small the mode is generated by the divergence of the cross-channel sediment flux which is of diffusive origin. With increasing influence of non-linear terms (measured in the model by the Strouhal number ϵ) the growth of bottom modes is first reduced, but for stronger values of ϵ an enhancement is found. Analysis of the mode in the latter case revealed that its formation is due to the divergence of the along-channel flux of mean concentration by the tidal residual current. This current is generated due to tide-topography interaction related to differential bottom friction (see Zimmerman (1981)). It turns out that advective fluxes caused by overtides and settling lag effects are an order of magnitude smaller.

In the case that the advective sediment flux dominates over the diffusive flux a second type of bottom mode is obtained, viz. local modes which scale with the embayment width. The corresponding bottom patterns manifest themselves near the entrance of the embayment and are referred to as tidal sand bars. They resemble the modes already found by Seminara and Tubino (1998) in a local morphodynamic model of an open tidal channel. The formation of these modes is mainly due to the divergence of the sediment fluxes which describe the transport of mean background concentration by topographically-induced residual currents. The residual circulation cells turn out to have an almost 90° spatial phase shift with respect to the bottom patterns. Such behaviour can also be observed in complex models of semi-enclosed seas (see e.g. Ridderinkhof (1988a,b)).

Experiments with the complex model Delft2D-MOR, a full process-based numerical morphodynamic model, revealed that it is able to qualitatively reproduce the results of the idealised model concerning the formation of bottom modes. This was found by analysing the output of the complex model, starting from an initial bathymetry which consisted of a bottom-eigenmode with a small amplitude. Quantitative differences between the model results are caused by the different formulations and solution procedures used in both models.

Acknowledgement

The authors thank WL|Delft Hydraulics for providing the DELFT2D-MOR (Delft3D) code.

3.A One-dimensional morphodynamic equilibrium

In this appendix it is shown that the expressions given in eq. (3.10) indeed represent equilibrium solutions of the model equations for the short tidal embayment, as discussed in section 3.2.5. Upon direct substitution of eq. (3.10) in the continuity equation (3.3) and using $\zeta = \cos(t)$, it follows that

$$\left[(\epsilon\cos(t) + 1 - h_{\mathrm{eq}})\, u_{\mathrm{eq}}\right]_x = \sin(t),$$

which yields

$$u_{\rm eq} = \frac{-\sin(t)}{h_{{\rm eq},x}}, \qquad\qquad h_{{\rm eq},x} = \text{constant}.$$

Note that this solution is consistent with the kinematic boundary condition at the landward side, as given in (3.7b), since the intersection position $\hat{x}$ between bottom and free surface is now given by $-1 + h_{\rm eq}(x) = \epsilon\cos(t)$.

Now suppose that $h_{\rm eq}(x=1) < 1$. Then $x = 1$ represents a solid vertical wall at which the normal component of the water flux should vanish. However, this is inconsistent with the solution found above, which shows that $u_{\rm eq}$ is finite for all x. Hence $h_{\rm eq}(x=1) = 1$ which allows for run-up of the tidal wave. Together with the boundary condition $h_{\rm eq}(x=0) = 0$ it thus follows

$$h_{\rm eq}(x) = x, \qquad\qquad u_{\rm eq} = -\sin(t).$$

Substitution of the expressions (3.10) in the concentration equation (3.8) yields

$$a\,C_{{\rm eq},t} = u_{\rm eq}^2 - C_{\rm eq},$$

which can be solved by straightforward means. The result is given in eq. (3.11), with

$$< C_{\rm eq} >= \frac{1}{2}, \qquad \hat{C}^{c2} = -\frac{1}{2}\frac{1}{1+4a^2}, \qquad \hat{C}^{s2} = \frac{-a}{1+4a^2}.$$

3.B The eigenvalue problem: final equations

$\mathcal{O}(1)$ velocity components:

$$\begin{array}{lll}
\text{cont.} & \cos t: & \left[(1-h_{\rm eq})u_0^{c1}\right]_x + l(1-h_{\rm eq})v_0^{c1} = 0, \\
 & \sin t: & \left[(1-h_{\rm eq})u_0^{s1}\right]_x + l(1-h_{\rm eq})v_0^{s1} = \left[\hat{u}^s\tilde{h}\right]_x, \\
\text{vort.} & \cos t: & v_{0,x}^{s1} + lu_0^{s1} + rl(1+h_{\rm eq})u_0^{c1} + r\left[(1+h_{\rm eq})v_0^{c1}\right]_x = 0, \\
 & \sin t: & -v_{0,x}^{c1} - lu_0^{c1} + rl(1+h_{\rm eq})u_0^{s1} + r\left[(1+h_{\rm eq})v_0^{s1}\right]_x = -rl\hat{u}^s\tilde{h}.
\end{array}$$

$\mathcal{O}(1)$ harmonic components concentration:

$$\begin{array}{rcl}
2a\,C_0^{s2} + (1+a\mu l^2)C_0^{c2} &=& -\hat{u}^s u_0^s, \\
-2a\,C_0^{c2} + (1+a\mu l^2)C_0^{s2} &=& \hat{u}^s u_0^c.
\end{array}$$

$\mathcal{O}(\epsilon)$ velocity components:

$$
\begin{aligned}
\text{cont. } 0: &\quad [(1-h_{\rm eq})<u_1>]_x + l(1-h_{\rm eq})<v_1> = -\tfrac{1}{2}u^c_{0,x} - \tfrac{1}{2}lv^c_0,\\
\cos 2t: &\quad \left[(1-h_{\rm eq})u_1^{c2}\right]_x + l(1-h_{\rm eq})v_1^{c2} = -\tfrac{1}{2}u^c_{0,x} - \tfrac{1}{2}lv^c_0,\\
\sin 2t: &\quad \left[(1-h_{\rm eq})u_1^{s2}\right]_x + l(1-h_{\rm eq})v_1^{s2} = -\tfrac{1}{2}u^s_{0,x} - \tfrac{1}{2}lv^s_0,\\
\text{vort. } 0: &\quad rl(1+h_{\rm eq})<u_1> + [r(1+h_{\rm eq})<v_1>]_x = -\tfrac{1}{2}\left[\hat{u}^s v^s_{0,x}\right]_x\\
&\qquad -\tfrac{1}{2}l\left[\hat{u}^s u^s_0\right]_x + \tfrac{1}{2}rl\hat{\zeta}^c u^c_0 + \tfrac{1}{2}r\hat{\zeta}^c v^c_{0,x},\\
\cos 2t: &\quad 2v^{2s}_{1,x} - 2lu_1^{s2} + rl(1+h_{\rm eq})u_1^{c2} + r\left[(1+h_{\rm eq})v_1^{c2}\right]_x = \tfrac{1}{2}\left[\hat{u}^s v^s_{0,x}\right]_x\\
&\qquad +\tfrac{1}{2}l\left[\hat{u}^s u^s_0\right]_x + \tfrac{1}{2}rl\hat{\zeta}^c u^c_0 + \tfrac{1}{2}r\hat{\zeta}^c v^c_{0,x},\\
\sin 2t: &\quad -2v^{c2}_{1,x} + 2lu_1^{c2} + rl(1+h_{\rm eq})u_1^{s2} + r\left[(1+h_{\rm eq})v_1^{s2}\right]_x = -\tfrac{1}{2}\left[\hat{u}^s v^c_{0,x}\right]_x\\
&\qquad -\tfrac{1}{2}l\left[\hat{u}^s u^c_0\right]_x + \tfrac{1}{2}rl\hat{\zeta}^c u^s_0 + \tfrac{1}{2}r\hat{\zeta}^c v^s_{0,x}.
\end{aligned}
$$

$\mathcal{O}(\epsilon)$ concentration components:

$$
\begin{aligned}
a\,C_1^s + a\mu l^2 C_1^c + C_1^c &= \hat{u}^s u_1^{s2} - \frac{1}{2}a\left[\hat{u}^s C_0^{s2}\right]_x\\
&\quad -a\left[u_0^c<\hat{C}> + \frac{1}{2}u_0^s\hat{C}^{s2} + \frac{1}{2}u_0^c\hat{C}^{c2}\right]_x\\
&\quad -al\left[v_0^c<\hat{C}> + \frac{1}{2}v_0^s\hat{C}^{s2} + \frac{1}{2}v_0^c\hat{C}^{c2}\right],\\
-a\,C_1^c + a\mu l^2 C_1^s + C_1^s &= 2\hat{u}^s<u_1> - \hat{u}^s u_1^{c2} + \frac{1}{2}a\left[\hat{u}^s C_0^{c2}\right]_x\\
&\quad -a\left[\hat{u}^s<C> + u_0^s<\hat{C}> + \frac{1}{2}u_0^c\hat{C}^{s2} - \frac{1}{2}u_0^s\hat{C}^{c2}\right]_x\\
&\quad -al\left[v_0^s<\hat{C}> + \frac{1}{2}v_0^c\hat{C}^{s2} - \frac{1}{2}v_0^s\hat{C}^{c2}\right],\\
3a\,C_1^{s3} + a\mu l^2 C_1^{c3} + C_1^{c3} &= -\hat{u}^s u_1^{s2} + \frac{1}{2}a\left[\hat{u}^s C_0^{s2}\right]_x\\
&\quad -\frac{1}{2}a\left\{\left[u_0^c\hat{C}^{c2} - u_0^s\hat{C}^{s2}\right]_x + l\left[v_0^c\hat{C}^{c2} - v_0^s\hat{C}^{s2}\right]\right\},\\
-3a\,C_1^{c3} + a\mu l^2 C_1^{s3} + C_1^{s3} &= \hat{u}^s u_1^{c2} - \frac{1}{2}a\left[\hat{u}^s C_0^{c2}\right]_x\\
&\quad -\frac{1}{2}a\left\{\left[u_0^c\hat{C}^{s2} + u_0^s\hat{C}^{c2}\right]_x + l\left[v_0^c\hat{C}^{s2} + v_0^s\hat{C}^{c2}\right]\right\}.
\end{aligned}
$$

Time-mean concentration equation:

$$
\begin{aligned}
(1+a\mu l^2)<C> &- a\mu <C>_{xx} + \frac{1}{2}a\epsilon^2\hat{u}^s C^s_{1,x} = \hat{u}^s u_0^s\\
&- a\epsilon^2\left\{\left[<u_1><\hat{C}>\right]_x + l<v_1><\hat{C}>\right\}\\
&- \frac{1}{2}a\epsilon^2\left\{\left[u_1^{c2}\hat{C}^{c2} + u_1^{s2}\hat{C}^{s2}\right]_x + l\left[v_1^{c2}\hat{C}^{c2} + v_1^{s2}\hat{C}^{s2}\right]\right\}.
\end{aligned}
$$

Bottom evolution equation:

$$\begin{aligned}
\omega\tilde{h} &= -\left[F_x^x + lF^y\right], \\
F^x &= \frac{1}{2}a\epsilon^2\left[\hat{u}^s C_1^s + 2 < u_1 >< \hat{C} > + u_1^{c2}\hat{C}^{c2} + u_1^{s2}\hat{C}^{s2}\right] \\
&\quad -a\mu < C >_x - \kappa\tilde{h}_x, \\
F^y &= \frac{1}{2}a\epsilon^2\left(2 < v_1 >< \hat{C} > + v_1^{c2}\hat{C}^{c2} + v_1^{s2}\hat{C}^{s2}\right) + a\mu l < C > + \kappa l\tilde{h}.
\end{aligned}$$

Boundary conditions:

The conditions at $x = 1$ are

$$\begin{array}{lll}
\mathcal{O}(1): & u_0^c = 0 & \mathcal{O}(\epsilon): \quad < u_1 >= \frac{1}{2h_{\mathrm{eq},x}}\left(u_{0,x}^c + lv_0^c\right) \\
& u_0^s = -\hat{u}^s\frac{\tilde{h}_x}{h_{\mathrm{eq},x}} & \qquad\quad u_1^{c2} = \frac{1}{2h_{\mathrm{eq},x}}\left(u_{0,x}^c + lv_0^c\right) \\
& & \qquad\quad u_1^{s2} = \frac{1}{2h_{\mathrm{eq},x}}\left(u_{0,x}^s + lv_0^s\right).
\end{array}$$

The conditions at $x = 0$ are derived from the lateral momentum equation at this location, as given in section 3.2.5. They read

$$\begin{array}{lll}
\mathcal{O}(1): & v_0^c = 0 & \mathcal{O}(\epsilon): \quad r < v_1 > \; = -\frac{1}{2}\hat{u}^s v_{0,x}^s \\
& v_0^s = 0 & \qquad\quad 2v_1^{s2} + rv_1^{c2} \; = \frac{1}{2}\hat{u}^s v_{0,x}^s \\
& & \qquad\quad -2v_1^{c2} + rv_1^{s2} \; = \frac{1}{2}\hat{u}^s v_{0,x}^c.
\end{array}$$

Chapter 4

Intermediate modelling of tidal inlet systems

Abstract

In order to identify mechanisms which may determine the morphology of tidal inlet systems, experiments with a shallow water model and sediment transport model of intermediate complexity are carried out and interpreted. A highly schematised geometry is used, consisting of a rectangular outer area connected to a rectangular basin by a narrow strait. The bottom topography is either flat or constantly sloping in the landward direction and the bed is composed of fine sand. Forcing at the open boundary consists of prescribed water levels, which can represent a (shore-parallel) progressive tidal wave or a fully standing wave. The symmetry breaking effects of Coriolis force and a progressive Kelvin wave on the tidal motion, the mean flow field and the mean sediment transport field are investigated. Tidal ellipticity properties on the outer delta are also discussed. Experiments for a rectangular basin without outer area are carried out in order to compare the intermediate model results with those of a 1D idealised model. The overall agreement is satisfactory. Next the influence of earth rotation and of the progressive wave in the outer sea on mean sediment transport in the basin is investigated. It turns out that both effects, which cannot be included in the idealised model, lead to different patterns of erosion and deposition. In both sets of experiments the effects of a progressive Kelvin wave were found to be dominant over earth rotation effects in the flow and mean sediment transport fields.

4.1 Introduction

Tidal inlets are found along many coasts, including the east coast of North America and the Wadden Sea area (North-West Europe). A tidal inlet system consists of an inner basin which is connected to the outer sea by a narrow strait. Its shallow seaward extension is called the outer delta. Most of these systems are characterised by moderate to strong tides (compared to wave effects), a complex bathymetry (channels and shoals) and residual circulation cells (see e.g. FitzGerald (1996) and references therein). Quasi-realistic models have demonstrated that the tidal hydrodynamics (Ridderinkhof (1988a), see also Ridderinkhof and

Zimmerman (1992)) and the morphologic evolution (cf. Wang et al. (1995); Cayocca (2001)) of such systems (over periods of several years) can be simulated rather well. However, due to their complexity it is difficult to gain fundamental knowledge from such models. Alternatively, idealised models have been analysed for the tidal motion (Friedrichs and Aubrey, 1994; Lanzoni and Seminara, 1998) and the morphology (Schuttelaars and De Swart, 1999; Van Leeuwen et al., 2000) in sheltered embayments. A problem with these models is that they cannot easily be extended to more realistic tidal inlet systems. The general aim of the present study is to provide a link between quasi-realistic models and idealised semi-analytical models. This is done by carring out experiments with a numerical model for the water motion, which is supplemented with a simple sediment transport routine, using simplified geometries. The model is therefore referred to as an intermediate model.

The focus of this work is on properties of tidal motion, mean flow and sediment transport. The motivation for this choice is that both tidal asymmetry and residual currents induce mean transport of sediment (Groen, 1967; Postma, 1969; Van de Kreeke and Robaczewska, 1993; Van der Molen, 2000), whilst knowledge about the latter is important to understand bathymetric changes. Field data and model studies of Dutch Wadden Sea basins indicate that tidal current characteristics and residual circulations have an asymmetrical pattern (Ridderinkhof, 1988a). Figure 4.1(a) shows the observed tidal ellipses on the outer delta and in the strait of the Marsdiep, the southernmost inlet in the Wadden Sea. Clearly the tide is more elliptical on the northern side than on the southern side. Figure 4.1(b) shows the presence of residual eddies near the Zeegat van het Vlie. It can be seen that both the size and the strength of the circulations vary considerably. According to Sha (1989b) the asymmetry of tidal properties on the outer delta is due to the interaction between the shore-parallel tidal currents and the currents in the strait. Figure 4.1(c) shows an overshoot of the flood current. The absence of such an overshoot during ebb would explain the difference in tidal ellipticity shown in figure 4.1(a). If that is true then this degree of asymmetry should change if the characteristics of the tidal wave in the outer sea change from a progressive to a more standing character. This is relevant because along the east coast of the United States much smaller tidal phase variations occur than in the Wadden Sea. There is also another source of symmetry breaking: the Coriolis force. Therefore in this paper the separate and combined symmetry breaking effects of earth rotation and of a shore-parallel tidal wave on the hydro- and morphodynamics are investigated. Using a highly schematised inlet system, distinction can be made between these effects and other (topographical) influences.

Furthermore, the intermediate model is used to test results obtained previously with an idealised model (Schuttelaars and De Swart, 1996) which also includes sediment transport. They showed that the linearly sloping bottom is a stable equilibrium bottom profile for a rectangular basin with M_2 forcing. If the solution of the idealised model is also found by the intermediate model, extensions can be added and investigated which could not be included in the idealised model. Specific items in this respect are the effect of earth rotation and that of a progressive tidal wave on mean sediment transport and the relative contributions of advective and diffusive processes to the tidally averaged sediment flux.

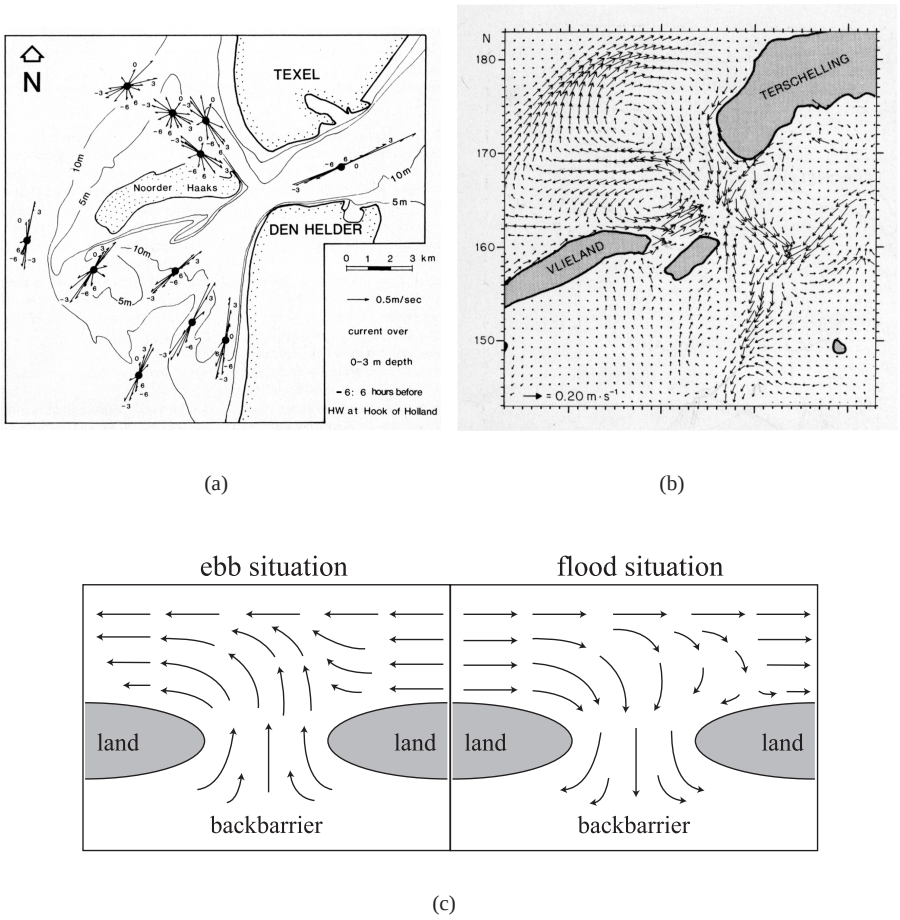

Figure 4.1: Results from previous studies: (a) observed tidal ellipses in the Marsdiep inlet (from Sha (1989b), (b) numerical model results from Ridderinkhof (1988a), showing residual circulation cells near the Vlie inlet, (both tidal inlets are located in the western part of the Wadden Sea), (c) ebb and flood situation in the conceptual model of Sha (1989b) with an overshoot of the current during flood.

4.2 The model

The numerical model HAMSOM (HAMburg Shelf Ocean Model) is used to compute the water motion. This model is based on the shallow water equations (see appendix 4.A) and developed by Backhaus (1983). Here only the one-layer version is used. An adjustment has been made to include linear bottom friction next to quadratic bottom friction. This is relevant for comparison with the idealised model results. For this reason the HAMSOM model was chosen instead of the quasi-realistic model Delft2D-MOR used in the previous chapter, which

uses quadratic bottom friction and does not allow for model modifications. The HAMSOM code has also been extended with a module which describes the suspended load transport of fine sand (grain size of order $2 \cdot 10^{-4}$ m). This formulation explicitly accounts for the effect of settling lags. The characteristic deposition timescale is of the order of a few minutes.

4.2.1 Geometry

The geometry represents a highly schematised tidal inlet system consisting of an inner basin which is connected through a narrow inlet to the adjacent sea. Lengths, widths and depths can be varied. Figure 4.2 shows the default geometry and the bottom profiles used in this paper. The values are representative for a typical Wadden Sea inlet system (the Frisian Inlet system, see Oost (1995)). The bottom profile is flat in the outer area and the strait and has a linearly sloping bottom in the basin. This geometry resembles a tidal inlet system near equilibrium conditions (Schuttelaars and De Swart, 1996). With a maximum M_2 amplitude of 1.0 m, the minimum depth is kept at 2 m below the undisturbed water level to avoid drying and flooding of banks. Hypsometric effects are therefore not included in these experiments. The model

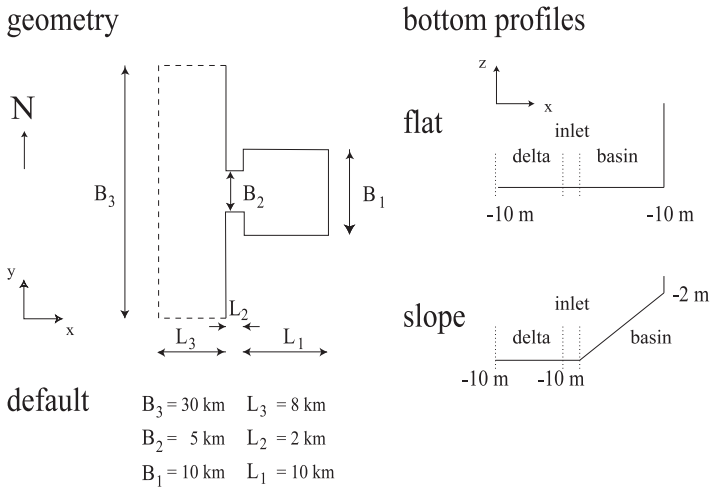

Figure 4.2: The geometry and depth profiles used in the extended HAMSOM model simulations. Top view (left) and depth profiles along central axis (right). The dashed lines in the top view plot represent open boundaries where free surface elevations are prescribed.

is forced by prescribed free surface elevations at the open boundaries (the dashed lines in figure 4.2). Only M_2 forcing has been applied. The nature of the tidal wave can be varied from travelling to a full standing wave and the typical friction timescale is of the order of one day. The default set-up includes a gridsize of ~ 400 m in the x-direction (landward direction, west to east) and ~ 600 m in the y-direction (alongshore direction, south to north) and a time step of 60 seconds. Simulations were always performed for a period of three weeks with output only on the last four days. The default case further includes a horizontal diffusion coefficient

for the water motion of 10 $m^2 s^{-1}$. Due to the difference in research aims concerning the tidal flow field (outer area characteristics) and mean sediment transport (comparison to idealised model), different default geometries, bottom friction parameterisation and tidal amplitudes were used.

4.2.2 Sediment transport formulation

To account for sediment transport the HAMSOM model was extended with a sediment transport module. The concentration of suspended sediment is determined by

$$\frac{\partial C}{\partial t} + \vec{\nabla} \cdot \left(\vec{u}C - \mu \vec{\nabla} C \right) = \alpha \vec{u}^2 - \gamma C. \tag{4.1}$$

Equation (4.1) is the conservation equation for the *depth-integrated* concentration C. The time evolution of the amount of sediment in the water column is determined by advective and diffusive transport of the sediment and by deposition of sediment on the bed or erosion of it from the bed. The parameters and variables used are: $\vec{u} = (u, v)$ the depth-averaged velocity vector, consisting of the cross-shore (u) and along-shore (v) velocity components, $\mu \sim 50$ $m^2 s^{-1}$ a horizontal diffusion coefficient, $\alpha \sim 10^{-2}$ $kgsm^{-4}$ an erosion coefficient and $\gamma \sim 4 \cdot 10^{-3}$ s^{-1} a deposition coefficient. For more information on this parameterisation see Dyer (1986) and Van Rijn (1993). The values are representative for the Frisian Inlet system (Oost, 1995). It is assumed that the depth-averaged velocity exceeds the critical depth-averaged erosion velocity for the larger part of the tidal cycle, so that the critical velocity for erosion is set to zero.

The settling time scale $2\pi/\gamma$ is of the order of a few minutes, whereas the time scale of the water motion is the tidal period $2\pi/\sigma$. The ratio of the settling time scale over the tidal period is the parameter $a = \sigma/\gamma \sim 10^{-2}$. An approximate solution to eq. (4.1) can be found by a perturbation method, using the fact that a is a small parameter. In zeroth order this leads to a balance between erosion and deposition near the bed, which determines the depth-integrated concentration given by C_0. The first-order correction to C_0 is also used and is given by C_1:

$$C_0 = \frac{\alpha}{\gamma} \vec{u}^2, \qquad C_1 = -\frac{1}{\gamma} \left\{ \frac{\partial C_0}{\partial t} + \vec{\nabla} \cdot (\vec{u} C_0) - \mu \vec{\nabla}^2 C_0 \right\}.$$

The depth-integrated concentration implemented in the sediment module is therefore $C = C_0 + C_1$. Used boundary conditions consist of no sediment flux through solid walls and no diffusive boundary layers at the seaward and landward boundary. The sediment flux $\vec{F}$ is determined by equation (4.2) and accounts for both diffusive and advective sediment transport:

$$\vec{F} = \vec{F}_{adv} + \vec{F}_{diff} = \vec{u}C - \mu \vec{\nabla} C. \tag{4.2}$$

Divergence and convergence of the sediment flux will determine locations of erosion and deposition, respectively.

4.3 Residual circulation patterns and tidal characteristics

Experiments were carried out to investigate whether the present model is able to simulate similar tidal characteristics as those obtained by Ridderinkhof (1988a) and those discussed in Sha (1989b). This means that the effects of earth rotation and a Kelvin wave passing the inlet entrance on the water motion (including the tidally averaged circulation) are investigated. The default case represents a standing wave in the outer sea and excludes the effects of earth rotation. The standing wave forcing without Coriolis effects is not the situation found in the Wadden Sea system, but was chosen as a reference case to investigate the separate symmetry breaking effects of the progressive wave following the coast and the effects induced by earth rotation. The strength of the progressive wave is determined by the imposed phase difference between the southern and northern boundary and denoted by the time difference Δt. This time difference is defined as the time it takes for high water to reach the northern open boundary, starting at the southern open boundary. The progressive wave represents a Kelvin wave which on the Northern Hemisphere always travels with the coast on the right-hand side. Quadratic bottom friction and an M_2 amplitude of 1.0 m are used. Results are shown for the default geometry with a sloping bottom (see fig. 4.2).

4.3.1 Tidal asymmetry on the outer delta

First, it is considered to what extent the conceptual model of Sha (1989b) is confirmed by the results of the present model. Sha's model attributes the asymmetry in the morphology and tidal current characteristics in the outer area to the interaction of the shore-parallel tidal current and the current in the strait. In figure 4.3 current ellipses are shown for the default situation (i.e., a standing tidal wave is forced in the outer sea), next with Coriolis effects included (fig. 4.3(b)) and finally for the case of default settings but with forcing by a progressive tidal wave (fig. 4.3(c)). This wave is travelling from south (bottom of picture) to north (top of picture) and has a time lag over the open boundary of 3000 s in figure 4.3(c). Note that 3000 s is the maximum time lag allowed and represents the time needed by a propagating Kelvin wave to travel 30 km. A decrease in the amplitude due to friction is not incorporated in the boundary conditions. This is because the frictional length scale of the progressive wave is much longer than the length of the western (seaward) open boundary. As can be seen from figure 4.3(b) earth rotation causes both an increase in tidal ellipticity and spatial differences in the orientation of the tidal ellipses over the outer area, compared with the default situation. A strong decrease in tidal ellipticity on the outer delta is observed (figure 4.3(c)) if the Kelvin wave is imposed. The latter forcing induces much stronger flood and ebb velocities, causing the tidal ellipses to become more bi-directional. The combined effect of earth rotation and a progressive Kelvin wave yields the same result as in figure 4.3(c). A clear difference in ellipticity between the northern and southern part of the outer area is not found, except in a very small region attached to the northern headland (not visible here). The polarisation of the tidal current in figures 4.3(a),4.3(b) is clockwise, whilst in figure 4.3(c) (representative for Wadden Sea basins) it is anti-clockwise. Sha (1989b) found clockwise polarisation of tidal currents (figure 4.1(a)) from data of the Marsdiep inlet in the Dutch Wadden Sea. The difference with the model result of figure 4.3(c) may be attributed to the fact that the Marsdiep inlet has a much larger basin length than that of the basin considered in our experiments. Conse-

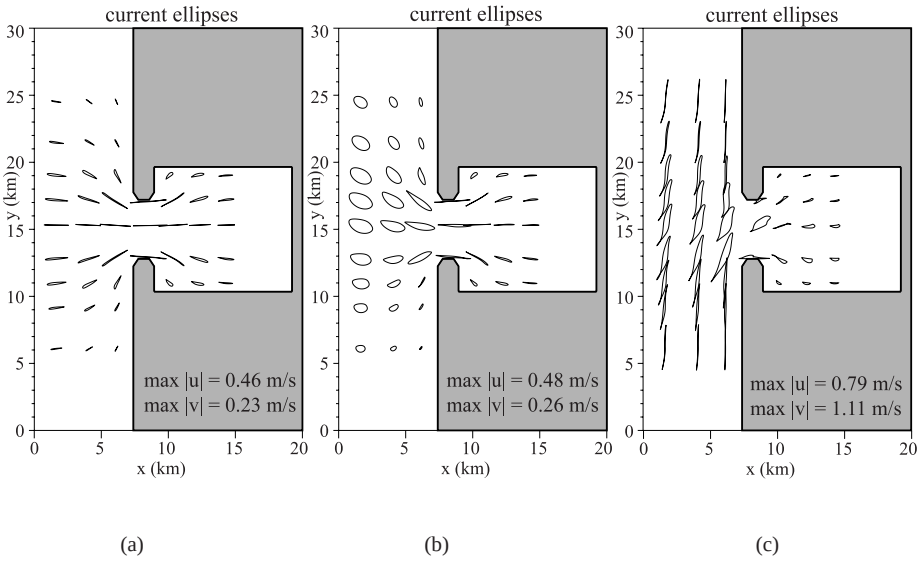

Figure 4.3: Current ellipses on some locations for a sloping bottom in the inner basin and (a) default case (no Coriolis effects and no travelling tidal wave imposed), (b) default case with Coriolis effects and (c) default case with tidal wave travelling from south to north, time lag between southern and northern boundary $\Delta t = 3000$ s. Direction of rotation is (a) clockwise, (b) clockwise, (c) anti-clockwise. Grey area is land.

quently tidal characteristics in both inlet systems are different, e.g. in the Marsdiep basin the tidal amplitude increases towards the land due to resonance behaviour. Also the presence of a large shoal on the outer delta of the Marsdiep inlet may affect the polarisation of the tidal current. Experiments with a basin geometry resembling the Marsdiep Inlet system (with $B_3 = 30, B_2 = 4, B_1 = 20, L_3 = 14, L_2 = 6, L_1 = 50$ km, see fig. 4.2) showed indeed clockwise rotation of the tidal current in the outer delta region in front of the inlet, with more circular tides in front of the downstream located headland. The forcing included a passing tidal wave and the effects of earth rotation were taken into account. The inclusion of a shoal in the bathymetry, at the approximate location of the Noorderhaaks, caused an increase in the circularity of the tidal current north of the shoal.

The velocity fields during maximum ebb and maximum flood in the strait for the case of the progressive tidal wave are shown in figure 4.4. As can be seen in figure 4.4(b), an overshoot of the flood current when entering the embayment was not found in runs with the present geometry. When the strait is made very narrow (~ 1 km) and the described forcings are maintained an overshoot of the flood current is found, but this is not a realistic situation for the inlets in the Dutch Wadden Sea. Thus the present results do not fully support the conceptual ideas introduced by Sha (1989b).

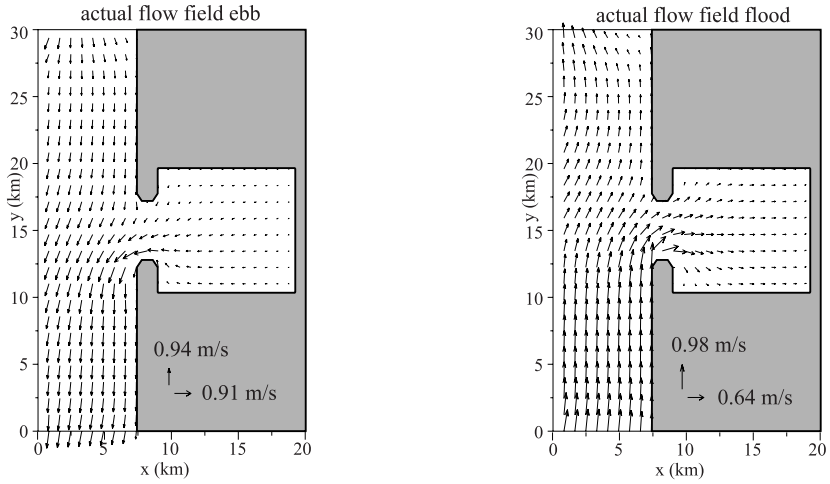

(a) (b)

Figure 4.4: Flow field at (a) maximum ebb and (b) maximum flood, for a sloping bottom in the inner basin. Arrows are drawn for every second gridpoint. Default case with combined effects of Coriolis and a tidal wave travelling from south to north, time lag between southern and northern boundary $\Delta t = 3000$ s. Grey area is land.

4.3.2 Mean flow field

The tidally averaged flow field is shown for the default case (figure 4.5(a)), the default case with Coriolis effects (figure 4.5(b)) and for the default case with a progressive Kelvin wave with a time lag over the open boundary of 3000 s (figure 4.5(c)). Without the Coriolis force and with forcing by a standing tidal wave four identical residual circulation cells around the inlet are found. These cells are the result of tidal rectification induced by frictional boundary layers near the sidewalls and they are referred to as *headland eddies*. The mechanism can be described as follows: during the flood stage (defined here as $u > 0$ in the strait) positive (negative) tidal vorticity is generated at the northern (southern) side of the inlet and transported by tidal currents into the basin. During the ebb stage negative (positive) vorticity is produced on the northern (southern) side of the inlet and advected to the outer sea. This results in the quadrupole pattern of figure 4.5(a). For more details about the underlying physics see Stommel and Farmer (1952); Zimmerman (1981); Chadwick and Largier (1999).

When the Coriolis force is included the joint action of earth rotation and bottom friction causes an oblique orientation of the tidal ellipses with respect to the central axis (see figure 4.3(b)). Also the circularity of the ellipses changes over the outer area between south and north. Process analysis revealed that in this case additional vorticity (besides the vorticity discussed above) is generated in the outer sea due to cross-shore shear of the longshore ve-

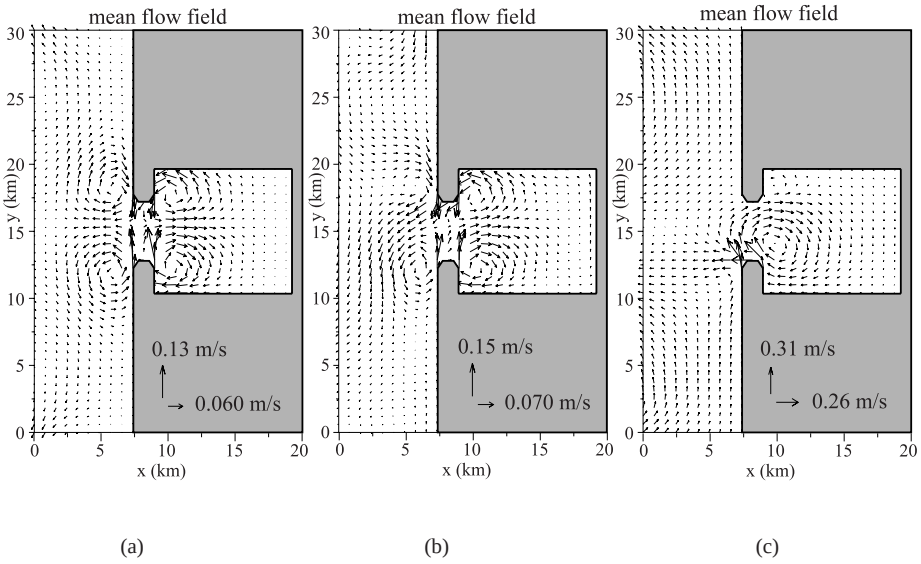

Figure 4.5: Mean flow field as simulated for a sloping bottom in the inner basin and (a) default case (no Coriolis force, time lag $\Delta t = 0$ s), (b) default case with Coriolis force and (c) default case with a tidal wave travelling from south (bottom of picture) to north (top of picture), time lag between southern and northern boundary $\Delta t = 3000$ s. Grey area is land, the arrows below the basin show the absolute maximum velocity in each direction.

locity component (i.e., $\partial v/\partial x$). Due to the Coriolis force the along-shore velocity increases, causing this mechanism of vorticity production to be more effective than in the previous case without Coriolis effects. Consider the situation during flood and distinguish between two stages: one during which $v > 0$ at the southern side of the outer sea and one during which $v < 0$ at the northern side. Then during the first flood stage negative vorticity, generated at the southern side of the outer area, is imported into the basin. During the second flood stage import takes place of additional positive vorticity which is produced at the northern side. The asymmetrical distribution of the tidal current properties and vorticity production over the outer area results in a net transport of negative vorticity into the basin. During ebb the same mechanism causes a net additional export of positive vorticity towards the outer area. This explains why in figure 4.5(b) the southern (northern) residual circulation cells in both the outer area and in the basin are strengthened (weakened) when compared with those shown in figure 4.5(a). The production of vorticity by the Coriolis force itself is not large enough to be important here. Bottom frictional torques due to the sloping bottom were also found to be of minor importance: the same results were obtained for a flat bottom topography.

If a weak phase difference over the open boundary is imposed (time lag $\Delta t = 1500$ s, not shown here) and earth rotation excluded, the mean flow field is dominated by a large

southern basin cell and a smaller northern basin cell. A strong phase difference over the open boundary ($\Delta t = 3000$ s, figure 4.5(c)) results in an even more dominant southern basin cell and a disappearing northern one. In the outer area a remnant of the southern cell can still be seen. The flow in the seaward part is now too strong for the cells in the outer delta to develop (as can be seen by comparing the maximum velocities in figures 4.5(b) and 4.5(c)). The pattern shown in figure 4.5(c) can be understood as follows. As the flow in the outer area now has a travelling wave character the shore-parallel tidal current and the current in the strait have a phase difference. Process analysis showed that also in this case the governing mechanism is related to the generation of tidal velocity shear due to side-wall friction. Still the mechanism resulting in the headland eddies of figure 4.5(a) is active. Since the first part of flood is now much longer in duration than the second part of flood, the result is a stronger net import of negative vorticity than in the previous case. This causes the negative residual circulation cell inside the basin to be strengthened while the positive one is weakened. Again, the same results were found for a flat bottom topography, indicating the minor importance of bottom frictional torques here.

Including both Coriolis and the progressive tidal wave results in the same pattern as in figure 4.5(c). Thus the model results seem to indicate that in systems like the Western Dutch Wadden Sea the Kelvin wave following the coast has a much stronger symmetry breaking effect than the Coriolis force. However, they do not explain the residual flow pattern shown in figure 4.1(b). This is because the residual circulation cells in the Wadden Sea are largely the result of tidal rectification related to bottom frictional torques induced by a laterally sloping bottom (Ridderinkhof, 1988a).

4.3.3 Mean sea level

Figure 4.6 shows the mean sea level for the three cases presented above. In the default case a symmetrical pattern around the inlet axis is found, consisting of a set-up in the basin and in the northern and southern part of the outer area and a set-down in the inlet. A mean sea level set-down in the inlet and set-up in the basin of $\mathcal{O}((cm))$ was also found by Ridderinkhof (1988a) and are considered to be general features in inlet systems. They can be understood from Bernoulli's principle: as the flow accelerates and decelerates along a streamline during both entering and exiting the inlet, the divergence of tidal stress (second term from the right in eq (4.3) along a streamline, a Reynolds stress) is balanced by the water level gradient. This gradient will be negative when entering the inlet and positive when exiting the inlet (because velocities are larger in the strait than in the outer area and basin), causing a set-down over the inlet in the direction of the flow. In the cross-inlet direction the set-down at the headlands is the result of the balance between centrifugal acceleration and the water-level gradient (Ridderinkhof, 1988a).

With only Coriolis force to break the symmetry, a stronger set-down is found near the northern headland than near the southern headland (figure 4.6(b)). In the cross-inlet direction the balance is now between centrifugal acceleration, Coriolis acceleration and the water-level gradient (Ridderinkhof, 1988a). As the first of these does not change sign between ebb and flood (while the Coriolis acceleration does), the water-level gradient will be stronger during flood (negative gradient) than during ebb (positive gradient), resulting in a stronger mean water-level minimum on the side of the northern headland.

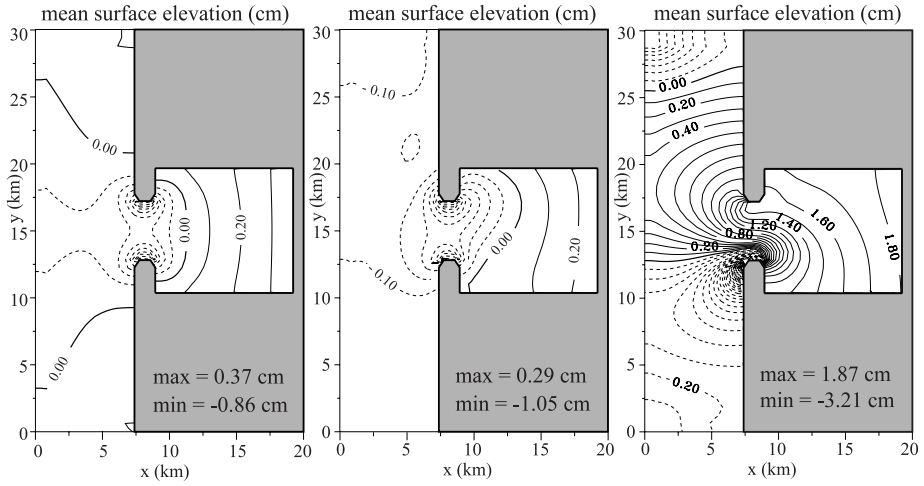

Figure 4.6: Mean surface elevation results for a sloping bottom in the inner basin and (a) default case , (b) default case with Coriolis and (c) with progressive tidal wave travelling from south to north, time lag between southern and northern boundary $\Delta t = 3000$ s. Contour lines are drawn for each 0.1 cm, dashed lines represent negative surface elevation. The thicker solid line is the zero line. Grey area is land.

The progressive tidal wave generates a higher set-up at the end of the basin as well as a set-up in the northern part of the outer delta (figure 4.6(c)). This increase in mean water-level values is strongly dependent on the imposed phase difference: in case of the progressive wave with $\Delta t = 1500$ s the maximum set-up is 0.97 cm and the maximum setdown -1.82 cm. The results shown here indicate a strong dependence of the tidal current ellipses, mean flow field and mean surface elevation on the phase difference imposed at the open boundary of the outer delta. Thus the influence of the time lag of the tidal wave travelling along the shore on the mean sea surface level is much larger than that of earth rotation effects.

4.4 Mean sediment transport

In the second series of experiments the emphasis is on tidally averaged sediment transport. The results of the previous section have shown that tidal characteristics in the outer sea strongly influence the water motion inside the basin. Here the connection to two-dimensional, idealised models is made. First it will be studied whether the present numerical model confirms the earlier obtained results of 1D idealised models (Schuttelaars and De Swart, 1996, 1999). The latter suggest that sediment transport in a basin tends to zero if the depth de-

creases in the landward direction with a constant slope. The idealised models also assume that, if there is no connecting strait, then at the transition embayment-sea a zero divergence of the net sediment flux occurs. When agreement is found for the one-dimensional case the model can represent the idealised model. The same boundary conditions as used in the previous section for water elevation at open sea are imposed on the rectangular embayment used in idealised model studies by (Schuttelaars and De Swart, 1999) to ascertain the influence of the travelling tidal wave and earth rotation effects on the water motion and sediment transport in the basin. These effects are neglected in idealised model studies.

To check and extend the findings of idealised model studies with the present model, the geometry is simplified to a rectangular embayment (see figure 4.2, with $L_2 = L_3 = 0$ km, $L_1 = 20$ km and $B_2 = B_1 = 10$ km). The default case now includes a uniform M_2 amplitude of 1.5 m at the open boundary and linear bottom friction, in accordance with the formulations used in the idealised model. Results are discussed for a horizontal flat bed and for a sloping bottom profile (figure 4.2).

4.4.1 Comparison with 1D idealised results

Figure 4.7 shows the advective and diffusive sediment flux (see eq. (4.2)) along the central axis of the embayment computed with the intermediate model and the idealised model for both a horizontal bottom and a constantly sloping bottom. The fluxes have been scaled with their maximum values. The profiles of the mean fluxes calculated with the two models show

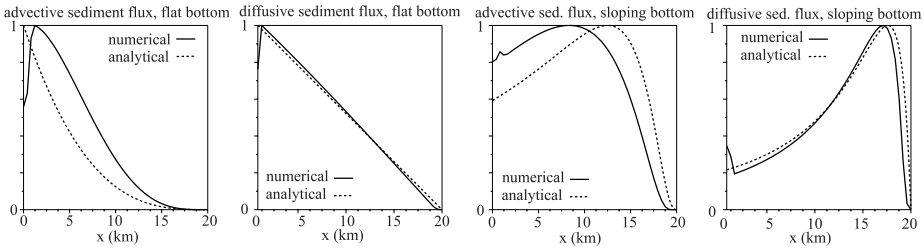

Figure 4.7: Profiles of tidally averaged fluxes along the central axis of the basin, computed with the 1D analytical model and with the intermediate numerical model; (a) advective sediment flux, horizontal bottom, (b) diffusive sediment flux, horizontal bottom, (c) advective sediment flux, sloping bottom and (d) diffusive sediment flux, sloping bottom.

good comparison. The maximum values of the mean (denoted by $< \cdot >$) fluxes are

in kg/(ms) →	$< F_{adv} >$	$< F_{diff} >$	$\frac{<Fadv>}{<Fdiff>}$
model ↓		flat bottom	
Intermediate	$1.45 \cdot 10^{-5}$	$2.08 \cdot 10^{-4}$	0.070
Idealised	$2.25 \cdot 10^{-5}$	$4.11 \cdot 10^{-4}$	0.055
		sloping bottom	
Intermediate	$6.08 \cdot 10^{-5}$	$2.33 \cdot 10^{-4}$	0.26
Idealised	$7.60 \cdot 10^{-6}$	$3.81 \cdot 10^{-4}$	0.02

In case of a flat bottom the magnitudes of the fluxes agree as well. However, the results from the intermediate model show an increase in mean sediment transports in the case of a sloping topography, whilst in the idealised model sediment fluxes decrease when the bottom approaches the equilibrium profile. This is because in the idealised model a degenerate version of the momentum equations is solved, in which the effect of bottom friction is ignored. The latter causes additional phase differences between velocity and concentration (apart from those generated by settling lag effects) and thus induces additional mean sediment transport. Thus the present intermediate model results indicate that bottom friction should be accounted for when computing mean sediment transport.

The resemblance between the models appears to hold as long as the forcing is not too strong (causing larger water-level set-up, larger velocity values) and as long as no partial drying and flooding of shoals occurs. Since the latter process is essential to reach morphodynamic equilibrium in the idealised models, the conclusion is that the intermediate model is not yet suitable for simulating morphodynamic equilibria. However, it can be used to study the influence of physical processes that cannot be incorporated in the idealised model in the non-equilibrium conditions considered in this paper.

4.4.2 Effect of earth rotation

The influence of earth rotation on the mean flow field and mean sediment transport is investigated by slowly increasing the Coriolis parameter f. Results are shown in figure 4.8 for 30° North and 52° North. Without Coriolis a symmetrical outflow of water and inflow of sediment is found. The HAMSOM model allows for a net water flux (Stokes drift) into the basin due to frictional effects, which results in a small outward directed mean flow component. Figure 4.8 shows that with increasing Coriolis a residual cell with anti-cyclonic rotation occurs in the inlet entrance. Its presence is clear for f values representing latitudes of 20 ° and more. The same pattern was found for a flat bottom topography. The presence of this residual circulation cell appears to be a consequence of the imposed boundary condition at the entrance (prescribed water level without cross-channel variation). For nonzero values of f this induces a cross-channel velocity component at this location of which the amplitude increases with f. In combination with the presence of along-channel water depth gradients a bottom frictional torque occurs at the entrance. Process analysis revealed that this frictional torque dominates over the one induced by planetary vortex stretching. The result is that during flood negative vorticity is produced which is transported into the basin. During ebb,

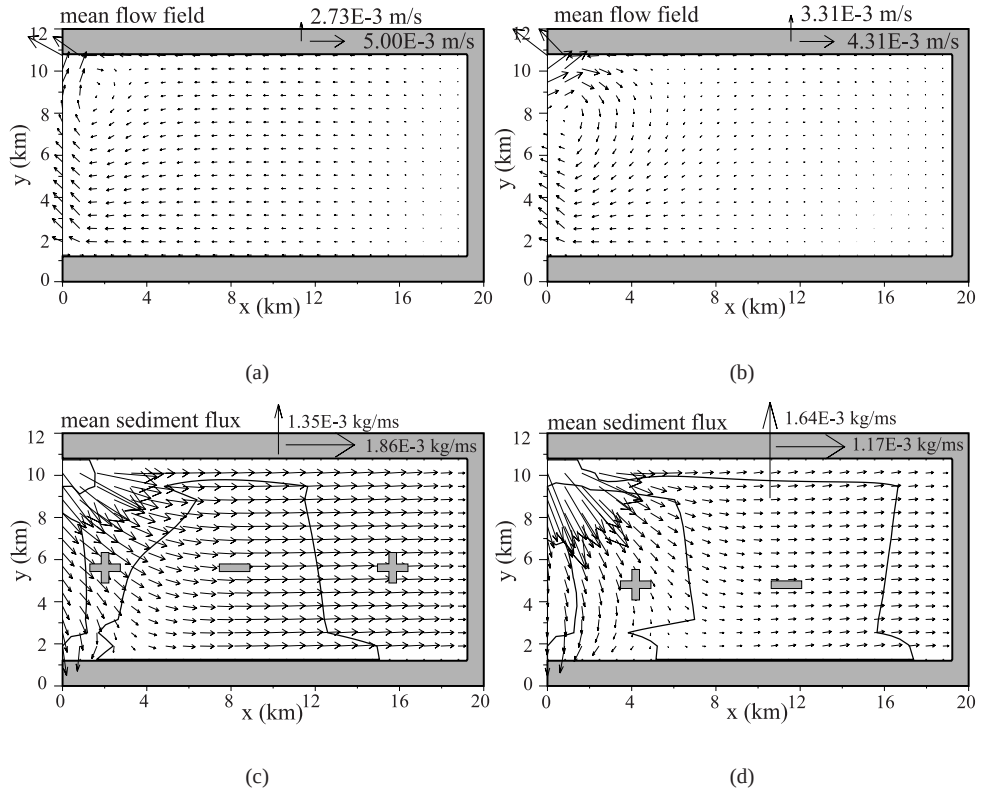

Figure 4.8: Mean flow field (top) and mean sediment flux field (bottom) for default settings and Coriolis: (a), (c) 30° North, (b), (d) 52° North. The drawn line is zero convergence of sediment flux, the grey signs indicate deposition (plus) and erosion (minus) areas.

positive vorticity is produced which is transported out of the basin, causing a net build up of negative vorticity in the basin. The length of the cell is determined by the the tidal excursion length, which can be estimated at $U * T \sim 6$ km. A sloping bottom enhances the strength of the cell since the current, deflected by earth rotation, experiences a cross-current slope. The residual circulation cell is therefore a result of the imposed boundary condition, but can also be interpreted as the result of an outside source of negative vorticity during flood, e.g. caused by outer delta topography.

The tidally averaged sediment transport is inward directed (purely landward directed for $f = 0$) and curves to the right as the Coriolis parameter increases. Figures 4.8(c), 4.8(d) show a convergence of the sediment flux near the seaward and landward boundary of the embayment, resulting in deposition of sediment in those areas. The erosion in the central area is weaker and extends further into the basin as Coriolis effects become smaller. At the same time, the magnitude of the sediment fluxes decreases. This is mainly due to the decrease of the advective flux in the landward direction, caused by the decrease in the landward directed

velocity.

Figure 4.9 shows the advective and diffusive mean sediment transport patterns for the two cases. Figure 4.9(a) shows that advection of sediment in the water column causes erosion on

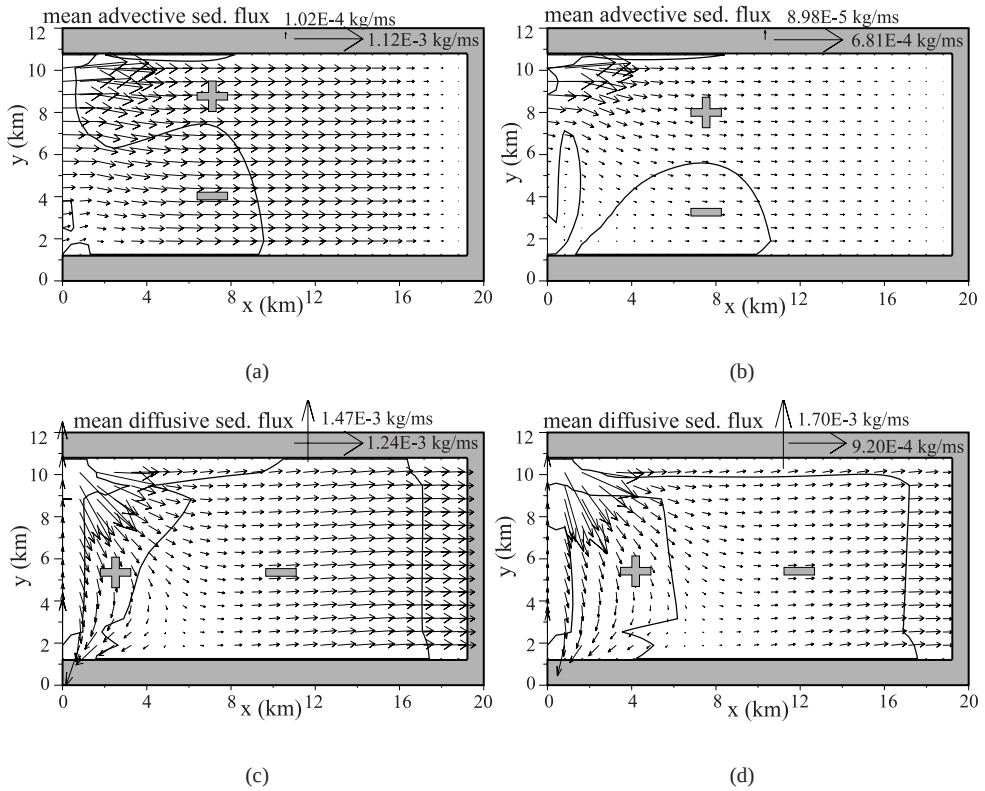

Figure 4.9: Mean advective sediment flux field (top) and mean diffusive sediment flux field (bottom) for default settings and Coriolis: (a), (c) 30° North, (b), (d) 52° North. The drawn line is zero convergence of the plotted sediment flux, the grey signs indicate deposition (plus) and erosion (minus) areas.

the south-western side of the basin, while sediment deposition occurs in the northern part and at the end of the basin. Sediment transported by diffusion (figure 4.9(c)) is deposited in small areas near the seaward and landward boundary, whilst in the rest of the basin erosion takes place. The combined effect shown in figure 4.8(c) can therefore be interpreted as being largely determined by diffusive fluxes, although advective fluxes are not negligible. When the Coriolis parameter is increased to represent 52° North, the mean advective sediment flux in the landward direction (figure 4.9(b)) experiences a stronger decrease than the diffusive mean sediment flux (figure 4.9(d)) in that direction. This causes the region of dominance of the diffusive mean sediment flux to extend, leading to an enlargement of the erosion area. Finally, note that the pattern of the mean advective sediment flux and that of the mean flow field are clearly different. This implies that the mean advective sediment flux is largely determined

by correlations between the fluctuating (rather than by the steady) components in velocity and concentration fields. In other words, the mean advective flux is determined by tidal asymmetry rather than by residual currents. This is also indicated by the weakness of the residual circulation, which is of the order of mm/s. The role of tidal asymmetry and residual circulation in determining the advective sediment flux is further investigated in Chapter 5.

4.4.3 The progressive tidal wave

The effect of a progressive tidal wave travelling from south to north is again investigated, now with an amplitude of 0.5 m and a time lag over the open boundary of 1500 s. This is done in order to reduce the dominating effect of the progressive Kelvin wave on the mean flow field found in the previous experiments. Figure 4.10 shows the results for the mean flow and mean sediment flux in case of a progressive tidal wave for two cases: no Coriolis effects (figures 4.10(a), 4.10(c)) and with Coriolis effects (52 ° North, figures 4.10(b), 4.10(d)). The flow field is in both cases characterised by an inflow point on the northern side of the entrance, with northern and southern deflection. Maximum velocity values are increased by a factor of 10 compared to those obtained with only Coriolis effects (figure 4.8(b)). Including both earth rotation effects and a progressive tidal wave results in a northward shift of the point of inflow and smaller maximum velocities (figure 4.10(b)). Again, the imposed boundary condition of constant water-level amplitude at the open boundary is not natural: in figure 4.6(c) a mean water-level gradient of about 5 cm was found across the inlet. Therefore, the boundary condition at the entrance will affect the mean flow field near the inlet. The results can be interpreted as being representative for the situation with a source of vorticity outside the basin during flood.

The mean sediment flux field in figure 4.10(c) is convergent in large parts of the embayment, indicating the formation of shoals in these areas. If also earth rotation is incorporated, then the effects of both the progressive tidal wave and earth rotation on the erosion-deposition pattern (see figure 4.10(d)) can be recognised. Compared to figure 4.10(c) the area of erosion has clearly extended, in particular towards the southern part of the embayment. Figure 4.11 shows the separate effects of the advective and diffusive mean sediment flux for the two cases. From this it can be seen that in case of no Coriolis effects the net erosion-deposition pattern (see figure 4.10(c)) is determined by diffusive and advective contributions which have a similar magnitude. Including earth rotation effects causes the advective mean sediment flux to decrease and the basin becomes more diffusively dominated. Note that in case of a progressive tidal wave the pattern of the mean advective sediment transport resembles that of the mean flow field. This means that the mean advective fluxes are now largely determined by the residual current (rather than by tidal asymmetry).

4.5 Conclusions and discussion

The experiments with the numerical model have indicated that for tidal basins, resembling those located in the western part of the Wadden Sea, the asymmetry in the flow field can be mostly attributed to phase differences of the large-scale tidal wave along the coast, rather than to the direct effect of earth rotation. Residual circulation cells were found which depend

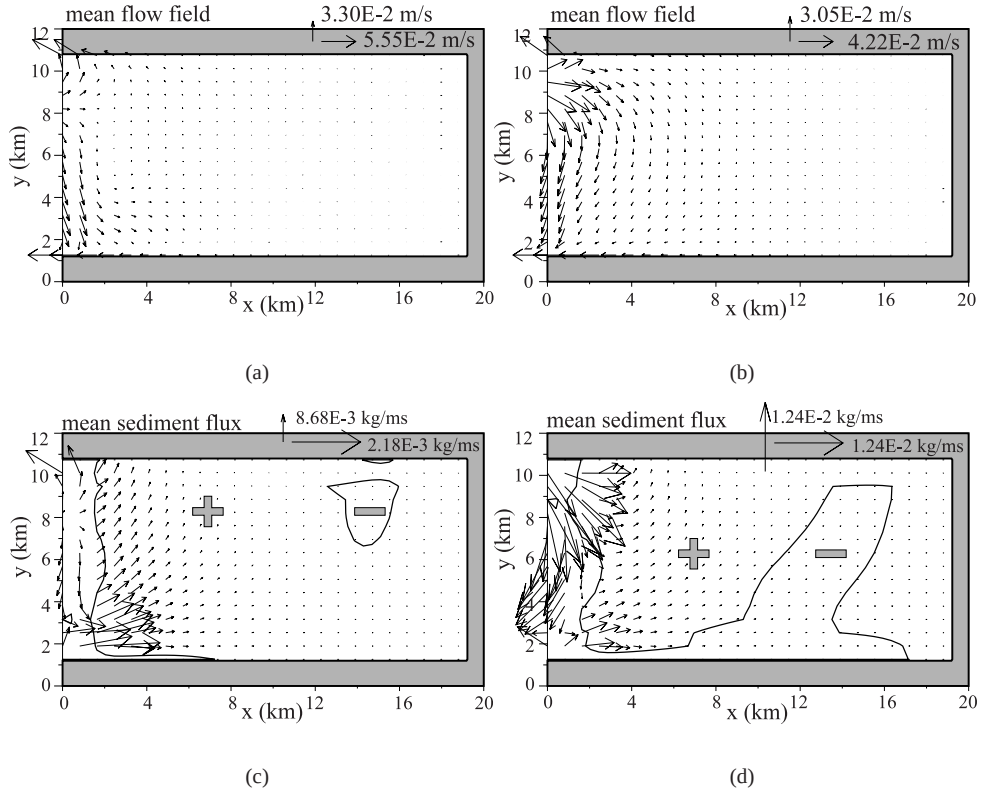

Figure 4.10: Mean flow field (above) and mean sediment flux field (below) for (a), (c) only a progressive tidal wave, (b), (d) progressive tidal wave with Coriolis effects (52° North). The drawn line is zero convergence of sediment flux, the grey signs indicate deposition (plus) and erosion (minus) areas. The values indicate maximum sediment transport in each direction. Dark grey area is land.

on the prescribed boundary conditions at open sea. In the present experiments (no lateral slopes in the bottom topography) residual circulation cells were found to be mainly caused by advection of tidal vorticity by tidal currents, generated by velocity shear due to sidewall friction. Vorticity production due to Coriolis torques and bottom frictional torques appears to play only a minor role. In case of no Coriolis effects and a standing tidal wave the main source of vorticity is the lateral shear of the along-channel velocity component. However, with earth rotation included and a progressive tidal wave the cross-shore shear of the shore-parallel tidal current is the main source of vorticity production.

The mean sea level patterns were also analysed. It was found that with increasing phase differences of the tidal wave over the open sea boundary an increase of the mean set-up in the basin occurs. Near the seaward entrance it also causes an increase of the cross-channel sea surface gradient with a large set-down at the southern tip.

Analysis of the tidal velocity field revealed no presence of an overshoot of the flood

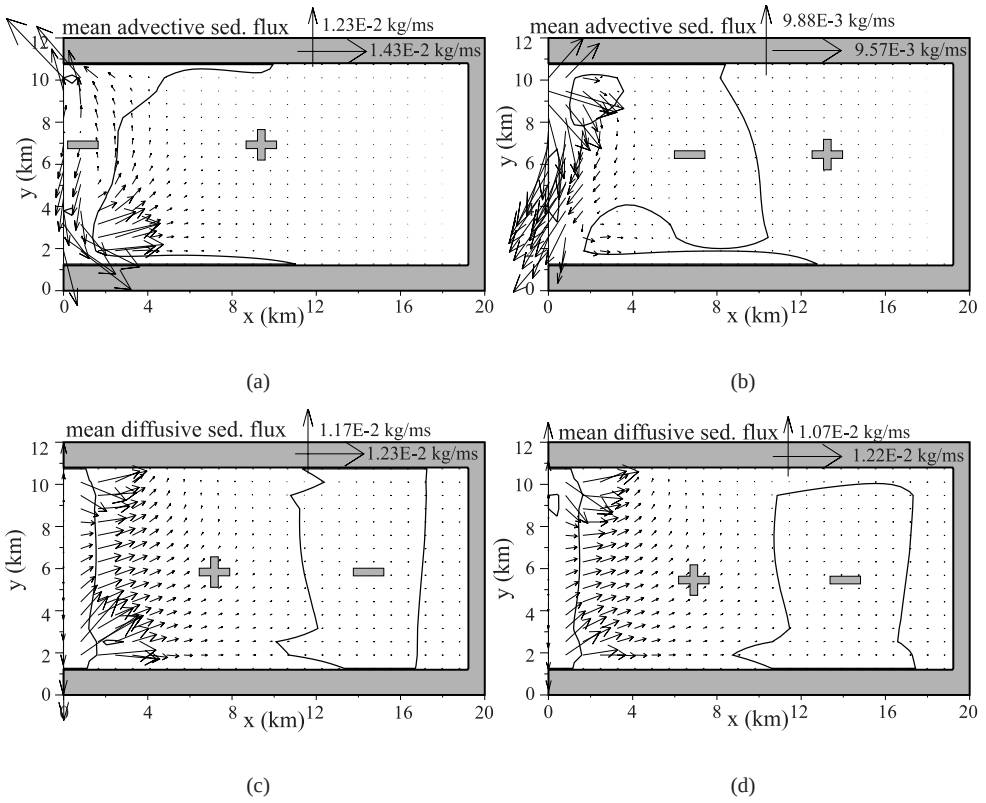

Figure 4.11: Mean advective sediment flux field (top) and mean diffusive sediment flux field (bottom) for default settings: (a), (c) progressive wave, $\Delta t = 1500$ s (b), (d) Coriolis force (52° North) and progressive wave ($\Delta t = 1500$ s). The drawn line is zero convergence of the plotted sediment flux, the grey signs indicate deposition (plus) and erosion (minus) areas.

current entering the basin. Stronger tidal ellipticity on the northern part of the outer delta was found only in a very small region attached to the northern headland. The conceptual model of Sha (1989b) is therefore only partly supported by these experiments. The field data results for the Marsdiep inlet system (figure 4.1(a)), in particular the large area with elliptical tidal currents, are assumed to be caused by two effects. One is the geometry of the basin: its length is much larger than that of the basins considered in this study, resulting in different tidal characteristics. The second is the complex morphology of the outer delta of the Marsdiep, in particular the presence of the large sandy shoal 'Noorderhaaks'. Experiments with a model geometry resembling the Marsdiep Inlet system showed a much larger area of increased tidal ellipticity connected to the northern headland for a flat bottom topography. Including a shoal near the inlet entrance resulted in a further increase of tidal ellipticity in that region. For this geometry clockwise rotation of the tidal current was found in the outer area in front of the inlet and partly in front of the northern headland. This is consistent with the field data shown

in figure 4.1(a).

With regard to sediment transport and morphology, the present intermediate model only partly confirms the results previously obtained with idealised morphodynamic models. In particular it was found that in case of a sloping bed, bottom frictional forces cannot be neglected in the momentum balance, as is done in the idealised model. Nevertheless, the present model is a convenient tool to study the influences of additional physical processes which cannot be easily realised in the idealised model. Here the role of earth rotation and a progressive tidal wave following the coast were investigated in this respect. It turned out that both the Coriolis force and the tidal wave characteristics cause significant and different patterns of sediment erosion and deposition. An interesting result is that, in the studied short embayment (its length being much smaller than the tidal wave-length) the mean sediment flux caused by the joint effect of earth rotation and a progressive tidal wave is diffusively dominated. With decreasing influence of the Coriolis force advective fluxes become more important and the latter appear to be mainly determined by the steady components of the velocity and sediment concentration. In contrast, in case of a standing tidal wave advective fluxes are controlled by the fluctuating components of velocity and concentration.

Results of the present model indicate that it is a helpful tool to gain further understanding about the hydrodynamic and morphodynamic processes in tidal inlet systems. In this sense it serves as a link between quasi-realistic models, conceptual models and idealised models. However, its application is as yet limited because a number of processes are not accounted for. The effect of waves plays an important role on the outer delta (Sha, 1989b). Drying and flooding of shoals (hypsometric effects, see Friedrichs and Aubrey (1994)) have to be properly accounted for. In this respect the work of Delfina (2000) offers a possible solution. Also a more sophisticated sediment transport formulation is necessary. In the case of a rectangular basin without outer delta the water level at the entrance is not adjusted for loss of amplitude due to bottom friction or cross-inlet gradients. This obvious lack should be corrected by either a different analytical definition of the water level at the entrance or by including an outer delta in the geometry. The latter would involve an extension which cannot be incorporated in the idealised model, hampering comparison with the idealised model results.

Chapter 5 will investigate the analysis of tidal components contributing to the advective sediment transport and the influence of outer delta morphology on the tidal motion and mean sediment transport patterns.

Acknowledgement

The authors thank prof. J. Backhaus from the University of Hamburg, Inst. für Meereskunde, for providing the HAMSOM code and dr. E. Spee from IMAU for the software extensions.

4.A Equations for water motion in the HAMSOM model

The HAMSOM-code used in the present paper solves the one-layer version of the shallow water equations:

$$\frac{\partial \vec{u}}{\partial t} + \left(\vec{u} \cdot \vec{\nabla}\right) \vec{u} + f\vec{e}_z \times \vec{u} = -g\vec{\nabla}\zeta - \frac{\vec{\tau}_b}{\rho(H+\zeta)} + A_h \nabla^2 \vec{u}, \tag{4.3}$$

$$\frac{\partial \zeta}{\partial t} + \vec{\nabla} \cdot [(H+\zeta)\,\vec{u}] = 0.$$

Here $\vec{u} = (u, v)$ is the depth-averaged velocity vector, ζ is the elevation of the free surface with respect to the undisturbed level, H is the undisturbed water depth, t is time and $\vec{\nabla} = (\partial/\partial x, \partial/\partial y)$. Furthermore, f is the Coriolis parameter, $\vec{e}_z$ a unity vector in the vertical, g the acceleration due to gravity, ρ is the water density and A_h the diffusion coefficient. For the bed shear stress two different formulations are used:

$$\vec{\tau}_b = \rho r \vec{u} \qquad \text{or} \qquad \vec{\tau}_b = \rho c_d |\vec{u}| \vec{u}.$$

Here r is a linear friction coefficient ($r \sim 10^{-3}$ ms^{-1}) and c_d is a drag coefficient, which is assumed to be constant ($c_d \sim 0.002$).

Chapter 5

Initial formation and long-term evolution of bottom features

Abstract

This study focuses on the dynamics of tides and of morphological patterns in tide-dominated inlet systems, such as those located in the Dutch Wadden Sea. Forcing with the leading tidal constituent is applied at the seaward boundary, such that a tidal wave travels along the coast from west to east. The objective is to gain further knowledge about the dominant mechanisms responsible for the presence of shallow outer deltas (or ebb-tidal deltas) on the seaward side of tidal inlet systems and for the occurrence of channels and shoals. This is done by analysing the results of a hydrodynamic model (HAMSOM), extended with parameterisations for sediment transport, which is applied to a highly schematised geometry which resembles the Frisian Inlet system. This fast and flexible model is used in particular to verify a conceptual model, formulated by Sha (1989c), stating that sediment deposition is favoured on the downdrift side of the outer delta (with respect to the direction of tidal propagation) due to weaker and more eccentric tidal currents in this area. The present model only partly confirms this hypothesis and shows that long-term morphological simulations are necessary to understand the observed asymmetry of outer deltas. Furthermore, the model shows that the initial formation of the outer delta is mainly due to convergence of the tidally averaged sediment flux induced by the combined effect of tidal stirring and transport by residual currents, whilst the initial formation of channels and shoals in the basin is due to net sediment transport caused by tidal asymmetry. Settling lag effects and diffusive sediment fluxes only have a minor effect on the formation of these patterns.

The versatility of the model is investigated by comparing its results with that of a complex numerical morphodynamic model (Delft2D-MOR) applied to the Frisian Inlet system. The overall agreement between the results for tidal characteristics and initial sediment erosion-deposition patterns, computed with the two models, is quite good. Next, the complex model is used to simulate the long-term morphological evolution of the Frisian Inlet. It is demonstrated that this model, which is forced by tides only, is able to simulate the gross characteristics of the observed bathymetry fairly well. This includes the presence of a double-inlet system with two clearly recognisable outer deltas having different sizes. Moreover, channels and shoals develop, but no migration of these features is found. Contrary to what has been reported in earlier studies the role of the 'Engelsmanplaat', an erosion-resistive shoal in the middle of the Frisian Inlet, was not found to be crucial for the morphodynamic stability of this inlet system.

5.1 Introduction

It has been noted by Hayes (1979); Hubbard et al. (1979); Davis (1996) and others that significant parts of the world's coastal system are characterised by series of barrier islands separated by tidal inlets. The behaviour of water motion and morphology in these areas is strongly controlled by offshore wave and tidal forcing. The present study focuses on a specific class of inlet systems, viz. those characterised by both strong shore-parallel tidal currents and strong currents in the strait. Such systems are e.g. found in the Dutch Wadden Sea (see Ehlers (1988)). They are characterised by a complex bathymetry, consisting of a shallow outer delta (or ebb-tidal delta) and a network of channels and shoals. Typical tidal velocity amplitudes in the channels are of the order of 1 ms^{-1}. Most of the channels on the outer delta of tide-dominated inlets have an updrift orientation with respect to the direction of tidal propagation in the outer sea (Sha and Van den Berg, 1993). Further analysis of field data (Sha, 1989a; Oost, 1995; Israel and Dunsbergen, 2000) has revealed that the channels on the outer delta show cyclic behaviour on a period of 20-80 years, depending on the inlet. Tidal current properties, such as intensity, phase and eccentricity, are highly variable in these inlet systems. Strong tide-topography interactions are the cause of significant non-linear overtides and residual currents (Ridderinkhof, 1988a), providing very effective mixing in these areas (Ridderinkhof and Zimmerman, 1992). The strong currents cause net transport of sediments, resulting in changes of the bed level which in turn affect the behaviour of the water motion.

The main objective of the present study is to identify and understand the physical mechanisms causing the presence of an outer delta on the seaward side of a tide-dominated inlet and why this outer delta has a preferred updrift asymmetry. Sha (1989b,c) formulated a conceptual model to explain the observed updrift asymmetry of outer deltas of tide-dominated inlet systems. He attributed this to the interaction between shore-parallel tidal currents and currents in the strait, causing tidal currents on the downdrift side of outer deltas to be weaker and more eccentric than on the updrift side (a definition of tidal eccentricity is given in appendix A). This would cause preferred sediment deposition on the downdrift side of the outer delta. Channels and shoals forming in this area would then migrate under the influence of waves and aeolian processes. This model is simple and transparent, but it is based on conceptual ideas rather than on physical analysis. It is therefore important to test these ideas with process-oriented models, based on physical laws for the water motion, sediment transport and bottom changes. Such quasi-realistic models for tidal inlets are nowadays available, see e.g. Van de Kreeke and Robaczewska (1993); Wang et al. (1995); Hibma (1999). So far, such models have not been used to test the conceptual ideas of Sha (1989b,c). Moreover, these models are so complex that it is difficult to gain fundamental knowledge about the physical processes involved.

This motivates the use of less complex models in which highly schematised tidal inlet systems and filtered equations of motion are used. In order to address the objective of this study such a model should at least be able to describe eccentricity of horizontal tidal currents, such as the recent model of Hench et al. (2002). However, this model excludes sediment transport and the analysis is focused on motion on tidal timescales only. The results presented in Chapter 4 analysed tidal properties and sediment erosion-deposition patterns for idealised inlet geometries, using the HAMSOM model developed by Backhaus (1983, 1985) extended with sediment transport routines. The mechanism of Sha (1989b,c) was not fully supported

by the numerical experiments presented in Chapter 4. However, it was not considered to what extent the findings are representative for realistic tidal inlets. Besides, the possible formation of an outer delta was not investigated, nor that of channels and shoals in this area.

Therefore, in this chapter a similar simplified model is analysed as that discussed in Chapter 4, but with the emphasis on understanding tidal properties and net erosion-deposition patterns on the seaward side of the inlet. In order to check the validity of this model its results are compared with those of a complex morphodynamic model (Delft2D-MOR) which uses realistic coast-lines and a more advanced sediment transport formulation. The latter has been successfully used by Wang et al. (1995) and Hibma (1999) to model the water motion and morphological evolution of the Frisian Inlet, which is located in the Dutch Wadden Sea. As this model is available for comparison the Frisian Inlet is considered in this study as a prototype tide-dominated inlet. It is assumed that the large-scale processes ($\mathcal{O}(km)$) that form the aim of this chapter (mechanisms for outer delta formation) are controlled by horizontal processes, so that depth-averaged model versions are used. In order to study the long-term morphological evolution of tidal inlets the feedback of the changing bottom to the water motion has to be taken into account. As this facility is not yet available for the simplified model, such simulations are carried out with the complex model.

The conceptual model is discussed in more detail in section 5.2. Next, characteristics of the Frisian Inlet system are presented in section 5.3, followed by a description of the simplified and the complex model in section 5.4. The results of both models with regard to the initial formation of channels and shoals are presented in section 5.5. Long-term evolution of the bathymetry is investigated in section 5.6, followed by a discussion and conclusions.

5.2 Tidal properties near an inlet: a conceptual model

Here the conceptual ideas of Sha (1989b,c) with regard to the observed asymmetry of channel and shoal formation on the outer deltas of tide-dominated inlets are briefly recapitulated. He considers a system which is characterised by a single inlet, with a shore-parallel current in the outer area which slightly lags the current in the strait.

According to Sha (1989b,c), the interaction between the shore-parallel tidal currents and the currents in the strait causes an overshoot of the tidal flow during flood (see figure 5.1(a)). This results in almost circular tidal currents on the downdrift side of the inlet which have smaller amplitudes than the almost bi-directional tidal currents on the updrift side. This idea seems to be supported by field data of tidal currents on the outer delta of the Marsdiep inlet, the southernmost inlet of the Dutch Wadden Sea, see figure 5.1(b). These considerations suggest that sediment deposition (and thus shoal formation) preferably takes place on the downdrift side of the inlet. Consequently, the mean water depth on the downdrift side is smaller than on the updrift side, forcing the main channel on outer delta to have an updrift orientation. Sha (1989a) also argues that after their formation the shoals move in the downdrift direction under the influence of wind and waves and ultimately attach to the downdrift barrier island. Thus his hypothesis is that tidal currents are responsible for shoal formation and wind and waves cause shoal migration on the outer delta.

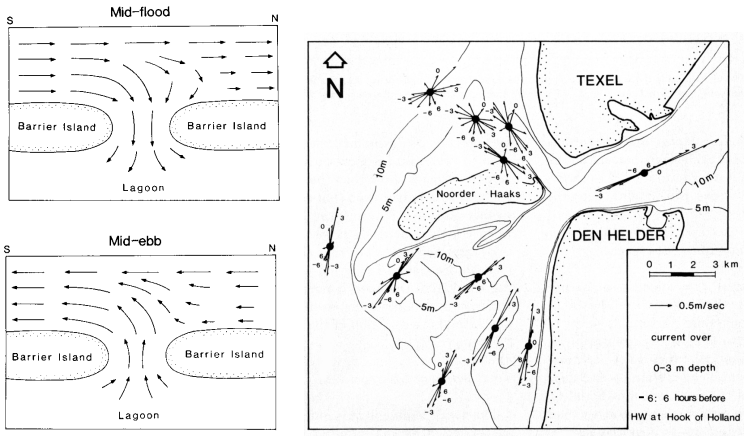

(a) (b)

Figure 5.1: Results from Sha (1989a,b), (a) expected tidal flow patterns during mid-flood and mid-ebb, and (b) observed current roses at various locations on the outer delta of the Marsdiep Inlet system, located in the Dutch Wadden Sea (see figure 5.2(a)). Tidal current vectors rotate anticyclonic (clockwise) on the downdrift side of the outer delta.

5.3 The Frisian Inlet system

In order to study the initial and long-term formation of bottom features a prototype tide-dominated inlet is considered, viz. the Frisian Inlet. This inlet is located in the Dutch Wadden Sea, between the barrier islands Ameland and Schiermonnikoog, see figure 5.2. It consists of a wide basin (nowadays its length and width are approximately 20 km and 10 km, respectively). Most of the bottom material is fine sand (mean grain size of $200 \cdot 10^{-6}$ m). In the inlet a supra-tidal shoal (called the Engelsmanplaat) is located. It consists of consolidated sediment which is much more resistive to erosive forces than sand. Thereby, the Engelsmanplaat causes a rather effective separation of two sub-inlet systems called the Pinkegat (on the west) and the Zoutkamperlaag (on the east). As can be seen in the figure both subsystems have their own ebb-tidal delta: the one of the Pinkegat (with a seaward extension of about 3 km) is about half the size of that of the Zoutkamperlaag.

This inlet system has been extensively studied in the past, providing ample reference material, (see in particular Oost, 1995). Horizontal water motion in this area is largely driven by tides, with the semi-diurnal M_2-consituent being the dominant component. Characteristic sea surface amplitudes are about 1 m and maximum tidal currents are of the order of 1 ms^{-1}; the tidal wave propagates along the coast from west to east at about 15 ms^{-1}. The mean wind and waves come from the southwest and cause drift currents of about 0.1 ms^{-1} and significant wave heights of 1 m. This system is a mixed-energy tide-dominated inlet system according to the classification of Hubbard et al. (1979) and Gibeaut and Davis jr. (1993).

The morphology and morphological developments of the Frisian Inlet have been exten-

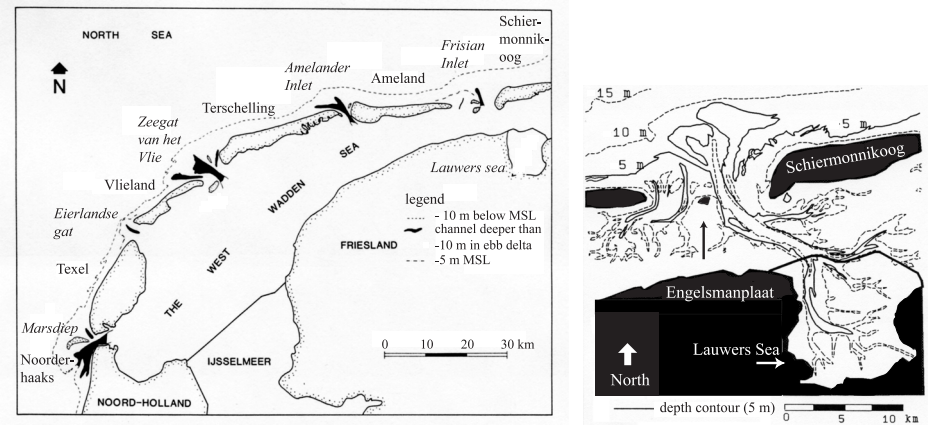

(a) (b)

Figure 5.2: Location (a) and detailed map (b) of the Frisian Inlet system, the prototype tide-dominated inlet that is used in the present study. From Sha (1989b) and Wang et al. (1991) respectively.

sively described by Oost (1995), most notably the morphodynamic response of the inlet to the closure of the Lauwers Sea in 1969 (before that year the surface area of the inner basin was about 30% larger). Presently, on both ebb-tidal deltas and in the inner basin a complex pattern of channels and shoals is observed. The Pinkegat area and adjacent ebb-tidal delta are characterised by cyclic formation entailing downdrift migration and the disappearance of channels; the typical timescale is between 20 and 40 years. Nowadays, the channels in the Zoutkamperlaag do not migrate, but before 1969 cyclic bar behaviour was observed in this area as well.

Recent field data of the water motion at various locations in the Frisian Inlet have been discussed by Van de Kreeke and Dunsbergen (2000). It follows from their analysis that the eccentricity of tidal currents in the basin area is small with both cyclonic and anti-cyclonic orientation. Only one station was situated on the ebb-tidal delta, so that the spatial distribution of eccentricity in this area cannot be reconstructed from data.

5.4 Model descriptions

5.4.1 The HAMSOM model with added sediment transport routines

The simplified model that is considered in this study uses the HAMSOM model (HAMburg Shelf Ocean Model), developed by Backhaus (1985), with supplementary routines to compute sediment fluxes and erosion-deposition patterns. The HAMSOM code calculates the water motion from solving the shallow water equations, including Coriolis terms. Here, the one-

layer version of the model is used, i.e. the depth-averaged version.

The tidal inlet system is highly schematised: it consists of a rectangular inner basin which is connected through a narrow strait to the adjacent sea. Figure 5.3 shows the default geometry and default depth profile. The geometric (and other parameter) values are representative for the Frisian Inlet system and have been obtained from the data presented by Oost (1995). Note that the central axis of the strait does not coincide with that of the inner basin. The default bottom neither contains an outer delta, nor any channels and shoals: the depth is constant in the basin and decreases linearly in the outer sea in the off-shore direction. The motivation for this choice was to investigate whether the interaction between tidal currents and this initial bathymetry (to be expected after a storm-induced flooding of the backbarrier area) would result in the formation of features like an ebb-tidal delta and channels and shoals. The model is forced by prescribed free surface elevations at the open boundaries (the dashed

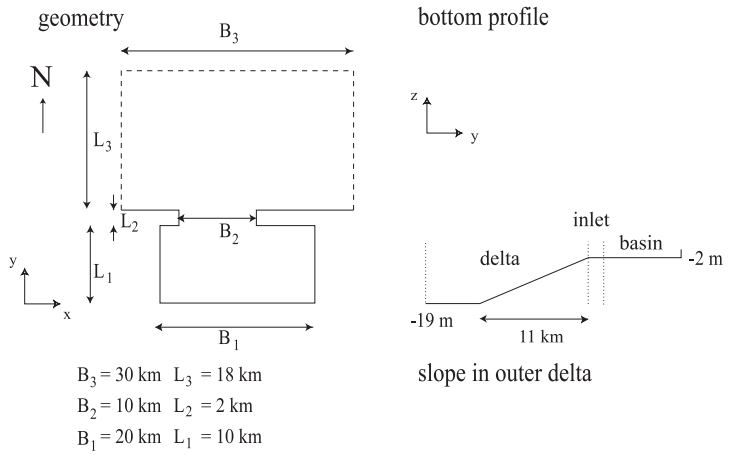

Figure 5.3: The geometry and depth profiles used in the HAMSOM model simulations. Topview (left) and depth profile along central axis (right). The dashed lines in the topview plot represent open boundaries where free surface elevation is prescribed.

lines in figure 5.3). The default setup includes a gridsize of about 200 m in the landward direction (west to east) and about 300 m in the alongshore direction (south to north) and a time step of 60 s. For further numerical details see Stronach et al. (1993).

The HAMSOM model has been extended with routines which compute the volumetric sediment transport per unit width, $\vec{F}$. Here, a formulation for suspended load sediment transport is used, i.e.

$$\vec{F} = \vec{F}_{adv} + \vec{F}_{diff} = \frac{1}{\rho_s}\left(\vec{u}C - \mu\vec{\nabla}C\right). \tag{5.1}$$

Here, $\rho_s \sim 2650\,\mathrm{kgm}^{-3}$ is the grain density, $\vec{u}$ is the depth-averaged velocity vector, C is the *depth-integrated* sediment concentration and μ is a horizontal turbulent eddy viscosity coefficient ($\mu = 100\ \mathrm{m}^2\mathrm{s}^{-1}$). Finally $\vec{\nabla}$ is the horizontal nabla vector of which the components

are partial derivatives with respect to the horizontal coordinates. Note that this flux consists of an advective and diffusive part.

The depth-integrated concentration follows from the concentration equation for fine sand (typical grain size of $2 \cdot 10^{-4}$ m) and reads

$$\frac{\partial C}{\partial t} + \vec{\nabla} \cdot (\vec{u}C - \mu\vec{\nabla}C) = \alpha H(\frac{\vec{u}^2 - u_c^2}{u_c^2})(\vec{u}^2 - u_c^2) - \gamma C. \tag{5.2}$$

Here, t is time, the first term on the right-hand side is the sediment pick-up function and the second term describes sediment deposition. The parametrisation for the sediment pick-up function is adopted from Dyer and Soulsby (1988), with $\alpha = 10^{-2}$ kgsm^{-4} an erosion coefficient, $\gamma = 4 \cdot 10^{-3}$ s^{-1} a deposition coefficient and H the Heaviside function. The critical velocity for erosion is represented by u_c and set to zero here. The motivation is that actual currents are much larger than u_c during most of the tidal cycle.

The concentration equation itself is not solved, but an approximate solution for C is obtained by applying a perturbation method, using the fact that the deposition time scale (typically of order $1/\gamma \sim 250$ s) is much smaller than the tidal period. This means that the main balance in the concentration equation is between the sediment pick-up and deposition term, which determines the zeroth-order solution C_0. The correction to this solution is denoted by C_1, such that $C = C_0 + C_1$. These solutions are

$$C_0 = \frac{\alpha}{\gamma} H(\frac{\vec{u}^2 - u_c^2}{u_c^2})(\vec{u}^2 - u_c^2), \tag{5.3a}$$

$$C_1 = -\frac{1}{\gamma}\left\{\frac{\partial C_0}{\partial t} + \vec{\nabla} \cdot (\vec{u}C_0)\right\}. \tag{5.3b}$$

Note that if settling lag effects are neglected (i.e., $C_1 = 0$) and no diffusive fluxes are considered then the flux would be $\vec{F} \sim |\vec{u}|^2\vec{u}$, which is a generalisation to two dimensions of the flux used by Van de Kreeke and Robaczewska (1993).

Information about the erosion-deposition pattern can then be obtained from the divergence of this flux. As the interest here is in bottom changes on a morphological timescale (order of years) which is much longer than the tidal period, it is useful to compute the divergence of the tidally averaged flux (indicated by brackets). Mass conservation of sediment then implies that

$$\vec{\nabla} \cdot < \vec{F} > = -\frac{\partial z_b}{\partial t}, \tag{5.4}$$

where z_b is the bed level with respect to the undisturbed water level $z = 0$. Hence if the left-hand side is positive (negative) there will be local erosion (deposition) of sediment.

It should be remarked that the present version of this simplified model is not able to simulate the dynamic interaction between the changing bottom topography and the water motion. Hence the model yields information about the *initial* sediment erosion-deposition patterns, given a specific bathymetry, but it cannot be used for long-term morphodynamic simulations.

The experiments with the simplified model that are discussed in this paper were done with forcing by the semi-diurnal M_2-tide only. Tidal residual currents and overtides are generated

internally by nonlinear shallow water terms and bottom friction. The standard quadratic bottom stress law

$$\vec{\tau}_b = \rho c_d |\vec{u}| \vec{u}, \qquad c_d = \frac{g}{C_z^2}, \tag{5.5}$$

was applied, with $\vec{\tau}_b$ the bottom stress vector, ρ the water density, c_d the drag coefficient, C_z the Chezy coefficient and g the acceleration due to gravity. Results are shown only for a constant value of the drag coefficient: $c_d = 0.0025$. A progressive tidal wave with a constant amplitude is prescribed at the shore-parallel outer boundary. The free surface amplitude is set at the southern boundary at 1.0 m and the typical friction timescale is of the order of one day. Simulations were carried out for a period of two weeks with output only on the last two days.

5.4.2 The Delft2D-MOR model

The quasi-realistic model that is used in this study is called Delft2D-MOR. This is a process-based numerical morphodynamic model developed by Delft Hydraulics. The water motion is calculated by solving the shallow water equations. The model uses a curvilinear grid with high resolution in the strait and lower resolution in the basin and at sea. The geometry resembles the actual geometry of the Frisian Inlet. At the open boundaries the water elevation is prescribed, whilst at the closed boundaries the condition of zero water flux across the boundary is imposed. Only M_2 elevations were used, which had an amplitude of 1.14 m. These open boundary conditions were taken from a complex model which simulates the entire Dutch Wadden Sea. The bottom friction formulation applied here is quadratic and uses a depth-dependent drag coefficient according to the formulation of Manning, for details see Soulsby (1997). A staggered grid is used and the Alternating Direction Implicit (ADI) technique is applied in the numerical scheme (for details see Stelling and Leendertse (1992)). The model uses a drying- and flooding procedure that keeps at least 30 cm of water in every gridpoint.

Bed level changes are calculated from the divergence and convergence of the tidally averaged sediment flux $< \vec{F} >$, as denoted by equation (5.4). The morphodynamic timestep is determined by a prescribed maximum relative change in the bottom profile. The formulation for the volumetric sediment flux per unit width, $\vec{F}$, is a total-load formulation which has been proposed by Engelund and Hansen (1972) and reads

$$\vec{F} = \frac{0.05 |\vec{u}|^4 \vec{u}}{\sqrt{g} C_z^3 (s-1)^2 d_{50}}. \tag{5.6}$$

Here C_z is the Chezy coefficient which is computed with the Manning formulation, see e.g. Ridderinkhof (1988a); Van de Kreeke and Robaczewska (1993) and Soulsby (1997). Furthermore, $\vec{u}$ is the depth-averaged velocity vector, g is the gravitational acceleration, $s \sim 2.65$ is the ratio between grain density and fluid density and d_{50} is the mean diameter of the sediment, which is of the order of 2×10^{-4} m for the area of interest. Within the Delft2D-MOR model the magnitude and direction of the sediment transport are corrected for the presence of bottom slopes. This means that sediment is more easily transported downhill than uphill.

Finally it should be remarked that the Delft2D-MOR model computes the feedback from the changing bottom to the water motion. Thus, the model is in principle suitable to simulate long-term morphological developments. It was already demonstrated by Wang et al. (1995)) that simulations with a previous version of the model yield bottom patterns that resemble observed phenomena. They found that the period over which reliable solutions are found is limited to a few years, because of the accumulation of numerical errors during the computation. Since then the model has been significantly improved and it is expected that simulations over longer periods will be possible.

The experiments with Delft2D-MOR were carried out with the depth-averaged equations of motion and using a typical grid size of 200 m. As in the case of the simplified model forcing due to both wind and waves were neglected, only prescribed M_2 tidal elevations were prescribed at the open boundary which were adopted from Hibma (1999). The hydrodynamic timestep was set at 1 minute and the timestep for instantaneous sediment transport calculation was 2 minutes.

5.5 Results for the Frisian Inlet system

In this section results are presented of experiments which were carried out with both the simplified and the complex model to test the conceptual ideas of Sha (1989b,c) (discussed in section 5.2). The numerical experiments were performed for several tidal cycles and at each gridpoint a Fourier analysis was made of the tidal velocity components of the last two tidal periods (representing nontransient behaviour). From this the characteristics of the M_2 tidal ellipse (long axis, eccentricity, orientation and phase) and the residual current were computed, according to the definitions given in Prandle (1982) or Pugh (1987), see also appendix A. The net sediment flux at each gridpoint was computed by using the parameterisation discussed in section 5.4.1 and from the divergence of this flux the sediment erosion-deposition pattern was obtained.

5.5.1 Water motion

First, model results are presented in order to verify the hypothesis of Sha (1989b,c) that during flood an overshoot of the tidal current occurs on the downdrift side of the inlet and that the currents there are weaker and more eccentric than those on the updrift side. Figure 5.4 shows the actual flow field during maximum flood (top) and maximum ebb (bottom) in the strait, calculated with the simplified model (left) and complex model (right). From this it can be seen that the models yield similar spatial patterns. The largest velocity differences are found in the strait, near the two barrier islands, and are due to the different geometrical representations of the headlands. With both models a phase difference between shore-parallel tidal currents and currents in the strait is obtained. This can be understood from the fact that the tide in the outer sea has a more travelling wave character, whilst in the strait and inner basin it has a more standing nature. However, no clear indication of an overshoot of the tidal current on the downdrift side of the inlet is observed in the flow patterns. Additional experiments with the complex model and a realistic bathymetry did not reveal this overshoot either.

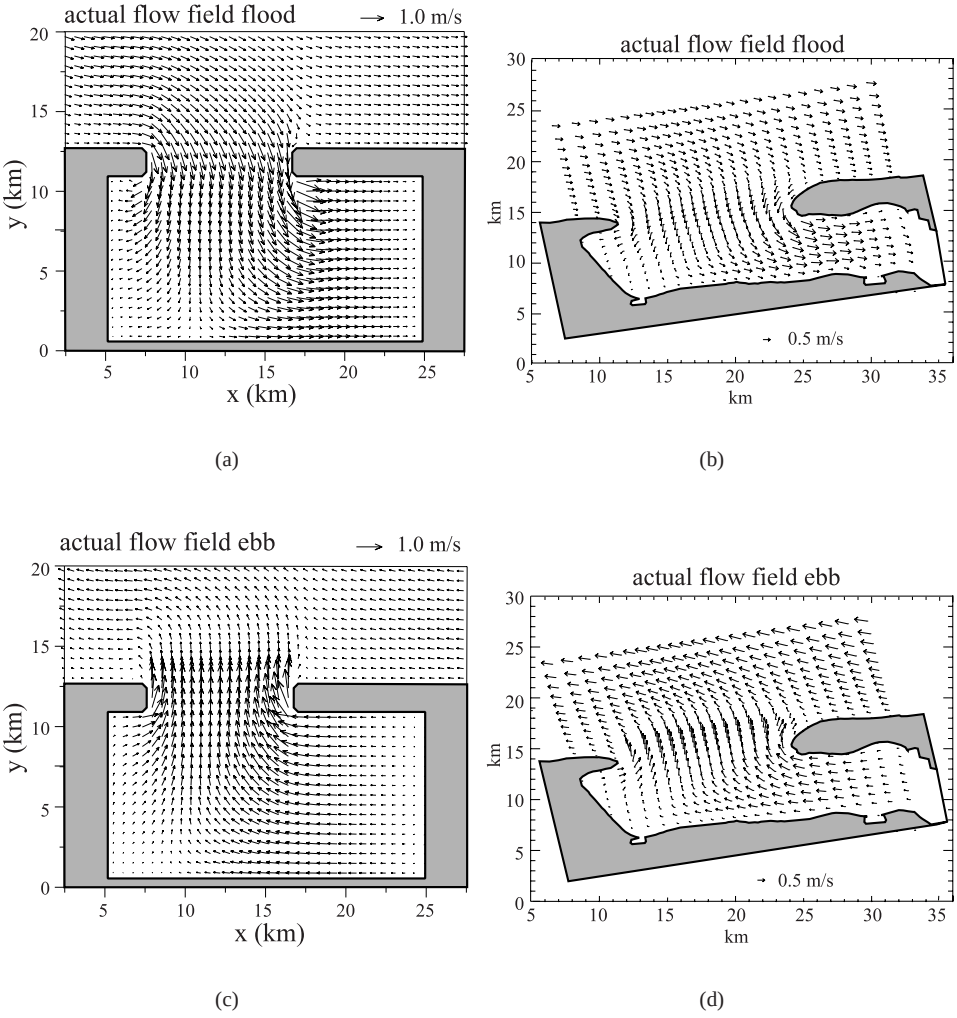

Figure 5.4: Actual flow field at the time of a maximum flood current in the strait (top) and maximum ebb current (bottom) for both the simplified model (left) and the complex model.

In figure 5.5 contour plots are shown of the M_2 long axis, i.e. the maximum tidal current, (top) and of the M_2 tidal eccentricity (bottom), calculated with the simplified model (left) and complex model (right). The results of the simplified model and of the complex model are globally consistent, although there are some specific differences. Both show large tidal currents at the transition basin-outer sea with local maxima in the vicinity of the two barrier islands. The observed asymmetry in the patterns is mainly due to two facts: the central axis of the basin is shifted downdrift with respect to the central axis of the strait and the width of

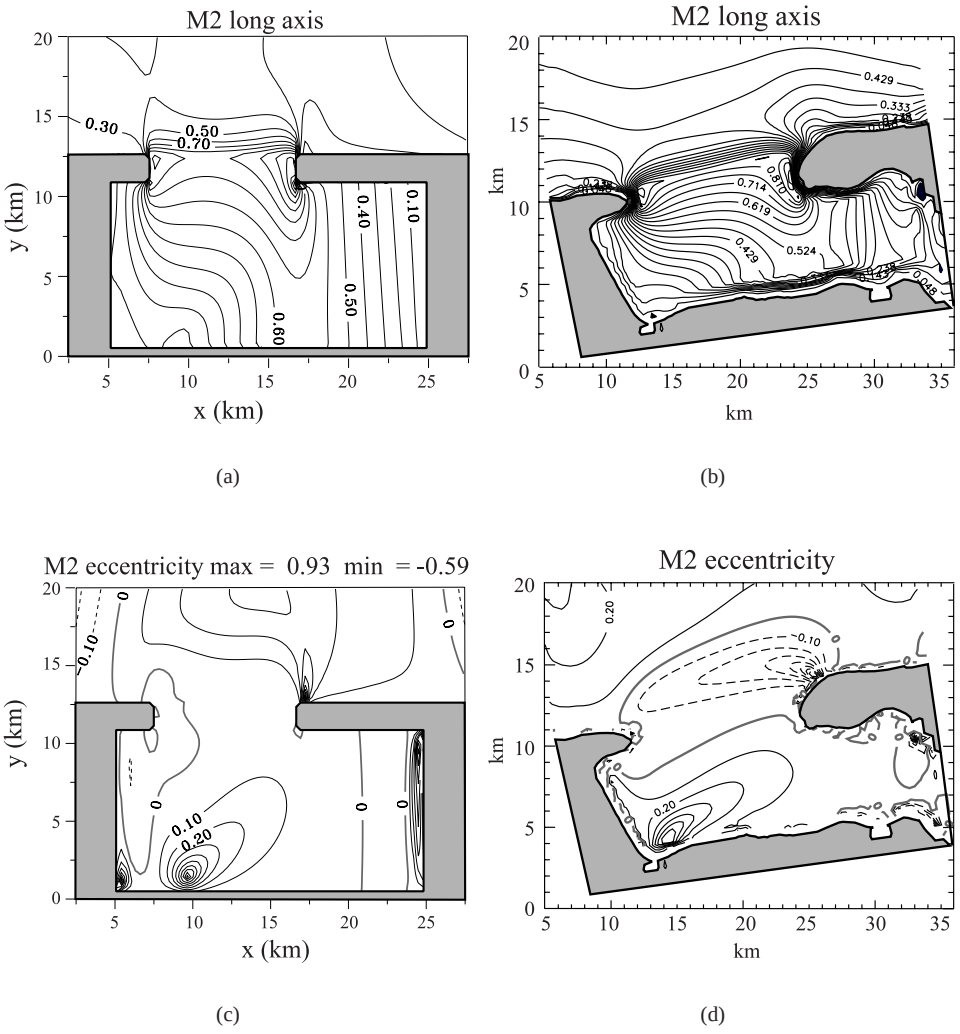

Figure 5.5: Contour plots of the M_2 long axis (maximum tidal current) (top) and of the M_2 eccentricity calculated with the simplified model (left) and with the complex model (right).

the strait is rather large. This was concluded from performing additional experiments with the simplified model (results not shown) in which the position of the strait, with respect to that of the basin, and the width of the strait were varied.

With regard to the eccentricity of the M_2 tide it is particularly interesting to see that both models yield a nearly circular tide at the downdrift side of the inlet. Hence, they confirm this characteristic of the field data for the Marsdiep Inlet system shown in figure 5.1(b), but the simplified model predicts cyclonic (anti-clockwise) rotation of the current vector in

this area, whilst the complex model shows anti-cyclonic rotation. Detailed analysis of the simplified model results shows that this is due to the parameterisation of the drag coefficient in the bottom friction term: the simplified model uses a depth-independent formulation whilst DELFT2D-MOR uses a depth-dependent one. This results in a stronger alongshore flow in the case of the simplified model and a reduced phase difference between the alongshore current and the current in the strait. Flow patterns for the simplified model show that the ebb current in the strait slightly precedes the ebb current in the outer area, resulting in a eastward orientated outflow as the outer sea still experiences flood currents. When the alongshore current turns to ebb the outflow of the strait turns westwards and a cyclonic rotation of the tidal current is found. The transition from ebb to flood occurs first in the outer area and later in the strait and basin. Additional experiments show that if the friction coefficient is sufficiently increased, the same pattern of eccentricity is obtained with the simplified model as that found in DELFT2D-MOR (shown in figure 5.5(d)). The currents in the outer area then precede the currents in the strait during the whole tidal cycle. Clearly the eccentricity is a very sensitive parameter with respect to the formulation used for bottom friction. As the rest of the results shows good agreement with the complex model, the simplified model experiment using quadratic bottom friction with the friction parameter $c_d = 2.5 \cdot 10^{-3}$ ms^{-1} is used in this chapter.

The last aspect of the water motion that is discussed concerns the residual flow. The motivation for doing this is that it is an important factor to understand net transport of sediment. In figure 5.6 the residual current patterns are shown as computed with the simplified model (left) and with the complex model (right). The two models yield residual currents in the strait

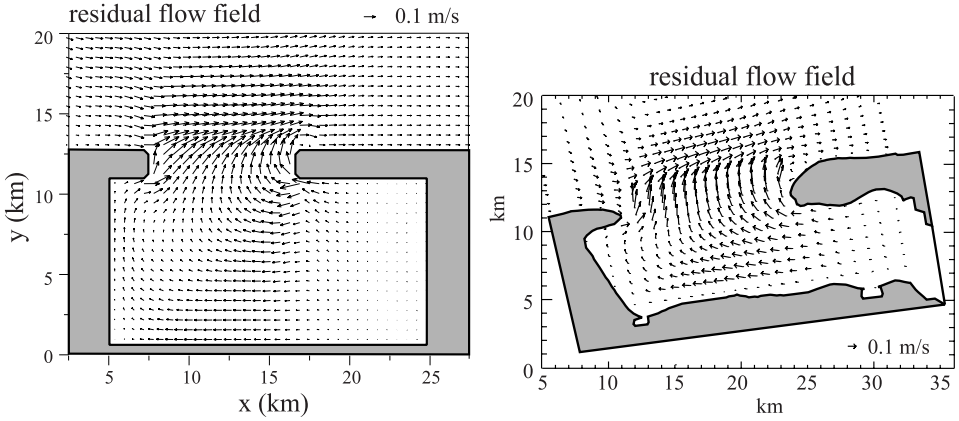

Figure 5.6: Depth-averaged and tidally averaged currents calculated with the simplified model (a) and with the complex model (b).

which are directed to the open sea. The residual flow on the outer delta is in the direction of tidal wave propagation. The lack of channels and shoals in the bathymetry prevents the

generation of residual circulation cells: the inlet is too wide to generate the circulation cells found in Chapter 4. Additional experiments were done with the complex model using a realistic bathymetry and only M_2 forcing. These results are remarkably similar to those obtained with the complex model of the Frisian Inlet, including the forcing by many tidal constituents and a realistic bathymetry (see Hibma (1999)). It appears that the gross characteristics of the water motion can be described by the leading tidal constituent and internally generated overtides.

The results of figure 5.6 can be understood from the fact that the tide in the strait is a partially standing wave, hence the phase difference between tidal elevations and tidal velocities is less than 90^o, in particular near the inlet. The tidal wave transports mass into the basin (Stokes' drift) and mass conservation implies that there must be a residual current in the opposite direction to compensate for this mass flux. Seaward of the strait the residual current is caused by tide-topography interaction in the way described by Zhang et al. (1996) and others. Since the mean water depth decreases towards the land the amplitude of the landward (y) velocity component increases in that direction (continuity effect). The Coriolis force then induces an x-component of the velocity being slightly out of phase with the y-component because of bottom friction. Non-linear advection of this x-momentum by the y-component of the tidal current causes the presence of a net flow in the positive x-direction in the outer sea.

5.5.2 Sediment fluxes and erosion-deposition patterns

Figure 5.7 shows the net volumetric sediment flux per unit width (top) and erosion-deposition pattern (bottom) computed with the simplified model (left) and with the complex model (right). The sediment flux and erosion-deposition pattern of the complex model were calculated with the Engelund-Hansen formulation, eq. (5.6), and those of the simplified model were obtained with the suspended load formulation eq. (5.1). Results of the complex model obtained with the suspended-load transport formulation (not shown) do not show any marked difference with those found with the Engelund-Hansen formulation. Note that the main mutual differences between the two formulations are that the Engelund-Hansen flux does not account for settling lag effects and it does not explicitly deal with diffusive flux contributions. The sediment flux patterns shown in figures 5.7(a) and 5.7(b) are quite similar. Thus it may be concluded that, in the present case, settling lag effects and diffusive fluxes only play a marginal role in the transport of sediment. Noticeable are the seaward-directed flux in the strait and nearby outer sea and the landward-directed flux in the basin. This is called a bed-load parting zone, and is a common feature at the entrance of tidal straits and inlets (Harris et al., 1995). Furthermore, the sediment flux directions are such that there is net transport of sediment from the inlet to the open sea. This can either indicate the tendency to form an outer delta or indicate that the inlet system will close. Long-term morphodynamic simulations will show which of these two possibilities is found here. The basin tries to adjust its bathymetry by redistributing sediment.

The sediment erosion-deposition patterns in figures 5.7(c), 5.7(d) show that in the strait net erosion occurs, particularly on the sides. This indicates the tendency to form two channels. On the seaward side of the inlet and near the basin boundaries net deposition of sediment is observed. Note that all patterns are slightly asymmetrical: the most significant changes

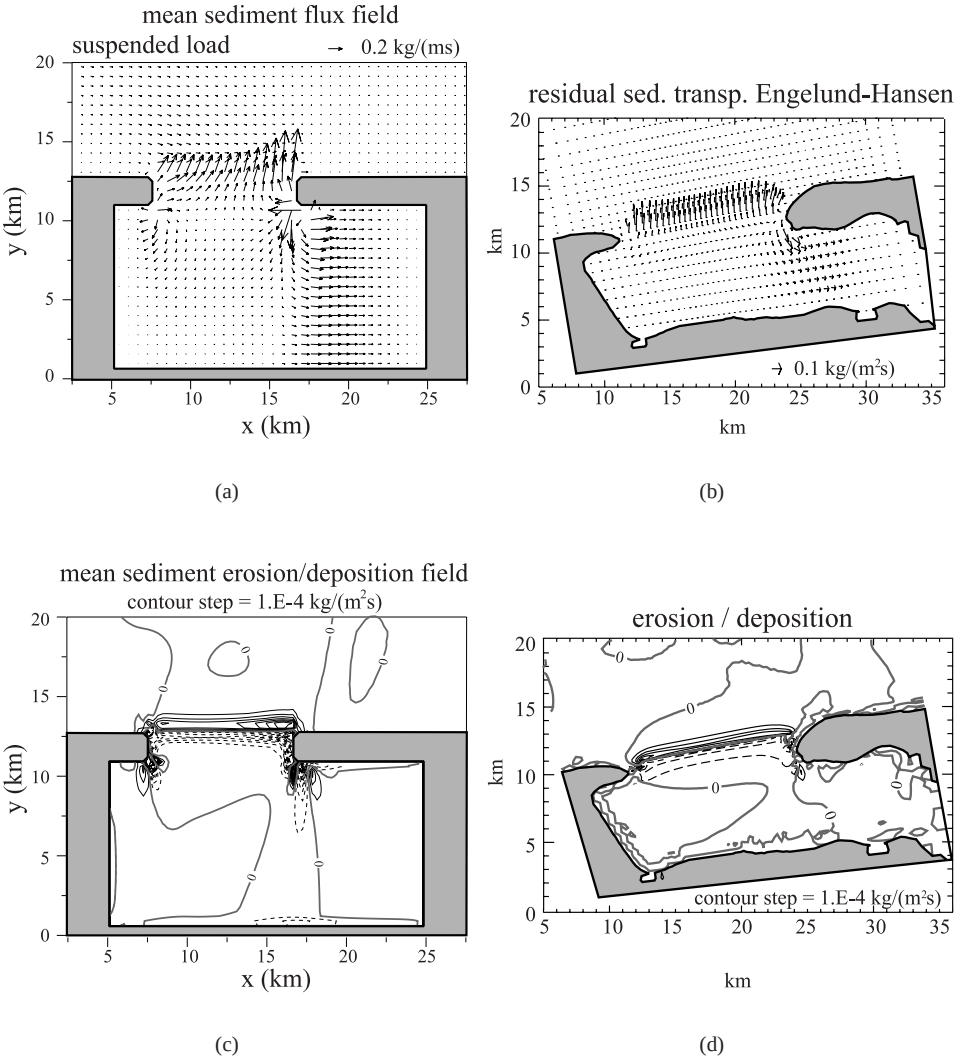

Figure 5.7: Net volumetric sediment flux per unit width (top) and sediment erosion-deposition pattern (bottom) computed with the simplified model (left) and complex model (right). Dashed lines represent negative contour lines and refer to erosion, drawn lines represent deposition. Grey areas are land.

seem to occur near the downdrift island. However, the model results do not clearly confirm the idea of Sha (1989b,c) that on the downdrift side of the inlet preferred deposition occurs. In particular in the area where tidal eccentricity is large (see figures 5.5(c) and 5.5(d)) erosion, rather than deposition, is found. Moreover, the initial erosion-deposition patterns do not reveal that channels tend to develop with a preferred updrift orientation. A remarkable aspect

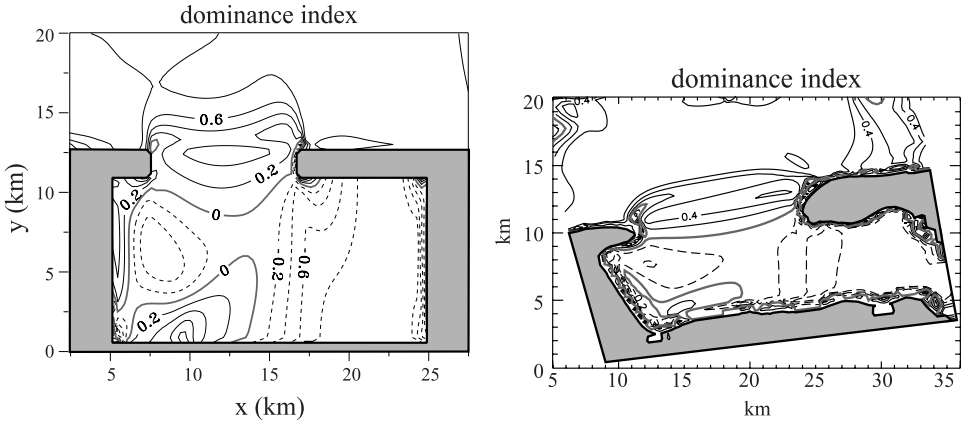

(a) (b)

Figure 5.8: Contour plots of the dominance index I_D defined in equation (5.7) calculated with the simplified model (a) and with the complex model (b). Dashed lines represent negative contour lines. The step between contour lines is 0.2.

is that, on the seaward side of the strait, the direction of the net sediment flux coincides with that of the residual current, whereas they have opposite directions in the basin. This indicates that in the two areas different physical processes control the net transport of sediment. As it was already found that settling lag effects and diffusive fluxes are of minor importance in this case, the two possible mechanisms that remain are: a combination of stirring by tides and transport by residual currents and by tidal asymmetry. The underlying mechanisms have been explained by Van de Kreeke and Robaczewska (1993), see also appendix B. The relative contributions of both mechanisms to the total net transport can be quantified by a so-called dominance index used by Van der Molen and De Swart (2001) which is defined as

$$I_D = \frac{|\vec{F}_{\rm res}| - |\vec{F}_{\rm asym}|}{|\vec{F}_{\rm res}| + |\vec{F}_{\rm asym}|}. \tag{5.7}$$

Here $\vec{F}_{\rm res}$ and $\vec{F}_{\rm asym}$ are the magnitudes of the transport related to residual currents and tidal asymmetry, respectively. Expressions for the latter can be obtained by expressing the sediment flux (e.g. $\vec{F}$ in eq. (5.6) or $\vec{F}_{adv}$ in eq. (5.1)) in terms of Fourier coefficients of the tidal flow. Note that I_D can attain values between -1 and +1; positive (negative) values indicate that sediment transport related to residual currents (tidal asymmetry) prevails.

Contour plots of this dominance index are shown in figure 5.8 for both the simplified model and complex model. These results reveal the importance of combined tidal stirring and transport by the residual current on the seaward side of the inlet and the dominance of tidal asymmetry in the basin. Thus the model results presented here probably indicate the tendency of the inlet system to form an outer delta. The underlying process is that sediment,

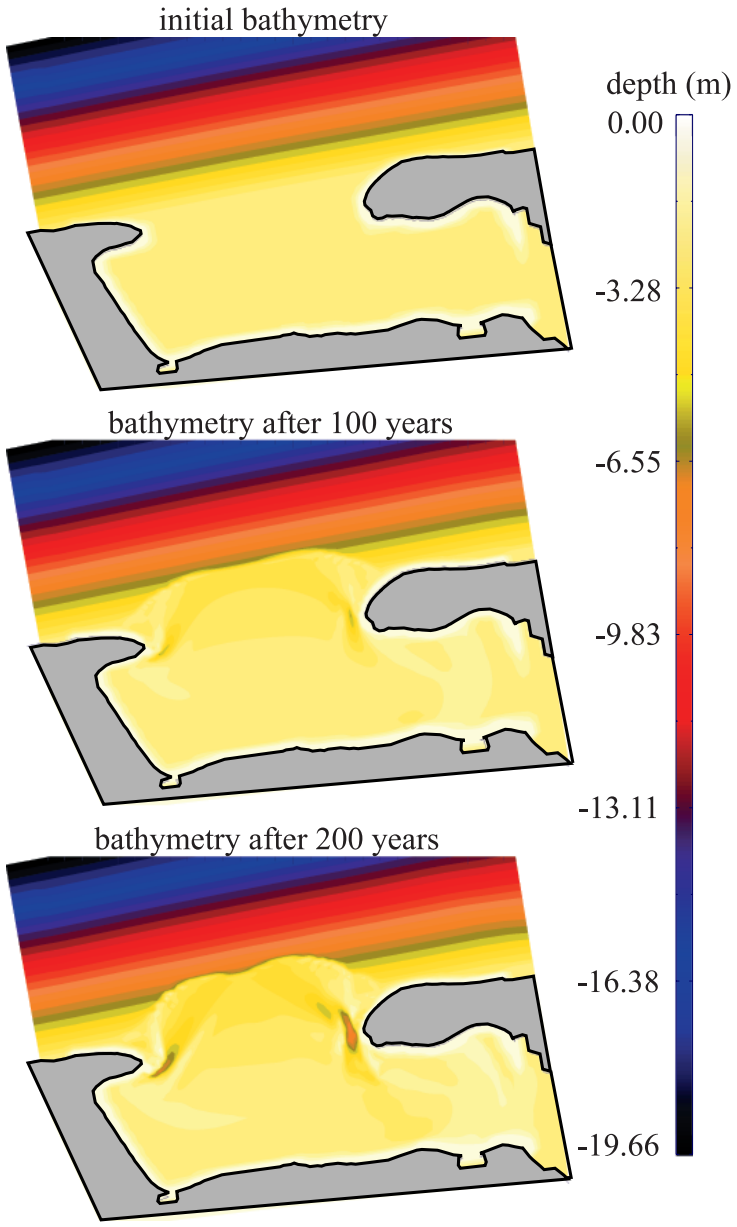

Figure 5.9: In this figure the initial bathymetry and the bathymetry, computed with the complex model, after 100, and 200 years are shown. Initially the depth in the basin is 2 m and it increases linearly in the outer sea. The black lines represent the coastal boundaries and grey area is land.

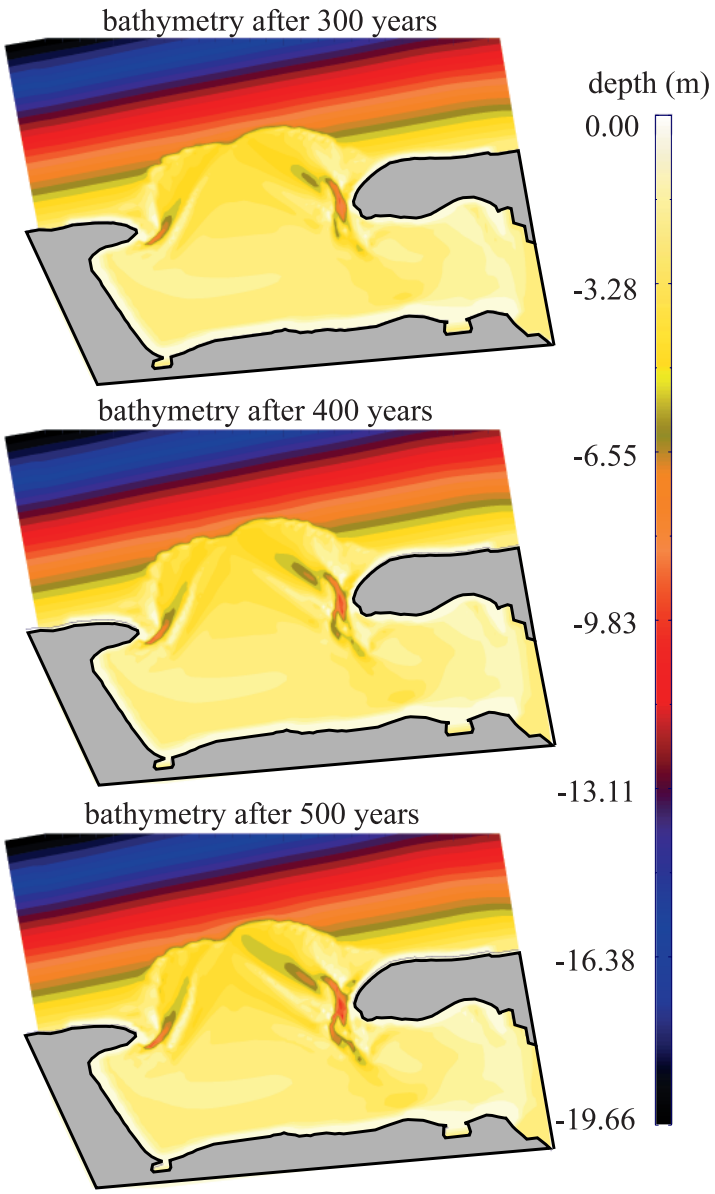

Figure 5.10: Here the bathymetry after 300, 400 and 500 years is shown. The black lines represent the coastal boundaries, grey area is land.

being mainly eroded in the strait, is transported by the combined effect of tidal stirring and residual currents towards the outer sea and deposited seaward of the strait. Besides, part of the sediment that is eroded in the strait is transported into the basin by tidal asymmetry and deposited on the landward side of the barrier islands.

It is important to emphasise that the model results do not confirm the hypotheses of Sha (1989b,c) with regard to preferred deposition of sediment on the downdrift side of the inlet and the related updrift orientation of main channels on the outer delta. This may be attributed to the fact that the present runs were done for a fixed bathymetry, hence they only represent initial erosion, transport and deposition of sediment. Apparently, the development of asymmetrical morphological patterns is a long-term process which involves the mutual feedback between tidal currents and the erodible bottom. This is further investigated in the next section.

5.6 Long-term development: model simulations

The long-term behaviour of bottom features was studied by performing model runs in which the interaction between tidal motion and the changing bed level was explicitly accounted for. As already explained such experiments could only be carried out with the complex (DELFT2D-MOR) model. As an initial state the bathymetry of the previous section was used: a flat horizontal bottom in the basin (water depth of 2 m) and a constantly sloping bottom in the outer sea. All parameter values were the same as those in the previous section and thus representative for the Frisian Inlet system. Recall that the forcing was only due to prescribed M_2 tidal elevations at the open boundaries and that the Engelund-Hansen formulation (5.6) was used to compute the volumetric sediment fluxes per unit width. The morphodynamic timestep was of the order of 1 year (i.e. during this time the bottom is kept fixed); within the simulation it changed slightly since it was updated internally in the model after each calculation of a new bathymetry. In figure 5.10 the evolution of the bathymetry from the initial stage up to 500 years is shown. The results show that the inlet system indeed forms an outer delta and does not close itself. At first there is no outer delta but the results of the previous section already indicated the tendency for sediment deposition in the area seaward of the inlet. After 100 years depths have clearly decreased here, so indeed an outer delta develops. Note that at this stage its spatial pattern is still rather symmetrical and that two channels are forming in the inlet, near the tips of the two barrier islands. At $t = 200$ years it becomes clear that two distinct outer deltas develop and that the channels in the inlet are still deepening and protruding further into the basin. Besides, a clear asymmetrical pattern develops: the eastern channel in the neighbourhood of the downstream barrier island (Schiermonnikoog) is becoming larger and deeper than the western channel. With the deepening of the channels the outer delta is extending, the eastern outer delta becoming larger than the western one. The orientation of the outer deltas is changing as well. The outer delta of the eastern tidal inlet system becomes updrift-oriented, whilst the other one becomes downdrift-oriented. So the entire system becomes asymmetrical. After 200 years this degree of asymmetry further increases and even channel branching can be observed in the eastern part of the basin. After 300 years the seaward extension of the outer delta slows down considerably, so apparently at $t = 500$ years a kind of large-scale morphodynamic equilibrium is reached.

The asymmetrical patterns only appear after a long time. This indicates that the evolution

of the asymmetry of the outer delta is a long-term, non-linear process which involves the feedback between tidal motion and the erodible bottom. Moreover, it is important to remark that in the present simulations the downdrift orientation is not related to wave effects, as argued by e.g. Sha and Van den Berg (1993) and FitzGerald (1996), as the latter have not been included in the model. Finally note that in these simulations the presence of the 'Engelsmanplaat', an erosion-resistive shoal in the middle of the Frisian Inlet, has not been explicitly dealt with. Nevertheless a clear double-inlet system develops. These results indicate that the Engelsmanplaat does not play a crucial role in the stability of the Frisian Inlet, as was suggested earlier by Wang et al. (1991).

5.7 Discussion

The model results of the previous section require some further discussion. Below they are compared with field data of the Frisian Inlet, as well as with those of other model studies. Besides, the long-term behaviour of the model is analysed in further detail, with particular emphasis on the observed fact that the growth of the outer delta seems to saturate after about 200 years. Finally the sensitivity of the model results to changing initial conditions is briefly discussed.

First the results of the long-term model simulation at $t = 500$ years (figure 5.10) are compared with the observed bathymetry of the Frisian Inlet system, see figure 5.2. Some remarkable similarities can be seen. Both the model and the field data show the presence of two separated subsystems, the Pinkegat on the west and the Zoutkamperlaag on the east. The model also yields an eastern outer delta which is larger than the western outer delta. Moreover, the orientations of the outer deltas seem to correspond with the orientation of the outer deltas in the Frisian Inlet, an updrift-oriented Zoutkamperlaag and a downdrift-oriented Pinkegat (although the orientation of the Pinkegat varies with time). Even the branching of the main ebb channel in the eastern inlet is reproduced by the model. So the conclusion is that the present model is able to simulate the observed gross characteristics of the Frisian Inlet rather well.

On the other hand many features which are present in the original Frisian Inlet system are not captured by the model. The Zoutkamperlaag shows a sequence of channels branching into smaller and shallower channels towards the land, which is not seen in the model results. It also has to be concluded that at the end of the simulation the system shows a tendency to form multiple channels on the outer delta, which is not realistic.

Once more it should be emphasised that the only forcing of the water motion is the M_2-tide, and consequently no wind or waves are needed to build up the outer delta. Formation of channels and bars with this forcing is found, but no migration. This is in agreement with the ideas of Sha (1989a) that waves and aeolian processes are responsible for cyclic behaviour of channels and shoals. The findings are also consistent with those of Cayocca (2001) who investigated the morphodynamic evolution of the Arcachon Basin (France) with a numerical model forced by only M_2-tides.

Another point of discussion is related to the question whether the bathymetric evolution found in the previous subsection is such that the system tends to a large-scale morphodynamic equilibrium which is characterised by outer deltas with specific dimensions. In order

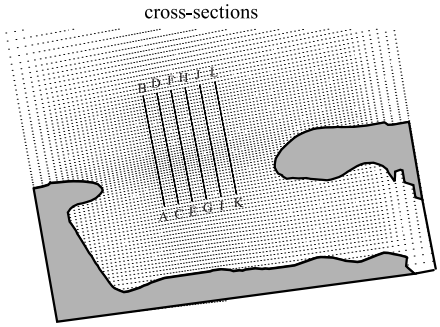

Figure 5.11: The position of the cross-sections shown in figure 5.12.

to investigate this in further detail the morphology is examined in cross-sections through the outer delta at certain locations. Figure 5.11 shows the location of the cross-sections, whilst the morphology at these cross-sections at specific times is shown in figure 5.12. This demonstrates that the outer delta is extending seaward, but the speed of this development is gradually slowing down. The fastest development is in the first 300 years of the simulation. After this time the profiles are becoming more peaked.

Finally the sensitivity of the model results with respect to changes in the bathymetry are briefly discussed. Experiments were carried out by setting the mean water depth in the basin to 1.5 m and 3.0 m, respectively. The motivation for these choices is that the tidal wave becomes more (less) damped, because bottom friction increases in shallower water. Consequently, bed shear stresses and sediment transports increase (decrease) and the morphological evolution will generally be faster (slower). The results show that also in these two cases a double-inlet system develops with two clearly recognisable outer deltas. However, there is now a marked difference in evolution timescales: in case of an initial water depth of 1.5 m in the basin the eastern outer delta develops much faster than the western outer delta. When the initial water depth is 3.0 m in the basin the opposite occurs: the western outer delta evolves on a much shorter timescale than the eastern outer delta. The final extension of the outer deltas seem similar in these experiments. The dependence of the morphological timescales of the eastern and western outer delta on the water depth is not yet fully understood. One important aspect is that with increasing water depth the tidal wave in the basin becomes less damped. Consequently, the net landward mass flux due to Stokes drift decreases, resulting in a smaller residual current and tidal asymmetry and thereby in smaller sediment fluxes. It seems that this effect is stronger in the Zoutkamperlaag than in the Pinkegat. Differences in tidal resonance characteristics of the eastern and western basin, due to their different lengths are not likely to be important. It appears that in both basins the frequency of the M_2- and M_4-tide is much larger than any possible resonant frequency.

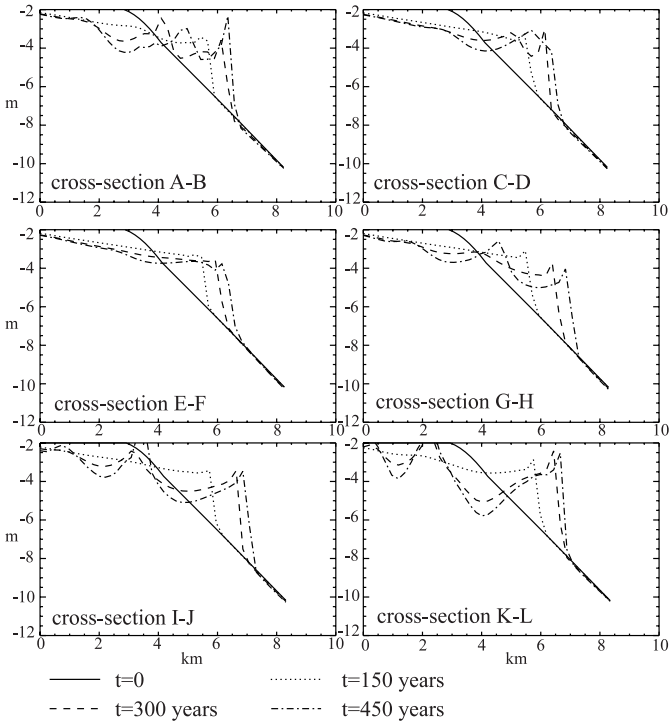

Figure 5.12: Six cross-sections from the basin to the sea at different times. The horizontal axis shows the length of the sections in km, whilst the vertical axis shows the depth in m. The cross-sections start in the basin and extend towards the end of the outer delta, see figure 5.11. Here A-B is a cross-section through the Pinkegat, the location of E-F is just between the two channel systems and K-L is a cross-section through the Zoutkamperlaag.

5.8 Summary and conclusions

In this paper results have been presented of numerical experiments with process-oriented hydro- and morphodynamic models which were carried out to gain more fundamental understanding about the morphodynamics of tidal inlet systems. The specific objectives were twofold. One was to verify a conceptual model, formulated by Sha (1989a,c), stating that the formation and spatial asymmetry of ebb-tidal deltas in tide-dominated inlet systems is due to the interaction between shore-parallel tidal currents and currents in the strait. The second was to identify the dominant physical mechanisms causing the initial formation and long-term behaviour of the ebb-tidal deltas and channels and shoals in a prototype tide-dominated inlet system: the Frisian Inlet, located in the Dutch Wadden Sea.

The conceptual model results were verified by performing runs with a simplified depth-averaged numerical model which calculates tidal motion, sediment fluxes and sediment

erosion/deposition for a fixed bathymetry. The model was applied to a highly schematised geometry of the Frisian Inlet. Furthermore the bathymetry was taken to be flat and horizontal in the basin (depth of 2 m) and constantly sloping in the outer sea. The numerical model results indicate that tidal currents are weaker and more eccentric on the downdrift side of the inlet than on the updrift side, which is consistent with the conceptual model. However, no overshoot of the tidal current is observed during flood and no clear tendency for preferred sediment deposition on the downdrift side of the inlet is found. The conclusion is therefore that the conceptual ideas of Sha (1989a,c) are only partly confirmed by the model results shown here. This conclusion does not depend on the precise formulation of the sediment transport. In fact both a suspended-load and total-load formulation yielded almost the same transport patterns. This implies that, for the case studied, settling lag effects and diffusive sediment fluxes only marginally contribute to the total tidally averaged sediment flux. Consequently, the two important mechanism controlling the net transport are the combined stirring of sediment by tides and subsequent transport by residual currents and tidal asymmetry. Quantitative analysis of the sediment fluxes has shown that they are mainly driven by the first mechanism on the seaward side of the strait whereas tidal asymmetry is the dominant factor in the basin. The spatial pattern of the sediment flux is such that there is a clear tendency to deposit sediment both on the seaward and on the landward side of the barrier islands.

The subsequent development of the bathymetry was investigated by performing long-term simulations with the complex model of the Frisian Inlet system, starting from the symmetrical bathymetry as described above. It was found that the system develops into a double-inlet system with two clearly recognisable outer deltas having both an asymmetrical shape. The eastern outer delta is characterised by an updrift-oriented main channel and has a larger dimension than the western outer delta, which has a downdrift-oriented channel. In the initial phase (a few hundreds of years) the outer deltas rapidly extend seaward, but after about 500 years the increase of their sand volume is much slower. Despite this behaviour, channels are still developing, indicating that the final state is not steady.

The conclusion is that the asymmetrical shape of outer deltas and the preferred direction of channels can only be found from long-term morphodynamic simulations. This suggests that strongly nonlinear feedback between tidal motion and erodible bottom are important to understand these properties. Details of this complicated process are not yet understood, but at least the numerical results show some interesting aspects. First, the fully developed bathymetry computed with the numerical model has many similarities with the observed bathymetry of the Frisian Inlet. This includes features like two outer deltas, the eastern one being larger than the western one, the presence of channels on the outer delta and branching of channels in the eastern part of the basin. Furthermore, the orientation of the main channel on the western outer delta is downdrift-oriented, a property which is usually attributed to the action of waves and wind (Sha and Van den Berg, 1993; FitzGerald, 1996). However, since the water motion in the present model is only driven by tides this puts such a statement in a different perspective. It is also worthwhile to remark that no migration of channels and shoals occurs in the model. This is consistent with the model study of Cayocca (2001) and with the hypothesis of Sha (1989a) that migration of shoals is induced by wind, waves and aeolian processes. Finally, it is important to remark that in the

model simulations no account was made of the possible effect of the 'Engelsmanplaat', a nonerodible shoal in the middle of the Frisian Inlet. It was suggested by Wang et al. (1995) that the Engelsmanplaat could be an important factor for the morphodynamic stability of the Frisian Inlet. This statement is not confirmed by the model results presented here, which show smooth behaviour even in the absence of this shoal.

Acknowledgement

The authors thank prof. J. Backhaus from the University of Hamburg, Inst. für Meereskunde, for providing the HAMSOM code and dr. E. Spee from IMAU for the software extensions. WL| Delft Hydraulics is thanked for permission to use the Delft3D model (here called DELFT2D-MOR). The simulations with this model were performed by drs. M. van der Vegt from IMAU.

5.A Tidal eccentricity

As shown by Prandle (1982) the behaviour of the horizontal velocity of a specific tidal constituent (with radian frequency ω) can be described by a tidal ellipse. This ellipse can be decomposed into two circular horizontal tides rotating in opposite directions with amplitudes W_+ and W_- and phases ϕ_+ and ϕ_-:

$$u = W_+ \cos(\omega t - \phi_+) + W_- \cos(\omega t - \phi_-),$$
$$v = W_+ \sin(\omega t - \phi_+) - W_- \sin(\omega t - \phi_-).$$

The amplitudes and phases can be expressed in terms of the Fourier coefficients of the velocity components u and v, as given by the expressions

$$u = u_c \cos(\omega t) + u_s \sin(\omega t),$$
$$v = v_c \cos(\omega t) + v_s \sin(\omega t).$$

Thus, using both expressions for u, v, W_+, W_-, ϕ_+, ϕ_- can be expressed in terms of the amplitudes u_c, u_s, v_c, v_s.

Instead of the amplitudes W_+, W_- and phases ϕ_+, ϕ_- the tidal ellipse can also be characterised by the following four quantities:

$$U = W_+ + W_- \qquad \Theta = \frac{1}{2}(\theta_+ + \theta_-),$$
$$V = W_+ - W_- \qquad \Psi = \frac{1}{2}(\theta_+ - \theta_-).$$

Here U and V are the long and short axis of the ellipse, respectively. Furthermore Θ is the phase at which the tidal current reaches a maximum and Ψ is the orientation of the long axis with respect to the x-axis. Finally, the eccentricity of the tide is defined as

$$e = \frac{V}{U},$$

i.e., it is the ratio of the short and long axis of the tidal ellipse.

5.B Net sediment transport: role of residual currents and tidal asymmetry

In order to illustrate how residual currents and overtides contribute to net sediment transport the concepts of Van de Kreeke and Robaczewska (1993) are briefly summarised. Consider the simple one-dimensional sediment transport formulation

$$F = \hat{F} u^3, \tag{5.8}$$

where $\hat{F}$ is a constant. Assume the velocity field to be of the form

$$u = u_0 + u_2 \cos(\omega t) + u_4 \cos(2\omega t - \beta). \tag{5.9}$$

Here u_0 is the residual current, u_2 and ω are the amplitude and frequency of the M_2-tide and u_4 and β are the amplitude and phase of the M_4-tide, respectively. In many tide-dominated areas this is a good representation of the main velocity component.

The net sediment transport $< F >$ induced by this velocity field is found from substituting eq. (5.9) into eq. (5.8) and averaging the result over a tidal period. In case that $u_2 \gg |u_0|, u_4$, a condition which is often met in the field, it follows that

$$< F >=< F >_{\rm res} + < F >_{\rm asym}, \;\; < F >_{res} = \frac{3}{2}\hat{F} u_2^2 u_0, \;\; < F >_{asym} = \frac{3}{4}\hat{F} u_2^2 u_4.$$

The term $< F >_{\rm res}$ represents the transport due to the combined action of sediment stirring by tides and transport by the residual current. The contribution $< F >_{\rm asym}$ is the net transport due to tidal asymmetry: it is fully determined by the M_2- and M_4-constituents of the tidal velocity field. If $u > 0$ represents a flood current then $< F >_{\rm asym}$ is flood (ebb)-dominant if $\cos(\beta) > 0$ (< 0). In all these cases the tidal velocity curve is asymmetrical.

In this paper two-dimensional velocity fields and more sophisticated sediment transport formulations are used, but they still allow for the computation of the net transports induced by residual currents and tidal asymmetry, respectively.

Chapter 6

Summary and suggestions for further research

In this thesis the hydro- and morphodynamics of tidal inlet systems have been investigated with the use of process-based models. Here the main results are summarised and briefly discussed. Finally, a few suggestions for further research are given.

6.1 Summary

6.1.1 Main research topics

Tidal inlet systems consist of three geometrical parts: the actual inlet, the inner basin and the outer delta. The latter is a shallow area located seaward of the inlet. The emphasis of the research was on tide-dominated (compared to other forcing agencies such as waves) inlet systems, as e.g. those located in the Dutch Wadden Sea. The specific research questions focused on two main aspects. The first was the physics of morphological pattern formation in the inner basin. The second was the hydro- and morphodynamic interaction between the inner basin and outer sea, including the dynamics of the outer delta. This resulted in five specific research questions (Q_1 to Q_5, see section 1.5) which are re-addressed below.

6.1.2 Morphodynamic equilibria in tidal basins

In the past, idealised models (simplified equations of motion and simplified geometry) have been used to find morphodynamic equilibria (defined by steady bottom profiles) for tidal basins. Schuttelaars and De Swart (1996) showed that for short tidal embayments (short with respect to the tidal wave-length) such morphodynamic equilibria exist which consist of the constantly sloping bottom in the landward direction. However, the field data presented in Chapter 2 (figure 2.1) show that in the Dutch Wadden Sea this is not always quite true: most bottom profiles are slightly convex or concave. It was hypothesised in this thesis that the departure from the constantly sloping bottom might be due to the sediment transport

formulation, the effects of tidal flats (hypsometric effects) (Speer and Aubrey, 1985) or width convergence (Friedrichs and Aubrey, 1994).

To investigate the influence of these aspects (research question Q_1) a one-dimensional (cross-sectionally averaged) idealised model was derived and analysed in Chapter 2. Results are discussed for the case that sea level variations at the seaward open boundary only consist of the leading tidal constituent (here the M_2 tide). If a constantly sloping bottom is used then, in the case of a constant width and no tidal flats, the tidally averaged advective and diffusive sediment fluxes each vanish. Both width convergence and the presence of tidal flats cause net advective export of sediment in the system. At the same time width convergence leads to an increase of the net diffusive sediment flux in the landward direction. The influence on the equilibrium bottom profile for a converging basin with tidal flats and advective and diffusive sediment transport of the same order of magnitude is negligible: the seaward directed net advective transport is compensated by the increased landward-directed net diffusive flux. The evolution of the bed towards the equilibrium bottom profile in this case is dominated by diffusive processes. When a rectangular embayment with tidal flats is considered a slightly concave equilibrium bottom profile is found. Here the net seaward transport by advective processes is not compensated by diffusive effects. The use of a sediment deposition formulation related to the depth-averaged concentration leads to an increase in sedimentation and a convex equilibrium bottom profile compared to the case of sediment deposition related to the depth-integrated concentration. A reduction of the embayment length causes an import of sediment into the basin. This import is of the same magnitude as is predicted by field data after the closure of the Lauwers Sea (in the Frisian Inlet system). Sea level rise also causes sediment import.

6.1.3 Channel-shoal formation in the basin

Once a one-dimensional equilibrium profile has been found for the basin a two-dimensional perturbation analysis can show which two-dimensional patterns might appear as free instabilities on this profile. Schuttelaars and De Swart (1999) applied this method and found global bottom patterns (covering the entire basin area) that comprises channels and shoals. Seminara and Tubino (1998) on the other hand found local bottom patterns (with length scales of the order of the basin width) which resemble tidal sand bars. However, it is hard to compare these results as the two models are widely different. Schuttelaars and De Swart (1999) considers a semi-enclosed basin with weak bottom friction and only diffusive sediment transport, whereas Seminara and Tubino (1998) examine an open channel with frictionally dominated tidal flow and only advective transport of sediment.

In order to bridge this gap the idealised model of Schuttelaars and De Swart (1999) for a semi-enclosed basin was extended in Chapter 3 to account for advective as well as diffusive transport of sediment (research question Q_2). Both strong and weak bottom friction were considered. Bottom patterns were determined using a linear stability analysis, which means that amplitudes of the bed forms are not known. The resulting patterns turned out to be controlled by the relative strength of the diffusive flux (F_{diff}) and the advective flux (F_{adv}): the three different cases are listed below. The expe-

riments also showed that the advective sediment flux is governed by transport of the mean background concentration by the residual current. Thus, advective transport due to internally generated overtides and settling lag effects are of minor importance. The e-folding timescale of growth of the most preferred bottom pattern is of the order of decades. No migration was found, except in one case of dominant advective transport.

$F_{diff} \gg F_{adv}$ Global bottom patterns are found which scale with the embayment length and resemble a channel-shoal topography. These bottom patterns are similar to those found by Schuttelaars and De Swart (1999). Pattern growth is caused by the divergence of the cross-channel diffusive flux because the mean concentration above the bar is lower than in the trough. The sediment transport is illustrated in figure 6.1(a).

$F_{diff} \ll F_{adv}$ Local bottom patterns are found near the entrance which scale with the embayment width. These patterns resemble the patterns found by Seminara and Tubino (1998) and are referred to as tidal sand bars. Growth of these patterns is caused by divergence of the advective along-channel sediment flux (related to transport of mean concentration by the residual current). This mechanism is illustrated in figure 6.1(b).

$F_{diff} \sim F_{adv}$ Global bottom patterns are found, which have similar characteristics as for the diffusively dominated case. Bottom pattern growth is caused by the divergence of the along-channel and cross-channel advective flux and by the divergence of the cross-channel diffusive flux. Here the advective transport of sediment follows the residual current, but the transport of sediment from bar to trough is counteracted by diffusive sediment transport in the opposite direction, This can be seen by combining figures 6.1(a) and 6.1(b).

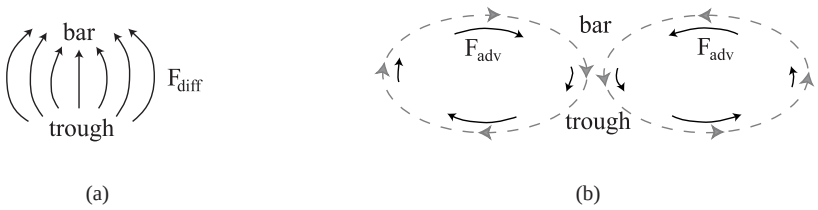

Figure 6.1: A topview sketch of the mechanism for bottom pattern growth in the case of (a) dominant diffusive transport and (b) dominant advective transport. The drawn lines indicate net sediment transport, the dashed lines indicate the residual current pattern.

The results were qualitatively confirmed by experiments with the complex numerical model DELFT3D (in this thesis referred to as DELFT2D-MOR), developed by WL|Delft Hydraulics. A quantitative comparison was not possible due to model differences and the fact that amplitudes of the idealised model results were not known.

6.1.4 Interaction between basin and outer sea

The model results discussed so far concern the basin area. The idealised models require conditions for both the water motion and the bed level at the seaward boundary. Such conditions are difficult to determine in this context because they actually depend on the exchange of both water and sediment between the inner basin and the outer sea. Therefore, the interactions between the outer sea and the basin (research question Q_3) were studied in Chapters 4 and 5. A numerical model was analysed in Chapter 4 to represent a complete tide-dominated inlet system. This model consists of the hydrodynamical model HAMSOM (developed by Backhaus (1983), see also Backhaus (1985)) with added routines for suspended sediment transport and is referred to as an intermediate model. Far away from the inlet a shore-parallel tidal wave is prescribed as a boundary condition. The symmetry-breaking effects of earth rotation and a shore-parallel travelling tidal wave on the water motion and sediment transport pattern were studied. Residual current patterns were analysed as the results of Chapter 3 showed that advective sediment transport is dominated by the residual current.

The experiments showed that the effects of earth rotation and of a shore-parallel tidal wave lead to different residual current patterns and different erosion/deposition patterns in the basin. However, for the conditions found in the Dutch Wadden Sea the shore-parallel travelling tidal wave has a much stronger symmetry-breaking effect on the water motion than earth rotation. In Chapter 5 it was found that the initial sediment erosion and deposition patterns show a line of zero divergence across the strait. This indicates that the idealised morphodynamic boundary condition there (keeping the bottom fixed) is justified for initial development. However, long term evolution indicates a seaward shift of this line of no bottom change, thus indicating the influence of the outer delta on the basin evolution.

6.1.5 Outer delta dynamics

Research question Q_4 addresses the dynamics of outer deltas of tide-dominated inlet systems. Two remarkable characteristics are their spatial asymmetry (the main channel often has an updrift orientation with respect to the along-shore current) and cyclic behaviour: shoals form, migrate and ultimately attach to the downdrift barrier island on a decadal timescale. A conceptual model to understand these characteristics was formulated by Sha (1989b,c). The core of his hypothesis is that the interaction between the shore-parallel tidal current and the current in the strait would cause an overshoot of the flood current on the downdrift side of the inlet. This side would therefore be characterised by weaker and more circular currents, which would favour deposition there. A shoal would develop which would force the main channel in an updrift orientation. Subsequent migration of this shoal would be due to wind and wave effects. This conceptual model of Sha was tested in this thesis in Chapter 5 with the intermediate model described in the previous section. Only forcing at the open boundary by the M_2 tidal current was applied, so that wind and wave effects were not included. The geometry resembled the asymmetrical geometry of the Frisian Inlet system (the symmetry axis of the inlet does not coincide with that of the basin). The initial formation of an outer delta was studied, starting from a flat bed with only a cross-shore slope in the outer sea. This topography was chosen to resemble the situation of a recently breeched barrier.

The results of Chapter 5 do not show an overshoot of the flood current. Nevertheless, a region of more circular and slightly weaker currents is found near the downdrift barrier island. The hydrodynamic results of Chapter 4 for a symmetrical inlet also did not reveal an overshoot of the flood current. These model results thus only partly support the hydrodynamical aspect of Sha's model. The initial sediment transport pattern in Chapter 5 show that this region is not a region of increased deposition, but rather one of slight erosion. Therefore the morphodynamic part of Sha's model is not confirmed by these experiments. The initial sediment transport pattern shows the tendency to form an outer delta by strong deposition just outside the strait. Inside the basin sediment is deposited behind the headlands, indicating shoal formation. The dominant mechanism for sediment transport in the basin was found to be tidal asymmetry, whilst stirring and transport by the residual current was the dominant mechanism in the strait and outer area. These results were not sensitive with respect to the sediment transport formulation.

Long-term simulations were performed with the full morphodynamic model DELFT3D to investigate the time evolution of the initial bathymetry. This was done because the initial sediment transport pattern showed no clear preferred orientation of the main channels on the outer delta. The result resembles the gross characteristics of the Frisian Inlet system rather well. The formation of two distinct outer deltas is found, each with their own size and main channel. The main channel of the eastern inlet system has a downdrift orientation, whilst the main channel of the western inlet shows an updrift orientation with respect to the direction of tidal wave propagation. Thus it can be concluded that forcing by tides alone can cause a preferred orientation of the main channel on the outer delta: wave effects are not a necessary condition for this development. No migration of channels was found, so that waves are probably important for this process (research question Q_5). The width of the inlet allows for the development of a double inlet system, so that the Engelsmanplaat (a consolidated shoal in the middle of the Frisian Inlet system) does not seem a necessary condition for its stability, as was suggested by Wang et al. (1991).

6.2 Suggestions for further research

In the previous chapters the limitations of the results obtained have been extensively discussed. Here only the general aspects are re-addressed. First the one-dimensional, idealised model for inner basins, as discussed in Chapter 2, is considered. This model is representative for sheltered, semi-enclosed basins and is as such a useful tool to study morphodynamic equilibrium bottom profiles. The one-dimensional, idealised model is based on a degenerated version of the momentum equation, stating that the surface elevation is spatially constant throughout the basin (short embayment assumption). Thus, among other things, the effect of bottom friction on the hydrodynamics is neglected. The comparison in Chapter 4 of experiments with the intermediate model and results of the one-dimensional idealised model suggests that this assumption leads to both qualitative and quantitative differences between the models. Therefore it is recommended to study the influence of relaxing the rigid lid approximation on the one-dimensional equilibrium bottom profile. The idealised model also

cannot handle drying and flooding of shoals. This should be incorporated to study the effect of forcing with the leading tidal constituent and the first overtide.

In Chapter 3 channel/shoal formation in the basin was studied with a two-dimensional, idealised model using a linear bottom stress formulation and a simplified dependence of the bottom friction term on the local depth. The model representation could be improved by including the more realistic quadratic stress law, which is more effective. A complete non-linear analysis of the two-dimensional idealised model would yield amplitudes for the bottom patterns presented in Chapter 3, allowing for a better comparison of the results with quasi-realistic models and field data. Another, simpler, extension of these results would be to include the first overtide in the hydrodynamic forcing. The results of Chapter 1 show the influence of the M_4 tide and of a flood or ebb-dominated system on the morphodynamic equilibrium bottom profile. It is suggested to perform this extension before a fully non-linear analysis is tried.

The experiments with the intermediate model mentioned in Chapter 4 indicated that basin length is an important parameter with respect to exchange processes between the basin and the outer sea: it influences the phase difference between the shore-parallel tidal current and the current in the strait. Therefore it would be interesting to slowly extend the basin length of the inlet system considered in Chapter 4 from 10 km ($\sim$ length of the Frisian Inlet basin) to some 60 km ($\sim$ length of the Marsdiep basin). Analysis of the hydrodynamic parameters would yield insight into resonance behaviour. The role of waves and of forcing with the M_0 (tidal residual) and M_4 (first overtide) tidal components should also be studied in this respect.

The results of Chapter 5, obtained with the full morphodynamic model, show asymmetrical outer delta development but no migration of shoals. Only after some 200 years of morphological development does an asymmetry become visible in the outer delta. Therefore it is recommended to perform experiments including the effects of wind and waves, to investigate channel migration and to see whether wave effects speed up the evolution process. This is expected as waves are very effective in stirring up sediment which can then be transported by the currents. These experiments should also consider the littoral drift along the coast and the effect of a critical erosion velocity in the sediment pick-up function (which was not included in the experiments included in this thesis). This would introduce the physical effect of scour lag.

The results mentioned in the previous section have answered the research questions to a large extent. For idealised model studies the rectangular geometry suffices and the morphodynamic boundary condition at the entrance has been justified. The hydrodynamical boundary condition should include the shore-parallel travelling tidal wave. New mechanisms for bottom pattern growth were found. Experiments with a full morphodynamic model successfully simulated outer delta development and added significant insight into the dominant mechanisms of this process. As listed above, the results have their limitations. All the models used make assumptions with regard to the physical reality and the results should always be interpreted within the model context. However, the use of three different types of models (idealised, intermediate an quasi-realistic) provides a varied basis which lends the results a broader context than the use of only one model can. In this thesis the results of one model are compared to those of another, different model. This approach has yielded much insight into the mechanisms of pattern formation and outer delta development.

Bibliography

Backhaus, J. O., A semi-implicit scheme for the shallow water equations for application to shelf sea modelling, *Cont. Shelf Res.*, *2*, 243–254, 1983.

Backhaus, J. O., A three-dimensional model for the simulation of shelf sea dynamics, *Deutsche Hydrographische Zeitschrift (German Journal of Hydrography)*, *38*, 165–187, 1985.

Bailard, J., An energetics total load sediment transport model for a plane sloping beach, *J. Geophys. Res. C*, *86*, 10 938–10 954, 1981.

Cayocca, F., Long-term morphological modelling of a tidal inlet: the Arcachon Basin, France, *Coastal Eng.*, *42*, 115–142, 2001.

Chadwick, D. B. and Largier, J. L., The influence of tidal range on the exchange between San Diego Bay and the ocean, *J. Geophys. Res. C*, *104*, 29,855–29,899, 1999.

Cleveringa, J. and Oost, A. P., The fractal geometry of tidal channel systems in the Dutch Wadden Sea, *Geol. en Mijnb.*, *78*, 21–30, 2000.

Davis, R. A. J., *Coasts*, Prentice Hall, New Jersey, 1996.

Davis, R. A. J., Regional coastal morphodynamics along the United States Gulf of Mexico, *Oceanographic literature review*, *45*, 1998.

De Jong, K., *Tidally averaged transport models*, Ph.D. thesis, Delft University of Technology, 1998.

De Jong, K. and Heemink, A. W., A long-term morphodynamic model for estuaries and tidal rivers, in *Management of sediment : philosophy, aims and techniques*, pp. 687–697, Oxford & IBH Publishing co., New Delhi, 1995.

De Jong, K. and Heemink, A. W., A model for long–term morphodynamic behaviour of tidal basins, long estuaries, and tidal rivers, Tech. Rep. 96–153, Delft University of Technology, 1996.

De Swart, H. E. and Blaas, M., Morphological evolutions in a 1d model for a dissipative tidal embayment, in *Physics of Estuaries and Coastal Seas*, edited by J. Dronkers and M. Scheffers, pp. 305–314, PECS 1996, Balkema, Rotterdam, 1998.

De Vriend, H. J., Mathematical modelling and large-scale coastal behaviour, Part 1 : physical processes, *J. Hydraul. Res.*, *29*, 727–740, 1991.

De Vriend, H. J. and Ribberink, J. S., Mathematical modelling of meso–tidal barrier island coasts. part ii: Process–based simulation models, in *Advances in coastal and ocean engineering*, edited by P.-F. Liu, pp. 151–197, World Scientific, Singapore, 1996.

Delfina, A., Two-dimensional shallow flow equations for partially dry areas, *Water Resources*

Res., *36*, 3251–3264, 2000.

Dyer, K. R., *Coastal and estuarine sediment dynamics*, John Wiley & Sons, Chichester, 1986.

Dyer, K. R. and Soulsby, R. L., Sand transport on the continental shelf, *Ann. Rev. Fluid Mech.*, *20*, 295–324, 1988.

Ehlers, J., *The morphodynamics of the Wadden Sea*, Balkema, Rotterdam, 1988.

Engelund, F. and Hansen, E., *A monograph on sediment transport in alluvial streams*, Technical Press, Copenhagen, 1972.

Escoffier, F. F., The stability of tidal inlets, *Shore & Beach*, *8*, 114–115, 1940.

Fenster, M. and Dolan, R., Assessing the impact of tidal inlets on adjacent barrier island shorelines, *J. Coastal Res.*, *12*, 294–310, 1996.

FitzGerald, D. M., Shoreline erosional–depositional processes associated with tidal inlets, in *Hydrodynamics and sediment transport of tidal inlets*, edited by D. Aubrey and L. Weishar, pp. 186–225, Springer–Verlag, New York, 1988.

FitzGerald, D. M., Geomorphic variability and morphologic and sedimentologic controls on tidal inlets, *J. Coastal Res.*, *23*, 47–71, 1996.

Fredsoe, J. and Deigaard, R., *Mechanics of coastal sediment transport*, World Scientific, Singapore, 1992.

Friedrichs, C. T., Stability shear stress and equilibrium cross–sectional geometry of sheltered tidal channels, *J. Coastal Res.*, *11*, 1062–1074, 1995.

Friedrichs, C. T. and Aubrey, D. G., Tidal propagation in strongly convergent channels, *J. Geophys. Res. C*, *99*, 3321–3336, 1994.

Friedrichs, C. T. and Hammick, J. H., Effects of channel geometry on cross-sectional variation in along channel velocity in partially stratified estuaries, in *Buoyancy effects on coastal and estuarine dynamics*, edited by D. G. Aubrey and C. T. Friedrichs, pp. 283–300, American Geophysical Union, Washington D.C., 1996.

Friedrichs, C. T. and Madsen, O. S., Nonlinear diffusion of the tidal signal in frictionally–dominated embayments, *J. Geophys. Res. C*, *97*, 5637–5650, 1992.

Friedrichs, C. T., Armbrust, B. D., and De Swart, H. E., Hydrodynamics and equilibrium sediment dynamics of shallow, funnel-shaped tidal estuaries, in *Physics of Estuaries and Coastal Seas*, edited by J. Dronkers and M. Scheffers, pp. 315–327, PECS 1996, Balkema, Rotterdam, 1998.

Gibeaut, J. C. and Davis jr., R. A., Statistical geomorphic classification of ebb-tidal deltas along the west-central Florida coast, *J. Coastal Res.*, *18*, 165–184, 1993.

Glaeser, D. J., Global distribution of barrier islands in terms of tectonic setting, *J. Geol.*, *86*, 283–297, 1978.

Groen, P., On the residual transport of suspended matter by an alternating tidal current, *Neth. J. Sea Res.*, *3*, 564–575, 1967.

Harris, P. T., Pattiaratchi, C. B., Collins, M. B., and Dalrymple, R. W., What is bedload parting?, in *Tidal signatures in modern and ancient sediments*, edited by B. Flemming and A. Bartholomä, no. 24 in Special Publications, pp. 3–18, Blackwell Science Ltd, Oxford, 1995.

Hayes, M. O., Barrier island morphology as a function of tidal and wave regime, in *Proceedings of the coastal symposium on barrier islands*, edited by S. P. Leatherman, pp. 1–28, Academic Press, New York, 1979.

Hayes, M. O., General morphology and sediment patterns in tidal inlets, *Sed. Geol.*, *26*, 139–156, 1980.

Hench, J. L., Blanton, B. O., and Leuttich Jr., R. A., Lateral dynamic analysis and classification of barotropic tidal inlets, *Cont. Shelf Res.*, in press, 2002.

Hibma, A., Process-based modelling of tidal inlet systems, Tech. Rep. Z2575, WL—Delft Hydraulics and RIKZ, 1999.

Hicks, M. D., Hume, T. M., Swales, A., and Green, M. O., Magnitudes, spatial extent, time scales and causes of shoreline change adjacent to an ebb-tidal delta, Katikati Inlet, New Zealand, *J. Coastal Res.*, *15*, 220–240, 1999.

Hubbard, D. K., Oertel, G. F., and Nummedal, D., The role of waves and tidal currents in the development of tidal inlet sedimentary structures and sand body geometry: examples from North Carolina, South Carolina and Georgia, *J. Sediment. Petrol.*, *49*, 1073–1092, 1979.

Inman, D. L. and Nordstrom, C. E., On the tectonic and morphologic classification of coasts, *J. Geol.*, *79*, 1–21, 1971.

Israel, C. G. and Dunsbergen, D. W., Cyclic morphological development of the Ameland Inlet, the Netherlands, in *River, Coastal and Estuarine Morphodynamics Vol. 1*, edited by G. Seminara and P. Blondeaux, pp. 705–714, RCEM 1999, Genova, 2000.

Jeuken, M. C. J. L., *On the morphologic behaviour of tidal channels in the Westerschelde estuary*, Ph.D. thesis, Netherlands Geographical Studies, 279, Faculty of Environmental Sciences, Utrecht University, The Netherlands, 2000.

Kana, T. W., Hayter, E. J., and Work, P. A., Mesoscale sediment transport at Southeastern US tidal inlets: conceptual model applicable to mixed energy setting, *J. Coastal Res.*, *15*, 303–314, 1999.

Krol, M., On a Galerkin–averaging method for weakly nonlinear wave equations, *Math. Appl. Sci.*, *11*, 649–664, 1991.

Lanzoni, S. and Seminara, G., On tide propagation in convergent estuaries, *J. Geophys. Res. C*, *103*, 30 793–30 812, 1998.

Leatherman, S. P., *Barrier island handbook*, University of Maryland Press, College Park, 1988.

Li, C. and O'Donnell, J., Tidally driven residual circulation in shallow estaries with lateral depth variation, *J. Geophys. Res. C*, *102*, 27 915–27 929, 1997.

Michel, D. and Howa, H. L., Morphodynamic behaviour of a tidal inlet system in a mixed-energy enviroment, *Phys. and Chem. of the Earth*, *22*, 339–343, 1997.

Mulder, H. P. J., Sediment transport in the Friesche Zeegat basin field survey of 1991, Tech. Rep. GWAO-93.606X, Rijkswaterstaat, Tidal waters division, 1993.

Oertel, G., Ebb-tidal deltas of Georgia estuaries, in *Estuarine Research*, edited by L. Cronin, vol. 2, pp. 267–276, Academic Press, New York, 1975.

Oost, A. P., *Dynamics and sedimentary development of the Dutch Wadden Sea with emphasis on the Frisian Inlet.*, Ph.D. thesis, Utrecht University, 1995.

Oost, A. P. and De Boer, P. L., Sedimentology and development of barrier islands, ebb-tidal deltas, inlets and backbarrier areas of the Dutch Wadden Sea, *Senckenbergiana Maritima*, *24*, 65–115, 1994.

Perillo, G. M. E., *Geomorphology and sedimentology of estuaries*, Elsevier, Amsterdam, 1995.

Postma, H., Hydrologische problemen in estuariumgebieden, *Kon. Maatsch. voor Natuurkunde "Diligentia", 47*, 197–210, in dutch, 1969.

Postma, H., Hydrography of the Wadden Sea, Tech. rep., Working group Sticht. Veth Steun Waddenonderz., Leiden, 1982.

Prandle, D., The vertical structure of tidal currents, *Geophys. Astrophys. Fluid Dyn.*, *22*, 29–49, 1982.

Prandle, D., Tides in estuaries and embayments, in *Tidal hydrodynamics*, edited by B. B. Parker, pp. 125–152, John Wiley & Sons, New York, 1991.

Pugh, D. T., *Tides, surges and mean sea-level*, John Wiley & Sons, 1987.

Ranasinghe, R. and Pattiaratchi, C., The seasonal closure of tidal inlets: Wilson Inlet - a case study, *Coastal Eng.*, *37*, 37–56, 1999.

Ranasinghe, R., Pattiaratchi, C., and Masselink, G., A morphodynamic model to simulate the seasonal closure of tidal inlets, *Coastal Eng.*, *37*, 1–36, 1999.

Ridderinkhof, H., Tidal and residual flows in the western Dutch Wadden Sea 1 : numerical model results, *Neth. J. Sea Res.*, *22*, 1–22, 1988a.

Ridderinkhof, H., Tidal and residual flows in the western Dutch Wadden Sea 3 : vorticity balances, *Neth. J. Sea Res.*, *24*, 9–26, 1988b.

Ridderinkhof, H., On the sensitivity of the large scale transport and distribution of fine-grained sediments in a tidal basin to the formulation of the erosion-deposition cycle, in *Physics of estuaries and coastal seas*, edited by J. Dronkers and M. Scheffers, pp. 145–153, PECS 1996, Balkema, Rotterdam, 1998.

Ridderinkhof, H. and Zimmerman, J. T. F., Chaotic stirring in a tidal system, *Science*, *258*, 1107–1111, 1992.

Ridderinkhof, H., van Haren, H., Eijgenraam, F., and Hillebrand, T., Ferry observations on temperature, salinity and currents in the Marsdiep inlet between the North Sea and Wadden Sea, in *Proceedings of EUROGOOS conference Rome 1999*, Elsevier, accepted.

Rinaldo, A., Fagherazzi, S., Lanzoni, S., Marani, M., and Dietrich, W. E., Tidal networks 2. Watershed delineation and comparitive network morphology, *Water Resources Res.*, *35*, 3905–3915, 1999.

Robinson, A. H. W., Cyclical changes in shoreline development at the entrance to Teignmouth Harbour, Devon, England, in *Nearshore sediment dynamics and sedimentation*, edited by J. Hails and A. Carr, pp. 181–200, John Wiley & Sons, London, 1975.

Sanders, J. A. and Verhulst, F., *Averaging methods in nonlinear dynamical systems*, Springer–Verlag, New York, 1985.

Schramkowski, G. P., Schuttelaars, H. M., and De Swart, H. E., The effect of geometry and bottom friction on local bed forms in a tidal embayment, *Cont. Shelf Res.*, *22*, 1821–1834, 2002.

Schuttelaars, H. M. and De Swart, H. E., An idealized long-term morphodynamic model of a tidal embayment, *Eur. J. Mech., B/Fluids*, *15*, 55–80, 1996.

Schuttelaars, H. M. and De Swart, H. E., Initial formation of channels and shoals in a short tidal embayment, *J. Fluid Mech.*, *386*, 15–42, 1999.

Schuttelaars, H. M. and De Swart, H. E., Multiple morphodynamic equilibria in tidal embayments, *J. Geophys. Res. C*, *105*, 24 105–24 118, 2000.

Schuttelaars, H. M., Schramkowski, G. P., and De Swart, H. E., Initial formation of estu-

arine sections, in *Proc. of the International conference on River, Coastal and Estuarine Morphodynamics 2001*, edited by S. Ikeda, pp. 443–452, ASCE, New York, 2001.

Seminara, G. and Tubino, M., On the formation of estuarine free bars, in *Physics of Estuaries and Coastal Seas*, edited by J. Dronkers and M. Scheffers, pp. 345–353, PECS 96, Balkema, Rotterdam, 1998.

Sha, L. P., Cyclic morphological changes of the ebb-tidal delta, Texel inlet, The Netherlands, *Geol. en Mijnb.*, pp. 35–48, 1989a.

Sha, L. P., Sand transport patterns in the ebb tidal delta off Texel inlet, Wadden Sea, The Netherlands, *Mar. Geol.*, *86*, 137–154, 1989b.

Sha, L. P., Variation in ebb-delta morphologies along the West and East Frisian Islands, The Netherlands and Germany, *Mar. Geol.*, *89*, 11–28, 1989c.

Sha, L. P. and Van den Berg, J. H., Variation in ebb-tidal delta geometry along the coast of The Netherlands and the German Bight, *J. Coastal Res.*, *9*, 730–746, 1993.

Smith, J. D. and McLean, S. R., Spatially averaged flow over a wavy surface, *J. Geophys. Res. C*, *82*, 1735–1746, 1977.

Soulsby, R., *Dynamics of marine sands*, Thomas Telford Publications, London, 1997.

Speer, P. E. and Aubrey, D. G., A study of nonlinear tidal propagation in shallow inlet/estuarine systems. part 2: Theory, *Est., Coastal and Shelf Sci.*, *21*, 207–224, 1985.

Stauble, D. K., An overview of Southeast Florida Inlet morphodynamics, *J. Coastal Res.*, *18*, 1–27, 1993.

Stelling, G. S. and Leendertse, I. I., Approximation of convective processes by cyclic ADI methods, in *Proc. Estuarine and Coastal Modelling*, edited by M. L. Spaulding, pp. 771–782, ASCE, Tampa, Florida, 1992.

Stommel, H. and Farmer, H. G., On the nature of estuarine circulation, Tech. Rep. Ref. 52-51, 52-63, 52-88, Woods Hole Oceanogr. Inst., Woods Hole, Mass., U.S.A., 1952.

Stronach, J. A., Backhaus, J. O., and Murty, T. S., An update on the numerical simulation of oceanographic processes in waters between Vancouver Island and the mainland: the GF8 model, *Ocean. Mar. Biol. Ann. Rev.*, *31*, 1–86, 1993.

Uncles, R. J. and Stephens, J. A., Distribution of suspended sediment at high water in a macrotidal estuary, *J. Geophys. Res. C*, *94*, 14 395–14 405, 1989.

Van de Kreeke, J. and Dunsbergen, D. W., Tidal asymmetry and sediment transport in the Frisian Inlet, in *Interactions between Estuaries, Coastal Seas and Shelf Seas*, edited by T. Yanagi, pp. 139–159, Terra Scientific Publishing Company, Tokyo, 2000.

Van de Kreeke, J. and Robaczewska, K., Tide-induced residual transport of coarse sediment; application to the Ems estuary, *Neth. J. Sea Res.*, *31*, 209–220, 1993.

Van den Berg, J. H., Jeuken, C. J. L., and Van der Spek, A. J. F., Hydraulic processes affecting the morphology and evolution of Westerschelde estuary, in *Estuarine shores: Evolution, Environments and Human Alterations*, edited by K. Nordstrom and C. Roman, pp. 157–184, John Wiley & Sons Ltd., Chisester, 1990.

Van der Molen, J., A 2DH numerical model of tidally induced sand transport in the southern North Sea, in *Interactions between Estuaries, Coastal Seas and Shelf Seas*, edited by T. Yanagi, pp. 265–285, Terra Scientific Publishing Company, Tokyo, 2000.

Van der Molen, J. and De Swart, H. E., Holocene tidal conditions and tide-induced sand transport in the southern North Sea, *J. Geophys. Res. C*, *106*, 9339–9362, 2001.

Van Dongeren, A. R. and De Vriend, H. J., A model of morphological behaviour of tidal basins, *Coastal Eng., 22*, 287–310, 1994.

Van Leeuwen, S. M., Schuttelaars, H. M., and De Swart, H. E., Tidal and morphologic properties of embayments : effect of sediment deposition processes and length variation, *Phys. and Chem. of the Earth*, *25*, 365–368, 2000.

Van Rijn, L. C., *Principles of sediment transport in rivers, estuaries and coastal seas*, Aqua Publ., Amsterdam, 1993.

Van Straaten, L. M. J. U. and Kuenen, P. H., Tidal action as a cause of clay accumulation, *J. Sediment. Petrol., 28*, 406–413, 1958.

Wang, Z. B., Louters, T., and De Vriend, H. J., A morphodynamic model for a tidal inlet, in *Computing Modelling in Ocean Engineering '91 – Proceedings of the second international conference, Barcelona, 30 September – 4 October 1991*, edited by A. S. Arcilla et al., pp. 235–245, Balkema, Rotterdam, 1991.

Wang, Z. B., Louters, T., and De Vriend, H. J., Morphodynamic modelling for a tidal inlet in the Wadden Sea, *Mar. Geol., 126*, 289–300, 1995.

Williams, J. J. and Rose, C. P., Measured and predicted rates of sediment transport in storm conditions, *Mar. Geol., 179*, 121–133, 2001.

Zhang, X., Boyer, D. L., Pérenne, N., and Renouard, D. P., Mean flow generation along a sloping region in a rotating homogeneous fluid, *J. Geophys. Res. C*, *101*, 28 597–28 614, 1996.

Zimmerman, J. T. F., Dynamics, diffusion and geomorphological significance of tidal residual eddies, *Nature*, *290*, 549–555, 1981.

Zimmerman, J. T. F., On the Lorentz linearization of a nonlinearly damped tidal Helmholtz oscillator, *Proc. Kon. Ned. Akad. v. Wetensch., 95*, 127–145, 1992.

List of symbols

	dimension	description
A	m	amplitude of the prescribed M_2 elevation
A_4	m	amplitude of the prescribed M_4 elevation
A	-	18N $\times$ 18 N matrix
$\overline{b}$	m	width of the channel at mean slack level
$\tilde{b}$	m	actual width of the channel
B	m	width of the channel at low water or basin width
B	-	18N $\times$ 18 N matrix
B_0	m	width of channel at the entrance
$B_{1,2,3}$	m	width of the basin, inlet and outer area, respectively
c_d	-	drag coefficient
C	kg m^{-2}	depth-integrated concentration, in Chapter 2
		depth-integrated and width-averaged concentration in kg m^{-1}
$\tilde{C}$	kg m^{-2}	time-varying part of C
$\tilde{D}$	-	ratio of advective and diffusive sediment fluxes
F	m^2 s^{-1}	tidally averaged sediment flux
g	ms^{-2}	gravity constant
$g^{'}$	ms^{-2}	reduced gravity constant
G	-	ratio of vertical diffusion timescale and the deposition timescale
h	m	bottom elevation measured from the reference depth
H	m	reference depth at the entrance
Im$\{\cdot\}$	-	Imaginairy part of the complex variable $\cdot$
l	-	lateral wavenumber
L	m	length of the channel or basin
$L_{1,2,3}$	m	length of the basin, inlet ans outer area, respectively
m	-	longitudinal mode number
n	-	lateral mode number
$\vec{n}$	-	normal vector
N	-	number of gridpoints

p	-	bed porosity
r	m s^{-1}	friction coefficient
Re$\{\cdot\}$	-	Real part of the complex variable $\cdot$
s	m^{-1}	width convergence parameter
t	s	time
T^*	s	e-folding timescale of perturbation growth
u	ms^{-1}	depth-averaged velocity in the along-channel direction
u_c	ms^{-1}	critical erosion velocity
u_T	ms^{-1}	transport velocity
U	ms^{-1}	characteristic velocity
v	ms^{-1}	depth-averaged velocity in the cross-channel direction
w_s	ms^{-1}	fall velocity
x	m	longitudinal coordinate
y	m	lateral coordinate
z_b	m	bed level with respect to the undisturbed water level
α	kg s m^{-4}	erosion coefficient
β	-	deposition parameter
γ	s^{-1}	deposition parameter
δ	-	ratio of the tidal period and the morphodynamic timescale
ϵ	-	A/H, measure of the advective terms
ϵ_b	-	hypsometry parameter
ϵ_4	-	M_4 amplitude over M_2 amplitude
ζ	m	surface elevation
ζ_e	-	power of the depth-dependency of the erosion term
ζ_d	-	power of the depth-dependency of the deposition term
ζ_{tide}	m	surface elevation at the entrance
κ	-	bed slope coefficient
λ	-	ratio of the basin length over the tidal wave length
μ_*	m^2 s^{-1}	horizontal diffusion coefficient
μ_v	m^2 s^{-1}	vertical diffusion coefficient
ρ	kg m^{-3}	water density
ρ_s	kg m^{-3}	density of sand
σ	s^{-1}	tidal frequency
τ	s	morphological timescale
τ_b	kg m^3 s^{-4}	frictional bottom stress
ϕ	$^\circ$	relative phase difference between M_2 and M_4
Ψ	-	vector containing the 18 state variables
ω	s^{-1}	growth rate
Ω	s^{-1}	vorticity

Subscripts

0,1	zeroth order or first order contribution in ϵ respectively
adv	contribution due to advective sediment transport
asym	contribution due to tidal asymmetry
b	bedload transport
diff	contribution due to diffusive sediment transport
eq	variable in the equilibrium state
res	contribution due to residual currents
t, τ, x, y	derivative in t, τ, x, y

Superscripts

s	amplitude of the $\sin(t)$ part of the solution
c	amplitude of the $\cos(t)$ part of the solution
x,y	contribution to the sediment flux in the x or y direction
2,3	amplitude of the $\sin(2t), \sin(3t)$ or $\cos(2t), \cos(3t)$ part of the solution

Notation

$< \cdot >$	tidally average
$\hat{\cdot}$	amplitude of $\cdot$
$'$	perturbation

Samenvatting

Veel kusten, verspreid over de hele wereld, worden gekenmerkt door de aanwezigheid van getijbekkens (zie figuur 1.1 in Hoofdstuk 1). Deze bekkens bestaan uit een bassin dat via een (nauw) zeegat verbonden is met de zee. De waterbeweging in getijbekkens wordt gedomineerd door eb- en vloedstromen: golven en wind hebben veel minder invloed. Typische voorbeelden van dergelijke getijbekkens zijn de bekkens in de Nederlandse Waddenzee. Deze bekkens worden daarnaast gekenmerkt door een dominant dubbeldaags getij (M_2 genaamd, waarbij de M staat voor maansgeïnduceerd getij en 2 voor 2 maal daags hoog water). De maximale stroomsnelheden tijdens eb en vloed zijn ongeveer 1 m/s. De waterbeweging in de Waddenzee wordt tevens gekenmerkt door een getijgolf die zich parallel aan de kust voortplant van west naar oost. Deze golf ontstaat als gevolg van de geometrie van de Noordzee.

Dat getijbeweging over een zanderige bodem tot complexe bodemvormen kan leiden is te zien aan de bathymetrie (bodemweergave) van het Marsdiep en het Friese Zeegat, zie Hoofdstuk 1 figuur 1.4 en 1.5. De bodems van de Waddenzeebekkens laten complexe geul-plaat patronen in het bassin zien en ondiepe delen aan de zeewaartse kant van het zeegat. De diepte van de hoofdgeul neemt af richting het land. De lengteas van het kanaal vormt zo bij benadering een lineair oplopende bodem. Geulen en platen manifesteren zich in het hele bassin en vertonen soms de neiging tot verplaatsing (migratie). De ondiepte gelegen aan de zeewaartse kant van het zeegat wordt een buitendelta (of ebdelta) genoemd. Ook hier bevinden zich geulen en platen die zich kunnen verplaatsen. De hoofdgeul op de buitendelta is vaak naar het westen gericht, tegen de voortplantingsrichting van de langs de kust lopende getijgolf in.

In dit proefschrift worden resultaten beschreven van een studie naar de morfodynamica (dynamische bodemvorming) van getijbekkens. Het onderzoek spitst zich toe op drie hoofdaspecten: (i) het modelleren en analyseren van de fysische mechanismen die zorgen voor bodempatroonvorming in het bassin, (ii) het modelleren en analyseren van de uitwisseling van water en zand tussen de buitenzee en het bassin en (iii) het modelleren en begrijpen van de ontwikkeling van buitendelta's en de voorkeursrichting van de hoofdgeul aldaar. Het Friese Zeegat dient als prototype getijbekken in dit proefschrift. Er wordt gebruik gemaakt van 3 verschillende proces-geöriënteerde modellen, zo genoemd omdat ze bestaan uit een mathematische beschrijving van fysische processen. Een geïdealiseerd model omvat alleen de belangrijkste processen en maakt gebruikt van een simpele geometrie (hier een rechthoekig bassin). Vanwege het geringe aantal processen dat beschreven wordt is dit model geschikt voor fundamenteel onderzoek naar fysische basismechanismen: de stap van gevolg (model-

uitkomst) naar oorzaak (fysisch mechanisme) is klein. Een quasi-realistisch model daarentegen neemt juist zoveel mogelijk processen mee om een betrouwbare weergave van de werkelijkheid te bieden. Dit type model is geschikt om bijvoorbeeld de ontwikkeling van zeegaten te simuleren. Vanwege hun complexiteit zijn ze minder geschikt om mechanismen te identificeren. Als derde is in dit proefschrift ook nog een intermediair model geconstrueerd. Dit model gebruikt een quasi-realistische beschrijving van de waterbeweging en een geïdealiseerde beschrijving voor zandtransport. Het vormt dus een tussenstap in de overgang van een geïdealiseerd model naar een quasi-realistisch model.

In de bovengenoemde modellen wordt het zandtransport gemodelleerd: de getijbeweging woelt zand op van de bodem dat vervolgens getransporteerd en elders gedeponeerd wordt. Eenmaal los van de bodem kan een zandkorrel zich op twee verschillende manieren verplaatsen. Zand dat meegevoerd wordt in de waterkolom wordt zwevend stoftransport genoemd. Bodemtransport vindt plaats als zand als gevolg van stroming en bodemhellingen over de bodem stuitert, rolt en springt. De zandkorrels houden dan contact met de bodem, iets wat bij zwevend stoftransport niet gebeurd. Het transport van zwevend stof kan via twee mechanismen verlopen: transport door concentratieverschillen (diffusief transport) en transport door de stroming (advectief transport). In dit proefschrift wordt gekeken naar zwevend stoftransport van zand en de relatieve rol van advectief en diffusief transport daarin. Bodemtransport als gevolg van stroming wordt buiten beschouwing gelaten.

Bodemvormen in het bassin

De vorming van bodempatronen in het bassin gebeurt op vele tijd- en ruimteschalen. Zo vormen kleine zandribbels zich in enkele uren, terwijl grote geul-plaatsystemen die het hele bekken beslaan er tientallen jaren over doen om zich te ontwikkelen. In dit proefschrift is allereerst onderzoek gedaan naar evenwichtsbodems in de hoofdgeul van het bassin. Een evenwichtsbodem is een bodem die in evenwicht is met de waterbeweging zodanig dat er getij-gemiddeld geen zandtransport meer plaatsvindt. Dit getij-gemiddelde transport is het kleine verschil tussen de grote hoeveelheden zand die bij vloed naar binnen en bij eb naar buiten worden getransporteerd. De bodem verandert dan dus niet op de getij-tijdschaal. Figuur 2.1 in Hoofdstuk 2 laat zien dat in de waddenzeebekkens de bodems oplopen naar het land en gekenmerkt worden door zowel ”bolle” als ”holle” profielen. Waardoor deze verschillen veroorzaakt worden is niet bekend. In Hoofdstuk 2 worden verschillende mogelijkheden onderzocht, te weten de aanwezigheid van zandplaten langs het kanaal en een trechtervormige geometrie zoals bij estuariums (bijvoorbeeld de Westerschelde) word gevonden. Ook worden diverse wiskundige formuleringen voor erosie en depositie van zand getest.

De patroonvorming wordt in het proefschrift onderzocht met behulp van een geïdealiseerd model. De resultaten van Hoofdstuk 2 laten zien dat een ”hol” bodemprofiel wordt gevonden als advectief transport van zand dominant is, terwijl een ”bol” profiel ontstaat bij dominant diffusief transport. Als beide transportmechanismen ongeveer even sterk zijn blijken zowel zandplaten als breedte-afname in de richting van het land geen effect te hebben op de evenwichtsbodem en wordt weer een lineair oplopende bodem gevonden. Wanneer zanderosie en -depositie beschreven worden met behulp van de dieptegemiddelde zandconcentratie in de waterkolom leidt dit tot meer depositie dan wanneer de erosie en depositie beschreven

worden met de diepte-geïntegreerde concentratie in de waterkolom.

De bodem van de hoofdgeul geeft een globaal evenwichtsprofiel aan waarop zich een complex systeem van geulen en platen bevindt. Vanwege dit complexe systeem wordt in Hoofdstuk 3 onderzoek gedaan naar het ontstaan van geul-plaat patronen, waarbij de vorm van de geul niet meer vastligt zoals in Hoofdstuk 2. In dit proefschrift is het onderzoek naar patroonvorming op de bodem beperkt tot twee verschillende typen fenomenen: enerzijds geul-plaat patronen die even groot zijn als het bekken zelf (globaal patroon) en anderzijds getijdebanken die vaak aan de ingang van een getijbekken worden gevonden (lokaal patroon) en die lengteschalen hebben ter grootte van de bekkenbreedte. De ontwikkeling van deze fenomenen vindt plaats op langere tijdschalen (enkele tientallen jaren), zodat alleen het getijgemiddelde zandtransport van belang is. Voor een kort bekken is de lineair oplopende bodem naar het land een evenwichtsbodem. Hierop wordt vervolgens een verstoring aangebracht in de vorm van een klein bergje zand. Zo'n verstoring kan groeien via een positieve terugkoppeling: het kleine bergje zand beïnvloedt de waterbeweging zodanig dat er zand naar het bergje wordt getransporteerd dat daardoor groeit en de waterbeweging nog sterker beïnvloedt, enzovoorts. De vraag is dan of er zo'n positieve terugkoppeling bestaat en hoe het bijbehorende bodempatroon er uitziet. In tegenstelling tot eerdere studies is hierbij gekeken naar zowel dominant advectief transport van zand, dominant diffusief transport als gecombineerd advectief en diffusief transport van vergelijkbare grootte.

De resultaten van Hoofdstuk 3 laten zien dat er inderdaad een positieve terugkoppeling bestaat. Met behulp van *lineaire stabiliteitsanalyse* worden groeiende bodempatronen gevonden, waarvan vervolgens de ontstaansmechanismen worden onderzocht. Zowel globale geul-plaat patronen als lokale getijdebanken worden gevonden. De eerstgenoemde patronen ontstaan als het diffusieve zandtransport even groot of groter is dan het advectieve zandtransport. Hiervoor zijn twee verschillende mechanismen verantwoordelijk, afhankelijk van de relatieve sterkte van het advectieve transport. Lokale getijdebanken worden gevonden als het diffusieve transport veel kleiner is dan het advectieve transport. Beide bodempatronen kunnen tegelijkertijd voorkomen als het advectieve zandtransport sterk genoeg is. Dit advectieve transport bestaat uit transport van de achtergrondconcentratie door de reststroming (tijdsonafhankelijke stroming) van de waterbeweging.

Bassin-zee interactie

De interactie tussen het bassin en de buitenzee is van belang voor de processen in het bassin, zoals de juist beschreven bodempatroonvorming. De condities op de buitenzee worden namelijk niet meegenomen in het geïdealiseerde model en daarom wordt deze interactie onderzocht in Hoofdstuk 4 met het intermediaire model. Dit model is namelijk in staat om een iets complexere geometrie te bevatten, bestaande uit een rechthoekige buitenzee die via een nauwe zeestraat verbonden is met een rechthoekig bekken. Bij verschillende condities op de buitenzee (zoals de sterkte van de kustlangse getijgolf) wordt gekeken naar de residuele waterbeweging in het bekken. Hoofdstuk 3 heeft immers laten zien dat deze residuele of reststroming van groot belang is voor het advectieve zandtransport.

Uit de resultaten van Hoofdstuk 4 blijkt dat de getijgolf in de Noordzee die zich langs de waddenkust voortplant een grote invloed heeft op het reststromingspatroon in het bassin.

De effecten van aardrotatie zijn, vergeleken met die van de getijgolf, van minder belang voor de waterbeweging in het bekken. Beide effecten leiden echter tot niet-verwaarloosbaar zandtransport in een rechthoekig bekken en beïnvloeden op deze wijze de vorming van bodempatronen.

Het ontstaan van buitendelta's

Het ontstaan van buitendelta's wordt onderzocht in Hoofdstuk 5. Een mogelijk mechanisme voor het ontstaan van asymmetrische buitendelta's werd geformuleerd door Sha (1989*b,c*). Zijn hypothese is dat de interactie tussen de stroming door het zeegat en de stroming langs de kust resulteert in een gebied met lage snelheden voor de kust van het stroomafwaarts gelegen eiland. De term stroomafwaarts heeft hier betrekking op de voortplantingsrichting van de getijgolf langs de kust. Voor de Waddenzee is dit in noord/oostelijke richting. De lagere snelheden zouden aanleiding zijn tot meer depositie van zand aldaar, waardoor zich een zandplaat gaat vormen. Deze plaat zorgt er vervolgens voor dat de hoofdgeul op de buitendelta wel stroomopwaarts gericht moet liggen. De zandplaat zou zich kunnen verplaatsen door wind- en golfwerking en zo uiteindelijk tegen het stroomafwaarts gelegen eiland "aanlopen". Dit fenomeen is onder andere bekend van het eiland Texel, waarbij over honderden jaren al enkele zandpaten zijn aangeland op de zuidwestkust. Verwacht wordt dat ook de zandplaat Noorderhaaks deze ontwikkeling zal volgen.

In Hoofdstuk 5 is het Friese Zeegat als voorbeeld gekozen, omdat er een quasi-realistisch model bestaat dat is afgesteld op dit zeegat. Dit maakt een vergelijking mogelijk tussen het intermediaire model en het quasi-realistische model. Interessante kenmerken van het Friese Zeegat zijn de twee subsystemen, het Pinkegat en de Zoutkamperlaag, die van elkaar gescheiden worden door de Engelsmanplaat, een compacte afzetting van klei die slechts langzaam erodeert. Beide systemen hebben een eigen buitendelta en hoofdgeul, waarbij die van de Zoutkamperlaag groter zijn dan die van het Pinkegat. Daarnaast heeft de Zoutkamperlaag een groter bassin. In het Pinkegat komt migratie van geulen en platen voor, in de Zoutkamperlaag niet meer sinds de afsluiting van de Lauwerszee (1969).

Eerst worden intiële patronen van zandtransport bestudeerd met behulp van het intermediaire model, om te zien of er aanwijzingen gevonden kunnen worden voor het spontaan ontstaan van buitendelta's. In het model is de bodem in het bassin en de zeestraat derhalve vlak en ondiep met een helling in de buitenzee, representatief voor een recent doorgebroken kust. De asymmetrische vorm is opgenomen in de modelgeometrie, de Engelsmanplaat niet. De resultaten laten zien dat er een gebied met lagere snelheden is aan de zeekant van het stroomafwaarts gelegen eiland. Dit is dus in overeenstemming met de hypothese van Sha. Het bijbehorende zandtransport-patroon laat zien dat er zand vanuit het zeegat naar buiten wordt getransporteerd en vlak voor de ingang wordt neergelegd. Dit gebeurt onder invloed van de zeewaarts gerichte reststroom die ontstaat in het bekken teneinde het door de getijgolf geïnduceerde landwaarts gericht transport te compenseren. Ook wordt er zand vanuit het zeegat naar binnen getransporteerd en vlak achter de eilanden gedeponeerd. Dit transport is het gevolg van interactie van het dubbeldaagse getij met een intern gegenereerde "hogere harmonische" van het getij. De hogere harmonische is hier een getijcomponent met de dubbele frequentie van het dubbeldaagse getij, veroorzaakt door interactie van de stroming met de

bodem (M_4 getij). Interne herverdeling van zand in het bekken wijst op geul/plaatvorming en op de vorming van een dubbel zeegat. De verdeling van erosie- en depositiegebieden op de buitendelta is echter symmetrisch: er is geen extra depositie voor het stroomafwaarts gelegen eiland. In het gebied met lagere snelheden vindt zelfs lichte erosie plaats. Er is dus geen bewijs gevonden voor de hypothese van Sha voor het ontstaan van asymmetrische buitendelta's.

Aangezien er nog geen sprake is van een bepaalde voorkeursrichting van de hoofdgeul op de buitendelta wordt ook naar de lange-termijnontwikkeling van het zeegat gekeken. Dit wordt gesimuleerd met behulp van het quasi-realistische model, zodat de morfologische evolutie van de buitendelta bestudeerd kan worden. De resultaten van Hoofdstuk 5 laten zien dat zich een dubbel zeegat ontwikkelt, waarbij het oostelijke zeegat de grootste geul en buitendelta vormt. Blijkbaar is de Engelsmanplaat niet essentieel voor de stabiliteit van het Friese Zeegat. Pas na zo'n 200 jaar bodemevolutie wordt er enige asymmetrie zichtbaar in het systeem: de hoofdgeul van het oostelijke getijbekken krijgt een stroomopwaartse (hier westelijke) richting op de buitendelta en ontwikkelt zich sneller dan de hoofdgeul van het westelijke systeem. Op grond van deze resultaten kan worden geconcludeerd dat de oriëntatie van de hoofdgeul, en daarmee de ruimtelijke asymmetrie van de buitendelta, wordt bepaald door niet-lineaire processen. Migratie van geulen en platen wordt niet gevonden. Verwacht wordt dat golfprocessen daarvoor essentiëel zijn.

Dankwoord

Nu dit boekje er eindelijk ligt wil ik nog een aantal mensen bedanken voor hun bijdrage. Een proefschrift schrijven is namelijk niet de éénmensactie die het lijkt.

In de eerste plaats, natuurlijk, Huib de Swart. Het enthousiasme waarmee hij op zoek gaat naar fysische mechanismen kent geen grenzen, wat resulteert in een inspirerende en gedetailleerde begeleiding. Ik heb heel veel van hem geleerd, met name wat het is om een goede onderzoeker te zijn.

In de tweede plaats wil ik Henk Schuttelaars bedanken voor zijn model (wat ik heb uitgebreid), zijn toezicht in vooral de eerste jaren van mijn onderzoek en zijn humor. Zijn eigen proefschrift vormde de leidraad voor Hoofdstuk 2 en 3, waar vervolgens als vanzelf het onderzoek van Hoofdstuk 4 en 5 uit voortvloeide. Maarten van der Vegt droeg een substantiëel zandsteentje bij aan Hoofdstuk 5, waarvoor dank. Mijn promotor Will de Ruijter wil ik bedanken voor zijn heldere en constructieve commentaar op mijn werk. Hoewel hij wat meer op afstand aanwezig was, was hij toch altijd geïnteresseerd in de resultaten. Ook de leden van de leescommissie ben ik dankbaar voor het kritisch doorlezen van het uiteindelijke manuscript.

De sfeer op het IMAU is altijd geweldig geweest en dat komt gewoon omdat er geweldige mensen werken. De kustenclub binnen het IMAU Natuur & Sterrenkunde zorgde voor een inspirerende en tevens vriendschappelijke werksfeer. Ook de IMAU-zwemclub, met onder anderen Meinte, Margreet, Lianke, Janine en Carina, droeg bij aan de broodnodige ontspanning. George Schramkowski wordt hartelijk bedankt voor de positieve berichtgeving tegenover de pers.

Herbert Koekkoek was een fijne en rustige kamergenoot in mijn eerste anderhalf jaar op het IMAU. Marcel Portanger wil ik bedanken voor de ettelijke keren dat hij mijn computer heeft gered na de zoveelste crash van de harde schijf. Piet Jonker was onmisbaar bij het creëren van voldoende schijfruimte en het onderhouden van de imauserver. Ook het secretariaat heeft in een wisselende bezetting veel ondersteuning geboden.

Mijn ouders, broer, verdere familie en vrienden wil ik graag bedanken voor hun geduld, alsmede hun ondersteuning en afleiding op het mentale vlak. Hopelijk kunnen ze met behulp van de nederlandstalige Samenvatting eindelijk begrijpen wat ik nou eigenlijk de afgelopen 4,5 jaar heb gedaan. Het achterstallig onderhoud in sociale contacten zal binnenkort worden aangepakt.

Als laatste wil ik graag drie mensen bedanken zonder wie ik waarschijnlijk de eindstreep niet gehaald zou hebben.

Marianne, jouw aanwezigheid in kamer 621 van het Buys Ballot Laboratorium maakte het promoveren tot een minder eenzame bezigheid. Omdat we vergelijkbaar werk deden onder dezelfde omstandigheden heb ik veel steun aan je gehad. Het gezamenlijk schelden op Huib, promoveren, Fortran, servers, Huib, modellen, Macjes, IDL enz. luchtte altijd enorm op. Bovendien is het gewoon gezellig met twee meiden op één kamer.

Gonda, jij hebt deze baan voor mij gevonden (”Ik heb hier een advertentie, dat is helemaal iets voor jou!”) en dus mag je me er ook weer vanaf helpen als paranimf. Onze emailcorrespondentie gaf de nodige relativering en afleiding tijdens werkuren en onze uitjes de nodige breaks. Je mentale steun was af en toe hard nodig, daarom is dit boekje ook enigzins van jou.

Johan, als vakgroep-collega en partner ben je de ideale paranimf. Wat mij betreft is onze relatie het mooiste resultaat van mijn promotieonderzoek bij het IMAU. Tijdens de 4,5 jaar die ik als oio (onderzoeker in opleiding) hier heb doorgebracht is behoorlijk afgeweken van de taakomschrijving in het originele onderzoeksvoorstel. De beschrijving van samenwerking met een postdoc op het NEESDI-programma met de opmerking *”The oio is expected to have close contacts with this postdoc”* (De oio zal nauw met deze postdoc in contact staan) is daarom met afstand het best gelukte onderdeel van die taakomschrijving. Ik hoop nog lang van deze ”close contacts” te mogen genieten.

Curriculum Vitae

Op 18 augustus 1972 zag ik het levenslicht in Schiedam. Na verhuizing naar Dordrecht volgde ik 2 jaar lang de HAVO/VWO-opleiding aan de Scholengemeenschap Zuid om vervolgens door te stromen naar het VWO op de (toen nog) Scholengemeenschap Noordendijk. In 1990 behaalde ik daar het VWO-diploma met een uitgesproken beta-pakket. De logische voorliefde voor wiskunde was gewekt en daarom vervolgde ik mijn opleiding van 1990 tot 1997 met de studie Technische Wiskunde aan de Universiteit Delft, met als specialisatie Mathematische Fysica. Het laatste jaar van mijn studie was gewijd aan een stage van 8 maanden bij het MARIN (MAritiem Research Instituut Nederland) te Wageningen, wat resulteerde in mijn afstudeerscriptie getiteld ”Finn-Hull interference, the force acting on the hull due to active fin stabilisers” bij Prof. A.J. Hermans van de vakgroep Toegepaste Analyse.

Tijdens de laatste fase van mijn afstuderen wees een vriendin mij op een vacature voor een onderzoeker in opleiding (oio) bij het Instituut voor Marien en Atmosferisch onderzoek Utrecht (IMAU), onderdeel van de Universiteit Utrecht. Na het spelen met bootjes tijdens mijn afstuderen was ik wel toe aan een iets natuurlijker onderwerp. In november 1997 begon ik als oio bij het IMAU in de vakgroep ’Fysische geografie en oceanografie van de kustzone’ onder supervisie van Huib de Swart. Het resultaat van dit onderzoek ligt voor u. Vanaf 1 februari 2002 ben ik voor 1 jaar in dienst van de Universiteit Utrecht om een kort onderzoek te doen voor Rijkswaterstaat.

Publications

Based on Chapter 2

S.M. van Leeuwen, H.M. Schuttelaars and H.E. de Swart, Tidal and morphologic properties of embayments: effect of sediment deposition processes and length variation, *Physics and Chemistry of the Earth, B, Vol. 25 (4)*, pp. 365-368, 2000

Based on Chapter 2 and 3

S.M. van Leeuwen and H.E. de Swart, The effect of non-linear and deposition processes on the morphodynamics of tidal embayments, in the proceedings of the I.A.H.R. symposium, *"River, coastal and estuarine morphodynamics", Vol. 1*, editor G. Seminara, Genova, pp 639-648, 2000

Based on Chapter 3

S.M. van Leeuwen and H.E. de Swart, The effect of advective processes on the morphodynamic stability of short tidal embayments, *Physics and Chemistry of the Earth, B, Vol. 26 (9)*, pp 735-740, 2001

S.M. van Leeuwen and H.E. de Swart, Tide-bottom interaction in an embayment model: the role of friction and advective processes, in preparation

Based on Chapter 4

S.M. van Leeuwen and H.E. de Swart, Intermediate modelling of tidal inlet systems: spatial asymmetries in flow and mean sediment transport, *Continental Shelf Research*, in press, 2002

Based on Chapter 5

S.M. van Leeuwen, H.E. de Swart and M. van der Vegt, Tidal characteristics and outer delta morphology: numerical experiments, in the proceedings of the second I.A.H.R symposium on *River, coastal and estuarine morphodynamics*, editor S. Ikeda, Japan, pp 473-482, 2001

S.M. van Leeuwen, M. van der Vegt and H.E. de Swart, Initial formation and long-term evolution of bottom features in tidal inlet systems: a model approach, under review for publication in *Estuarine, Coastal and Shelf Science*